A High Spatial Resolution Magnetovision Camera Using High-Sensitivity Quantum Well Hall Effect Sensors

A Thesis submitted to

The University of Manchester

For the Degree of

Doctor of Philosophy

In the Faculty of

Science and Engineering

2017

Chen-Wei Liang

School of Electrical and Electronic Engineering

Acknowledgement

This thesis is the result of three years research on "Using Quantum Well Hall effect magnetic field sensors in Non-destructive testing project". This was achieved at the University of Manchester, School of Electrical and Electronic Engineering. The course gave me the opportunity to learn, understand and practice circuit/system design.

I would like to thank all of the technicians from the numerous workshops who have been very hospitable. All of their help and support throughout the three years have made my research period more smooth and successful. In particular, I would like to thank Mr. Derrick Bradshaw who was very helpful and knowledgeable. With his guidance, support and suggestions, my circuits and prototypes have always been assembled successfully.

I would also like to thank to Dr. Zhichao Zhang who helped me to learn more about system design, research procedure and the underlying physics of analogue circuit design. From his example of strict adherence to research procedure, all of this research has been done with exceptional organisation and appropriate procedures.

Dr. Ertan Balaban provided extraordinary knowledge and experience on high speed digital circuit design, software design and digital signal processing. With his help on device programming and software development, my research on the magnetic field camera became possible and more successful.

Dr. Ehsan Ahmad provided much needed knowledge in semiconductor materials as well as the application of the physics behind my projects. With his guidance, my research was more organised and the physical mechanisms behind them was much more defined.

Dr. Mohammadreza Sadeghi, Dr Garduno N. Edson and Dr Kostakis Ioannis provided support throughout this PhD, but particularly in the early stages. With their help and support, I was able to make progress much more quickly.

Thanks is also due to Dr. James Sexton. Without his professional work in semiconductor fabrication, precision measurement and testing, this research would not have been possible. Dr. Sexton’s work included fabricating and supplying all the Quantum Well Hall effect sensors used during this research.

Finally, I would like to give my thanks and best wishes to my supervisor Prof. Mohamed Missous, who actively provided support, guidance and feedback throughout all of my research. I would also like to thank Prof. Missous on conducting the wafer growth and fabrication of the Quantum Well Hall effect sensors. He also provided his detailed knowledge and experience of the physics behind semiconductor design, as well as guidance on device optimisation and developing better fabricating procedures. With all of his active support, management and guidance, my research was much more successful.

Contents

List of Tables

List of Figures

Abstract

A systematic and detailed design, building and testing of a high-sensitivity real-time magnetovision imaging system for non-destructive testing (NDT) was the purpose of the research presented here. The magnetic imaging systems developed were all based on an ultra-high sensitivity Quantum Well Hall Effect (QWHE) sensors, denoted as the P2A, which is based on GaAs-InGaAs-AlGaAs 2DEG heterostructures. The research progressed from 0D (single sensor) to 1D (linear array) to 2D (two dimensional arrays) testing modalities.

Firstly, the measurement of thermal and shot noises, drift, detection limit, and dynamic offset cancellation of the QWHE sensor were studied in detail to set the framework and limitations of the fundamental QWHE sensors before their eventual use in the imaging systems developed subsequently. The results indicate that the measured data agrees well with calculations for thermal and shot noise when the input bias current is < 3 mA. The measured drift voltages of various QWHE sensors (P2A and P3A) are less than 200 μV when the sensor bias voltage is less than or equal to 2 V. A 4-direction dynamic offset cancellation technique was developed and the results show that the offset equivalent magnetic field of the QWHE sensors can be reduced from ~ 1mT to readings equal to the Earth magnetic field (~ 50 μT).

Secondly, a flexible 16 × 1 array and a 32 × 2 staggered array magnetic-field scanners were designed, built, and tested. The QWHE magnetometer had a field strength resolution of 100 nT, and a measurement dynamic range of 138 dB. The flexible 16 × 1 magnetic field scanner can be used to test uneven and/or curved surfaces. This gives the flexible magnetic field scanner better inspection capabilities in both welding hump and circular pipe samples. By the staggered arrangement of two sensor arrays, a 15.4 point per inch horizontal spatial resolution can be achieved for the staggered 32 × 2 magnetic field scanner. Both direct and alternating magnetic flux leakage (DC and AC MFL) tests with the QWHE magnetometer were accomplished to obtain graphical 2-dimensional magnetic field distributions. Both the shape and the location of defects can be identified. The results show that the sensor has high sensitivity and linearity in a wide frequency range which makes it an optimum choice for AC-MFL testing and both ferromagnetic and non-ferromagnetic materials can be investigated.

Thirdly, real-time 8 × 8 and 16 × 16 QWHE array magnetic-field cameras were designed, built, and tested. These prototypes can measure static magnetic field strengths in a 2-dimensional plane. Different shapes of magnets and magnetic field polarities can all be identified by the 8 × 8 magnetic field camera. The camera has a resolution of 3.05 μT, and a dynamic range of 66 dB (the minimum and maximum fields measurable are 3.05 μT and 6.25 mT) and a real time magnetic field measurement rate of 13 frames per second (FPS). By contrast the16×16 array magnetic field camera has an improved sampling rate of 600 frame per second and with the use of an interpolation technique, a spatial resolution of 40.6 point per inch can be achieved. The minimum and maximum detectable magnetic field for this magnetic field camera are 1.8 μT and 29.5 mT respectively leading to a record dynamic range of 84 dB for high quality imaging.

Finally, a novel, hand held, magnetovision system based on the real-time 16 × 16 QWHE array magnetic-field camera was developed for improved DC and AC electromagnetic NDT testing. The system uses a new super heterodyne technique for data acquisition using the QWHE sensor as a multiplier. This is the first report of such a technique in Hall effect magnetometry. The experimental results of five case studies demonstrate that the defects location and shape can be successfully measured with MFL in DC and AC magnetic field configurations *including depth profiling*. The major advantages of this real-time magnetic-field camera are: (1) its ease to use as a MFL testing equipment in both DC and AC NDT testing, (2) its ability to provide 2D graphical images similar to Magnetic Particle Inspection (MPI) but without its inherent health and safety drawbacks, (3) its capability to test both ferromagnetic and non-ferromagnetic materials for deep defects below the surface using low frequency alternating magnetic fields, and (4) its ability to identify materials (metals) by alternating external magnetic field illuminations, which has considerable potential in several applications such as security checking and labelling, magnetic markers for analysis, bio-imaging detection, and medical treatments amongst others.

Publications

Journal papers

1. M. Sadeghi, J. Sexton, **C. Liang** and M. Missous, "Highly sensitive nano Tesla Quantum Well Hall Effect Integrated Circuit using GaAs-InGaAs-AlGaAs 2DEG", IEEE sensors journal, November 2014, DOI: 10.1109/JSEN.2014.2368074.
2. **C.W. Liang**, E. Balaban, E. Ahmad, J. Sexton, M. Missous, "A Quantum Well Hall Effect linear isolator with wide frequency response and low gain temperature coefficient", Submitted to Sensors and Actuators A.
3. **C.W. Liang**, E. Balaban, E. Ahmad, Z. Zhang, J. Sexton, M. Missous, "A Real Time High Sensitivity High Spatial Resolution Quantum Well Hall Effect Magnetovision Camera", Submitted to Sensors and Actuators A.

Conference papers

1. **C.W. Liang,** E. Ahmad, E. Balaban, M. Missous "High Scan Speed High Spatial Resolution Quantum Well Hall Effect Magnetovision System with programmable AC coils illumination", 54th Annual Conference of BINDT, 8th-10th September 2015, Telford, UK.Code 116980; ISBN:978-0-903132-605
2. **C.W. Liang**, E. Ahmad, E. Balaban, J. Sexton, M. Missous, "A Quantum Well Hall Effect Magnetovision System for Non-Destructive Testing", 19th World Conference on Non-Destructive Testing, 13th -17th June 2016, Munich, Germany; Proceedings BB158, ISBN 978-3-940-283-78-8. **Keynote Presentation of conference session: *Mo.1.INew Methods (Sensor Concepts)*.**

Declaration

No portion of the work referred to in the thesis has been submitted in support of an application for another degree or qualification of this or any other university or other institute of learning

Copyright Statement

1. The author of this thesis (including any appendices and/or schedules to this thesis) owns certain copyright or related rights in it (the "Copyright") and s/he has given The University of Manchester certain rights to use such Copyright, including for administrative purposes.
2. Copies of this thesis, either in full or in extracts and whether in hard or electronic copy, may be made **only** in accordance with the Copyright, Designs and Patents Act 1988 (as amended) and regulations issued under it or, where appropriate, in accordance with licensing agreements which the University has from time to time. This page must form part of any such copies made.
3. The ownership of certain Copyright, patents, designs, trademarks and other intellectual property (the "Intellectual Property") and any reproductions of copyright works in the thesis, for example graphs and tables ("Reproductions"), which may be described in this thesis, may not be owned by the author and may be owned by third parties. Such Intellectual Property and Reproductions cannot and must not be made available for use without the prior written permission of the owner(s) of the relevant Intellectual Property and/or Reproductions.
4. Further information on the conditions under which disclosure, publication and commercialisation of this thesis, the Copyright and any Intellectual Property and/or Reproductions described in it may take place is available in the University IP Policy (see http://documents.manchester.ac.uk/DocuInfo.aspx?DocID=2442 0), in any

relevant Thesis restriction declarations deposited in the University Library, The University Library's regulations

(see http://www.library.manchester.ac.uk/about/regulations/) and in The University's policy on Presentation of Theses

Chapter 1
Introduction

1.1 Overview

Compared with all the different types of magnetic field sensors, Quantum Well Hall effect sensors fulfil the requirements of high magnetic sensitivity and reliability, low power consumption, small size factor, large signal-to-noise ratios, and low temperature dependence of output voltage; together with high yields and low cost. Consequently, Hall effect sensors have found ever increasing use in the fields of automation, industrial control, robotics and medical treatment/detection. Currently, commercial Hall effect sensors are mostly fabricated using traditional silicon Complementary Metal Oxide Semiconductor (CMOS)-based technology which have limited sensitivity (~10s of micro Tesla) but also benefit from a wealth of integrated electronics. Hall sensors using III-V semiconductor compounds can be easily purchased from Asahi Electronics. Low drift (GaAs), high sensitivity (InAs) and ultra-sensitivity (InSb) features for Hall effect sensors can be achieved by using different III-V compounds materials. To detect and explore low fields (~ nT), research and development on different types of Hall effect sensors based on pseudomorphic High Electron Mobility Transistors (pHEMT) have become one of the key objectives in industry and academia.

Non-destructive Testing (NDT) is the inspection of materials for surface cracks, internal flaws or metallurgical conditions, without compromising the samples under test. NDT is used for ensuring the integrity of the material or its suitability for in-service operation. NDT is not just a method for rejecting substandard materials, but is also a structural health monitoring technique to assure safe continued operation.

NDT is divided into various methods, each based on a particular scientific principle. The electromagnetic techniques most commonly used in industry include: (1) eddy current testing, (2) magnetic particle inspection, (3) magnetic flux leakage and (4) alternating current field measurement.

Eddy Current Testing (ECT) is used to detect near-surface defects and corrosion in metallic objects such as tubes, aircraft fuselages and similar structures. ECT is commonly applied to non-ferromagnetic materials, due to the fact that the depth of penetration is relatively small in ferromagnetic materials. The disadvantages of ECT are that it: (1) is very susceptible to magnetic permeability changes, (2) is only effective on conductive materials, (3) will not detect defects parallel to the surface, (4) is not suitable for testing large areas and/or complex geometries, (5) requires complex signal interpretation.

Magnetic Particle Inspection (MPI) is a technique for detecting surface and sub-surface defects. It is based on using dry or wet-suspension ferrous iron particles on magnetised ferromagnetic materials, such as iron, nickel, and some of their alloys. The major advantages of MPI are: (1) it is quick and relatively simple, (2) immediate indications of defects, (3) easily adapted for site or workshop use, (4) capable of examining both large and small objects, and (5) inexpensive compared to radiography and other NDT methods. However MPI has many disadvantages including: (1) being restricted to ferromagnetic materials, (2) messy due to the use of chemicals, (3) needs a relatively large electricity supply, (4) needs a high level of operator skill, (5) hazardous chemicals used can lead to the production of fumes or fire, (6) cannot be miniaturised or made portable.

Magnetic Flux Leakage (MFL) is another electromagnetic technique used for the non-destructive testing of steel samples. MFL is more commonly used in larger diameter pipes over long distances. Recently, the industry has turned its attention to using MFL to detect and quantify mechanical damage to pipes. An MFL testing sensor typically consists of a magnetic exciting apparatus and magnetic induction unit [1]. In practical applications, MFL detection systems typically use a magnetic yoke and detection coil [2–6]. Since there is little or no metal loss associated with mechanical damage, MFL signals arise from a complex combination of dent geometry and stresses in pipe walls [1]. However, using MFL to evaluate mechanical damage introduces numerous problems, including: (1) the MFL signal being a superposition of geometrical and stress effects, (2) the stress distribution around a mechanically damaged

region is very complex, consisting of plastic deformation and residual stresses and (3) the effect of stress on magnetic behaviour is not well understood [7].

Alternating Current Field Measurement (ACFM) techniques can replace conventional dye penetrant, magnetic particle and ultrasonic inspections, when sizing / profiling defects is required. ACFM is an electromagnetic technique for surface breaking cracks. This technique combines the advantages of the alternating current potential drop technique and ECT, able to perform defect sizing without calibration and can work without “hard” electrical contacts. The ACFM technique measures the disturbances in the magnetic field and uses mathematical algorithms to estimate the crack depth. This method demonstrates some limitations such as: (1) it can only be used for surface breaking cracks, (2) sizing models available for some materials but not all, (3) sizing models are based on planar cracks and so will not work on complex or branched cracks, (4) scanning with simple probes must be done in the expected direction of cracks and (5) transverse cracks can still be detected but cannot be sized without an additional scan.

In an attempt to solve many of the disadvantages of the above electromagnetic techniques, the present research has concentrated on developing a magnetovision scanning system using ultra-sensitive Quantum Well Hall effect sensors in both linear and 2D sensor array configurations.

1.2 Research aims

The key research aim of this work was the development and fabrication of a high performance magnetovision system using an ultra-sensitive Quantum Well Hall effect (QWHE) sensor array for non-destructive testing. To that effect, the following objectives were targeted:

1. In depth noise and drift measurements of the QWHE sensors.
2. Development of a 4-directional dynamic spinning current offset cancellation technique for removing offset voltages in the sensors.

3. Building and testing of a DC linear and 2D array QWHE magnetic field scanner (up to 16 × 16).
4. Design and fabrication of an alternating and static magnetic field QWHE 2D array magnetic camera using a superheterodyne technique.
5. Development of a 16 × 1 flexible QWHE array magnetic field scanner.
6. Development and implementation of camera measurement software.

Based on the objectives above, the design and fabrication of a high scanning speed, high spatial resolution QWHE magnetovision system with programmable AC illumination magnet field coils were successfully implemented. The sensor arrays were designed as magnetovision replacement or enhancement solutions to MPI, MFL and ACFM techniques. The 2D QWHE camera system features high refresh rate (maximum 600 frames per second), high spatial resolution (up to 40.6 point per inch), and programmable illumination alternating magnet field coils. The study is multidisciplinary and involved several techniques for the design, building and testing of the magnetovision system.

1.3 Thesis overview

Chapter 2 highlights and describes a series of electromagnetic non-destructive testing techniques. The methods of ECT, MFL, MPI, ACFM and magnetovision are discussed in detail; and are targeted for implementation in the Hall sensor arrays design, as described in Chapters 5 & 7.

Chapter 3 highlights a series of sub-theme paragraphs including heterojunctions and heterostructures, lattice-mismatches and pseudomorphic materials, Quantum Well and two-dimensional electron gas structures. The structures, behaviours, and operational principles of High Electron Mobility Transistors (HEMTs) and pseudomorphic High Electron Mobility Transistors (pHEMTs) are discussed in detail, in addition to four basic categories of their applications being compared. This chapter also summaries the results of the fabrication,

characterization and application of III-V heterostructure micro-Hall sensors in the published literature.

Chapter 4 describes the thermal noise, 1/*f* noise, shot noise, drift and detection limit measurements of the QWHE sensor. This chapter also outlines the dynamic quadrature offset cancellation technique with 4-types of spinning that was developed and implemented.

Chapters 5 - 6 detail the design, fabrication, testing and debugging of the single sensor magnetometer, 16 × 1, 16 × 1 flexible and 32 × 2 staggered linear Hall array magnetic scanners. This chapter also discusses the results of experimental work and validations associated with the single sensor magnetometer.

Chapters 7 - 8 describe the real time, high sensitivity, high spatial resolution QWHE magnetovision camera system, which include switches, amplifiers, programmable microcontroller, analogue and digital circuit boards. This chapter also discusses the refresh rate, spatial resolution, as well as the use of a superheterodyne technique and adjustable electromagnet. The experimental results have been presented to demonstrate the performance of this new magnetovision camera.

Chapter 9 summarises all the work undertaken (offset cancellation techniques, noise measurements, 1D and 2D QWHE array magnetometers and real time high spatial resolution QWHE magnetovision camera). Short and long term research in this relatively new NDT research topic is also discussed.

Chapter 2
Non-destructive testing and electromagnetic method inspections

2.1 Non-destructive Testing (NDT)

Non-destructive testing (NDT) is a collective name for several different analysis techniques which can be used to evaluate the properties, condition and remaining lifetime of materials and structures. Without compromising with the integrity of the sample, non-destructive testing techniques are widely used to find surface and internal flaws; and to check the metallurgical conditions. The applications of non-destructive testing include microstructure characterization, flaw detection, leak detection, location determination, dimensional measurements, determination of mechanical and physical properties, stress and strain measurements, dynamic response measurements and chemical composition determination. Non-destructive testing can be separated into different groups, based on their particular underlying scientific principles. The most common non-destructive testing techniques in industry are: (1) radiographic testing, (2) visual testing, (3) dye penetrant testing, (4) ultrasonic testing, (5) guided wave testing and (6) electromagnetic testing. Furthermore, in medical applications, where extremely small magnetic fields are present, numerous NDT technologies such as magnetic adaptive testing, ultrasonic testing, neutron radiographic testing, and superconducting quantum interference devices (SQUID) are used.

2.2 Electromagnetic testing

Electromagnetic testing is a group of non-destructive testing methods which involves principally electromagnetic forces or phenomena. The electric and magnetic fields are two main exhibitions of electromagnetic forces. Electric field is produced by electrically charged objects/particles, whereas magnetic field is produced by the movement of these electrically charged objects. The combination of these two fields is called an electromagnetic field. The

interaction of electromagnetic field and electric charge can be described using Maxwell's equations [8]. By measuring the interference between the electromagnetic field and tested objects, material properties and flaws can be characterised without destruction. In the following sections, the most common electromagnetic non-destructive testing methods are reviewed and described.

2.2.1 Eddy Current Testing (ECT)

ECT has been widely used in surface and sub-surface flaw detection and characterisation. The sensitivity of this technique is very dependent on the electrical conductivity and magnetic permeability of the sample under test, as well as the design of the search coils used to detect the resulting electromagnetic fields. Eddy current is usually induced by transmitter coils producing an alternating magnetic field. The magnetic field frequency can vary between 10 Hz and 10 MHz. Search coils can be designed to match different requirements. With customised searching coils, maximum efficiency can be achieved. The strength of the induced eddy current depends on the conductivity, permeability, and geometry of the metallic objects under test. When a crack is present in a tested subject's surface, the induced eddy current will deviate around or under the surface crack. This can be detected by measuring changes of the search coil impedances. Fig. 2.1 illustrates the principle of eddy current testing. Fig. 2.2 displays the schematic illustration of eddy current testing for detecting longitudinal defects on a pipe tube.

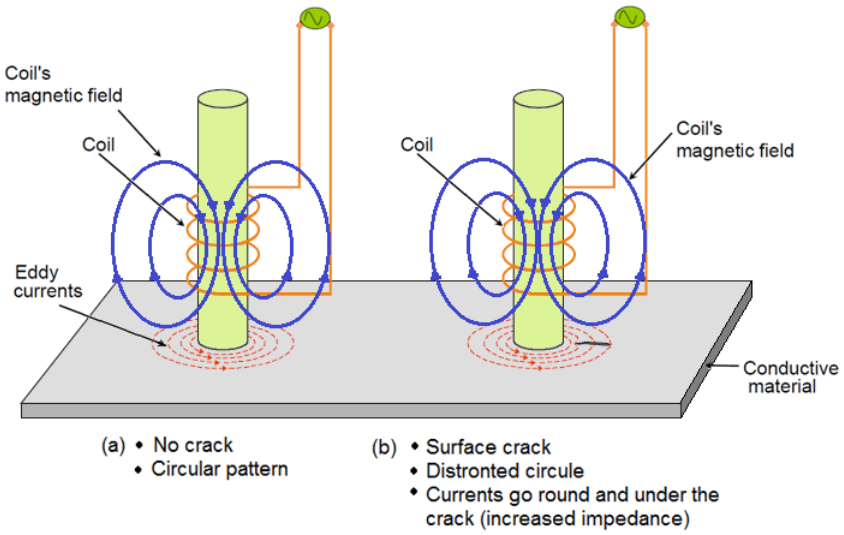

Fig. 2.1 Schematic illustration of eddy current testing for detecting surface flaws on a plate.

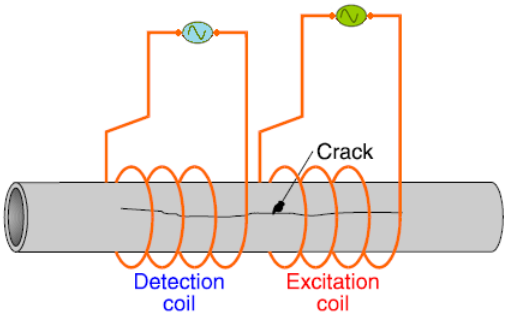

Fig. 2.2 Schematic illustration of eddy current testing for detecting longitudinal defects on a pipe tube.

Yusa et al. [9] designed an eddy current inspection apparatus with six different current probes to evaluate the efficiencies of welding. This setup is illustrated in Fig. 2.3. A probe was attached to a computer-controlled three-axial stage, with a single eddy current testing instrument, (Swan ECT aect2000s), used to excite the probe. The *x* and *y* component signals were obtained by this eddy current testing instrument and then digitised and stored on a computer. The results indicated that the reconstruction of the notches can be achieved by analysing the *x* and *y* components of eddy current testing signals with the use of uniform and suitable eddy current probes.

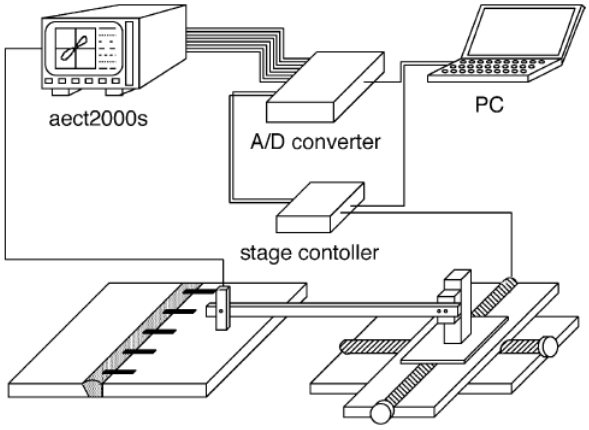

Fig. 2.3 Schematic illustration of experimental setup of eddy current inspections with six different current probes [9].

Radtke et al. [10] described a laser supported eddy current microscope for obtaining a real-time visualization of eddy current distributions. In this eddy current microscope, a laser beam is passed through a thin crystal which is integrated in the excitation coil. The polarization direction of the laser beam is rotated in this thin crystal which responds to the changes of magnetic field. The 2D distribution of the rotation angle is transformed into a grey scale image by using an optical setup which comprises a microscope, an illumination device, a polarizer and a charge-coupled device (CCD) sensor (Fig. 2.4). The results indicated that real-time magnetic field images with high spatial resolution could be measured.

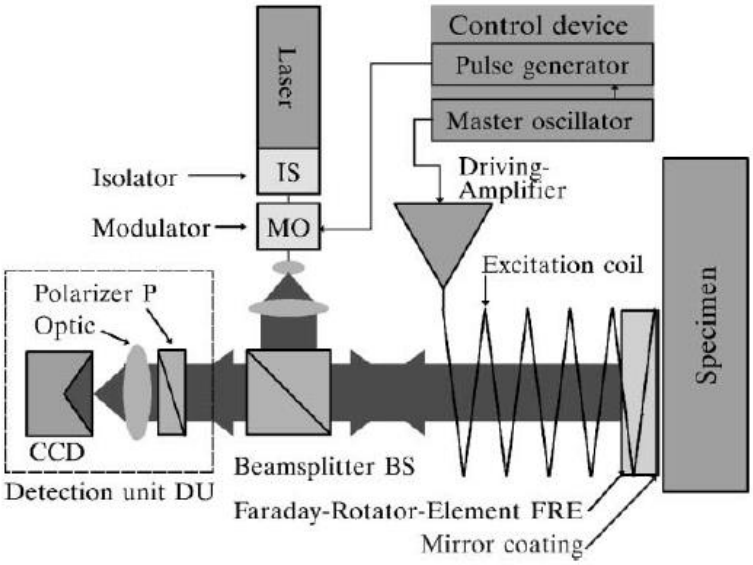

Fig. 2.4 Schematic illustration of the eddy current microscope [10].

2.2.2 Alternating Current Field Measurement (ACFM)

The basic technique of ACFM is measuring changes of magnetic field which are generated from the thin skin, near-surface induced current flows on electrically conductive objects. If a crack is present, the current flows paths will deviate around the crack which in turn, disturbs the induced magnetic field above the surface. The sensing probe of ACFM contains both field induction and field measurement coils. An excitation coil is driven with an alternating current to induce eddy current orthogonal to the crack direction on a target surface. Magnetic field is then induced by the eddy current on the sample surface under test. Two perpendicular magnetic field signals, B_x in the horizontal direction and B_z in the vertical direction, are measured. The strength of the horizontal magnetic field B_x is used to estimate the crack depth using mathematical algorithms, and the strength of the vertical magnetic field B_z is used to evaluate the length of the crack by measuring the distance between peak-to-peak values. Fig. 2.5 illustrates the interaction between induced eddy current and disturbed magnetic field when detecting surface crack.

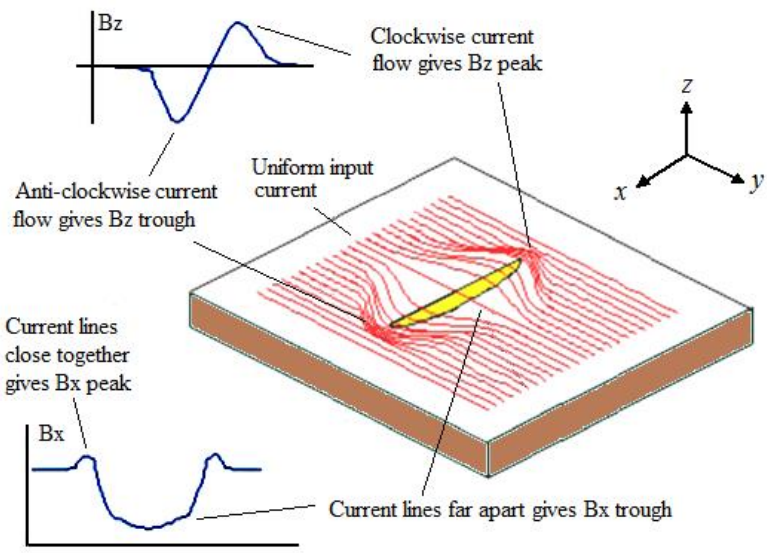

Fig. 2.5 Schematic showing of the operating principle ACFM.

When an ACFM probe is scanned across a test sample, sensing coils typically detect magnetic field strength signals B_x and B_z. The sensitivity of B_x (S_x) and the sensitivity of B_z (S_z) are given as follows [11]:

$$S_x = \frac{MX_{\max}}{MX_0} \tag{2.1}$$

$$S_z = \frac{MZ_{\max}}{MX_0} \tag{2.2}$$

where MX_0 is the amplitude of the B_x signal without defect, and $MX_{\max}$ and $MZ_{\max}$ are the maximum distortion of B_x and B_z above the defect. According to the principles of ACFM and its quantification algorithm [12,13], the distances L_z between peak and valley of the B_z component is directly related to the length of defect, and S_x and S_z are related to the depth of defect. In general, the characteristic vectors, i.e. S_x, S_z and L_z, affect the measurement accuracy of the ACFM technique.

Li et al. [11] designed an ACFM prototype system with a U-shaped probe to investigate the influence of induced frequency on the signal acquisition and the measurement accuracy of their ACFM system. The results show that 6 kHz is appropriate for crack inspection and sizing with reasonable accuracy. Nicholson and Davis [14] discussed the relationship between ACFM signal and Rolling Contact Fatigue (RCF) defects in railway tracks and wheels using a Finite Element Model (FEM) model developed using COMSOL Multiphysics software tools, verified for single and multiple RCF-type cracks. The response to semi-elliptical defects of surface length 2 mm to 40 mm and elliptical ratio 1:1 to 1.75:1, were simulated; and was shown that the ACFM signal is most sensitive to, and therefore able to accurately size RCF defects < 20 mm in surface length. Hasanzadeh et al. [15] constructed an aligning method by a Fuzzy Recursive Least Square Algorithm as a learning methodology for ACFM probe signals from a crack. The results showed that the combination of this fuzzy inference method and the method of adaptation for different crack shapes provide sufficient means as a priori empirical knowledge for training the system. Chen et al. [16] presented a double U-shaped

orthogonal inducer for ACFM, which could extend the limitation of the direction of tested cracks and decrease the loss of magnetic flux compared to the single rectangular inducer. The results showed that the relative errors of this probe were less than 10%, and it could suppress the lift-off disturbance effectively, which makes this 2-D ACFM probe array insensitive to lift-off distance. Knight et al. [17] indicated that the ACFM defect sizing capability may be compromised when it is used to inspect recently cold rolled connections. If a connection is cold rolled without first being defect free, subsequent inspections may estimate under crack depths with the standard interpretation. Inspection before rolling is therefore necessary.

2.2.3 Magnetic Particle Inspection (MPI)

MPI is one of the most universally used NDT methods. Its operating principle relies on spreading fine magnetic particles over the surface of a magnetised specimen under test, causing a congregation of particles at a discontinuity. This method is used to detect surface and near surface defects in ferromagnetic materials. The magnetic field of a magnetised material with surface-breaking flaw is distorted, causing local magnetic flux leakage around the flaw as shown in Fig. 2.6. The flux leakage can be displayed by covering the surface with very fine ferromagnetic particles, applied either dry or suspended in a liquid. The particles accumulate at the regions of flux leakage, producing a build-up which can be seen visually even when the crack opening is very narrow. Because magnetic flux lines don't travel well in air, when fine magnetic particles are applied to the surface, part of the magnetic particles will be drawn into the discontinuity, producing a visible indication of the defect on the surface of the material.

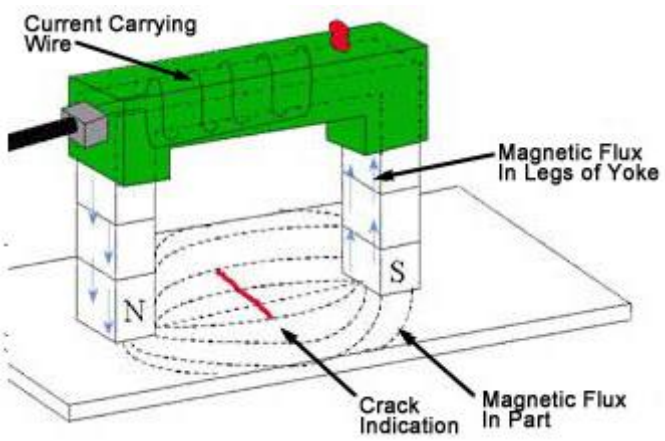

Fig. 2.6 Schematic illustration of constant field MPI method.
(Source: http://www.ventureinspection.co.uk/services/magnetic-particle-inspection/)

2.2.4 Magnetic Flux Leakage testing (MLF)

The magnetic flux leakage (MFL) technique is widely used to test high permeability magnetic alloys such as carbon steel. Because magnetic permeability is related to the skin depth of alternating current, eddy current testing is severely limited on ferromagnetic materials. This means that sub-surface and far surface defects are not detectable with eddy current methods.

The principle of MFL testing is shown in Fig. 2.7 [18]. Magnetic flux are produced or induced by solenoid wires. An external yoke magnet or electromagnet is used to saturate the magnetic flux inside the test material. When a defect is present in the test material, saturated magnetic flux will leak out of the material from the defect. A search coil is used to detect the leaking magnetic field. Defects on both the inner and outer sides can be detected. The magnetic field leakage of inner defects decreases as the sample thickness increases.

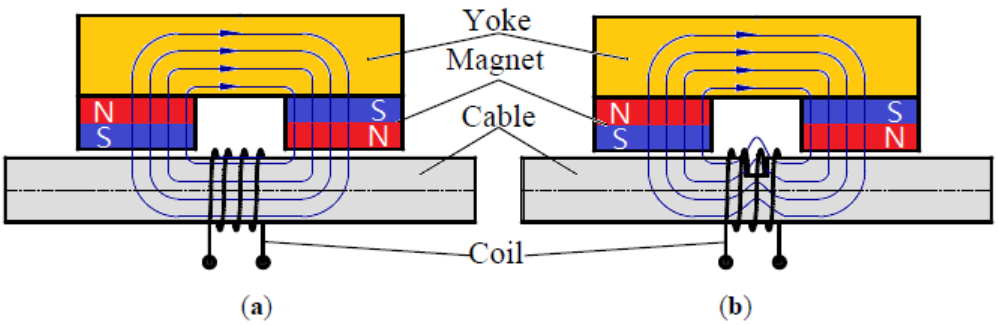

Fig. 2.7 Principle of MFL testing. (a) Undamaged cable; (b) Cable with metal loss [18].

There are two MFL methods that are widely used: alternating field MFL and constant field MFL [19]. Alternating field MFL methods concentrate the magnetic flux on the material surface, and is particularly sensitive to small surface defects from approximate 100 µm depth. In Fig. 2.8, two rotating yokes produce the magnetic flux for increased area coverage, with integrated magnetic field sensors that capture the flux leakage occurring at the defect locations.

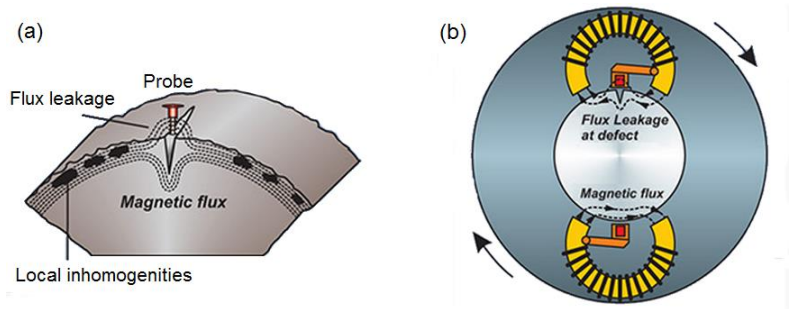

Fig. 2.8 Schematic illustration of alternating field MFL method [19].

Constant field MFL methods magnetise the material using two separate configurations, as shown in Fig. 2.9. Cross sectional magnetic flux, Fig. 2.9 (a), is provided by using a rotating DC electromagnet. The position of the poles of this magnet ensure the magnetic flux travels through the cross section of the sample. By rotating the magnet, 100% coverage of the sample can be achieved, meaning that longitudinally oriented defects can be detected, as well as defects on both the inner and outer sides of the sample surface. The flux leakage at the defect location is detected by rotating magnetic field sensors. Horizontal magnetic flux, Fig. 2.9 (b), is provided by two encircling coils which travels through the sample longitudinally. This is done for the detection of transverse-oriented defects. Several stationary magnetic field sensors on the circumference capture this flux leakage.

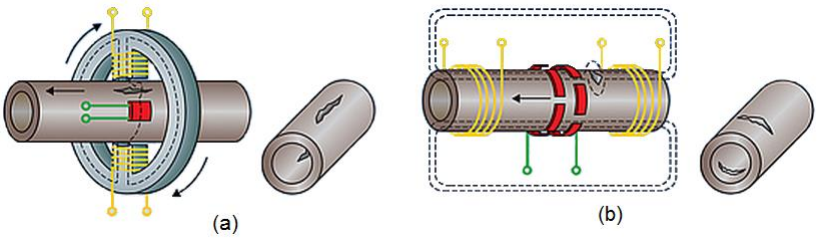

Fig. 2.9 Schematic illustration of constant field MFL method [19].

2.2.5 Magnetovision systems

The term "magnetovision" originates from thermal imaging systems which measure the distribution of heat with a thermal camera. The obtained colour thermal image can be presented as a relative magnetic field strength inside the material [20]. Therefore, magnetovision represents the visualisation of magnetic field distribution in a given space. A magnetovision system usually consists of a magnetometer, a two or three dimensional axial movement mechanism, data processing and visualization software. The following different modes of magnetovision signal acquisition are possible:

1. Magnetic field sensor moves in the measurement area on the sample.
2. Sample moves against the magnetometer.
3. The use of magnetic field sensor arrays (no mechanical movement).

Nowicki and Szewczyk [20, 21] developed and built a measurement scanning system as shown in Fig. 2.10 to study magnetic field vector distributions. Their results present the application of a weak magnetic fields magnetovision scanning system for the detection of ferromagnetic objects (Fig. 2.11). In this study, a mathematical model was suggested for the induction of the magnetic field on the axis of the magnet at a distance x from its centre:

$$B = \frac{\mu_0}{2\pi x^3} m = C \frac{1}{x^3} \tag{2.3}$$

where m is magnetic dipole moment (A m^2); μ_0 is magnetic permeability of vacuum; C is the induction replacement constant (T m^3). Since the value of the flux density B is reduced in proportion to the cube of the distance from the source, distortion B_1 caused by the object in the first measurement plane will be up to 8 times greater than the B_2 in the second plane. If other sources of magnetic field are at a significantly greater distance, i.e. $y >> x$, from the first measurement plane, their influence B_B on the value of magnetic induction in the planes P_1 and P_2 will be similar. Therefore:

$$B_{P1} = B_1 + B_{B1} \quad \text{and} \quad B_{P2} = B_2 + B_{B2} \tag{2.4}$$

Where B_{P1} and B_{P2} are the result of flux density measurement in planes P_1 and P_2, respectively; B_{B1} and B_{B2} are the background magnetic induction values in planes P_{B1} and P_{B2}, respectively. Assuming $B_{B1} \cong B_{B2}$ and $B_1 > B_2$. Then:

$$B_{P1} - B_{p2} \approx B_1 \tag{2.5}$$

Consequently, it is possible to get a rough magnetovision image, as shown in Fig. 2.11, where the sample is located at a short distance from the sensor, by subtracting the results of a measurement in the plane P_2 from the results in the plane P_1.

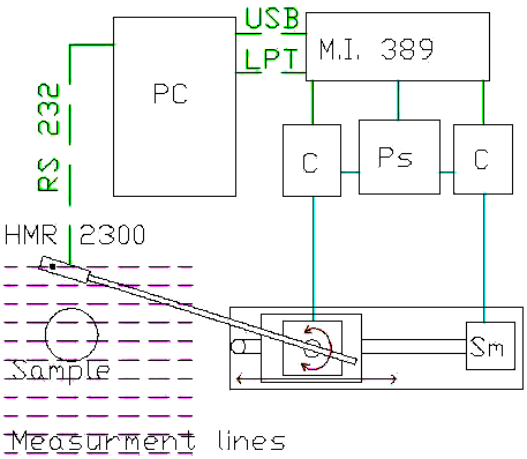

Fig. 2.10 Measurements data collected using scanning system developed in [20].

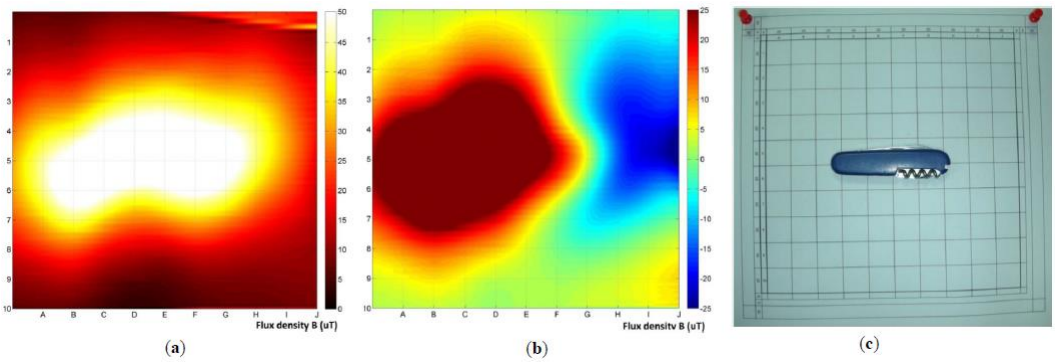

Fig. 2.11 Measurement of the position of ferromagnetic objects: (a) biplane differential measurement; (b) gradient measurement without background separation; and (c) a photograph of the actual position within 100 mm of the sample [20].

Kaleta and Wiewiórski [22] presented the design and measurement potential of their latest generation magnetic scanner, denoted as Magscanner-Maglab System (MMS). MMS

enables fast acquisition of 3D signals from magnetic sensors, visualising them as digital magnetic images for a variety of flat and cylindrical shaped samples. Fig. 2.12 schematically shows the location of the measuring head and how its position is ascertained by means of distance R_i and appropriate angles ϕ_i. Therefore, a 2D map of the magnetic field distribution can be obtained as a result of scanning the sample.

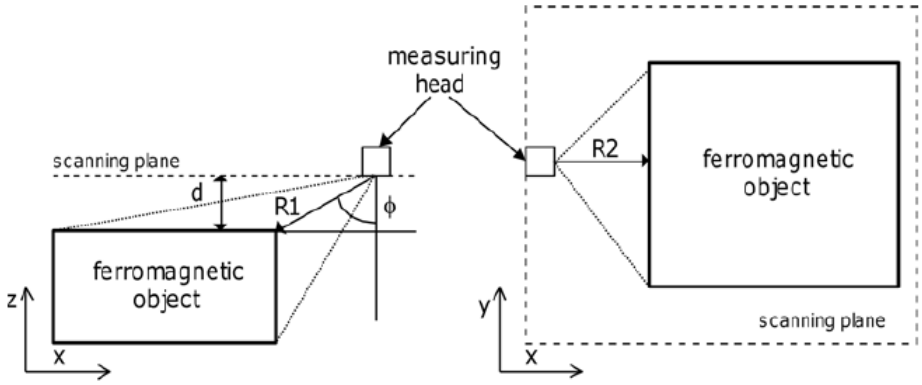

Fig. 2.12 Schematic illustration of scanning of the object plane [22].

Passive magnetic field sensors (such as magnetoresistive sensors and Hall sensors) were chosen to ensure that the magnetic field strength around the sample remained undisturbed. Fig. 2.13 shows the structure of the magnetovision system. A Hunt Engineering HERON card with a C6701 digital signal processor was used as the signal processing unit. The measurement data was digitised, decoded, digitally filtered, and Fourier transformed.

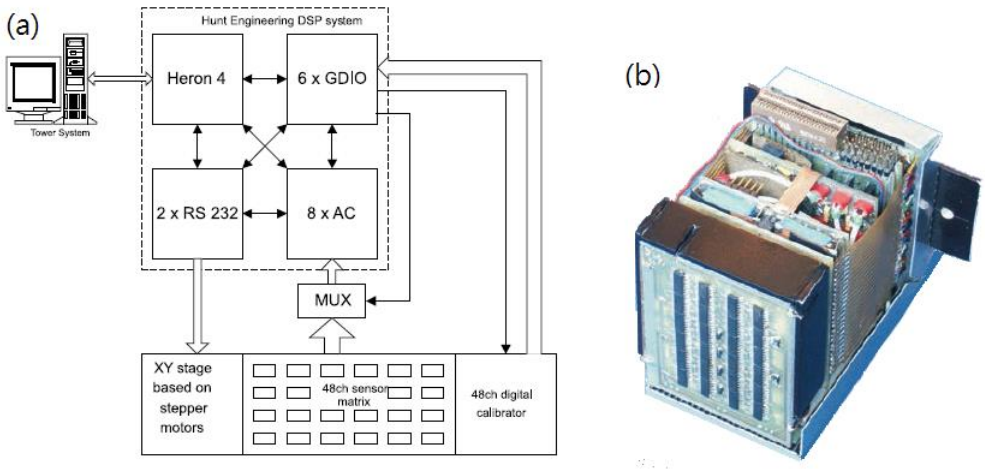

Fig. 2.13 Multi sensor magnetovision system: (a) system structure and (b) measuring head with 48 magnetic field sensors [22].

Fig. 2.14 depicts example results of monitoring a metal sheet forming process and determining the loss of stability by the metal sheet. The experience gained in the building of the system was then used to create magnetic field scanning devices based on 3D sensors.

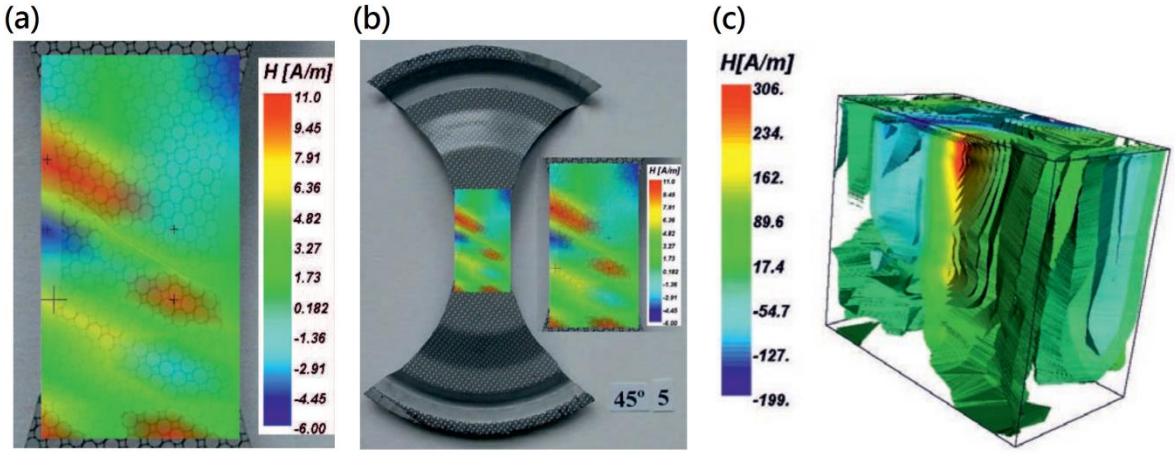

Fig. 2.14 Example results of (a) magnetic field map superimposed on the crack area, (b) die stamping with a crack, and (c) iso-surfaces of the magnetic field variation during metal forming [22].

Therefore, an MMS system can be used entirely autonomously or combined with a typical material testing machine for static load and fatigue testing. This type of system can be used to understand magneto-mechanical phenomena and determine defect type, as well as locating strain fields, areas of plastic deformations and cracks in industrial processes.

2.3 Conclusion

Non-destructive testing is a wide group of analysis techniques which can be used to assist in product development, checking or classifying incoming materials, monitoring, improving or controlling manufacture processes, verifying proper processing and assembly, inspecting in-service objects and much more. This is achieved without ***altering the integrity of the object under test***. Electromagnetic NDT methods are some of the most common methods used in the industry. Unlike other NDT methods, electromagnetic methods are generally safer, faster and relatively easy to operate. The most commonly used are ECT, MPI, ACFM and MFL testing, as well as SQUIDs which are widely used in medicine.

ECT methods are especially sensitive at detecting surface breaking defects; as well as

being able to obtain size and depth information of defects. However, these methods are not suitable for sub-surface and far surface inspection, as the skin depth is extremely thin when testing ferromagnetic materials. ACFM techniques and ECT have similar benefits and limitations. They are both effective at detecting surface defects and are both limited by the skin effect. Compared to ECT, the obtained data from ACFM is generally easier to interpret. MPI methods have the advantage of being relatively simple and cheap to perform, and can penetrate through entire samples when strong magnetic fields are used. However, in order to use MPI, the object surface must be prepared. The use of cleaning chemical solutions can pose additional health and safety concerns. Additional equipment is also required to record the inspection results. MFL testing can scan across samples at high speed, where the magnetic flux can easily penetrate through the object under test. However, the main drawback is that this technique can only be used on ferromagnetic materials.

Different electromagnetic NDT methods have their own specific situations where they work most effectively; and all have their own sets of limitations. Therefore, it is important to select the correct method to use in every case. This highlights the importance of NDT practitioner knowledge and skill. In addition to this, some working environments also create additional limitations and constrains on testing, such as undersea, enclosed areas, extreme temperature and high levels of radiation. Each method also requires various degrees of training to operate the testing method proficiently. The “Holy Grail” in electromagnetic NDT is therefore in the development of a new method which has the combined advantages of the existing methods, without the limitations imposed by them. This is the subject on which research presented in this thesis is based.

Chapter 3
Magnetic-field sensing and Quantum Well Hall effect sensors

3.1 Magnetic-field sensing

The formation of a magnetic field is through the coupled magnetic effect between electric currents and magnetic materials. In practical measurements, two different vector fields, **B** and **H**, are used to refer to the magnetic field and magnetising field strength respectively. **B**-field is defined as the vector field of the motion of a charged particle. The **H**-field is associated with the magnetomotive force caused by this movement of charge. In the International System of Units (SI), **B** is measured in Tesla, T, where 1 T = 1 Wb m^{-2}; and **H** is measured in amperes per meter (A m^{-1}). Therefore, the magnitude of **B** and **H** quantify the magnetic flux density and magnetic field strength, respectively. In general, **B** and **H** have the proportional relationship:

$$\mathbf{B} = \mu \mathbf{H} \tag{3.1}$$

where μ is the magnetic permeability of the material facilitating **B** and **H,** and has the SI units Henries per meter (H m^{-1}).

There are many different methods to detect magnetic fields, such as magnetic particles, a compass, magnetic field viewing film, induction coils, magneto-resistors, magnetic reed switch and Hall effect sensors. Magnetic particles are a very fine, magnetised ferromagnetic powder which can be attracted by external magnetic fields. They can be used to reveal (i.e. visualise) the magnetic flux. A compass is a simple magnet attached to a rotational axis which will align itself in the direction of the magnetic field. Magnetic field viewing film is a transparent film which contains magnetic liquid crystals. The external magnetic field will change the orientation of the liquid crystals, affecting their transparency. Induction coils use Faraday's Law of Induction to sense electromotive forces produced by magnetic induction. A

magneto-resistor is a thin ferromagnetic resistor film. The resistance can be changed by applying an external magnetic field since the force of the magnetic field will cause tensile deformation of the thin film. A magnetic reed switch is a magnet attached onto a spring. When the magnetic force is greater than the spring tension, the switch's metallic mechanisms will come into contact, completing the circuit. A Hall effect sensor is a device based on the application of Lorentz force, where the Lorentz force creates a voltage difference in a perpendicular direction to the electric (biasing) current passing through a conducting material. Some of the magnetic field detecting methods are able to visualise the magnetic field forces, and other are able to measure the different forces and physical phenomena interacting with the magnetic field.

3.2 Magnetic-field sensors and applications

A magnetic sensor can offer compact size with wide sensing ranges, with different detection directions to expand their scope of applications. In general, the detection of magnetic fields is performed without any physical contact with the sensor. In the food industry, magnetic sensors are often used in detecting residue metals in raw ingredients or products. In security gate systems, magnetic sensors are used to detect magnetic labels. In domestic DIY tools, magnetic sensors are used for pipe and cable proximity detectors. Additionally, magnetic sensors are also widely used as pushbutton switches in electrical appliances and electromechanical devices. In industrial and medical applications, magnetic sensors are used in the measurements of linear position, rotary position, ring magnet position and/or speed, encephalography imaging and magnetic resonance imaging. These applications are further detailed in the following sections.

3.2.1 Type of magnetic-field sensors

As previously mentioned, magnetic sensors are widely used in a wide range of applications, the most common being: search coils, fluxgates, SQUIDs, Hall-effect sensors, anisotropic magnetoresistors (AMR), giant magnetoresistors (GMR), magnetic tunnel

junctions (MTJ), giant magnetoimpedance (GMI) sensors, magneto-optic sensors, magneto-strictive-piezoelectric (MTS-PZT) composites, and microelectromechanical systems (MEMS) [23]. Their applications can be sorted into four basic categories:

1. Magnetic field imaging systems.
2. High-precision power meters.
3. Position sensors.
4. Medical/biological micro-sensors.
5. Magnetic imaging of domains.

3.2.2 Magnetic Field Imaging (MFI) systems

MFI is widely used in medical science as a non-invasive method for a precise study of the magnetic structure of the sample's surface, due to its high sensitivity and signal linearity over a wide range of magnetic fields. Cambel et al. [3] presented a series of highly-sensitive microscopic Hall probes and Hall probe arrays, based on Two-dimensional Electron Gas (2DEG) epitaxial structures of GaAs or InGaP/InGaAs/GaAs heterostructures, for detecting the magnetic fields near the surface of magnetic materials. These sensors were used in a complex scanning MFI system, which consisted of a linear Hall probe array and a high-precision *x*, *y*, *z* stepper. In their study, the Hall probes were placed on the top of the semiconductor mesa with the contact pads situated at the bottom (Fig. 3.1 (a)). The topology of the 8-probe Hall sensor array is illustrated in Fig. 3.1 (b). The biasing current was passed through contacts I+ and I– where the Hall voltage was obtained from the Hall probes 1 to 8. The Hall voltage was differentially measured between contacts 1+ and 1–, 2+ and 2–, etc. The results demonstrated that a magnetic field of magnetidue ~1 mT can be detected with high spatial resolution. The system that incorporated the Hall probe array, electronics, timer, and control software could be used for measurements of standard and high-temperature superconductors and other magnetic materials to obtain magnetic field images.

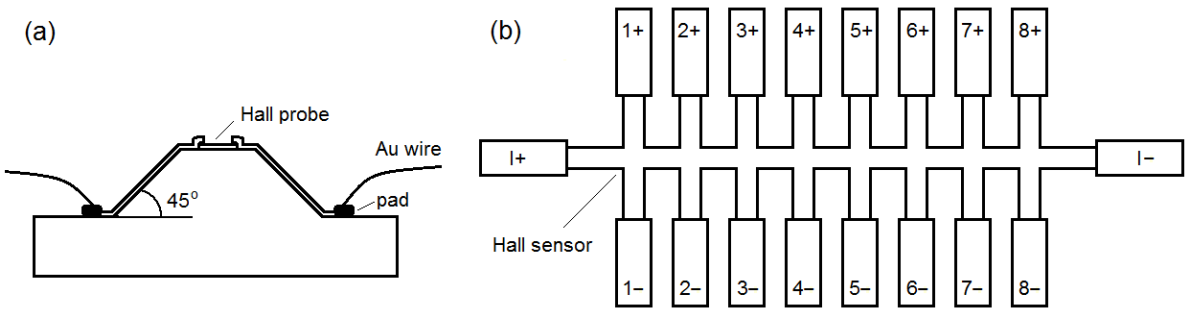

Fig. 3.1 (a) Cross-section and (b) topology of linearly Hall array [24].

In 2007, 10 μm InGaP/AlGaAs/GaAs Hall sensors were developed by Cambel et al. [25] for use in magnetic field imaging of superconducting samples. In the above mentioned structure, the InGaP cap layer provided a barrier with much lower surface density of states than the GaAs layer. The optical microscope image of the InGaP/AlGaAs/GaAs Hall sensor is shown in Fig. 3.2.

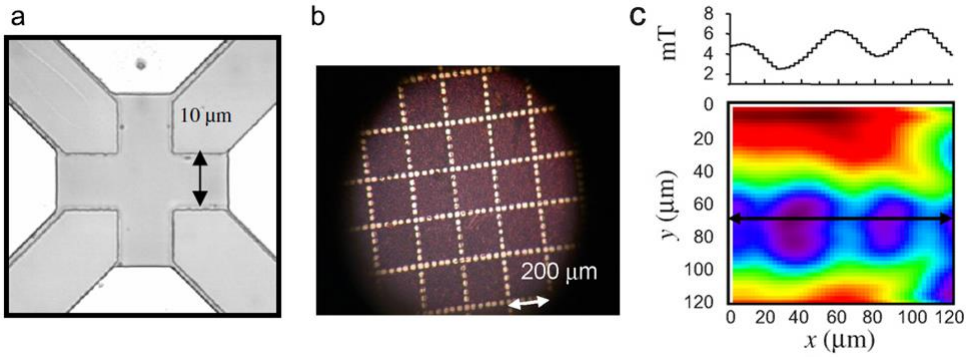

Fig. 3.2 (a) Image of the InGaP/AlGaAs/GaAs Hall sensor, (b) micrograph of 21 × 21 multi-granular sample, and (c) the magnetic structure of the artificially patterned grain boundaries [25].

3.2.3 High-precision power meters

Haddab et al. [26] investigated the reliability and stability of GaAs-based pseudomorphic quantum wells for high-precision power metering. The heterostructure was grown by Molecular Beam Epitaxy (MBE) and its operational principles are presented in Fig. 3.3. The core concentrates the magnetic field B, generated by a bias current. The magnetic field is proportional to the bias current. The output voltage V_{out} is the sum of the Hall voltage and the offset voltage:

$$V_{out} = K_H I_{bias}(t)B(t) + R_{off} I_{bias}(t) \tag{3.2}$$

where K_H is the magnetic sensitivity (V A^{-1} T^{-1}), R_{off} is the offset resistance (Ω), and I_{bias} is the bias current (A). The critical factors governing the metrology of this high-precision power meter are the offset resistance R_{off} and magnetic sensitivity K_H. The stability of R_{off} is of paramount importance attributing to the overall accuracy of the magnetic measurement. This power meter had excellent stability and reliability showing only 0.04% average change after temperature cycling tests (between -40 ℃ to 85 ℃ and 5 cycles in 42 hours). The meter had an impressive Mean Time to Failure (MTTF) of 3×10^{11} hours.

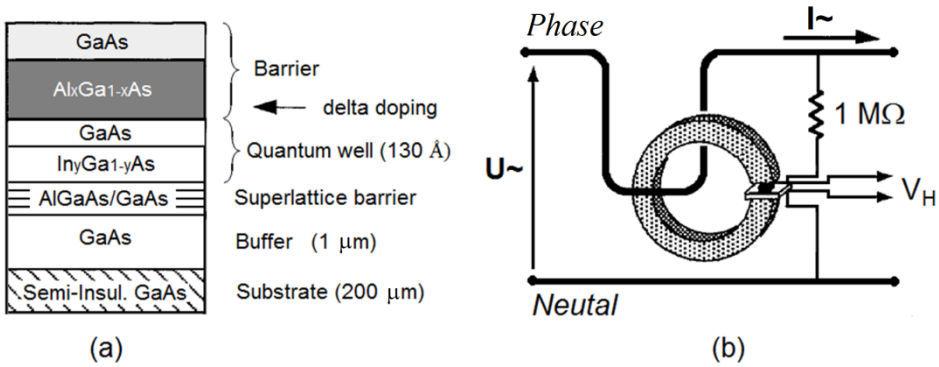

Fig. 3.3 (a) The heterostructure epitaxial layout and (b) schematic diagram of the sensing cell [26].

3.2.4 Position sensor: detection of tyre tread deformation

As previously mentioned, in many applications a magnetic sensor can be used as a position sensor. A 3D position sensor system using five highly sensitive InAs/GaSb heterostructures was developed by Yilmazoglu et al. [27] for the detection of tyre tread deformations. The position sensor employs five monolithically integrated Hall crosses, shown in Fig. 3.4. The integrated Hall sensor, Greek cross type, can measure the changes of magnetic field which are caused by the deformations of tyre tread created from constant speed, acceleration, and braking. The position sensors based on the InAs/GaSb heterostructures provide enhanced Hall sensitivities (0.6 T^{-1}) at 5 V bias voltage due to higher electron mobility of InAs at room temperature (2.6×10^4 cm^2 V^{-1}). However, there are numerous

drawbacks including severe temperature dependence of the output Hall voltage, due to the use of low band gap InAs material in sensors.

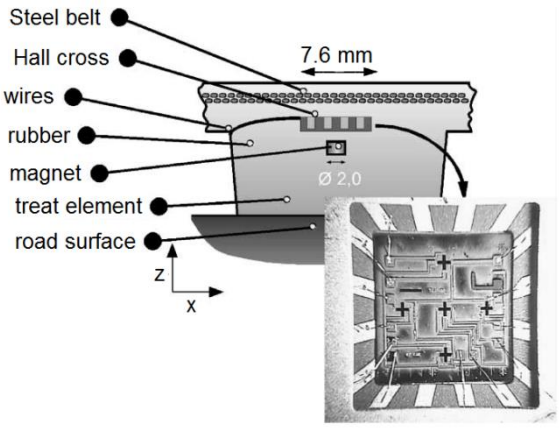

Fig. 3.4 Schematic diagram of the tread-deformation sensing in a section of a tyre [27].

3.2.5 Medical/biological micro-sensors

A prototype Hall biosensor platform was developed by Sandhu et al. [28]. Such biosensors enable large displacements of magnetic beads via low field inducing currents and are fully compatible with biomolecular processes, as shown in Fig. 3.5. The design of the micro-current lines incorporate sensors which have a 5 μm × 5 μm active area. The Hall sensors consists of 100 nm Ti and Au metals, capped with a 200 nm silicon nitride (Si_3N_4) layer deposited by RF-magnetron sputtering. An additional Ti/Au bilayer was deposited to facilitate chemical bonding between the thiolated probe oligonucleotides with the gold surface, for immobilisation experiments using hybridizing oligonucleotides.

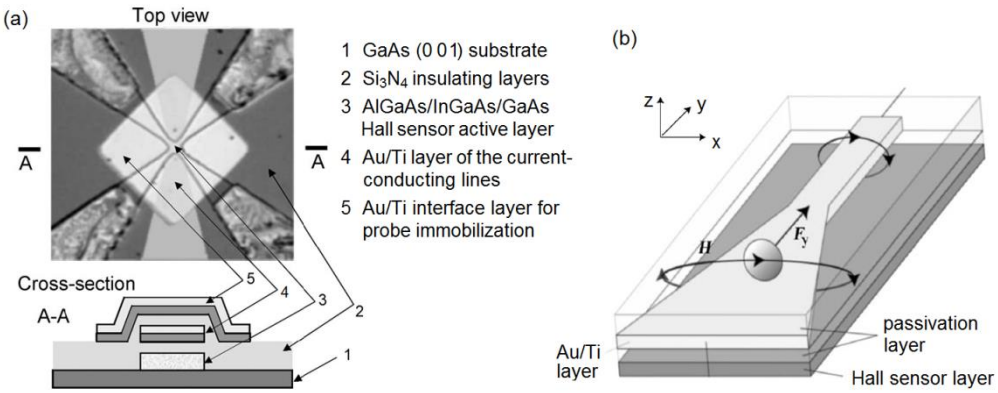

Fig. 3.5 Schematic diagrams of (a) the composite structure of a micro-Hall biosensor and (b) the micro-current line structures used to generate magnetic field gradients [28].

Fig. 3.6 illustrates the analytical process for the detection of complementary oligonucleotides. This process includes:

1. Immobilization of thiolated probe oligonucleotides.
2. Treatment with 6-hydroxy-1-hexanethiol.
3. Interaction with probe oligonucleotides allowing DNA hybridisation.
4. Washing with hybridisation buffer.
5. Attachment of magnetic labels via biotin-streptavidin bonding.

The in-situ magnetic beads were observed using a video microscope with digital recording.

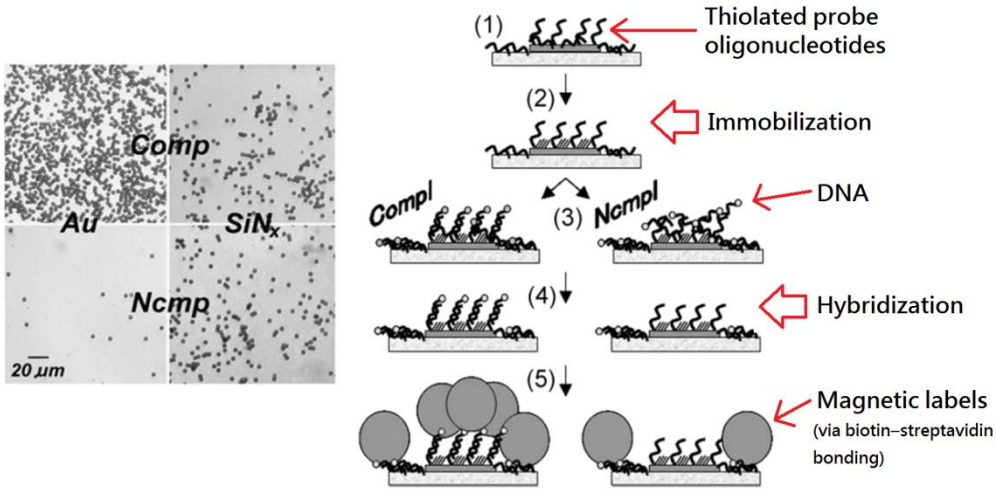

Fig. 3.6 Schematic diagram of the analytical process and images of actual results [28].

3.2.6 Magnetic imaging of domains

The characteristics of magnetic domains at ambient temperatures is vital in the magneto-electronics industry, requiring a deep understanding for the development of sensor systems. Currently, a well-used technology for the development of the magnetic information storage and magneto-electronic devices is the Scanning Hall Probe Microscope (SHPM). Primadani and Sandhu [29] used micro-Hall probes based on InGaAs/AlGaAs heterostructure with a 2DEG density of 2.2×10^{12} cm^{-2} and carrier mobility of 2×10^{4} cm^{2} V^{-1} s^{-1} at 77 K, to build a variable temperature scanning Hall probe microscope system (VT-SHPM). This was used

for the magnetic imaging of domains over large areas, within the operation conditions of cryogenic temperatures. Fig. 3.7 shows the VT-SHPM images of magnetic domains at different temperatures over the surface of 50 μm thick iron garnet films. This VT-SHPM overcomes the limitations of conventional cryogenic SHPM systems due to the varying temperature capabilities. The magnetisation enhanced by decreasing the temperature with its maximum value being at 160 K.

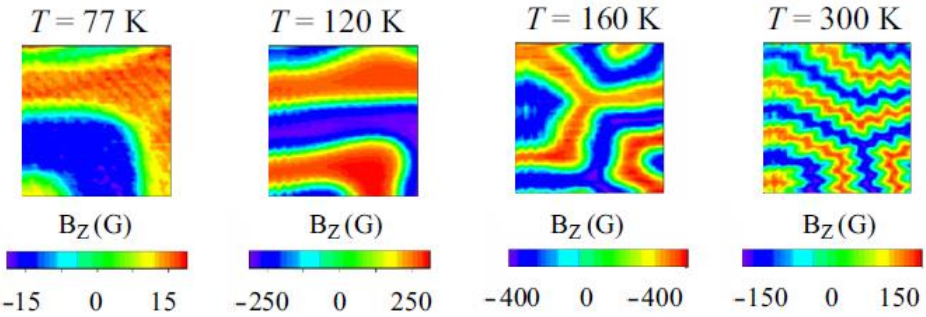

Fig. 3.7 The VT-SHPM images of magnetic domains at different temperatures [29].

Novoselov and Missous [30] reported a High-Concentration Two-dimensional Electron Gas (HC-2DEG) magnetic field sensor probes for domain wall measurements. These sensor probes have an activated sensing area dimension of 0.5 μm × 0.5 μm. Fig. 3.8 shows a microscope image of the HC-2DEG probe used with two different widths (0.5 μm and 1 μm) of Hall cross devices [30]. The dimension of this sensing area is much smaller than the domain width at room temperature (yttrium-iron has a domain width of ~14 μm at 300 K) [30]. With the small sensing area and a ~100 μT minimum detectable magnetic field resolution, these sensor probes can, at room temperature, with flux sensitivity down to 0.1 Φ_0, where Φ_0 is the flux quantum. It was reported that the resolution of this HC-2DEG probe could be increased up to 100 times when operating at 80 K.

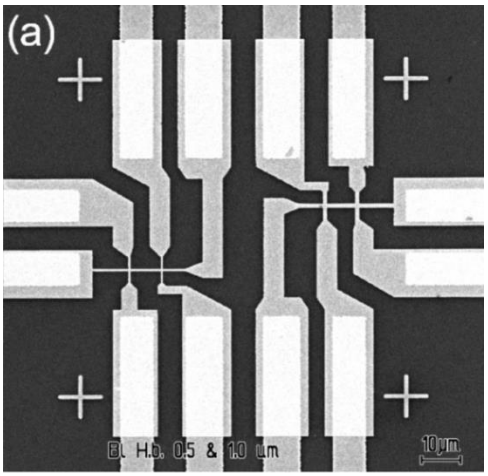

Fig. 3.8 The HC-2DEG Hall sensor probe picture with two set of 2 Hall cross devices. The widths of the two sets of Hall cross devices are 0.5 μm and 1 μm respectively [30].

The most important result stated by Novoselov and Missous [30] was the first ever demonstration of domain wall motion measurement at room temperature, using the (HC-2DEG) magnetic field sensor probes.

3.3 Quantum Well Hall effect sensors

Fig. 3.9 shows various magnetic field sensors and their dynamic ranges [31]. It is clear that SQUIDs have the best sensitivity, enough to measure magnetic fields as low as 10^{-15} T. Because of the extreme sensitivity of SQUIDs, such devices are an ideal choice for biological research and medicine. However, SQUIDs are based on superconducting loops containing Josephson junctions, which are bulky and very expensive. To maintain superconductivity, the entire device needs to be cooled down with liquid helium or liquid nitrogen. In comparison, 2DEG Hall effect sensors developed at Manchester in the last 12 years [31] have the widest measurement range compared to other devices, and have suitable sensitivity to measure magnetic fields as low as 10^{-9} T. The 2DEG Hall effect sensors exhibit unique properties, including low power consumption, low temperature coefficient, linear sensitivity, wide frequency response, compact size and low cost [31].

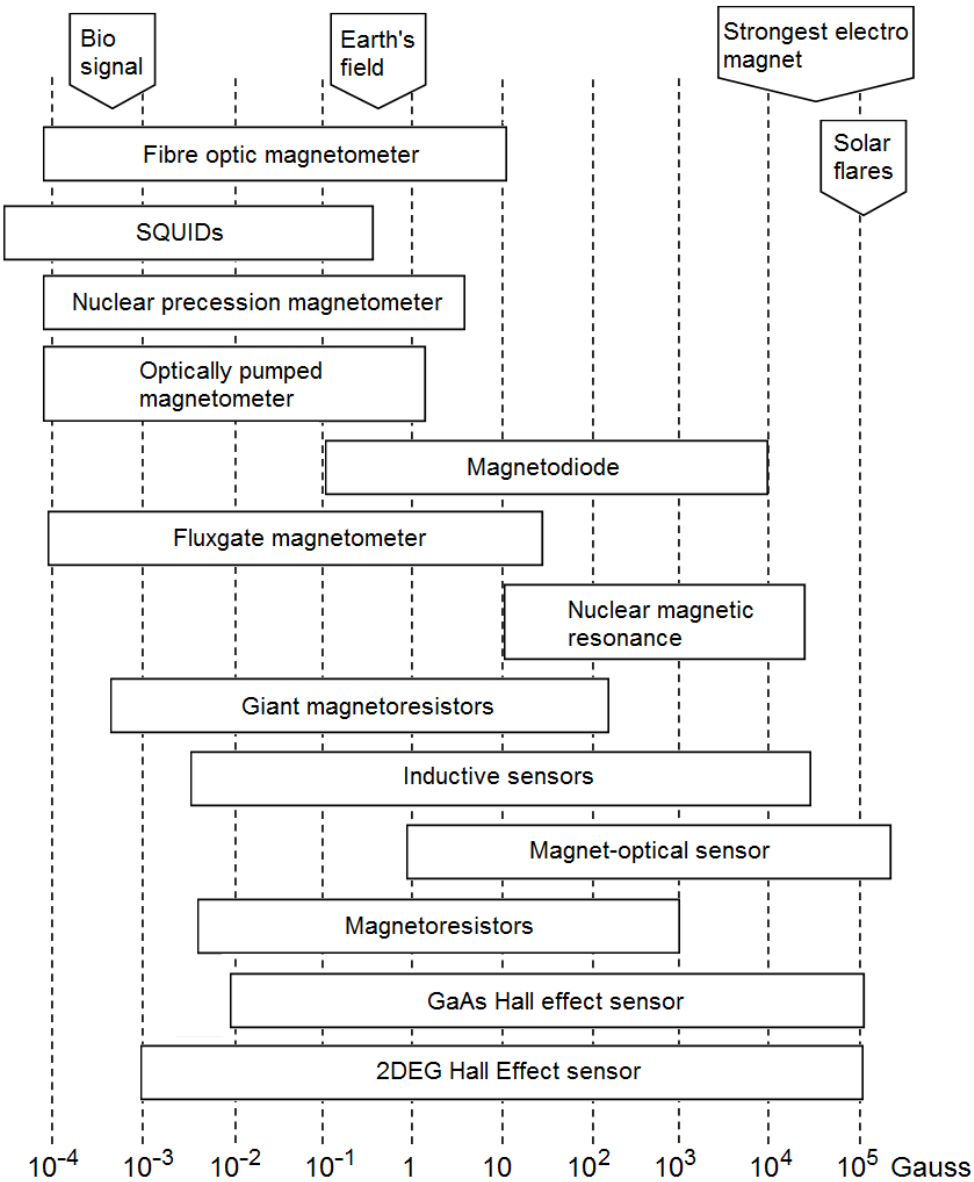

Fig. 3.9 Various magnetic field sensors and their dynamic ranges [31]

Many researchers have been striving to develop and optimise the growth/fabrication processes of Hall effect sensors in order to improve their magnetic sensitivity, reliability, power consumption, size, signal-to-noise ratio, low temperature dependence of output voltage and reduced manufacturing costs. Among all of these approaches, Hall effect sensors based on III-V heterostructures have been demonstrated as the most promising, which will be further validated in this research.

3.3.1 The Hall effect phenomena

The Hall effect is the phenomenon where a voltage difference (i.e. Hall voltage) is generated when electric current flows through a conductor when placed in a magnetic field. The generated voltage is perpendicular to both the direction of current and the applied magnetic field. This phenomenon was discovered by Hall in 1879 [32]. The Hall voltage is given by:

$$V_{\mathrm{H}} = \frac{R_{\mathrm{H}} IB}{d} \tag{3.3}$$

where V_{H} is the Hall voltage (V); I is the total biasing current through the sensor (A); B is the magnetic flux density (T); d is the thickness of the conductor, and R_{H} is the Hall coefficient ($R_{\mathrm{H}} = -1/ne$). Fig. 3.10 shows the electrical connection to the Hall sensor. In the case of a Hall device with finite contacts, V_{H} is given by:

$$V_{\mathrm{H}} = G\frac{R_{\mathrm{H}} IB}{d} \tag{3.4}$$

where G denotes the geometrical correction factor.

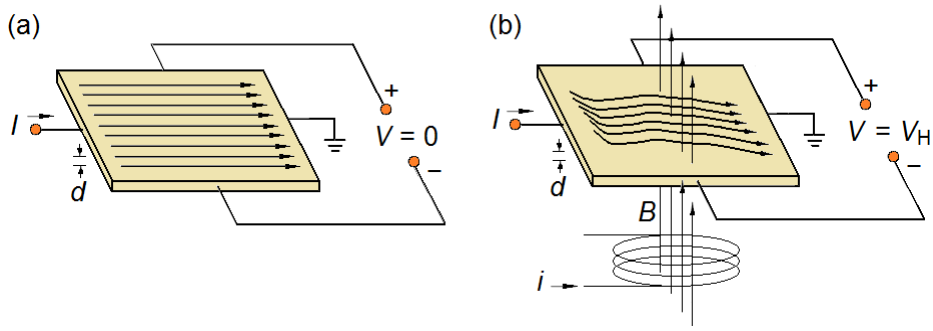

Fig.3.10 Schematic diagram of a Hall effect device (a) outside and (b) within a magnetic field.

For an extrinsic semiconductor, the Hall voltage can be expressed in terms of the bias voltage as [33]:

$$V_{\mathrm{H}} = \mu_{\mathrm{H}} \frac{w}{l} G V_{bias} B \tag{3.5}$$

where μ_H is the Hall mobility of the charge carriers; l and w are the length and width of the Hall device, respectively. The absolute sensitivity S_A of the magnetic sensor is defined as:

$$S_A = \frac{V_H}{B} = \mu_H \frac{w}{l} GV \tag{3.6}$$

The supply-current-related sensitivity is defined as:

$$S_I = \frac{S_A}{I} = \frac{1}{I}\frac{V_H}{B} \tag{3.7}$$

$$\therefore \quad V_H = IS_I B \tag{3.8}$$

By substituting the Hall voltage V_H in Eq. (3.7):

$$S_I = G\frac{|R_H|}{d} \tag{3.9}$$

If the plate is made of a strongly extrinsic semiconductor, R_H is given by:

$$R_H = \frac{r_H}{qn} \tag{3.10}$$

where r_H is a degeneracy constant (> 1), q is the elementary charge, n is the charge carrier density of the carrier electrons; and Eq. (3.9) attains the form:

$$\therefore \; S_I = G\frac{r_H}{qnd} \tag{3.11}$$

In low doped, thin doping gradient layers, the term nd should be replaced by the surface charge carrier density N_s. Then, S_I becomes:

$$\therefore \; S_I = G\frac{r_H}{qN_S} \tag{3.12}$$

where the term qN_S equals the charge carrier due to free electrons per unit area. The relative sensitivity depends on the surface density of charge carriers in the Hall effect device, any variation in the carrier density may cause an instability in the sensitivity of sensor.

The major advantages of Hall effect sensors are their excellent characteristics, simplicity of the operating principle, simple structure, and compatibility with microelectronics [34]. The development of Hall effect sensors will continue to take advantage of high-quality semiconductor materials and ever-improving fabrication methods available in the microelectronics industry. In particular, the improvements in the growth of the semiconductors will lead to a reduction of the $1/f$ noise and to the improvement of the long-term stability of Hall effect sensors. The improvements in the fabrication process will reduce voltage offset further. The integrated combination of Hall effect sensor with better interface and micro-processing electronic circuits will lead to the development of new magnetometer systems with high performance-price ratio.

3.3.2 Heterojunctions and Heterostructures

In recent years, "band gap engineering" has become an important research field. Band gap engineering involves the growth of two or more materials with different energy band gaps in an attempt to improve the electrical and optical properties of a material system. The techniques of Molecular Beam Epitaxy (MBE) and Metalorganic Chemical Vapour Deposition (MOCVD) are two major techniques to grow layers of similar crystalline structure on top of each other. For years, most of high-electron-mobility transistor wafers were grown by MBE. This is due to three main reasons:

1. The interfaces between layers are very smooth.
2. Changes in layer composition and doping can be made very abruptly.
3. Comparatively easy control of the background impurities [35].

Heterostructures have unique electrical and/or electro-optical characteristics that are attributed to their epitaxial structures, which consist of the growth of different semiconductor materials. Fig. 3.11 shows the difference between conduction and valence bands of some of

the most important heterostructures that can be used in high performance Hall effect applications [36]. When two materials with different energy band gaps are grown one on top of one another, discontinuities in the valence and conduction bands arise at the interface of the two semiconductor materials. This is called a heterojunction. The characteristics of a heterojunction depend mostly on how different their energy gaps (and exact band structures) are.

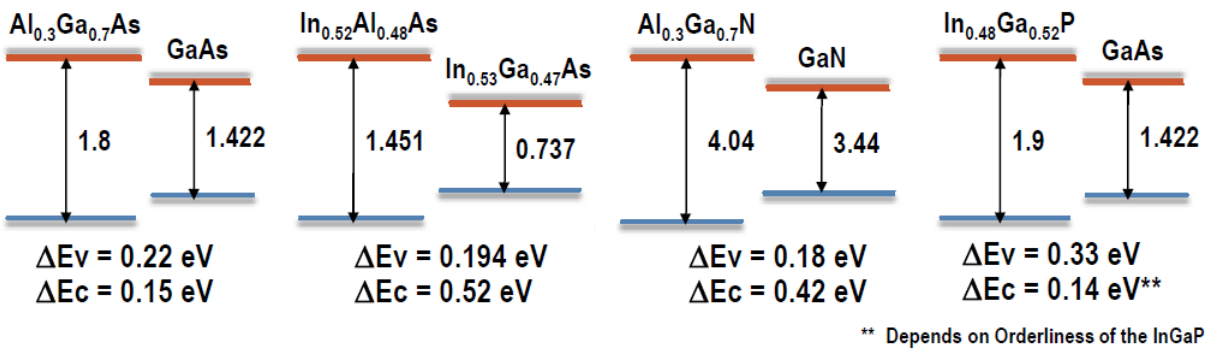

Fig. 3.11 Energy band diagrams for some heterostructures [35].

As mentioned above, a heterojunction is a junction in a single crystal between two different semiconductors. The two semiconductors have different band gaps and as their Fermi energy level (E_F) will try to align with each other to establish chemical and thermal equilibriums, band discontinuity in both conduction and valence bands (ΔE_c and ΔE_v) will occur in the depletion region. Fig. 3.12 shows the heterojunction band diagram of common heterojunctions.

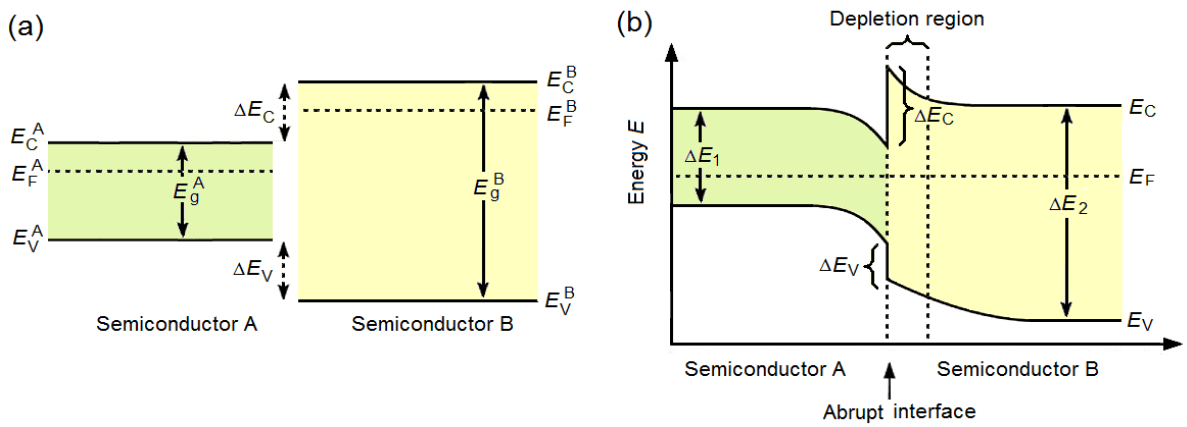

Fig 3.12 Energy band diagrams of heterojunction before contact (a) and after contact (b).

3.3.2.1 AlGaAs/GaAs Heterostructures

Sghaier et al. [37] investigated and proposed Hall devices based on AlGaAs/GaAs heterostructures. They demonstrated the importance of the use of Schrödinger–Poisson calculation to evaluate performances of devices such as Hall effect sensors and how to optimize them with respect to measurement of low magnetic fields. Moreover, they attempted to show that the electron mobility of the studied heterostructure may be enhanced without loss in interface electron concentration by both increasing the spacer thickness and by inserting a δ-doping in a narrow quantum well within the AlGaAs barrier. Kllnets et al. [38] investigated quantum well micro-Hall devices based on uniformly Si-doped $Al_{0.3}Ga_{0.7}As$/GaAs and Si-δ-doped heterostructures as a function of electric field. A comparison between them in terms of sensitivity and noise properties was also reported. The data showed that at high electric fields, doped-channel quantum well devices are beneficial over high-mobility structures and that the use of pseudomorphic InGaAs results in better performance than GaAs. A maximum signal-to-noise sensitivity of 138 dB T^{-1} was achieved at the temperature, frequency, and bandwidth of 300 K, 100 kHz, and 1 Hz, respectively. The results also suggest that a signal-to-noise sensitivity of 160 dB T^{-1} and a lowest detection limit of 10 nT were possible in doped-channel structures.

3.3.2.2 AlGaAs/InGaAs/GaAs heterostructures

Sileo et al. [39] proposed a new technological approach to fabricating a fully integrated three-axis Hall magnetic sensor. A 2DEG AlGaAs/InGaAs/GaAs multilayered structure constituted the sensing medium of a micromachined device, whereas an underlying strained InGaAs/GaAs bilayer allowed the self-positioning of the out-of-plane devices by a sacrificial layer removal and strain release. Both in-plane and out-of-plane devices showed excellent linearity versus magnetic field with an absolute sensitivity as high as 0.03 V T^{-1} at 0.6 V bias voltage. Lee et al. [40] fabricated quantum well Hall devices based on Si δ-doped $Al_{0.25}Ga_{0.75}As/In_{0.25}Ga_{0.75}As$/GaAs pHEMT materials, grown by the low-pressure metal organic chemical vapour deposition method. A Si δ-doped GaAs layer was introduced for the

first time in the Hall device to reduce the thermal variation of electron concentrations and to improve its temperature characteristics. A high electron mobility of 8100 $cm^2 V^{-1} s^{-1}$ with a sheet carrier density of 1.5×10^{12} cm^{-2} was achieved at room temperature. A minimum detectable magnetic field of 60 nT at 1 kHz, and 110 nT at 100 Hz, with one of the best temperature coefficients of –0.015% K^{-1} were obtained. Del Medico et al. [41] described the optimisation of the growth of pseudomorphic $In_{0.75}Ga_{0.25}As/In_{0.52}Al_{0.48}As$ heterostructures by MBE to develop new types of magnetic sensors using the properties of a 2DEG and the benefit of strain in pseudomorphic channels. A low sheet electron density of 9.84×10^{11} cm^{-2}, a high mobility of 13000 $cm^2 V^{-1} s^{-1}$ at room temperature, and a sensitivity of 580 V $A^{-1} T^{-1}$, with a temperature coefficient of –550 ppm $°C^{-1}$ between –80 and 85 °C were obtained. High signal-to-noise ratios corresponding to minimal detectable fields of 350 nT $Hz^{1/2}$ at 100 Hz, and 120 nT $Hz^{1/2}$ at 1 kHz were also measured.

However, the most promising data reported to date on AlGaAs-InGaAs-GaAs was by Haned and Missous [42]. The results shows that this 2DEG sensor has the capability to measure 1 μT static DC magnetic field when using dynamic quadrature offset cancellation techniques. Furthermore, a minimum detectable magnetic field of 100 nT at DC can be achieved by using an AC driving circuit with phase locking techniques to avoid low frequency flicker ($1/f$) noise.

3.3.2.3 InGaAs/InP heterostructures

Cambel et al. [43] investigated the noise properties of 2DEG InGaAs/InP Hall sensors of various dimensions. The results show that for large-scale sensors (0.2 mm linear dimensions) at 77 K and at 1 kHz, a low field detectability of better than 1 nT can be achieved, with the noises of the 2 and 10 μm sensors depending on bias current, frequency, applied magnetic field and temperature. Morvic and Betko [44] measured room temperature planar Hall effect and associated magnetoresistance. In the InP/InGaAs heterostructure Hall sensor, the planar sheet Hall coefficient was found to be about three orders of magnitude lower than that corresponding to the theoretical value calculated using the transversal magnetoresistance

parameter. This is associated with the extremely small thickness of the electrically active layer in these sensors. The ratio of the maximum Hall voltage and the maximum transversal Hall voltage was about 50 times lower in the InP/InGaAs heterostructure sensor than that in the bulk GaAs Hall sensor at the same magnetic field. Morvic and Betko [44] indicated that these Hall sensors are particularly suitable as elements of systems for precise measurements of arbitrarily oriented magnetic field.

3.3.2.4 InAs/AlGaSb heterostructures

Bekaert et al. [45] fabricated cross-shaped Hall sensors with high sensitivity and moderate temperature stability from quantum wells based on InAs/$Al_{0.2}Ga_{0.8}Sb$ heterostructure. The layers were grown on semi-insulative GaAs substrates by MBE technique. For the undoped quantum well structure, a maximum Hall mobility of 215000 cm^2 V^{-1} s^{-1} with sheet carrier concentration of 9×10^{11} cm^{-2} was obtained at 4.2 K. These transport properties resulted in sensitivities as high as $S_V = 3$ T^{-1} (for voltage drive) and $S_I = 650$ Ω T^{-1} (for current drive). Additional Si δ-doping in the middle of the InAs quantum well lead to improved temperature stability of the sensitivities but still far below what could be obtained with larger band gap materials. Bekaert et al. [45] indicated that Si δ-doping of the InAs quantum well resulted in improved temperature stability at reduced sensitivity. Behet et al. [46] fabricated Hall sensors with high sensitivity and moderate temperature stability from quantum wells based on an InAs/$Al_{0.2}Ga_{0.8}Sb$ heterostructure by MBE technique. Their results showed a maximum Hall mobility of 29500 cm^2 V^{-1} s^{-1} with sheet electron concentration of approximately 2×10^{12} cm^{-2} at room temperature for an undoped quantum well structure. For a cross-shaped sensor, these excellent transport properties resulted in sensitivities of $S_V = 0.9$ T^{-1} (for voltage drive) and $S_I = 300$ Ω T^{-1} (for current drive). Additional doping of the InAs quantum well lead to an improvement of the temperature stability of the input resistance and sensitivity in the temperature range of 173K to 423K.

3.3.2.5 Sn-doped n-InSb/i-GaAs heterostructures

Mironov et al. [47] reported Hall probes based on n-InSb/i-GaAs optimised Sn-doped MBE-grown heterostructures. The metallurgical thicknesses of the n-InSb epilayers lie in the range 1.1–10.5 μm, giving room-temperature mobilities of $9 \times 10^3 – 15 \times 10^3$ cm^2 V^{-1} s^{-1} with carrier densities of $0.96 \times 10^{18} – 2.56 \times 10^{18}$ cm^{-3}. Magnetotransport characterisation of the Hall probes over the range of temperatures 1.1 – 300 K and pulsed (τ = 120 ms) magnetic fields up to 52 T show extremely small temperature variations of Hall voltage. This allowed using the probes for various cryogenic applications without the need for Hall probe thermal stabilisation. These probes were then successfully used to measure the diamagnetic properties of various high-T_c and conventional superconductors. Mironov et al. [48] reported magnetotransport at fields up to 500 mT and low frequency noise characteristics are reported for miniature magnetoresistors with ferrite concentrators based on Sn-doped n-InSb/i-GaAs heterostructures grown by MBE. The thickness of the InSb epilayers lie in the range 0.55 – 1.5 μm giving room temperature mobilities of 2.5 – 5.5 m^2 V^{-1} s^{-1} with carrier densities of $0.5 \times 10^{17} – 1.5 \times 10^{17}$ cm^{-3}. The room temperature magnetoresistance (MR) for two terminal devices was as high as 115% at 50 mT. A high signal-to-noise ratio and a good temperature stability (0.5–0.83% K^{-1}) was observed for B < 60 mT. The resolution limits are 2.6 nT and 0.82 nT at 10^2 Hz and 10^3 Hz, respectively.

3.3.3 Quantum Well and Two-dimensional electron gas

As mentioned previously, a quantum well is formed in a heterostructure with a thin layer of a narrower band-gap semiconductor sandwiched between two identical larger band-gap materials. The layer of narrower band-gap semiconductor is called a quantum well and the two layers of a material with a wider band-gap are called barriers. Fig. 3.13 illustrates an example of an ideal undoped square shape quantum well for AlGaAs/GaAs/AlGaAs heterostructures.

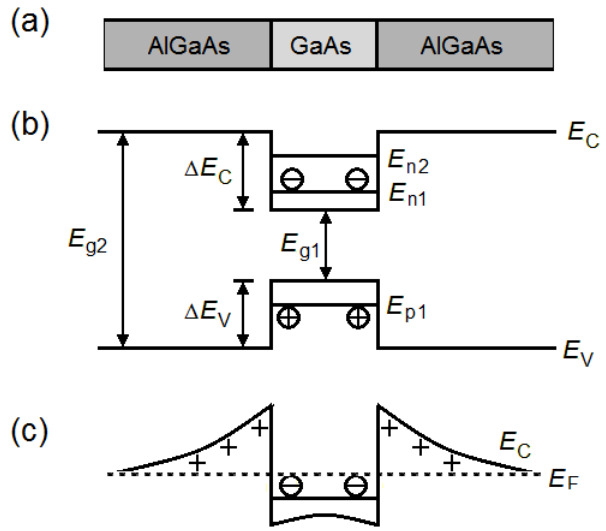

Fig. 3.13 An ideal undoped square shape quantum well: (a) structure, (b) energy band diagrams, and (c) conduction band diagrams [49].

Fig. 3.14 shows another example of the conduction band diagram of a simple AlGaAs/GaAs heterojunction epitaxial structure [31]. In this epitaxial structure, a wide band-gap AlGaAs layer is grown on top of a narrow band gap GaAs layer. A triangular quantum well is formed due to the differences in energy gaps between them. In the upper part of the AlGaAs supply layer, the doping is implemented in a very thin region (typically 3 – 4 mono-layers thick with concentration > 2×10^{12} cm^{-2}) to form a V-shaped potential well, in which the electron energies are quantised. The free electrons are introduced by doping the wide band gap AlGaAs supply layer. The electrons flow from the AlGaAs supply layer into the GaAs channel layer, thereby resulting in the accumulation of electrons in the potential well created at the heterojunction between supply and channel layers.

Because the energy level of donors in the supply layer is higher than the Fermi energy level (E_F), the electrons are free to move into the quantum well. The lowest quantised energy level (E_o) is lower than E_F, meaning that electrons will be trapped inside the quantum well. The resultant band structure only allows the electrons to move freely in the plane parallel to the undoped junction (i.e. free to move in two dimensions), and the absence of ionised donors from the supply layer will greatly increase the carrier mobility in this region [31].

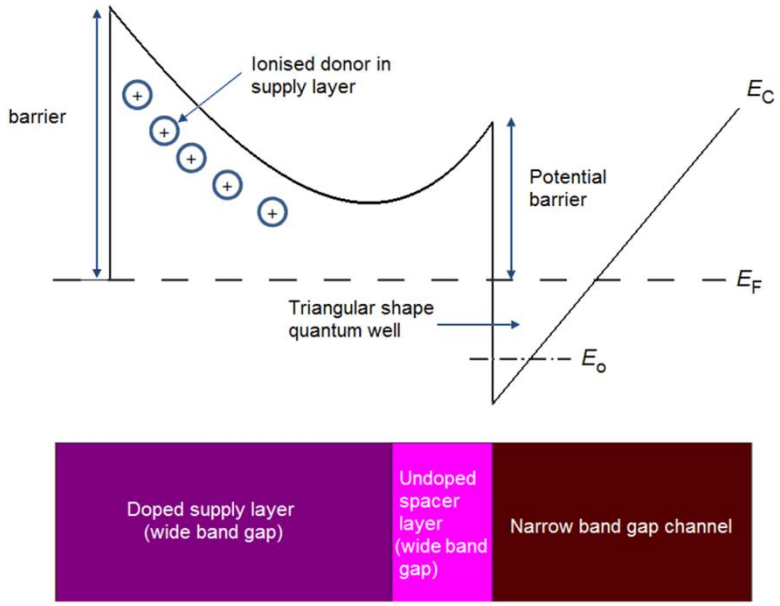

Fig. 3.14 Formation of Quantum Well at AlGaAs/GaAs heterojunction [31]

The quantum well can be grown as to 1 to 10 nm thin by MBE or MOCVD techniques, which is smaller than the electron mean free path (the De Broglie wavelength). Therefore, the trapped electrons in the quantum well can only move in two dimensions in the plan parallel with the barrier layers. The free carrier confined within this region is called a Two-dimensional Electron Gas (2DEG). In other words, a 2DEG is a gas of electrons only free to move in two dimensions due to electrons in the quantum well with discrete energy values.

A modulation doped field-effect transistor has a 2DEG with high electron mobility at low temperatures. There are two major doping types. One is bulk doping in which the impurities are incorporated all the way throughout the whole of the supply layer. Another is the δ-doping where the doping is concentrated in a very thin region of the supply layer (3–4 mono-layers thick) with a very high doping density (typically > 2×10^{12} cm^{-2}).

Fig. 3.15 shows the schematic real-space energy-band diagram of δ-doped and bulk-doped AlGaAs/GaAs heterostructures. The ionised impurities in the δ-doped epitaxial GaAs layer form a V-shaped potential well, and the electron energies are quantised for motion perpendicular to the growth surface [50,51]. In δ-doped structures, the energy quantisation E_o^{δ} occurs in a quantum well generated by the built-in electrostatic potential difference in the supply layer. By contrast, size quantisation in the bulk-doped structure is much smaller. If no

parallel conduction occurs in the $Al_xGa_{1-x}As$ layers, then the Fermi level E_F is at the bottom or below the bottom, of the conduction band in the $Al_xGa_{1-x}As$ heterojunction.

The advantages of the δ-doped heterostructure are the high concentration of the 2DEG, the high gate-breakdown voltage, the proximity of the 2DEG from the gate, and the high transconductance. In the high carrier concentration in the δ-doped epilayer, the carriers are able to climb the slope easily onto the thin spacer layer, as the result of the absence of the potential drop in the depletion layer, which exists in bulk doping. The electrons in a δ-doped layer can also now tunnel through the thin spacer layer and get trapped in the potential well, which results in increased carrier concentration in the quantum well.

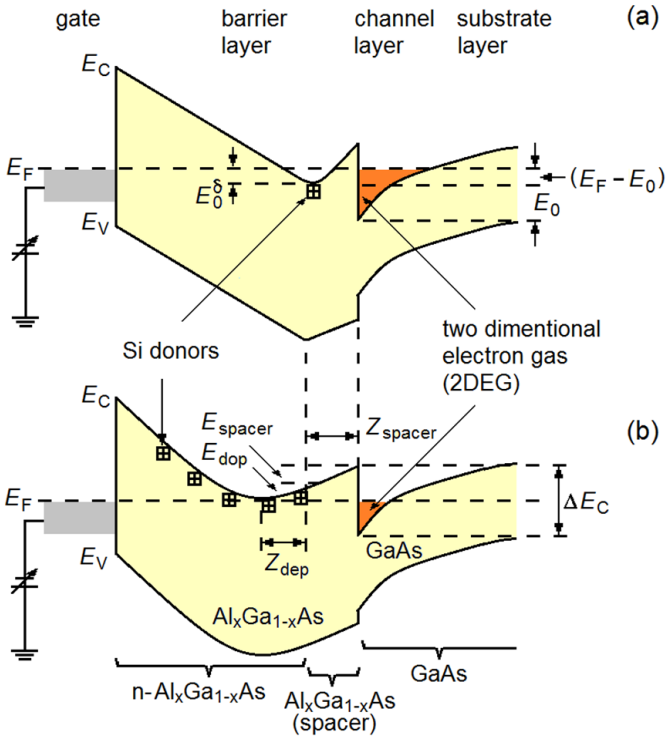

Fig. 3.15 Schematic real-space energy-band diagram of δ-doped (a) and bulk-doped (b) AlGaAs/GaAs heterostructures [51].

3.3.4 HEMT and pHEMT

A High Electron-Mobility Transistor (HEMT) is a heterostructure field-effect transistor incorporating a junction between two materials with different band gaps as the channel, instead of a doped region. In the HEMT structure, compositionally different layers are grown

in order to optimise and to extend the performance of the field-effect transistor. Fig. 3.16 shows the different band gaps (E_G) between conduction and valence bands of some heterostructures. Because HEMTs utilise an intentionally undoped channel thereby mitigating the deleterious effect of ionized impurity scattering (Figure3.16). Therefore, electrons confined to the heterojunction of HEMTs exhibit higher mobilities than those in metal oxide semiconductor field-effect transistors. Currently, the majority of high electron mobility transistors are grown by MBE. This is caused by a number of reasons: the interfaces between layers are very smooth, changes in layer composition and doping can be made very abrupt, and the control of background impurities is comparatively easy [49]. Today all HEMT structures on GaAs or InP substrates use an InGaAs channel. As mentioned above, the reason is that this material provides high electron mobility which increases with indium content. Additionally, depending on the use of GaAs or AlGaAs for the buffer layer the HEMT is either a single heterojunction HEMT or double heterojunction HEMT respectively.

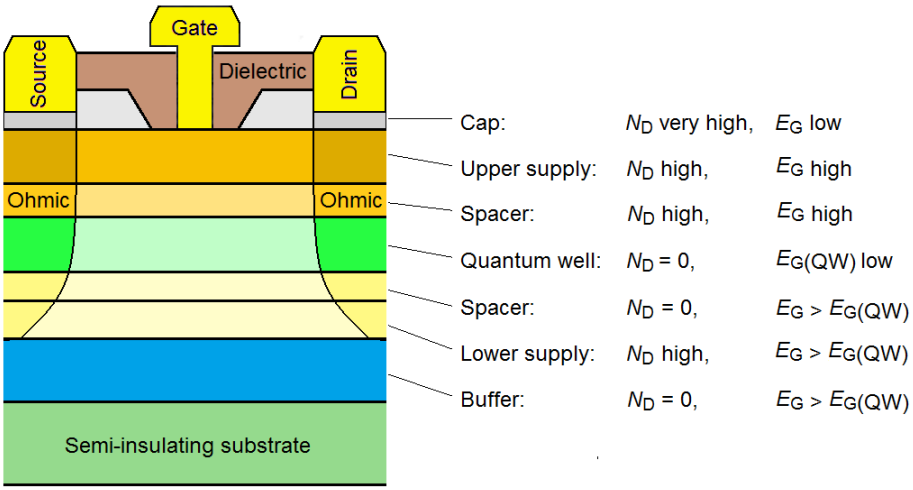

Fig. 3.16 HEMT layer schematic, N_D is the doping concentration; N_D in cap layer is very high for good ohmic contact formation; and N_D in the quantum well is zero for good electron transport and confinement.

Generally, the HEMT or pseudomorphic High Electron-Mobility Transistor (pHEMT) structures are grown on a semi-insulating GaAs or InP substrate by MBE or MOCVD. Then a buffer layer is epitaxially grown on the substrate in order to isolate defects from the substrate.

In the pHEMT structure, the two different materials used as heterojunctions have slightly different lattice constants. The epitaxial structure of pHEMT has a larger bandgap differences than otherwise possible, giving them better performance. GaAs or $Al_xGa_{1-x}As$ (typically $0.2 < x < 0.3$) is used as the buffer layer in GaAs-based HEMT and pHEMT. The band gap of $Al_xGa_{1-x}As$ is larger than that of GaAs, but $Al_xGa_{1-x}As$ is limited due to strain problems. To avoid the strain problem, the $Al_xGa_{1-x}As$ is grown to just below its thickness limit and a thin layer of GaAs is grown on top. This thin layer will relieve the strain and allow another layer of $Al_xGa_{1-x}As$ to be grown. In InP-based HEMT and pHEMT, the large band gap material is $In_xAl_{1-x}As$ (typically $x \geq 0.52$).

After buffer layer growth, the channel layer is grown next. The channel layers of HEMTs and pHEMTs are GaAs and $In_xGa_{1-x}As$ respectively. The most important point about the channel layer in the HEMT and pHEMT devices is a 2DEG that results from the band-gap difference between $Al_xGa_{1-x}As$ and GaAs in HEMT or between $Al_xGa_{1-x}As$ and $In_xGa_{1-x}As$ in pHEMT. The formation of 2DEG quantum well channel at AlGaAs/GaAs heterojunction is shown above in Fig. 3.17. To separate the 2DEG from any ionised donors generated by the pulse doping or n^+ active layer, an $AlxGa_{1-x}As$ spacer layer is grown on the top of channel layer. The remainder of the HEMT structure contains a donor layer doped $Al_xGa_{1-x}As$, an undoped $Al_xGa_{1-x}As$ Schottky contact layer, and a highly-doped GaAs layer. Finally, HEMTs and pHEMTs require ohmic contacts directly to the 2DEG, which are made with decreasing AlAs mole fraction shown in Fig. 3.16. In addition, Fig. 3.17 shows the energy band diagrams for a HEMT or pHEMT perpendicular to the source, showing the ohmic contacts through tunnel junctions [52].

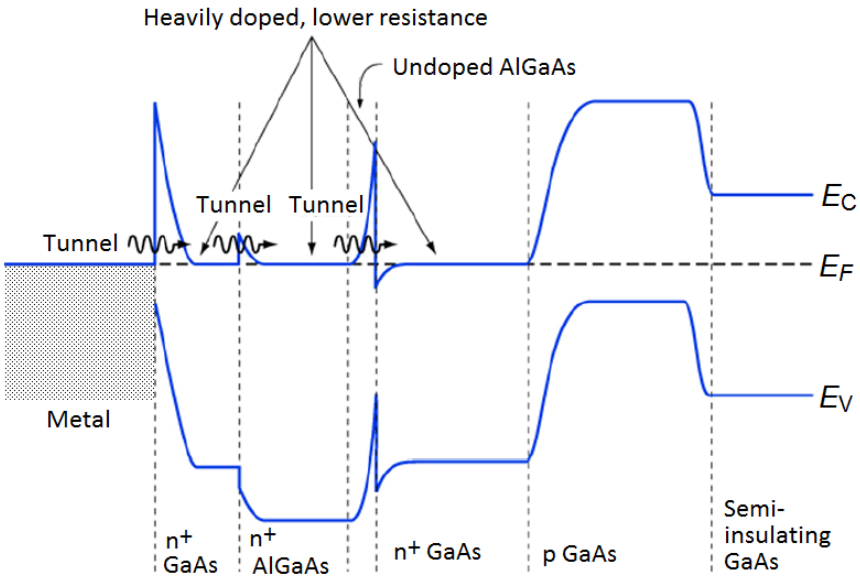

Fig. 3.17 The energy band diagram for a HEMT or pHEMT perpendicular to the source, showing the ohmic contacts through tunnel junctions [52].

Compared with the structure of a HEMT, a pHEMT structure is achieved by using an extremely thin layer of one of the materials, so the crystal lattice of the thin pseudomorphic layer simply stretches to fit the adjoining material. Lastly, this structure produces transistors with large band gap differences compared to HEMTs, which shows better transport performances, as shown in Fig. 3.18.

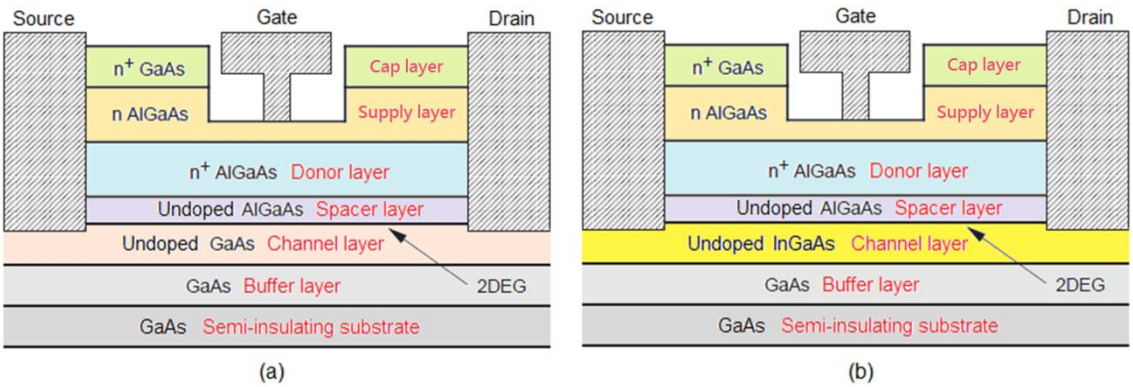

Fig. 3.18 Epitaxial structures of a basic AlGaAs/GaAs (a) HEMT and (b) pHEMT.

It is worth noting that 2DEG metamorphic structures can also be grown on GaAs, which have graded buffer layers in order to give a free choice of the lattice constant and indium composition in the $In_xGa_{1-x}As$ channel (x = 0.3 – 0.6). In general, GaAs-based and InP-based

pHEMTs have many advantages such as higher electron mobilities, higher saturated electron velocities, high conduction and valence bands [53, 54].

3.4 Conclusion

In this chapter, the role of **B** and **H**-fields in the measurement of magnetic field was discussed. The common technologies used for magnetic field sensing such as search coils, fluxgates, SQUIDs, Hall effect sensors, AMR, GMR, MTJ, GMI, MTS-PZT composites, and MEMS were introduced. Their major applications were categorised into six basic groups: magnetic field imaging systems, high-precision power meters, position sensors, medical/biological micro-sensors and magnetic imaging of domains. The principle and electrical connections of a Hall effect device without and within a magnetic field were also illustrated.

A series of sub-theme pairs inducting heterojunctions and heterostructures, lattice-mismatched and pseudomorphic materials, quantum well and two-dimensional electron gas, δ-doped and bulk doped layers, as well as Schottky and ohmic contacts were briefly discussed. The structures, behaviours and operational principles of HEMT and pHEMT devices were discussed. This knowledge and technologies are all needed for the research performed in this PhD. Furthermore, the conducting 2DEG channels of HEMTs and pHEMTs sit very close to the sample surface and are extremely sensitive to the detection of various physical properties, especially Hall effect phenomena in a magnetic field.

Chapter 4
Quantum Well Hall effect sensor characteristics

4.1 Introduction

In this chapter, a number studies on electronic noise characterization, analysis approaches, modelling, and offset cancellation techniques were investigated. Dai [55] discussed a cross-spectrum precision noise measurement and analysis method which include bias-variance trade off and average periodogram. Teng et al. [56] developed a unified high-frequency current noise model for Metal Oxide Semiconductor Field Effect Transistors (MOSFETs) which was validated in all operation regions. This drain current noise model unified the concept of thermal noise, diffusion noise and shot noise. All the equations of noise calculation could be reduced to the well-known equations in the strong and weak-inversion regimes. Wesson et al. [57] developed an optimised, least mean square and adaptive noise cancellation algorithm which can be used on microcontrollers to cancel the periodic 50/60 Hz noise adaptively. Dai [58] introduced a wavelet transform approach to analyse electric noise in a transistor. Based on this approach, the fractal and chaos characteristic of 1/f noise was obtained, the smaller burst noise pulse embedded in the thermal noise and 1/f noise could also be detected. Khunkhao et al. [59] proposed the noise matrix of low frequency shot noise associated with the photocurrent generated in double Schottky-barrier structures based on its simplified models. The results showed that the noise matrix developed could be applicable not only to planar metal–semiconductor–metal double Schottky-barrier structures under optical illumination, but also to the existing simple shot noise theory.

The origin of the offset phenomenon in Hall devices is mainly due to: crystal damage, geometrical errors in mask alignments, mechanical stress and strain, non-uniform temperature distribution and heat dissipation in the substrate [60]. Popovic et al. [34] indicated that the offset voltage of a Hall device is a quasi-static output voltage which exists in the absence of magnetic field conditions. Because of the symmetric nature of the Hall sensor, the Hall voltage

difference of the device V_H should be zero in a zero-magnetic field situation. However, Hall devices always have unstable factors such as small errors in geometry, variations in doping density, different ohmic contact resistances and numerous other possible causes. A mechanical stress in the Hall device in combination with the piezoresistance effect can produce an electrically non-symmetric situation. The result is a parasitic component in the Hall voltage which cannot be distinguished from the real quasi-static part of the Hall voltage. Therefore, the offset voltage of Hall devices which can mask or swamp genuine small magnetic fields must be cancelled. Some researchers have explored different methods to reduce the offset which includes improved methods of manufacturing and device symmetry improvements, static and dynamic compensation techniques, spinning bias current method and so on. The techniques of the offset reduction for a Hall device are summarised in the following sections.

4.2 Fabrication of Quantum Well Hall effect sensors

Currently, commercial Hall effect sensors are mostly fabricated on traditional silicon-based technology which have limited sensitivity but benefits from integrated electronics. The main difference between the AlGaAs-InGaAs-GaAs QWHE and conventional Si CMOS field-effect transistors is the high mobility Quantum Well (QW) channel. This is a thin layer of a narrow band-gap semiconductor ($In_{0.18}Ga_{0.82}As$) sandwiched between two larger band-gap materials (In this case $Al_{0.35}Ga_{0.65}As$ and GaAs). All devices studied here were grown by Solid Source MBE in a VG V90H system with 100 mm wafer growth capability. A thin layer of $In_{0.18}Ga_{0.82}As$ is sandwiched between two layers of $Al_{0.35}Ga_{0.65}As$ (Fig. 4.1(a)). Electrons from the high band-gap supply layer are transferred into the Quantum Well as this is energetically favourable for them. These electrons then accumulate at the interface and form a high mobility 2DEG [42, 61]. Three different 2DEG QWHE sensors named P2A, P3A and P15A were fabricated in this research. The difference between sensors P2A, P3A and P15A are the spacer layers increase from 50 Å to 100 Å to 200 Å, respectively. After fabrication, all the QWHE sensors were packaged in a surface mount SOT-143 configuration with typical dimensions of ~ 3 mm × 1.5 mm × 1.0 mm as shown in Fig. 4.1(b).

The sheet resistance of P2A QWHE sensor is approximately 270 Ω/sq. This sheet resistance is made up of a mobility μ ~ 7000 $cm^2 V^{-1} s^{-1}$ and electron carrier concentration of ~ 3.3 $\times 10^{12}$ cm^{-2} at room temperature (sheet resistance $R_s = 1/q\mu n$). The P2A QWHE sensor has resolutions of 1 μT at DC and < 10 nT at higher frequencies as reported previously [42]. The noise properties of the QWHE sensors are similar to those of GMR and AMR sensors but with outstanding linearity and compact size. The dynamic range of the QWHE devices is over 180 dB.

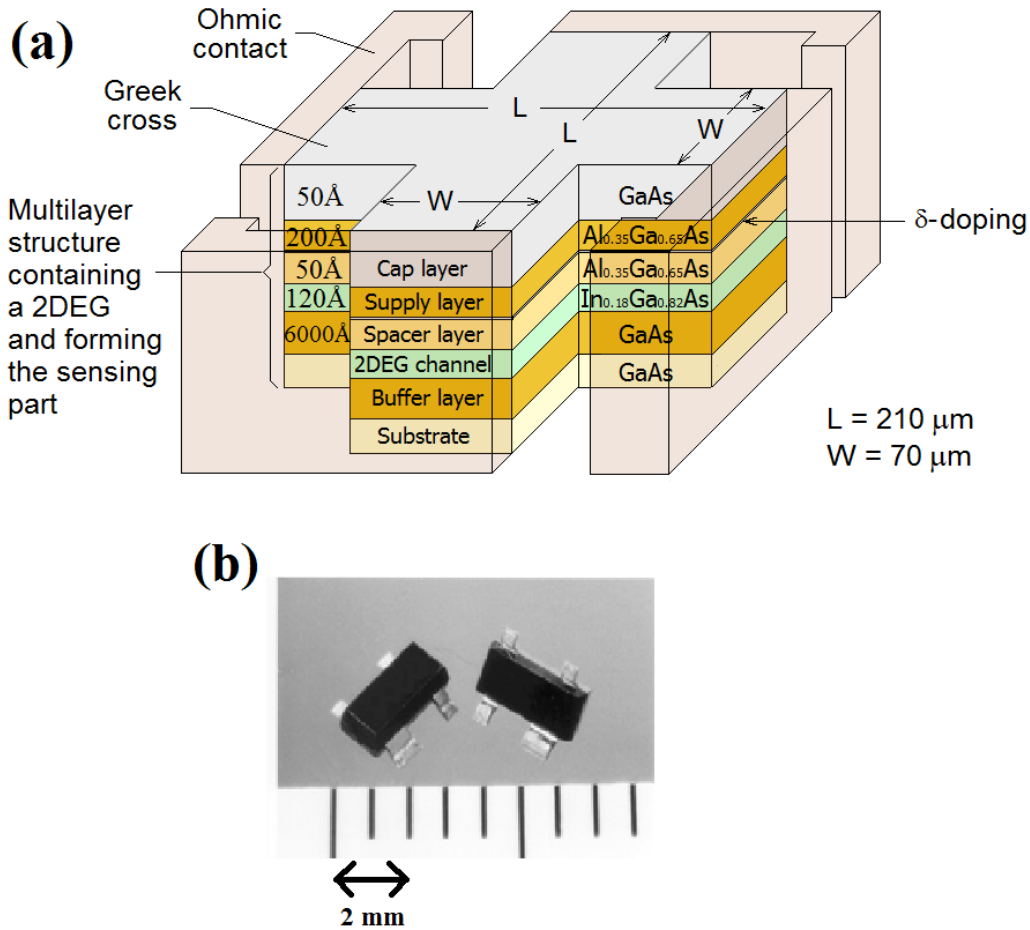

Fig. 4.1 (a) Schematic illustration of 2DEG Quantum Well Hall effect sensor (P2A) with the quantum well channel, and (b) packaged QWHE sensor in surface mount configuration.

4.3 Noise measurements

The electronic noise is a characteristic of all electronic circuits. It is generated by both

passive and active electronic devices. In electric circuits, there are five common noise sources:

1. Thermal noise.
2. Shot noise.
3. Flicker noise.
4. Burst noise.
5. Avalanche noise.

Thermal noise is an unavoidable voltage noise which is related to its resistance value, and shot noise is current noise associated with electric current flow. Other noises mostly depend on device/material types and manufacturing quality. The device noise can affect a device capability (such as signal to noise ratio) and detection limitation, it is important to obtain this characteristic information from the QWHE sensors studied in this research. With the noise characteristics measured, the theoretical limitations of the QWHE sensors can be obtained.

4.3.1 Equipment set-up

In the noise measurements, a spectrum analyser, a programmable branch amplifier and a current source were used. An Agilent 35670A Dynamic Signal Analyser (DSA) which can capture frequency spectra from DC to 102.4 kHz was used during the noise measurements. The DSA setting for noise measurements is listed as follows: input-low: grounded, AC coupling, 1600 line of resolutions, average time 100, average type RMS and Fixed input range 0 ~ 35 and 0 ~ 75 $mV_{p\text{-}p.}$ Another low noise programmable branch amplifier Stanford Research (SRS560) with variable gain from 1 to 50000 and a programmable filter was used. This amplifier has an input noise floor of 4 nV $Hz^{-1/2}$ with battery operation mode, which makes it suitable for noise measurements.

A PCB was designed and fabricated for holding the P2A QWHE sensor as shown in Fig. 4.2 (a). A BNC connector with a decoupling capacitor was used as a sensor bias current input, and two BNC connectors used as a Hall voltage differential signal output. The populated PCB was shielded with 8 layers of Aluminium foil as shown in Fig. 4.2 (b), with the shielding layer

connected to ground. A Howland current source was used to supply the input bias current. The diagram of the Howland current source is shown in Fig. 4.3. With the use of a TI OP27 low noise amplifier and a potentiometer in the current source circuit, both low noise and adjustable current output features can be achieved. The Hall voltage differential signals were amplified by the SRS560 amplifier with a gain of 60 dB, and were analysed by the Agilent 35670A Dynamic Signal Analyser.

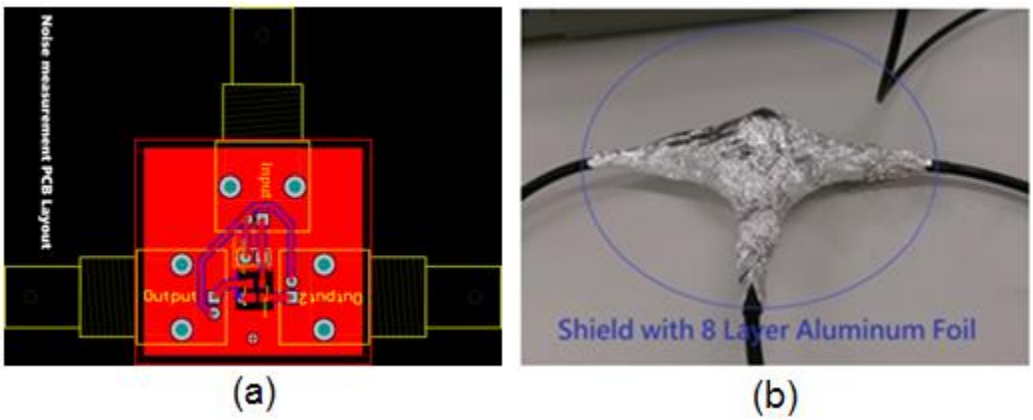

Fig. 4.2 Noise measurement equipment set-up of P2A Hall effect Sensor: (a) the PCB layout and (2) fully shielded system.

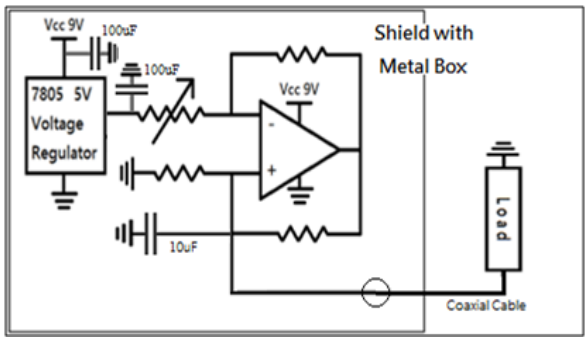

Fig. 4.3 Circuit diagram of the Howland current source.

4.3.2 Thermal noise

In the thermal noise measurements, the sensor was first disconnected from the bias current source. The noise signal of the tested QWHE sensor was measured through the differential BNC connectors on the PCB, which containing the sample under test. The differential signals were then transferred and amplified into a larger single-ended signal which was then connected to the spectrum analyser. Therefore, the measured noise was the sum of

the QWHE sensor thermal noise, cables and connector noise, amplifier input noise and spectrum analyser noise. The noise of cable and connector were minimised by using shielded 50 Ω BNC cables and connectors before and after amplification. With the symmetrical differential signal connection, the differential signal output from the QWHE sensor can also reject induced noise. To carry out the experimental measurements of the thermal noise for P2A QWHE sensor, the input noise characteristics of the SRS560 amplifier and Agilent 35670A spectrum analyser were obtained first.

The amplifier's input voltage noise of the SR560 low-noise preamplifier was approximately 4 nV $Hz^{-1/2}$ from 100 Hz to 100 kHz, and 10 nV $Hz^{-1/2}$ at 10 Hz, and rising to 40 nV $Hz^{-1/2}$ at 1 Hz) [34] as shown in Fig. 4.4. It must be noted that the voltage noise rise at low frequencies is the characteristic of flicker noise (1/f noise).

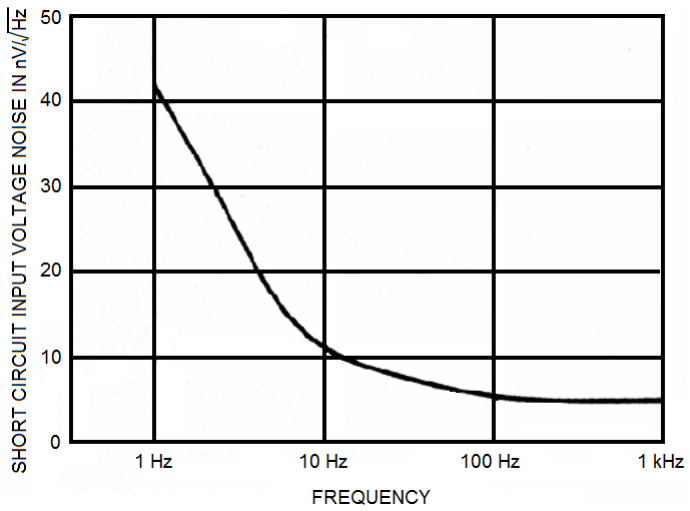

Fig. 4.4 The plot of input voltage noise versus frequency for the SR560 low noise pre-amplifier as provided by the manufacturer (Stanford research labs) [34].

In the thermal noise measurement of the P2A sensor, a 50 Ω BNC terminator was connected to the bias input as shown in Fig. 4.5. The theoretical thermal noise (V_n) of the P2A at 293 K is:

$$V_{n,\ \text{at}\ 293K} = (4kTR)^{-1/2} = (1.3806 \times 10^{-23} \times 293 \times 720)^{-1/2}\ \text{VHz}^{-1/2} = 3.42\ \text{nV Hz}^{-1/2} \tag{4.1}$$

where k is the Boltzmann's constant (1.3806×10^{-23} J K^{-1}), T is absolute temperature of the

P2A sensor in K, and R is the resistor value of the P2A sensor ~720 Ω. The spectrum analyser input noise is negligible compared the rest of the system, and therefore can be ignored. Hence, the obtained noise results are a combination of:

Measured noise = P2A thermal noise + SRS560 PreAmp noise + cable noise (4.2)

Fig. 4.5 An input short with a 50 Ω terminator was connected to the measurement system for the SRS560 input noise measurement.

The results of the thermal noise measurement of the P2A sensor are shown in Fig. 4.6. In the results, the red curve is the noise of the SRS560 amplifier and cables which is identical to the one provided by Stanford Research labs, which gave confidence in the measurement setup. The measured thermal noise of the P2A sensor was greater than the measurement system background noise. The results indicated that the noise spectrum below 10 Hz, which is the flicker noise region, was still dominated by the SRS560 amplifier. In addition, the 50 Hz mains noise was not properly rejected by the shielding. The measured thermal noise of the P2A sensor was found to be approximately 5 nV $Hz^{-1/2}$ which fits with the theoretical value of 3.42 nV $Hz^{-1/2}$.

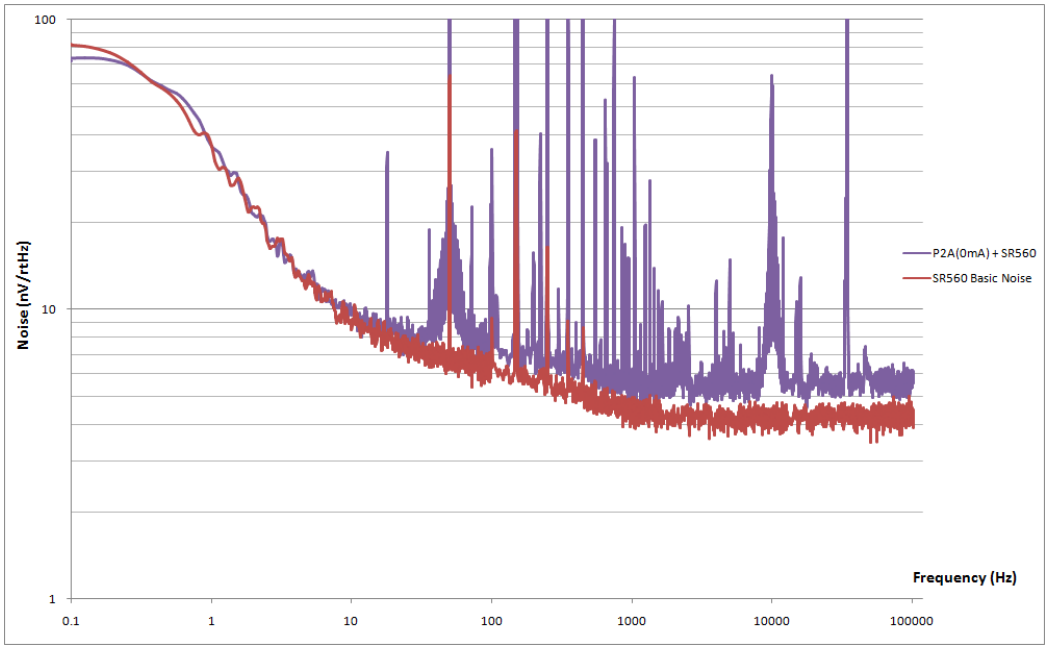

Fig. 4.6 Plot of noise results versus frequency from the thermal noise measurement of the P2A Hall effect sensor. The spikes are the 50 Hz pick-up and its harmonics.

4.3.3 Flicker noise and shot noise

The operational conditions of 1/*f* noise and shot noise measurements of the P2A sensor were: SRS560 low noise PreAmp gain = 1000 (AC Coupling), Agilent DSA-35670A (1600 line resolution), input low = GND, average (RMS) = 100, and bias current (0.5 ~ 5mA). The relationship between measured noises of the sensor can be described by the following equation:

$$\begin{aligned}\text{measured noise} &= \text{flicker noise} + \text{shot noise} + \text{thermal noise} \\ &+ \text{amplifier noise} + \text{cable noise}\end{aligned} \tag{4.3}$$

$$\text{where shot noise (current noise)} = \sqrt{2qI} = \sqrt{2 \times 1.602 \times 10^{-19} \times \text{bias current}} \tag{4.4}$$

Fig. 4.7 shows that the results of flicker noise and shot noise measurements of the P2A sensor. From Equation 4.4, the theoretical shot noise can be summarised as follows:

Theoretical Shot Noise (bias current = 0.5 mA) = 12.7 pA $Hz^{-1/2}$ × 720 Ω = 9.1 nV $Hz^{-1/2}$

Theoretical Shot Noise (bias current = 1 mA) = 17.9 pA $Hz^{-1/2}$ × 720 Ω = 12.9 nV $Hz^{-1/2}$

Theoretical Shot Noise (bias current = 3 mA) = 31.0 pA $Hz^{-1/2}$ × 720 Ω = 22.3 nV $Hz^{-1/2}$

Theoretical Shot Noise (bias current = 5 mA) = 40.0 pA $Hz^{-1/2}$ × 720 Ω = 28.8 nV $Hz^{-1/2}$

When the sensor bias current ≤ 1mA, the measured data approached the theoretical values of shot noise. When the bias current ≥ 3mA, the measured noise was greater than the theoretical values of shot noise. This was probably caused by some other effect happening in the QWHE sensor, such as crystal defects or trapping as surfaces.

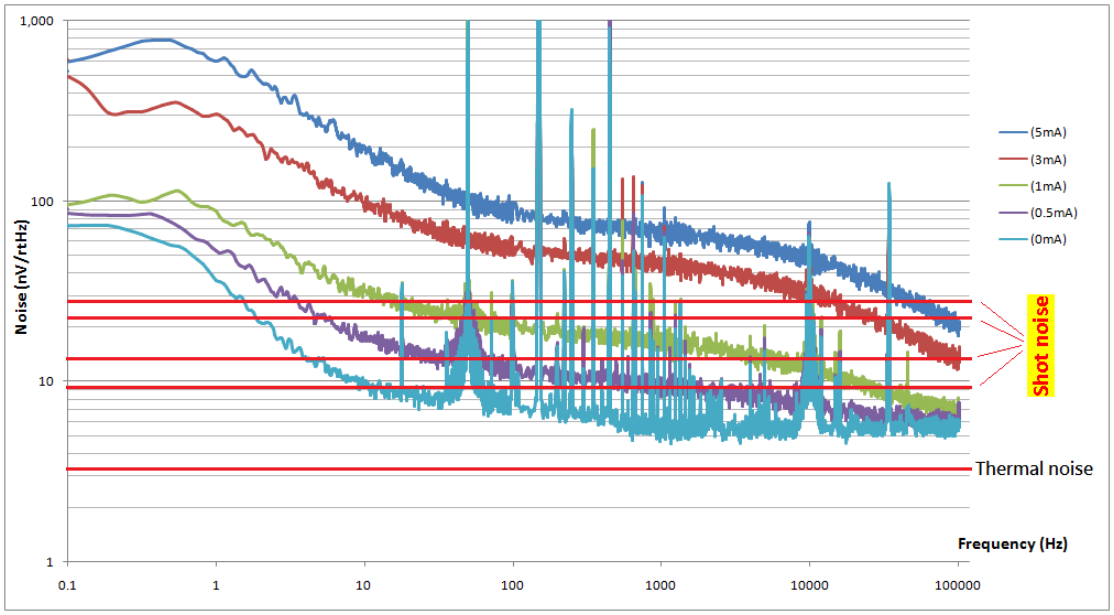

Fig. 4.7 The results of flicker noise and shot noise measurements of The P2A QWHE sensor.

4.3.4 Sensors detection limit and conclusions

From the results of the noise measurements shown in Fig. 4.6, the following equation was used to calculate the equivalent magnetic field noise floor (B_{min}) of the P2A sensor:

$$B_{\min}\ (\mathrm{T}) = 0.18\ \frac{\mathrm{nV}}{\mathrm{nT\ mA}} \times I\ \mathrm{mA} \tag{4.5}$$

where I is the sensor bias current. This equation can help us to understand the theoretical magnetic field detection limited of the P2A sensor (if phase lock-in techniques are not present). Fig. 4.8 shows the equivalent field strength of the noise floor versus frequency at different bias currents. Table 4.1 lists the summary of the theoretical detection limits of magnetic field of the P2A QWHE sensor.

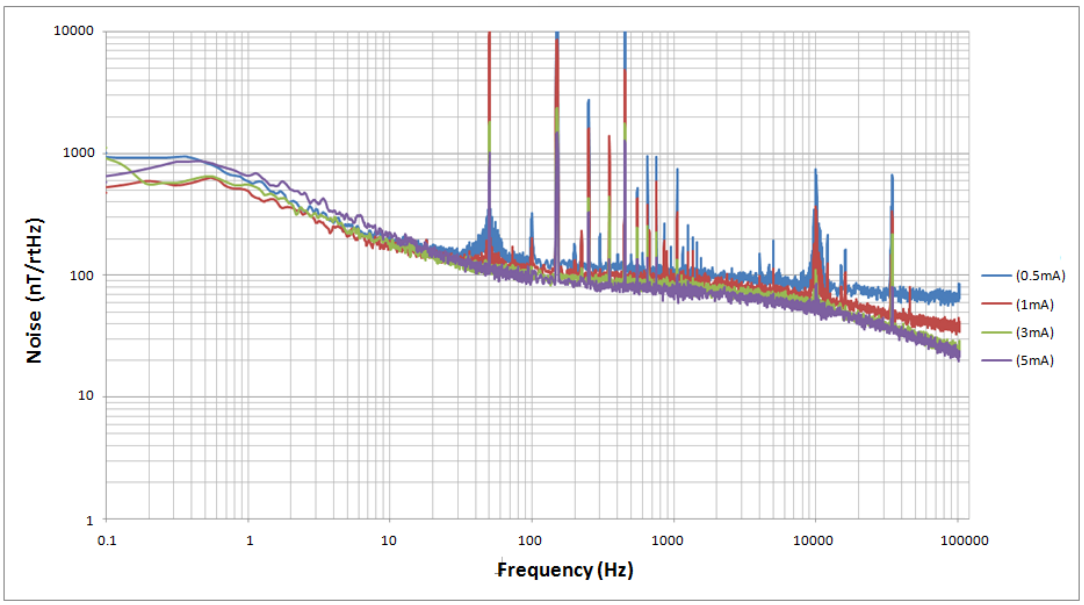

Fig. 4.8 The net noise values of 1/*f* and shot noises measurement versus frequency for the P2A QWHE sensor for various applied currents.

Table 4.1 Summary of the detection limit of B-Field using the P2A QWHE sensor.

Frequency	Detect limit (nT $Hz^{-1/2}$)	Frequency	Detect limit (nT $Hz^{-1/2}$)
1Hz	~ 600	5kHz	~ 60
10Hz	~ 200	10kHz	~ 50
100Hz	~ 100	100kHz	~ 20
1kHz	~ 70		

The result shows that the detection limit of the P2A sensor is smaller for higher input frequencies. Assuming that the noise floor increase with bias current is due to the shot noise of the P2A sensor; then the main factor affecting the limitation of the minimum detectable field that the P2A sensor is set by this shot noise. From the perspective of sensor detection limitation, the effect of increasing sensitivity and the effect of increasing noise floor cancel each other out when increasing the sensor bias current. The noise floor of this shot noise at frequencies greater than 10 kHz is less than or equal to the thermal noise at low sensor bias current conditions (≤ 1mA) which explains the mismatch situation after 10 kHz, shown in Fig. 4.8. These result showed that there is no benefit to using higher bias current for the P2A sensor when detecting magnetic fields below 10 kHz. However, if the frequency is greater than 10

kHz, or a superhetrodyne technique of biasing an alternating current is used, a current of ≥ 3 mA will be most effective to bias the sensor with, as there is significant improvement in the detection limit.

4.4 Drift voltage measurements

A drift in voltage is caused by the movement of charge carriers (electron holes and electrons) in response to changes in applied electric field. The drift voltage depends on the mobility of charge carriers in a given conducting medium. When an applied electric field is changed across two terminals of a Hall sensor, a drift voltage is produced in the initial stage due to the directional change of electron flow. This behaviour causes measurement errors when designing a magnetometer, therefore requiring this to be measured, understood and avoided.

An INA217 instrumentation amplifier (Gain = 51) and a function generator Agilent 33500B, was used to supply the pulse bias voltages to the sensor, used in the drift measurements. The INA217 instrumentation amplifier is a low-noise low-distortion amplifier which is ideal for low noise operations. The Agilent 33500B is a waveform generator with built-in arbitrary waveform and pulse capabilities. It consisted of eight upgradable models with 1 or 2 channels, 20 or 30 MHz bandwidth, and an optional baseband I-Q signal player. In this measurement, the period of pulse waveform, duty cycle, and edge were 15.6 ms, 4%, and 5 ns, respectively.

To understand the effect of initial and varying input sensor bias voltage/current on the drift voltage of the Hall voltage output, three different QWHE sensors: types P2A, P3A and P15A were tested. The key differences between the three sensors were their increasing input resistances, sheet resistance and sensitivities from the P2A to the P15A, as shown in Table 4.2 below.

Table 4.2 Sensitivity, sheet resistance and input resistance of each QWHE sensor.

Sensor	**Spacer (Å)**	**Input resistance (Ω)**	**Sheet resistance (Ω/sq)**	**Electron mobility (cm^2/Vs)**	**Sheet Carrier concentration (cm^{-2})**	**Sensitivity (mV/mA/mT)**
P2A	~ 50	~ 730	~ 270	~ 7000	~ 3.3×10^{12}	~ 0.18
P3A	~ 100	~1200	~ 460	~ 7500	~ 1.8×10^{12}	~ 0.32
P15A	~ 200	~3500	~ 1200	~ 7900	~ 6.5×10^{11}	~ 0.9

The value of mobility increases from P2A to P15A because the spacer layer increases from 50 Å to 100 Å to 200 Å, hence there is less carrier scattering occurring from the P2A to P15A. However, the increase in spacer layer decreases the carrier concentration as shown in Table 4.2. The P15A exhibits the best current sensitivity at the expense of a large input resistance. For best noise performance, the deciding factor is the sheet resistance, which is lowest for the P2A. The lower sheet resistance means the thermal noise will be minimal, therefore the detectability will be highest. Therefore, the P2A is expected to have the best detectability (lowest minimum magnetic field detectable) despite having the lowest current sensitivity. The lower sheet resistance of the P15A also introduces severe drift issues, as explored below.

The results of drift measurement with various applied bias voltages of the three sensors are shown in Fig. 4.9, Fig. 4.10, and Fig. 4.11. From these figures, the results indicate that the drift voltage has a high correlation with the QWHE sensors input bias voltage. The values of the drift voltage of the QWHE sensors were negative, positive, or both! From the results, the drift voltage was shown to be independent of applied bias voltage/current and has individual characteristics between sensors, getting more severe for the higher input resistance devices. Therefore, an applied voltage of < 3 V is needed to keep the drift at a minimum for all sensors.

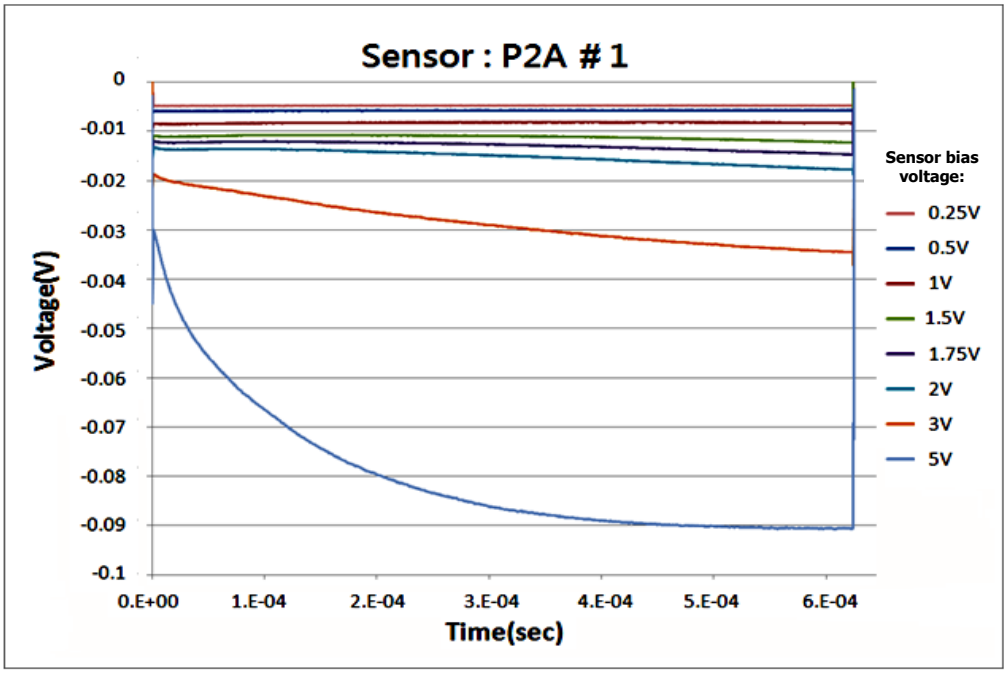

Fig. 4.9 Plot of output voltage versus time for drift measurements for P2A sensor (R = 730 Ω).

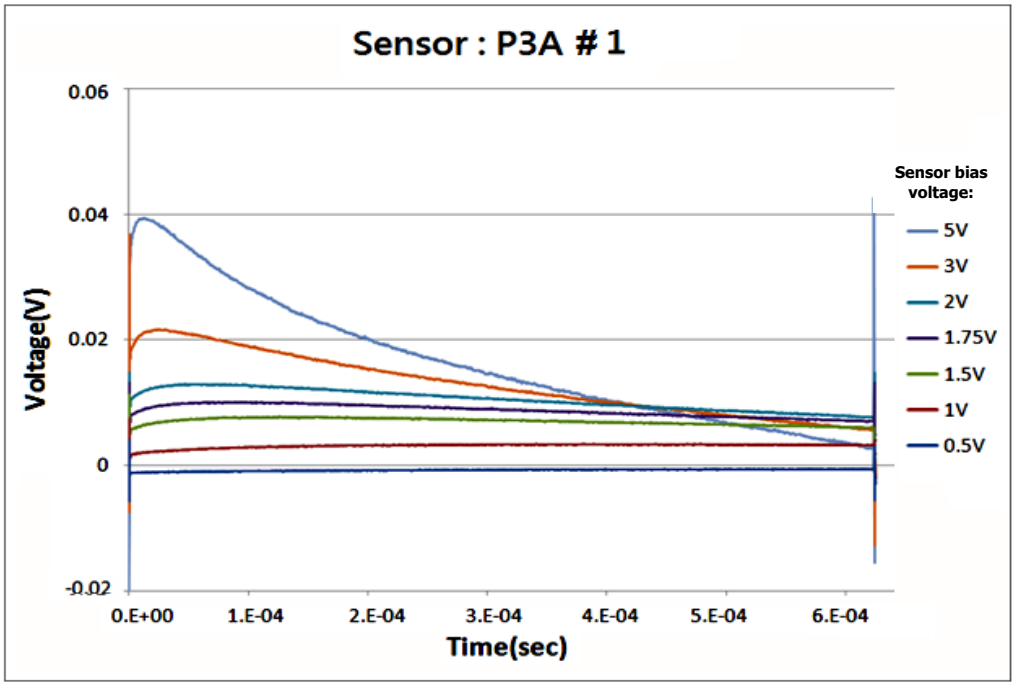

Fig. 4.10 Plot of output voltage versus time for drift measurements for P3A sensors (R = 1237 Ω).

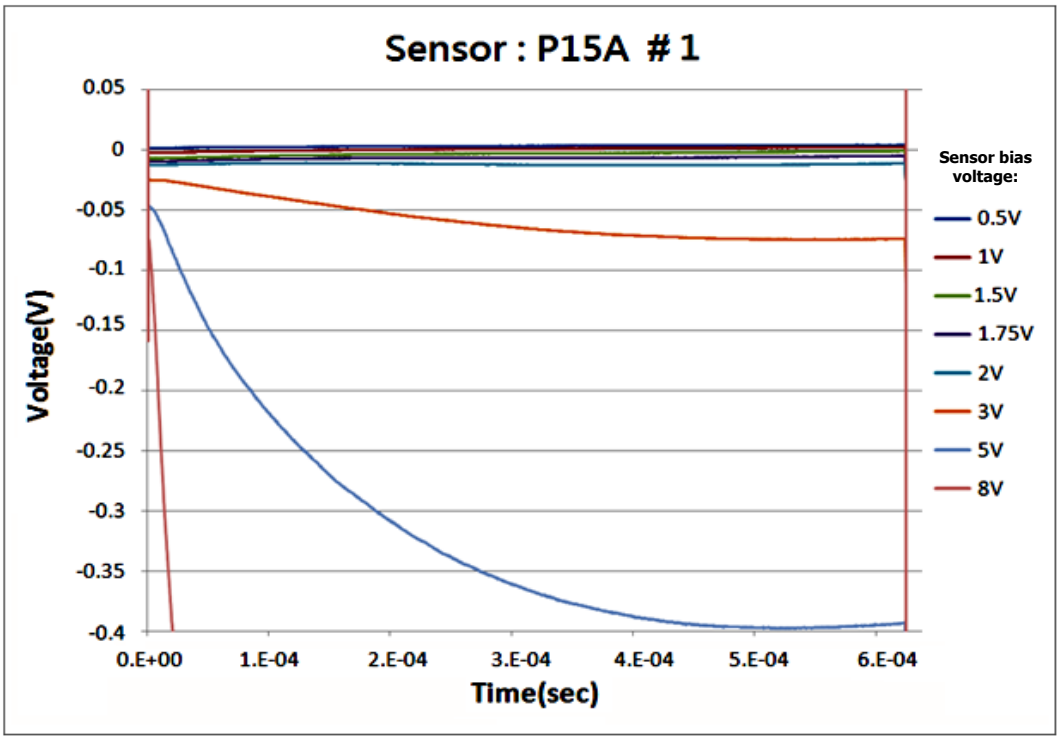

Fig. 4.11 Plot of output voltage versus time for drift measurements for P15A sensors (R = 3570 Ω).

It is clear from the data above that drifts of less than 90 μV can be obtained for the P2A for applied bias voltages less than or equal to 2 V and that it can outperform the other two higher sensitivity sensors. The P2A was therefore chosen for all subsequent system developments.

4.5 Offset measurements and dynamic offset cancellations

The offset voltage behaviour in Hall effect devices is mainly due to crystal damage, geometric errors in mask alignments, mechanical stress and strain, non-uniform temperature distribution, heat dissipation in the substrate [42]. Regarding the symmetrical nature of the device geometry, the output voltage of Hall effect devices V_H should equal to zero when there is no external magnetic field present [61]. However, Hall effect devices always have small errors in geometry, variations in doping density, differences in ohmic contact resistances, and other factors which causes asymmetric conditions and therefore offset voltage. Furthermore, mechanical stresses in the Hall effect device which can be caused by chip packaging, in

combination with the piezoresistance effect, can produce an electrical non-symmetrical situation. As a result, a parasitic component in the output Hall voltage which cannot be distinguished from the real quasi-static part of the Hall voltage exists. Therefore, the offset which can severely limit the application of Hall effect devices has to be measured, understood and cancelled.

4.5.1 Dynamic quadrature offset cancellation

In the dynamic quadrature offset cancellation operations, the quadrature states are generated by periodically switching the connection of the bias current inputs and the connection to the Hall voltage output in orthogonal orientations. Each state is defined by a set of signal switches which are controlled by a square wave signal generator. Furthermore, a low pass filter is used to average out the offset voltages of the Hall effect sensors. The Hall device equivalent circuit for discrete current spinning system can be implemented with four states (DC 4-types automatic spinning current approach), as shown in Fig. 4.12.

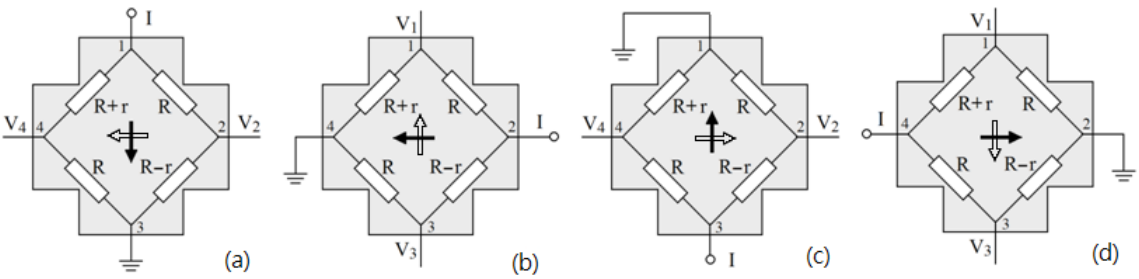

Fig. 4.12 Spinning current implementation of a Hall plate model. The direction of drive current (I) flow (solid arrow) and direction of Hall voltage (V_H) detection (hollow arrow) operate periodically in a clockwise direction.

When an external magnetic field is applied, the magnetic contribution to the output terminals voltage is $\pm V_H/2$. For the drive current (I) flowing through terminals 1 and 3, the voltage between terminals 2 and 4 ($V_{2\to4}$) is

$$V_{2\to4} = V_2 - V_4 = \left(V\frac{R}{2R-r} + \frac{V_H}{2}\right) - \left(V\frac{R}{2R+r} - \frac{V_H}{2}\right) \tag{4.6}$$

And for the drive current flowing through terminals 2 and 4, the voltage between terminals

3 and 1 ($V_{3\to1}$), terminals 4 and 2, and terminals 1 and 3 are

$$V_{3\to1} = V_3 - V_1 = \left(V\frac{R-r}{2R-r} + \frac{V_H}{2}\right) - \left(V\frac{R+r}{2R+r} - \frac{V_H}{2}\right) \tag{4.7}$$

$$V_{4\to2} = V_4 - V_2 = \left(V\frac{R}{2R+r} + \frac{V_H}{2}\right) - \left(V\frac{R}{2R-r} - \frac{V_H}{2}\right) \tag{4.8}$$

$$V_{1\to3} = V_1 - V_3 = \left(V\frac{R+r}{2R+r} + \frac{V_H}{2}\right) - \left(V\frac{R-r}{2R-r} - \frac{V_H}{2}\right) \tag{4.9}$$

Therefore, the average voltage between the outputs of the DC 4-types spinning current is

$$\begin{aligned}
V_{av} &= \frac{V_{4\to2} + V_{3\to1} + V_{2\to4} + V_{1\to3}}{4} \\
&= \frac{1}{4}\left[\left(V\frac{R}{2R-r} + \frac{V_H}{2}\right) - \left(V\frac{R}{2R+r} - \frac{V_H}{2}\right) + \left(V\frac{R-r}{2R-r} + \frac{V_H}{2}\right) - \left(V\frac{R+r}{2R+r} - \frac{V_H}{2}\right)\right. \\
&\quad \left. + \left(V\frac{R}{2R+r} + \frac{V_H}{2}\right) - \left(V\frac{R}{2R-r} - \frac{V_H}{2}\right) + \left(V\frac{R+r}{2R+r} + \frac{V_H}{2}\right) - \left(V\frac{R-r}{2R-r} - \frac{V_H}{2}\right)\right] \\
&= \frac{1}{4}\left[V\left(\frac{R}{2R-r} - \frac{R}{2R+r} + \frac{R-r}{2R-r} - \frac{R+r}{2R+r} + \frac{R}{2R+r} - \frac{R}{2R-r} + \frac{R+r}{2R+r} - \frac{R-r}{2R-r}\right)\right. \\
&\quad \left. + 8\times\frac{V_H}{2}\right] \\
&= \frac{1}{4}\left[0 + 4V_H\right] \\
&= V_H
\end{aligned} \tag{4.10}$$

Therefore, if the device connections are commutated between the above four states as shown in Fig. 4.12, the offset is eliminated when the drive current is kept constant.

4.5.2 Development of a 4-directional dynamic offset cancellation technique

The block diagram of the offset cancellation using the spinning-current technique is shown in Fig. 4.13, which consists of an external current source to supply a constant current to the Hall sensor via analogue signal switches for automatic offset cancellation. The analogue switches supply a square wave current which is controlled by a clock signal generator with a programmable timer (Sig Input-2 in Figure 4.13). Two analogue switches are used for flipping the signal (or current) to the Hall effect sensor. One of them is controlled by a clock signal generator with a programmable timer (Sig Input-1 in Figure 4.13), which supplies a square wave control signal. The commutated output from the analogue switching circuit is connected to an amplification stage consisting of an instrumentation amplifier. Finally, the filtered output is fed into a digital multi-meter to detect the reduced offset voltage. By programming the external dual-channel function generator to get a square wave input to the BNC control signal, the phase of 4-type spinning-current can be customised and controlled. In this study, the period of Sig Input-1 is double that of Sig Input-2.

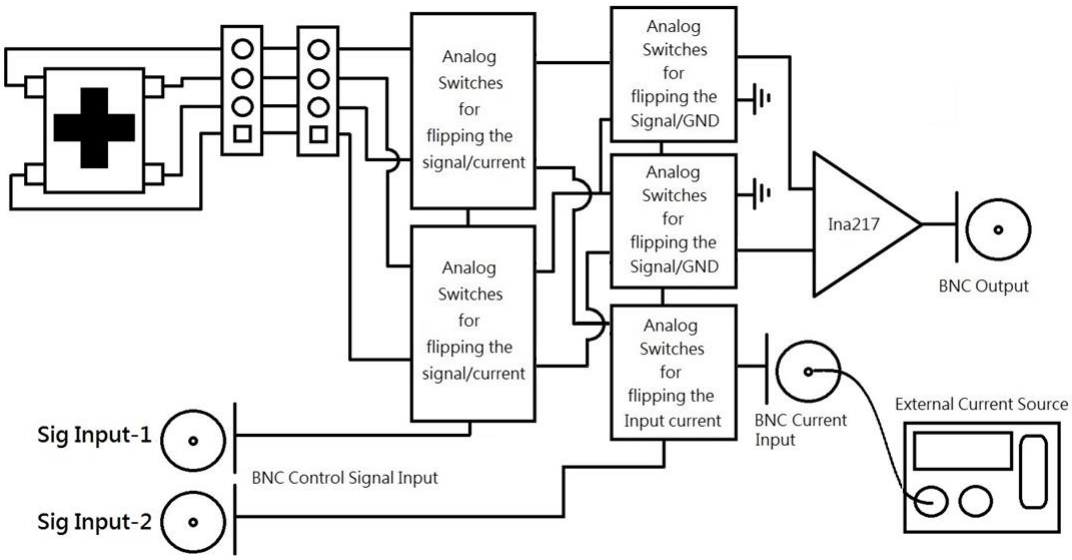

Fig. 4.13 Block diagram of the offset cancellation using the 4-types spinning-current technique.

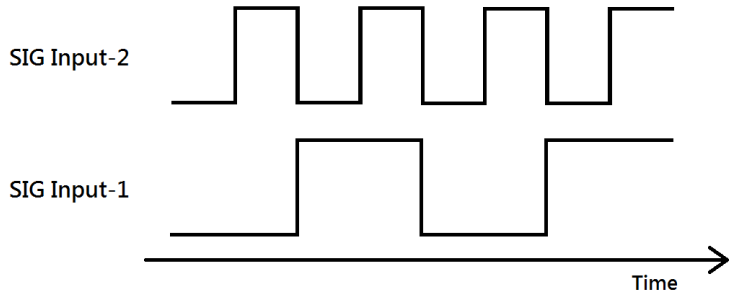

Fig. 4.14 Schematic illustration of square wave control signals for SIG Inputs-1 and -2.

A schematic illustration of the 4-type spinning technique phase is shown in Fig. 4.15. The direction of drive current flows (blue arrow) and direction of offset voltage detection (red arrow) alternates periodically in a clockwise direction. Thus, if the device connections are commutated between the above four states, the offset is eliminated as explained by Eq. 4.10 when the drive current is kept constant.

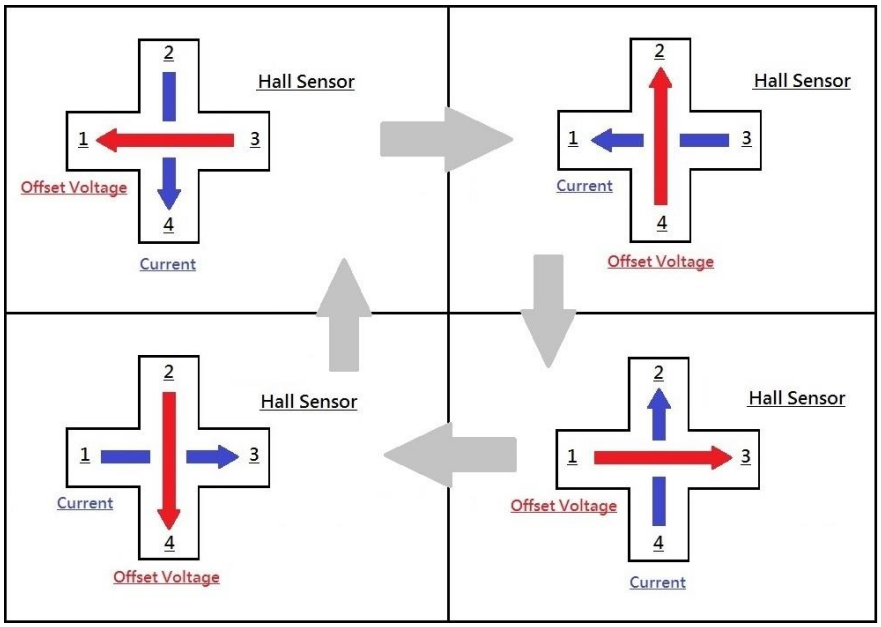

Fig. 4.15 Schematic illustration of the 4-type spinning technique phases. The direction of drive current flows (blue arrow) and direction of offset voltage detecting (red arrow) alternate periodically in clockwise direction.

Figs. 4.16 and 4.17 depict the architecture and PCB layout, of the dynamic quadrature offset cancellation circuit using 4-way spinning-current technique. As shown in Fig. 4.16, a voltage regulator LM7805 and a self-contained fixed linear voltage regulator, were used to maintain a steady voltage. Since the input voltage of the LM7805 must always be higher than

the output voltage (+5 V) by some minimum value (typically 2 V), two 9 V batteries are used to provide circuit power (for positive and negative power supply). The spinning current vector is generated by an external current source via an analogue switch MAX4606 with low on-resistance (≤ 5 Ω). Two quad analogue switches are used to change the input/output direction for different spinning directions. These three MAX4606 analogue switches were controlled by an external square wave control signal (SIG Input-2). Another two quad analogue switch MAX4606s were used to connect the applied current, as well as synchronise the changing outputs of the measured Hall voltage. These were controlled by an external square wave control signal (SIG Input-1).

As a result of these, the output signal was continuous; meaning that the offset could be removed via averaging and offsetting. A monolithic instrumentation amplifier INA217 was used in the amplification stage, as it was designed for high-precision data acquisition and instrumentation applications. The INA217 is a low-noise, low-distortion, monolithic instrumentation amplifier offering excellent accuracy. The current-feedback input circuitry provided a wide bandwidth even at high gain (200 kHz at G = 100). Following amplification, a HDR1X2 header was applied as a test point for connecting different Hall effect sensors. The pins 3, 6, 9, 11, and 14 of the two analogue switch MAX4606s were connected to the Hall sensor, so that a periodically connecting supply current (I) and the input of the instrumentation amplifier INA217, as shown in Fig. 4.16 could be achieved. In Fig. 4.16, two clock signals (CS) from external signal generators were required for the control of the two MAX4606s. The role of the external signal generators was to select suitable switches to maintain periodically correct connections. The clock signal generator with a frequency range from 5 Hz to 10 kHz was used as a square wave reference.

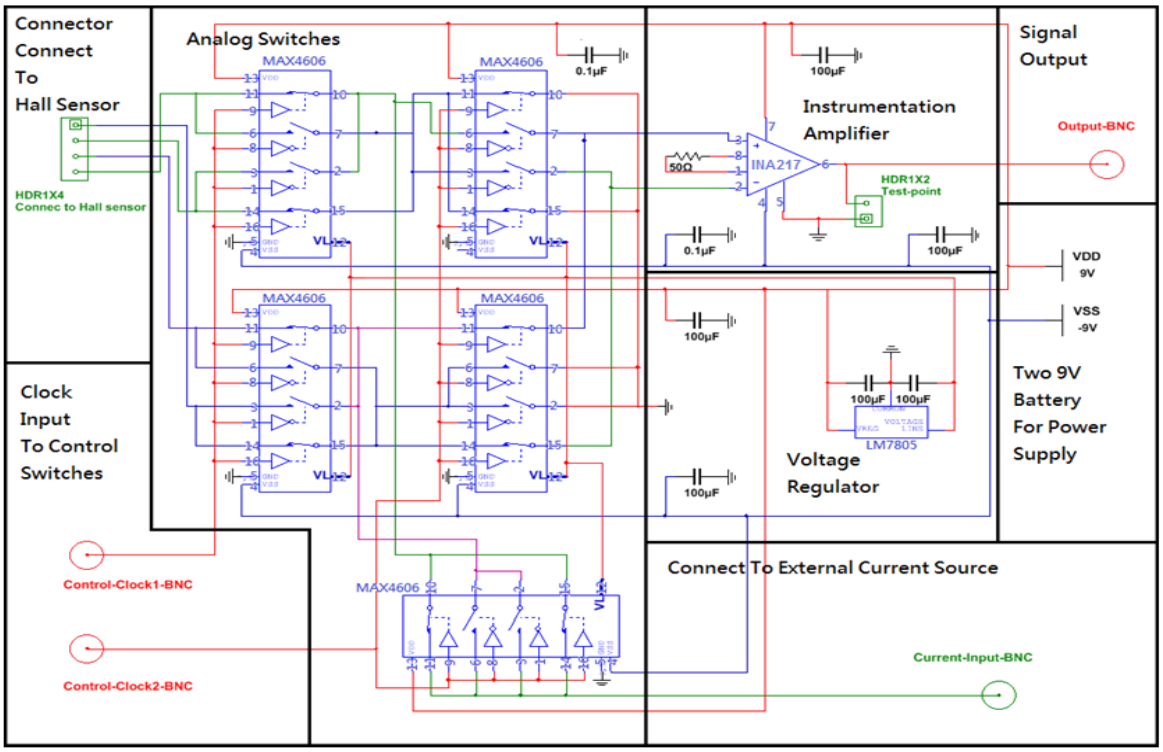

Fig. 4.16 Architecture of the automatic offset cancellation circuit using 4-type spinning current technique.

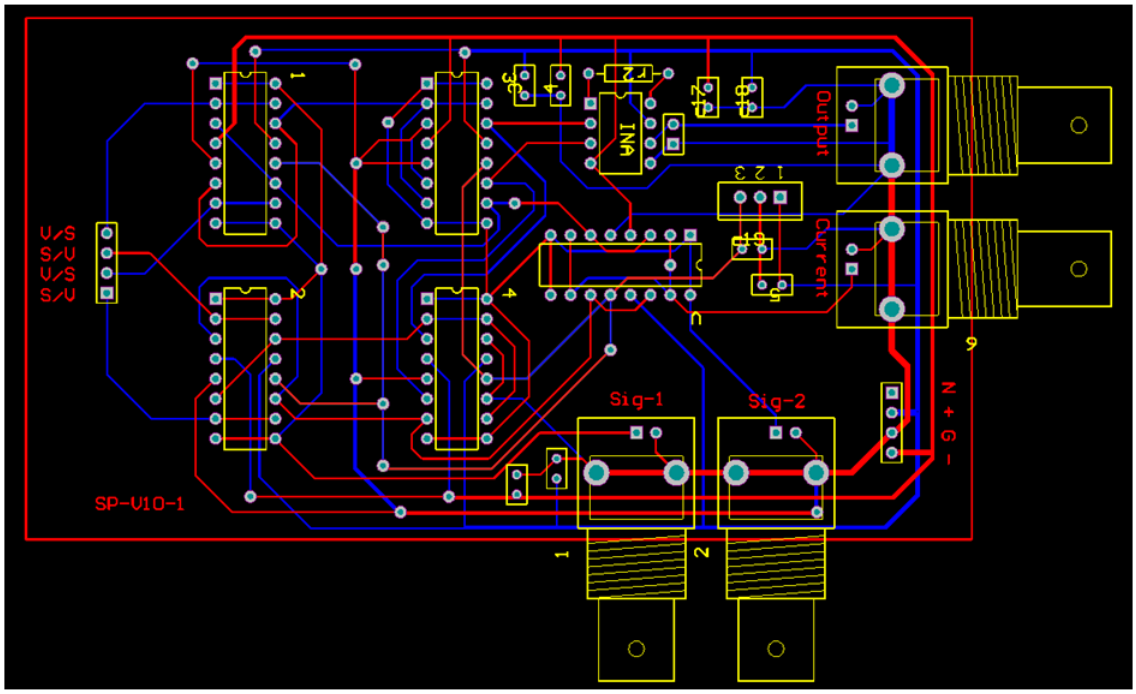

Fig. 4.17 The PCB layout of the offset cancellation using 4-type spinning current technique.

4.5.3 Offset measurements with 4-directional dynamic offset cancellation technique

Fig. 4.18 shows the plots of magnetic field versus frequency using the offset cancellation measurement on the P2A Hall effect sensor. The test results indicated that the offset cancellation using 4-type spinning current technique is accurate. The decrease of the "offset" magnetic field in the frequency range lower than 1 kHz is sharp at applied current of 1 mA. However, the variations of the offset magnetic fields with frequency at applied currents of 1, 2, and 3 mA were low when the frequency was greater than 1 kHz. The plots of residual magnetic fields versus applied current, for the offset cancellation measurement of the P3A QWHE sensor, are shown in Fig. 4.19. The measurement results of offset cancellation for P2A and P3A show that using the 4-type spinning current technique for cancelling the offset of QWHE sensors was successful, where the offset voltage of the Hall effect magnetometer (~ 50 μT) is comparable to the magnitude of the Earth's magnetic field when the applied frequency higher than 1 kHz. The magnitude of Earth's magnetic field ranges from 25 to 65 μT (0.25 to 0.65 gauss) with a medium value of 40 μT. The key benefit of automatic spinning operations occurs at higher frequency (≥ 1 kHz) and lower input currents to the Hall effect sensors. The results also show that the drift voltage variation of Hall voltage with applied current were small when the applied frequency higher than 1 kHz. Therefore, the frequency of 1 kHz is thus a critical voltage, and determines the suitability of the spinning current offset cancellation technique.

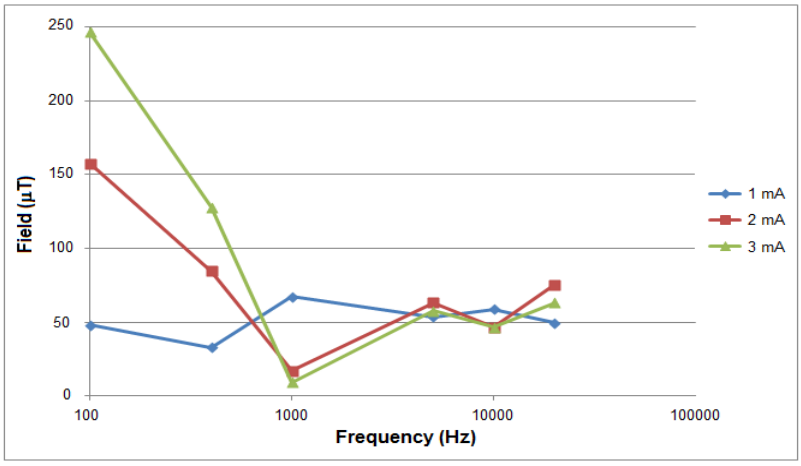

Fig. 4.18 Plots of equivalent magnetic field of offset voltage versus frequency for offset cancellation measurements, for the P2A QWHE sensor at different frequencies. The results show that the offset voltage equivalent magnetic field is comparable to Earth's magnetic field.

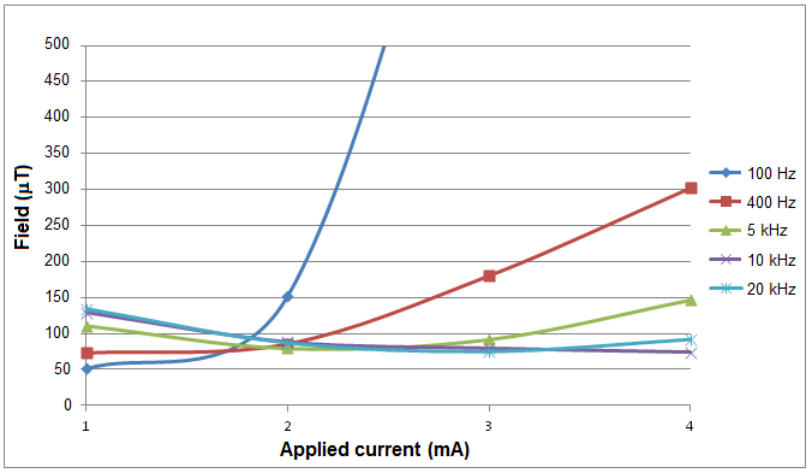

Fig. 4.19 Plots of equivalent magnetic fields of offset voltage versus applied current for offset cancellation measurement, for the P3A QWHE sensor.

4.6 Conclusion

A noise measurement setup for the different QWHE sensors was designed, with their noise characteristics being measured. The results indicated that the noise spectrum of P2A QWHE sensors is dominated by the SR560 amplifier with zero sensor bias voltage when the magnetic field is ≤ 10 Hz. However, the thermal noise and flicker noise of the P2A sensor is greater than the background noise floor for frequencies greater than 10 Hz, which gives confidence in the setup. From the results of flicker noise and shot noise measurements of the

P2A sensors (720 Ω), it can be summarised that the theoretical shot noises at applied currents of 0.5, 1, 3, and 5 mA were 9.1 nV $Hz^{-1/2}$, 12.9 nV $Hz^{-1/2}$, 22.3 nV $Hz^{-1/2}$, and 428.8 nV $Hz^{-1/2}$ respectively. The measured data agrees reasonably well with the calculations for theoretical thermal and shot noise when the input bias current is < 3 mA; where excess noise is visible for input bias currents > 3 mA. Therefore, the noise measurements of the P2A sensor demonstrate that there is a benefit in operating the P2A sensor under input bias current ≥ 3mA when the measured magnetic field is greater than 10 kHz or a superhetrodyne technique of AC bias current for the P2A sensor is used.

The results of drift measurements with various applied voltages on the P2A, P3A, and P15A QWHE sensors indicated that the drift voltage is highly dependent on the input impedance of the sensor. The values of drift voltages were found to be either positive, negative, or both! The results also demonstrate that drift voltage is dependent on applied voltage/current and is different for individual sensors. In order to get the best performance of the P2A QWHE sensors, a sensor input bias voltage ≤ 2 V is suggested to ensure the drift voltage is below 90 μV.

The mathematics of automatic offset cancellation with 4-type spinning current technique was described. The DC circuit and PCB designs of an offset cancellation circuit with 4-type spinning current technique was designed, built and tested. The results indicated that the decrease in the residual offset magnetic field for frequencies less than 1 kHz is sharp at applied currents of 1 mA or less. However, the variations of residual offset magnetic field with frequency at applied currents of 1, 2, and 3 mA were low when the frequency was greater than 1 kHz. The results of offset cancellation for P2A and P3A sensors show that using the 4-type spinning current technique is suitable for cancelling the offset of the Hall effect sensors, with the offset voltage of the Hall effect magnetometer approaching the magnitude of the Earth's magnetic field when the applied frequency was higher than 1 kHz. The key benefit of automatic spinning operations occurs at higher frequencies (≥ 1 kHz) and lower input currents to the QWHE sensors. The results also show that the drift voltage variations of Hall voltage

with applied current are small when the applied frequency is higher than 1 kHz. Therefore, the frequency of 1 kHz is a critical factor, determining the suitability of the spinning current offset cancellation technique.

Chapter 5
Quantum Well Hall effect magnetometer and Quantum Well Hall effect linear array magnetic-field scanner

Electromagnetic effects are the basis of many electromagnetic non-destructive testing methods. These including eddy current testing (ECT), magnetic flux leakage testing (MFL), magnetic-particle inspection (MPI) and alternating current field measurement testing (ACFM). Most of these methods use magnetic particles, induction coils and silicon-based Hall effect sensors as their sensing method to detect the direction and strength of the magnetic field. In some other specific cases, magnetoresistors can be used to detect the characteristic changes of magnetic behaviour in microstructures [66]. Although these magnetic field sensing methods have their own benefits, they do have several limitations as discussed to previously.

In this study, Quantum Well Hall Effect (QWHE) sensors have been used as the magnetic-field detection method to compete with commercial electromagnetic non-destructive testing methods. Compared to other magnetic-field sensors, QWHE sensors have excellent frequency-gain linearity, linear sensitivity and very high signal to noise ratios. This gives the QWHE sensors the ability to sense the alternating magnetic-fields in a wide frequency range without complex calibrations or data processing. The QWHE sensors also have the advantage of compact size, which make them suitable to be used in magnetic field sensing arrays. At the start of this research, a single element magnetometer and two linear array magnetic field scanners were designed, built and tested.

5.1 Quantum Well Hall effect magnetometer

A magnetometer is the basis of any magnetic field scanner or magnetovision system. Building a QWHE magnetometer can help with understanding the characteristics, drawbacks and the best operating conditions of the QWHE sensors under a variety of conditions. It is

also crucial to understand magnetic field behaviours of materials in this study, in which a high sensitivity alternating (AC) and direct (DC) magnetic field QWHE magnetometer can be used to understand the interaction of electromagnetic field in ferromagnetic and non-ferromagnetic materials. As a result, the design and testing of a high sensitivity, wide dynamic range, high signal to noise ratio, wide frequency response, as well as static and alternating magnetic fields QWHE magnetometer, is the foundation of all the work undertaken in this PhD thesis.

5.1.1 Circuit design and PCB layout

Fig. 5.1 depicts the block diagram of the DC and AC magnetic field QWHE magnetometer. In this research, the P2A QWHE sensor, as described previously, was chosen as the magnetic field sensing sensor in the design due to its high sensitivity, high signal to noise ratio, low offset voltage, low drift voltage and high stability characteristics. A constant current source was used to provide bias current for the sensor. With the use of a constant bias current to drive the QWHE sensor, this sensor has the features of a low temperature coefficient of output Hall voltage and high sensitivity stability. An extended arm design helped the magnetometer being used in narrow gap measurement situations. The amplified differential Hall voltage signals were converted into a single-ended signal by using an instrumentation amplifier. A programmable gain amplifier was used to increase the measurement dynamic range; and also be used as a buffer for charging up the sampling capacitor of the Successive Approximation Register Analogue to Digital Converter (SAR ADC). A low pass filter was integrated in the programmable gain amplifier circuit section for restricting high frequency noise.

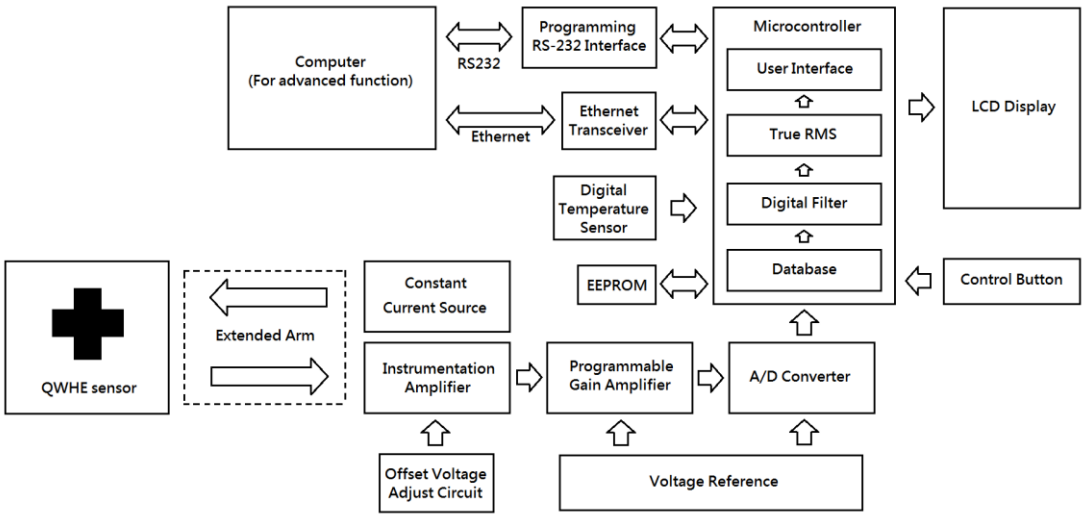

Fig. 5.1 QWHE magnetometer block diagram.

A high speed, high resolution, SAR ADC provided an adequate sample rate for the alternating magnetic field measurements with good resolution for faint magnetic field detection. With a powerful 16-bit/32-bit ARM7 microcontroller, signal processing and root mean square conversion could be performed inside the microcontroller chip. A temperature sensor was used to monitor the temperature changes of the magnetometer which could be used for automated temperature compensation. The measurement data was then converted to magnetic field strength in root mean squared units and displayed on a colour liquid crystal display (LCD). Two communication interfaces were designed in this magnetometer for computer communication purposes. An RS-232 protocol port was used for uploading and updating firmware; and a Fast Ethernet protocol port was used to upload measurement data to the computer, for advanced computer program features.

The circuit schematic of the QWHE magnetometer is shown in Appendix 1. In the circuit schematic, the circuit design was separated into six distinct sections, including:

1. Magnetic field sensing section (front end analogue section).
2. Analogue to digital conversion section which include programmable gain amplifier and voltage reference circuit.
3. Microcontroller section which include EEPROM and digital temperature sensor.
4. Ethernet section.

5. Function selection button section.
6. Power supply section.

A ground reference current source circuit, based on an OP484 operational amplifier was used to supply bias current to the sensor. The instrumentation amplifier TI INA163 features wide supply voltage operation, low input noise, good output voltage slew rate and good output current driving capability which make it an optimum for this magnetometer. With the offset correction circuit, offset voltage from the sensor and amplifier could be manually reduced. The TI PGA281 programmable gain amplifier which has the features of low flicker noise, wide input range, 60 dB amplification range with binary steps, low offset voltage and excellent common-mode rejection ratio was selected in this design. A Linear Technology LTC2364-18 18-bit SAR ADC with a throughput rate of 250 ksps and a signal to noise ratio of 97 dB was used in this design. Compared to other types of analogue to digital converters, the SAR ADC has the advantages of high sampling rate, low power consumption and compact package size which make it an optimal choice for a battery operated handheld magnetometer. A NXP LPC2387 ARM7 based microcontroller with built-in Ethernet MAC address feature was chosen in this design. This microcontroller comes with 70 general purpose IO pins and a built-in USB 2.0 controller which can be operated up to 72 MHz. With a Keil Microcontroller Development software, the microcontroller could be programmed in Keil C51 language which is similar to C language. A 128 x 160-pixel colour LCD with a Serial Peripheral Interface (SPI) bus interface was used to display the setting and the measured magnetic field reading. In the power supply section, two commercial Traco Power TMR3 DC-DC converters were chosen due to their compact size and good efficiency (~80%). These DC-DC converters were used to supply both positive and negative voltage to the analogue front end circuit. Two more voltage regulators were used to supply 5V and 3.3V for the digital circuit section and the rest of the circuit sections.

The PCB circuit layout of the QWHE magnetometer is shown in Fig. 5.2. The layout was designed with the Altium Designer software. A simple Two-layer PCB layout was used

in the design to reduce the prototype size. The P2A QWHE sensor in a SOT-143 package was mounted on the extended arm as shown in the left-hand side of Fig. 5.2. With the narrow-extended arm design, the magnetometer could be used to measure magnetic field strength in narrow gaps. The copper traces for differential Hall voltage signals were laid in a parallel configuration with the smallest gap between them to achieve better noise rejection. The DC-DC converter and digital circuit section were physically separated to avoid electromagnetic interference. A battery container was placed between the main circuits and power section circuits. An Ethernet jack was also placed on the right-hand side of the PCB layout for communication purpose between the computer and the magnetometer.

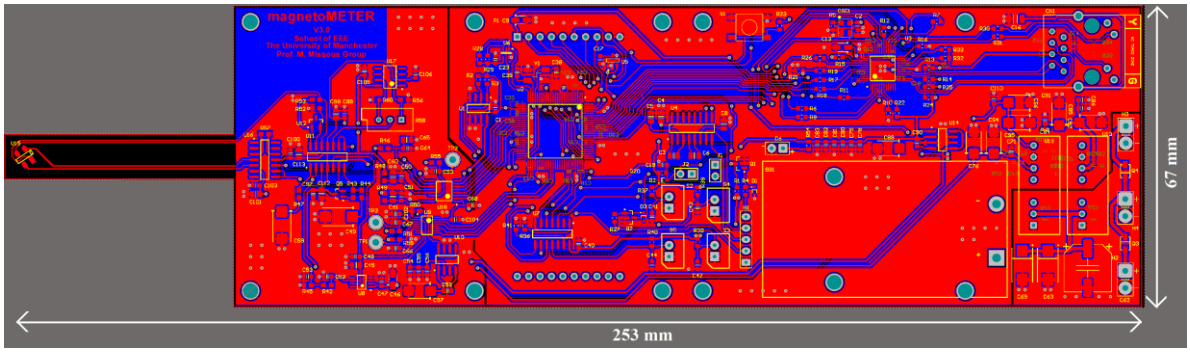

Fig. 5.2 PCB layout of the QWHE magnetometer

5.1.2 Program flowchart

In this magnetometer prototype, A Keil MDK-ARM Microcontroller Development Kit software was used to program the ARM7 microcontroller. The firmware user interface flowchart is shown in Fig. 5.3. When the device is powered on, a DC or AC magnetic field measurement function can be selected. With the DC magnetic field measurement function, the magnetometer take an average of several measurement data and convert the averaged data into magnetic field strength. A pre-set conversion ratio was defined in the program. By contrast, the AC magnetic field measurement function filtered DC signals and AC signals above 4 kHz. After then, root mean square values will be taken from the filtered signal. Thereafter, the processed data will be converted into a magnetic field strength with a pre-set conversion ratio. This program also provided different measurement range setting for both high accuracy measurements and high magnetic field strength measurements. A manual zero

offset calibration is required in this magnetometer. To null the offset, a zero-offset calibration button need to be pressed when the sensor probe located inside a zero-gauss chamber. When the magnetic field being measured, both measured voltage and related magnetic field strength will be displayed on the colour LCD. If the measured voltage is over range or overflow, the display reading will change to red colour to warn user.

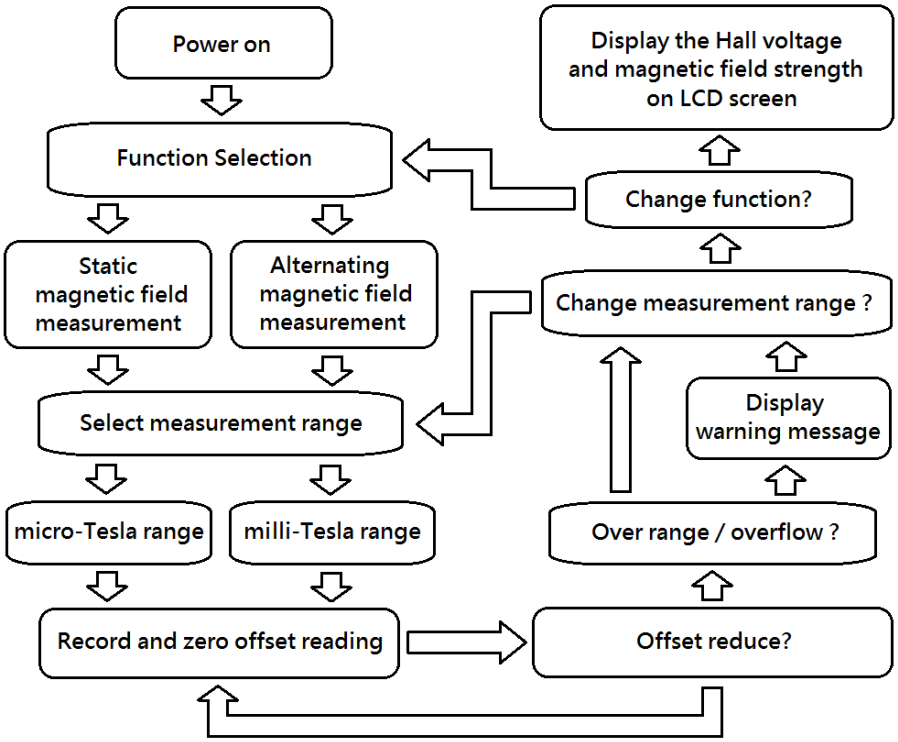

Fig. 5.3 Software flowchart of the QWHE magnetometer

5.1.3 Quantum Well Hall effect magnetometer prototype

This QWHE magnetometer prototype contained a colour LCD, a rechargeable lithium battery and four control buttons. Fig. 5.4 shows the picture of this QWHE magnetometer prototype. First stage amplifier gain and sensor bias current were set to 220 and 1 mA respectively. With the use of a programmable gain amplifier (gain = 0.125 ~ 128), both μT and nT range of magnetic fields could be measured. The extended arm which contained a QWHE sensor was about 50 mm long and 10 mm wide. With the use of a potentiometer in the offset adjust circuit, the offset voltage could be manually corrected to zero. The minimum B-field resolution for this magnetometer was 0.1 μT (100 nT), and maximum measureable B-

field was ±400 mT. Both peak-to-peak unit and root mean square unit could be selected. The frequency response of this magnetometer spanned from DC to 4 kHz. The experimental results of this QWHE magnetometer will be described in Chapter 6.

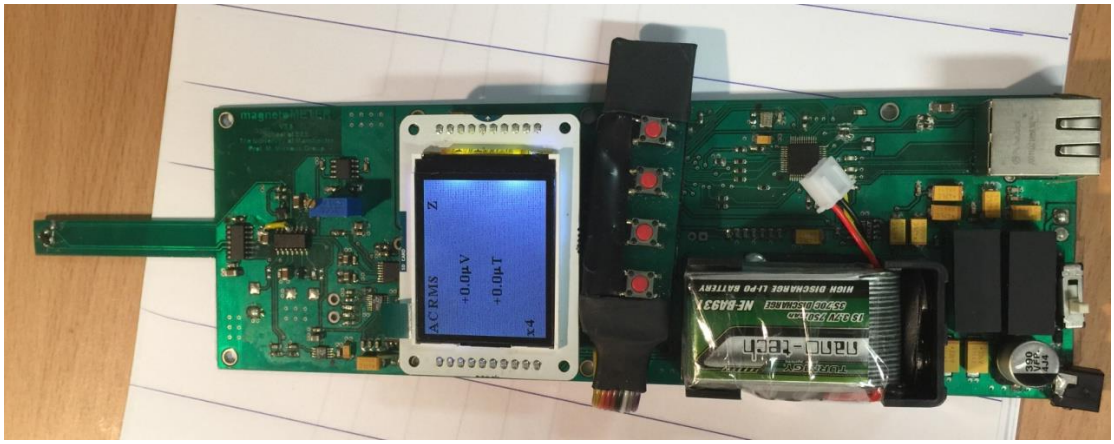

Fig. 5.4 Quantum Well Hall effect magnetometer prototype. The magnetometer dimensions are 253 mm × 67 mm × 20 mm.

5.2 Quantum Well Hall effect flexible 16 × 1 array magnetic-field scanner

In recent years, the rapid development of flexible electronic devices indicated their demand in various applications in testing complex and curved geometries. Flexible sensors and sensor arrays can be closely wrapped around curves and complex configurations of the tested objects. Stand-off distance between sensor and object can be reduced and the effective contact area can be increased. Without flexible structure, curved and uneven object inspections need to be performed from point to point which affect inspection efficiency. Chen and Ding [62] presented a flexible eddy current sensor array measurement system which could be used for conformable proximity sensing. This flexible eddy current sensor probe which consist of spiral coil arrays and a long flat cable was manufactured on a thin Flexible Printed Circuit Board (FPCB) substrate. However, with the thin sensor array and the long spiral coil leads, the sensor probe was resulted in small inductance and comparatively large resistance. Due to the compact size of the P2A QWHE sensor, the FPCB could be fabricated to hold these sensors as a flexible substrate. Unlike the coil arrays, static magnetic field measurement

is possible with this flexible QWHE sensor array. Compare to flexible eddy current array, higher sensitivity at low frequencies and a more durable structure can be achieved. In this study, a flexible 16 × 1 QWHE sensor array magnetic field scanner prototype was designed, assembled and tested.

5.2.1 Circuit design and PCB layout

Fig. 5.5 shows the 16 × 1 flexible QWHE sensor array magnetic field scanner circuit block diagram. This magnetic field scanner consisted of a constant current source for sensor excitation purposes, a set of multiplexers, signal amplifiers, an analogue to digital converter, a microcontroller and a colour LCD. The analogue multiplexers were used as selectors to connect to the different sensors. The switches were controlled by the digital output of the microcontroller. The Hall voltage output from the QWHE sensors was amplified through an instrumentation amplifier, and digitised through an analogue to digital converter. The digitised signal was collected and processed by the on-board microcontroller, and was finally displayed on a LCD in graphical format. The instrumentation amplifier INA217 featured wide supply voltage, low input noise, excellent output voltage swing and good output current drive which make it an optimal candidate for used in this 16 × 1 flexible QWHE sensor array magnetic field scanner.

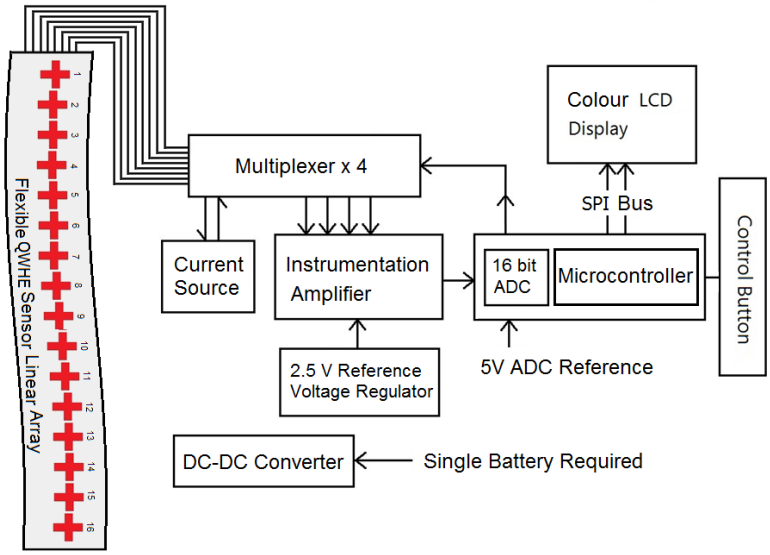

Fig. 5.5 16 × 1 flexible QWHEt sensor array magnetic field scanner block diagram.

The flexible 16 × 1 QWHE sensor array contained sixteen P2A magnetic field sensors and 10 mm pitch between each sensor. Each with a sensitivity of 0.17 mV mT^{-1} mA^{-1}. In order to achieve the required flexibility of the sensing area, the design was separated into three distinct parts:

1. Main circuit board.
2. Adapter board.
3. Flexible sensor array board.

The main circuit board contained two identical analogue modules as shown in Fig. 5.6. An OP27 based voltage controlled current source was designed to provide constant bias current for all 16 sensors. Each module used two CD4051 multiplexers to reduce the number of amplifiers required. A set of multiplexers were designed to connect between the sensor's differential Hall voltage signal outputs and instrumentation amplifiers differential inputs. The multiplexers were controlled by microcontroller with logic gates used to provide enough driving current. After multiplexing between different sensors, the analogue signal was amplified by an INA217 Instrumentation amplifier. The offset could be adjusted with the potentiometer setting of a voltage follower circuit which was connected to this amplifier for providing an output reference voltage. The amplified signals from both modules were then converted to digital data by an ADS1115 4-channel 16 bit Analogue to Digital converter. The digitised data was then collected by an ATmega328 microcontroller through an I^2C bus, and displayed on a 160 × 128 colour LCD.

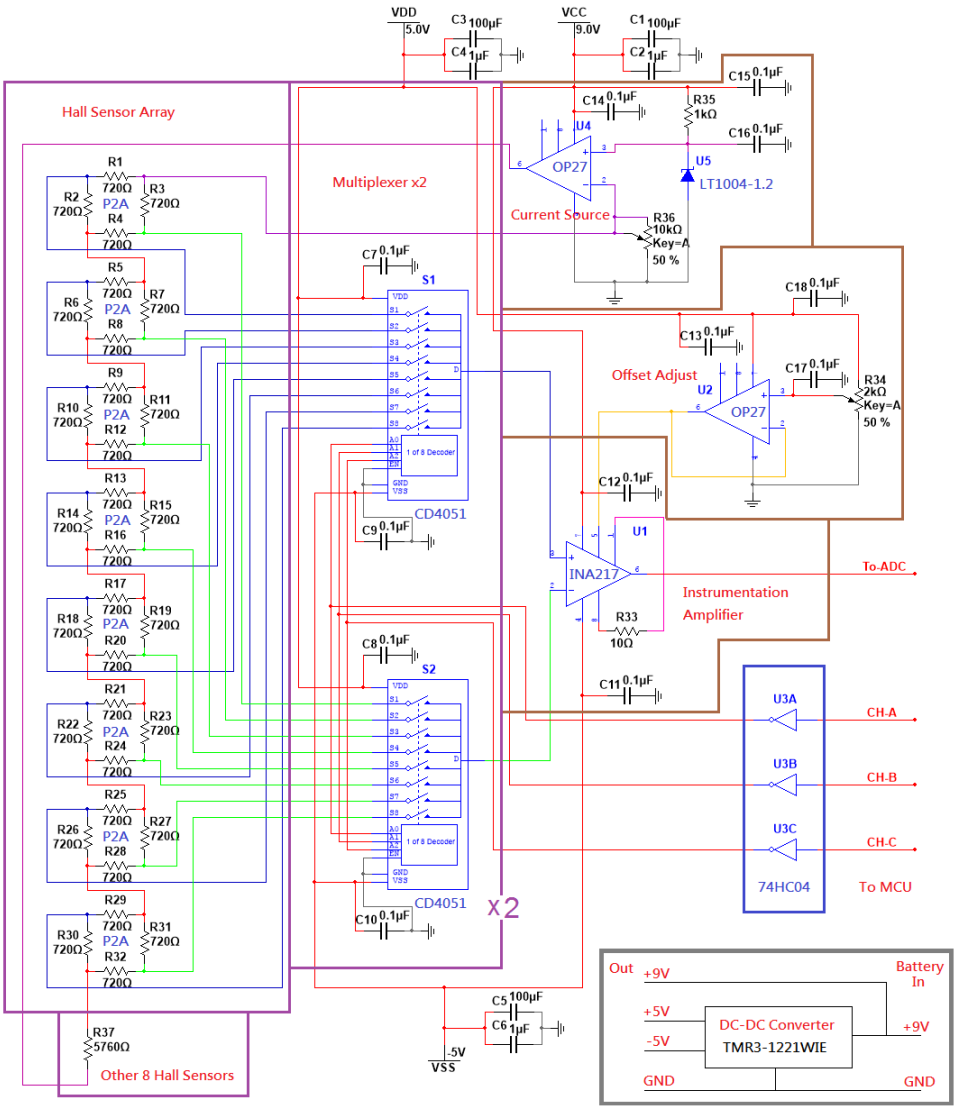

Fig. 5.6 Circuit schematic of the microcontroller controlled 16×1 flexible QWHE sensor array magnetic field scanner.

Fig. 5.7 (a) – (c) show the PCB design of the main circuit board, adapter board and flexible sensor array board for the prototype respectively. The adapter board was designed to connect between the main circuit board and the flexible sensor array board. With the swap of different adapter boards, different types of flexible sensor array could be used.

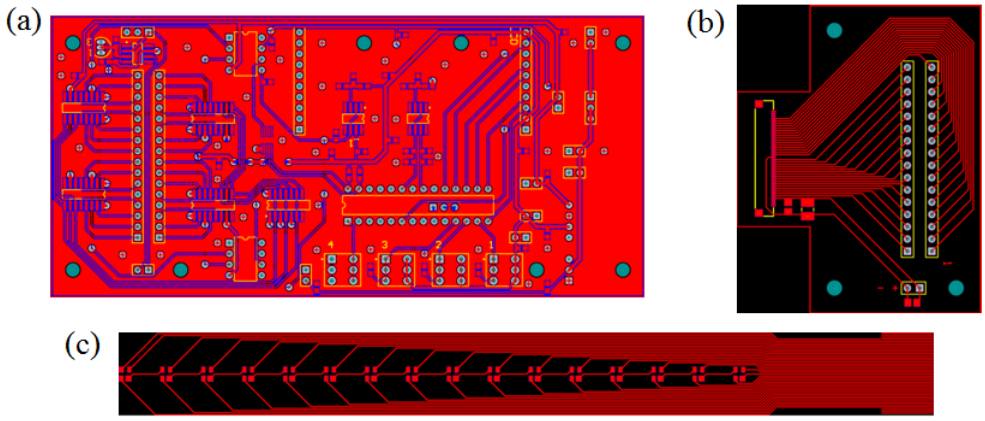

Fig. 5.7 Flexible QWHE sensor array magnetic field scanner PCB layouts: (a) main PCB board with a colour LCD, (b) flexible PCB to Main PCB board adapter, and (c) 16×1 flexible QWHE sensor array.

In the flexible sensor array, 16 QWHE sensors were designed to be mounted on FPCB structure. The actual FPCB based 16 × 1 flexible QWHE sensor array is shown in Fig. 5.8. Compare to other flexible substrate, FPCB has the advantage of a stable production process and better conductivity. Flexible Flat Cable (FFC) connectors was used to connect between the flexible sensor array and adapter board.

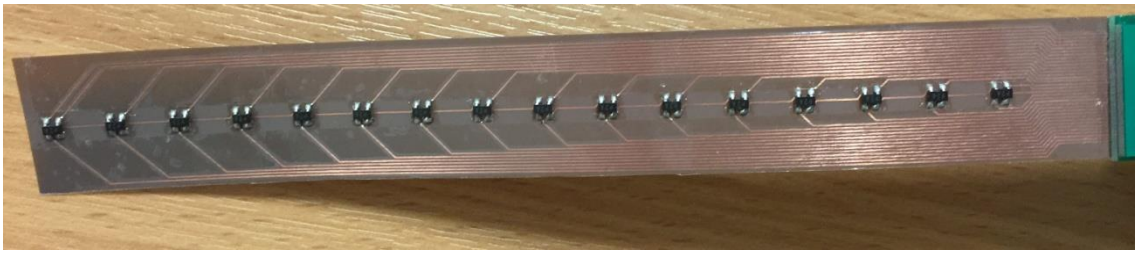

Fig. 5.8 16 × 1 flexible QWHE sensor array: Conventional copper based FPCB.

5.2.2 Program flowchart

The 16×1 flexible QWHE sensor array magnetic field scanner used a microcontroller to automatically select between sensors by changing the control setting of the analogue multiplexers, and recorded the measured value of each sensor. An 8-bit AVR Atmel ATmega 328 microcontroller with built-in 32 kB memory was selected for this design. An Arduino UNO development kit was used to program the microcontroller, where the program was written in C language, before being transferred to a low-level programming language through the Arduino IDE software.

The flowchart of this main program is shown in Fig. 5.9.When the magnetic field scanner powers on, the program starts by checking the reset conditions, enabling the Watch Dog Timer (WDT) and initiating interrupts of the output ports. Following these, the task manager has the ability to run many tasks concurrently. Once a task is initiated, it would run until it is abandoned or is manually shut down. The tasks in the operation of this magnetic field scanner are interdependent, the order in which they are started and stopped is critical.

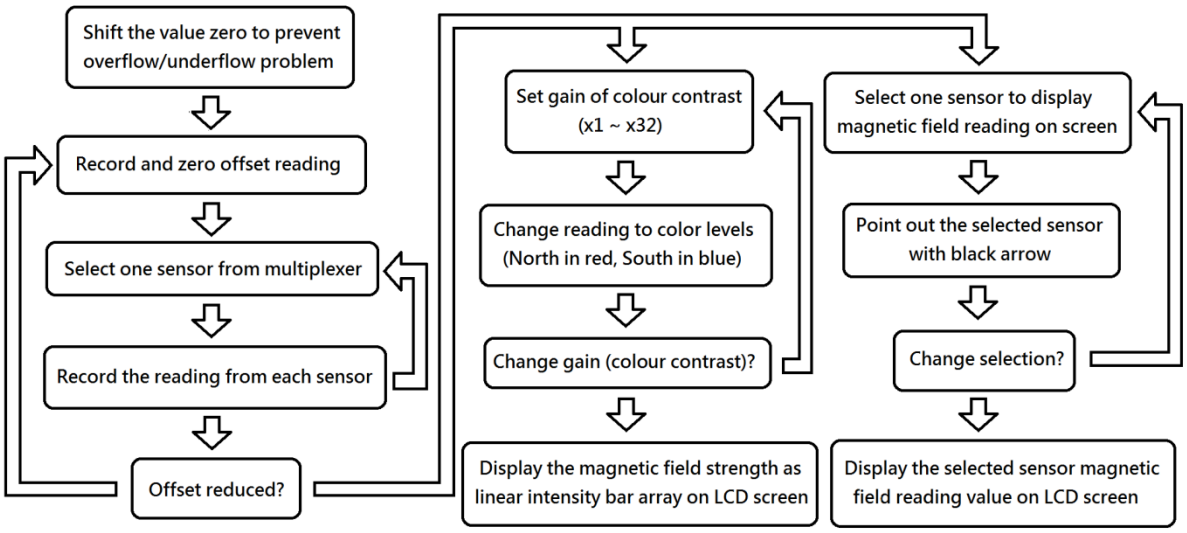

Fig. 5.9 Firmware flowchart of microcontroller-controlled 16 × 1 flexible Hall array magnetic field scanner.

It is normal for Hall effect sensors to have offset voltages when measuring under conditions of zero magnetic field. To reduce the effect of this offset voltage behaviour, a software offset cancellation was used. The manually measured value without external magnetic field is stored temporarily in the device memory until either another calibration is taken or the device is shut down. Different from the dynamic quadrature offset cancellation technique, the software offset cancellation is easy to setup and can give adequate accuracy with acceptable calibrations. The measured magnetic field data is acquired from a periodical operation of selecting different QWHE sensors. Two sets of analogue switches are used to multiplex between sensors for both supplying sensor bias current and outputting Hall voltage signals. After the magnetic field strength is acquired, the measured data is converted into colour block with the colour palettes representing the strength of the measured magnetic field. The results from the 16 sensors are then combined into a colour graph representing the location of each sensor. As mentioned previously, a colour LCD display is used as a device for displaying the graphical results. After a full measurement is completed, the process will automatically restart a new measurement run.

5.2.3 Quantum Well Hall effect flexible 16 × 1 array magnetic-field scanner prototype

The flexible 16 × 1 sensor array contained two acrylic cases for protection and two rechargeable 18650 lithium batteries for supplying power. Fig. 5.10 shows the prototype 16 × 1 sensor array magnetic field scanner. In this prototype, the current source could be set between 0.1 mA to 1 mA, where the analogue circuit gain could be changed from 40 dB to 60 dB. On the display screen, the sensor array magnetic field reading was designed to display as colour bars with the colour depth representing the magnetic field strength. Red and blue colours were used to display the magnetic field strengths representing north and south magnetic fields.

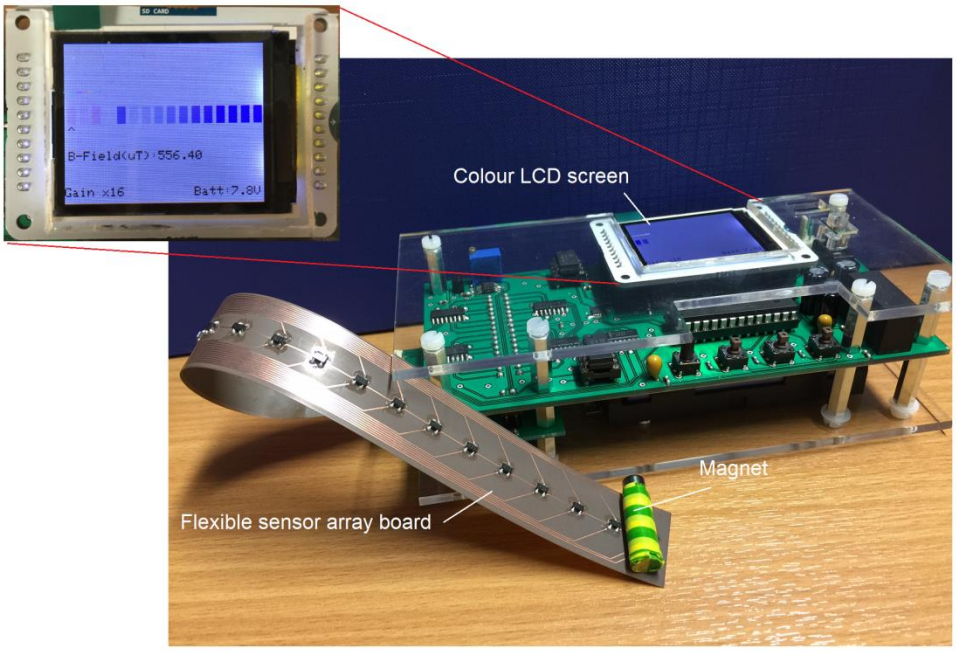

Fig. 5.10 The picture of the 16 × 1 flexible Hall array magnetic field scanner. The inset shows the measurement results of a small magnet scanned across the array.

The precise magnetic field measurement for an individual sensor could be read out by manually selecting between sensors using the device interface, a black arrow was used to pointing out the selected sensor. The remaining battery voltage was shown on the bottom right corner of the LCD screen.

With a setting of 1 mA sensor bias current and a total gain of 287, the relationship

between analogue to digital converter reading and applied magnetic field strength was found. The value of the Hall voltage is given by the following equation:

$$V_H = K \cdot A \cdot I \tag{5.1}$$

where V_H is the Hall voltage (V), K is the sensitivity of the QWHE sensor (mV mT^{-1} mA^{-1}), A is the circuit gain and I is the sensor bias current (mA). The analogue to digital converter input voltage range was from 0 to 5V, and a voltage of 2.5 V was used as a midpoint reference for a null magnetic field. The resolution of the ADC was 10-bit: 2^{10} (= 1024). The minimum detectable voltage which could be detected by the ADC was one ADC reading. The related voltage for each ADC reading could be calculated by the following equation:

$$\mathrm{V}_{\mathrm{oneADCreading}} = \frac{\text{Input voltage}}{\text{Resolution}} = \frac{5\ \mathrm{V}}{1024} = 4.88 \times 10^{-3}\ \mathrm{V} = 4.88\ \ \mathrm{mV}$$

Therefore, a minimum ADC value of 4.88 mV was readable. The sensor parameters were:

- P2A sensor sensitivity: K = 0.17 mV mT^{-1} mA^{-1}
- Sensor bias current: I = 1 mA
- Circuit total Gain: A = 287

The minimum detectable Hall voltage of this magnetic field scanner could then be worked out:

$$V_{H\,\min} = \frac{\mathrm{V}_{\mathrm{oneADCreading}}}{\mathrm{A}} = \frac{4.88\ \mathrm{mV}}{287} = 0.017\ \mathrm{mV}$$

The minimum detectable magnetic field (B_{min}) of the flexible 16×1 array can be calculated using the following equation:

$$B_{\min} = \frac{V_{H\,\min}}{K \cdot I} = \frac{0.017\ \mathrm{mV}}{0.17\ \mathrm{mV\ mT^{-1}\ mA^{-1}} \times 1\,\mathrm{mA}} = 0.1\,\mathrm{mT} = 100\ \ \mu\mathrm{T}$$

Therefore, the lower detectable limit of approximately 100 μT was obtained in this flexible 16 × 1 QWHE sensor array magnetic field scanner, which was approximately twice the value of the static Earth's magnetic field.

5.3 Quantum Well Hall effect 32 × 2 staggered array magnetic field scanner

Magnetic field scanners are widely used in industrial and medical applications. Tumanski and Liszka [63] designed a thin film magnetoresistance (MR) sensor array with a mechanical positioning system, as scanning methods for material testing purposes. Reyne [64] developed three electromagnetic actuation Micro-Opto-Electro-Mechanical Systems (MOEMS) for industrial applications which require a cheap solution for large and long range forces. The first was a resonant 1D magnetic scanner, the second a magnetic bi-stable matrix array of optical micro-switches and the last was a remarkable application of the properties of thick magnetostrictive thin layers to a 2D scanner. Tomasi et al. [65] presented a method to obtain magnetic resonance amplitude images that could picture the magnetic field due to arbitrary shaped magnetised objects. The method employed the gradient recalled echo sequence where two sets of data were obtained in separate experiments. One provides a phase reference image making it possible to eliminate the effect of the B_0 field in homogeneities.

In this study, a miniature slideable QWHE 32 × 2 sensor array magnetic field scanner with high sensitivity and high spatial resolution was designed and fabricated.

5.3.1 Circuit design and PCB layout

Fig. 5.11 shows the block diagram of the 32 × 2 staggered array magnetic field scanner. This magnetic field scanner assembly used a staggered arrangement of two linear sensor rows. Each row included 32 P2A QWHE sensors. In each linear row, the gap between each sensor was approximately 3.3 mm (130 mil). The staggered arrangement of two sensor rows was therefore able to reduce the pitch down to approximately 1.6 mm. When this 32 × 2 linear sensor array was used as a magnetic field scanner, the spatial resolution was 1.6 mm in the direction of scanning.

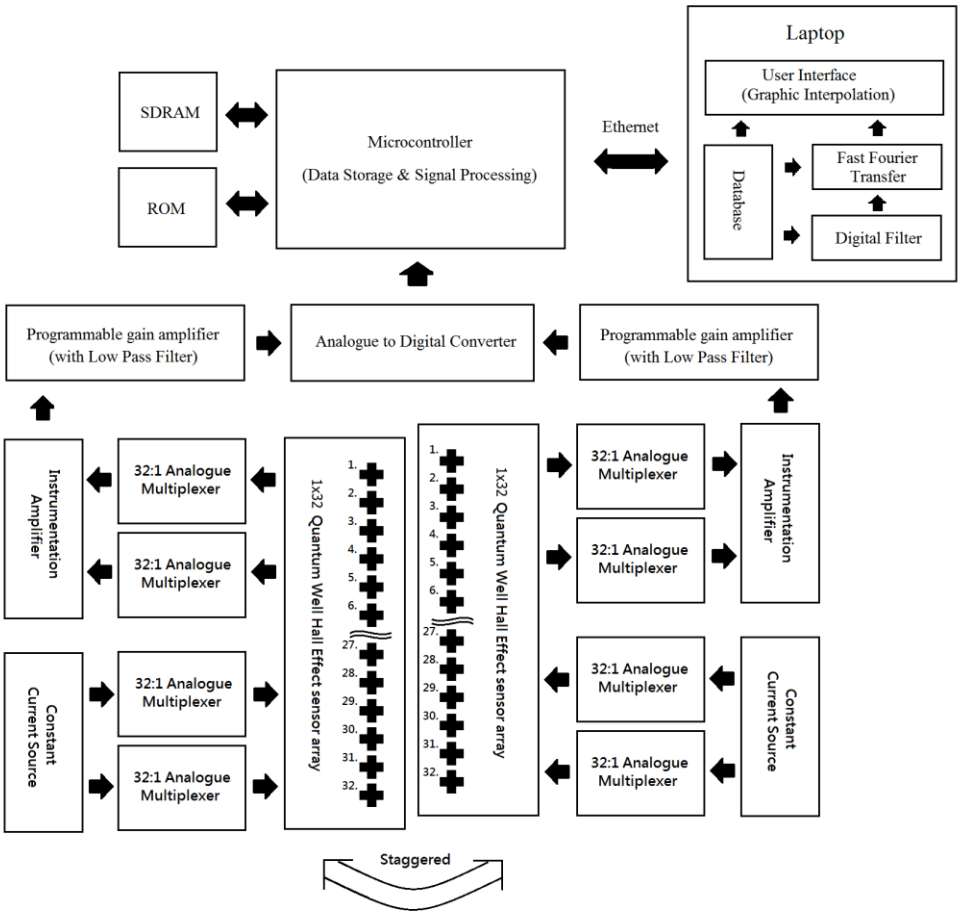

Fig. 5.11 Block diagram of the QWHE 32 × 2 staggered array magnetic field scanner. Note that two linear sensor rows were staggered to enhance the spatial resolution in the direction of scanning.

The signal sensing circuit was separated into two modules. Each module consists of 32 QWHE sensors, four 32:1 analogue multiplexers, an instrumentation amplifier and a constant current source. One set of analogue multiplexers were used to provide the bias current for the selected sensor, with another set of multiplexers being used to select between different sensor differential Hall voltage outputs. The control signals of the two sets of analogue multiplexers were applied from the main microcontroller. A programmable gain amplifier (PGA) was used as a buffer for feeding the current requirements of the analogue to digital converter sampling capacitors. With the programmable gain amplifier, the measurement dynamic range could be increased substantially. Low pass filters were also used to eliminate the high frequency noise before digitising the analogue signals. All the digitised data was collected by an ARM

processor based dual core microcontroller through high speed SPI bus; and stored into an external Synchronous Dynamic Random Access Memory (SDRAM). All the measurement data was uploaded to a computer through a high-speed Ethernet connector. With the use of digital signal filtering, Fast Fourier Transfer and graphic interpolation techniques, the collected data could be converted into colour palettes with different colour depths representing the strength of the measured magnetic field.

The analogue section circuit schematic of the staggered 32 × 2 array scanner is shown in Fig. 5.12. In order to address the total 64 QWHE sensors, eight Analog Devices ADG732 32:1 multiplexers were used. The ADG732 is a monolithic CMOS 32-channel multiplexer which has a 4 Ω on-resistance and 23 ns transition time. These 8 multiplexers were separated into 4 sets which are used to connecting the sensor bias current and the Hall voltage differential signal output separately. Two sets of 74HCT04 hex inverters were used to improve the driving current and convert the voltage level for multiplexer control purposes. Two OP27-based voltage to current converters were used to supply the sensor constant bias current via the multiplexers. Two extra voltage bias sources for operating the sensors with the superheterodyne technique could also be selected in this design. Instrumentation amplifiers (INA217) were used to amplify the Hall voltage differential signal output and transferring the differential signal into a single ended signal. After the first stage amplification, the output signal was transferred to the digital section of the circuit through a 60 pin analogue signal board-to-board connector. The transferred signal was received and amplified by a programmable gain amplifier in the digital circuit section. Low pass filters which were integrated in the programmable gain amplifier circuit were used to eliminate the high frequency noise. All the amplified signals were digitised through one high speed analogue to digital converter; stored into the microcontroller database. Some simple signal processing was performed inside the microcontroller. The processed data was then uploaded onto the computer program through an Ethernet connection.

This analogue circuit section of the staggered QWHE sensor array magnetic field scanner

was designed as an analogue swap module for the real-time 16 × 16 array magnetic-field camera, as described in Chapter 7. The digital circuit section which includes a programmable gain amplifier, analogue to digital converter, microcontroller and power supply section will be discussed in detail in Chapter 7.

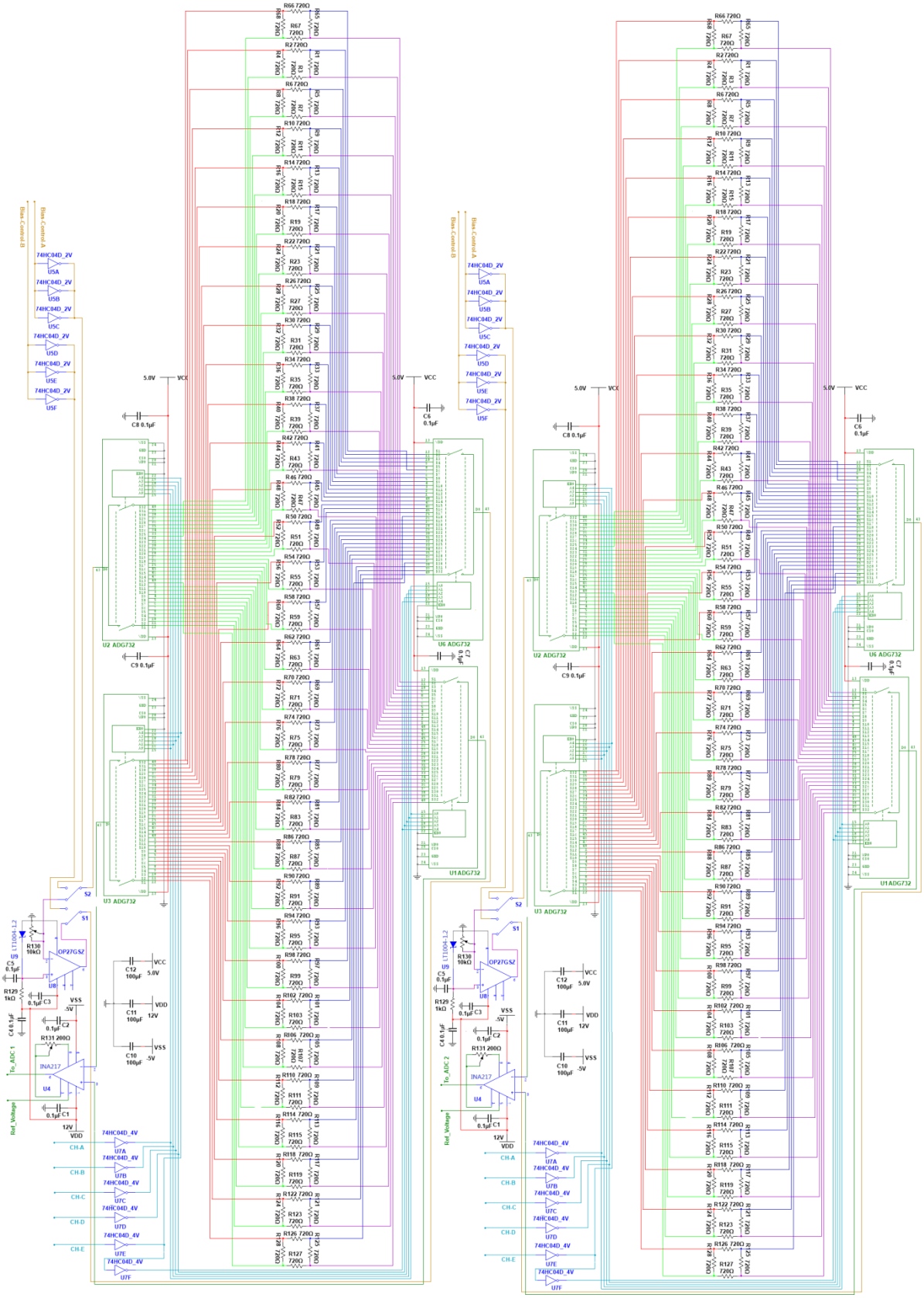

Fig. 5.12 Architecture of the 32 × 2 staggered linear Hall array magnetic field scanner. (High resolution version can be found in appendix **02**)

Fig. 5.13 shows the analogue circuit section of PCB layout of the Staggered 32×2 array. The PCB layout diagram was separated into a top layer section and a bottom layer section for clear display purposes. The dimension of the PCB was 195 mm × 205 mm. The staggered arrangement of two 32 × 1 QWHE arrays laid on the side of the PCB layout. In each sensor array, the distance between sensors was approximately 3.3 mm (130 mil). Therefore, the staggered arrangement of two sensor arrays could achieve 15.4 point per inch (PPI) magnetic field scanning spatial resolution. Ground layers were used to cover the amplification section and current source section to achieve better noise level.

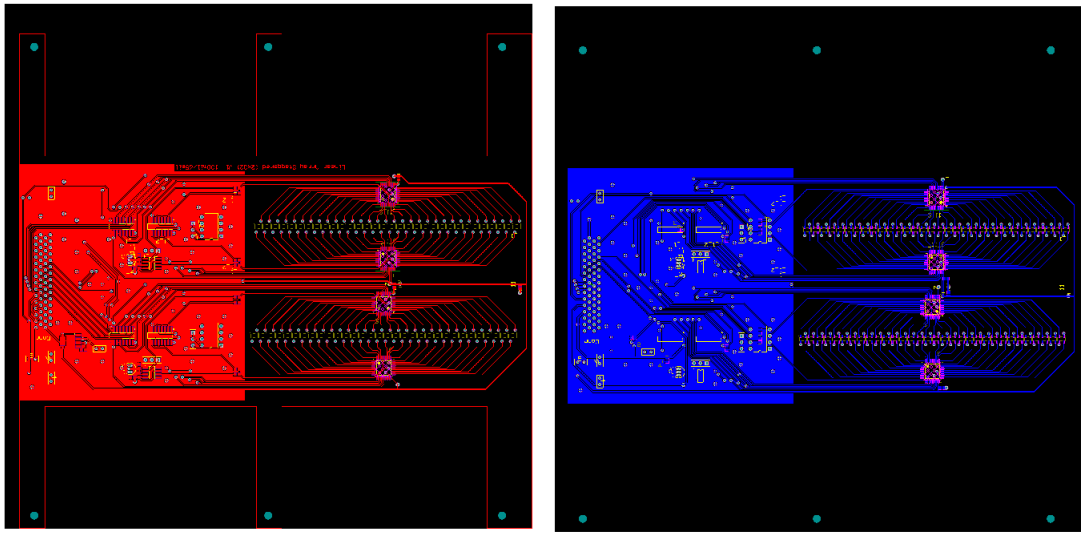

(a) (b)

Fig. 5.13 Analogue circuit section of PCB layout of the 32×2 staggered QWHE sensor array magnetic field scanner. (a) and (b) are the top layer and bottom layer of the PCB design respectively.

5.3.2 Program flowchart

The 32 × 2 staggered array scanner used a microcontroller to automatically control the multiplexer and record measurement values of each sensor. The operation of this magnetic field scanner was controlled by a pre-programmed firmware. A Keil Microcontroller Development Kit software was used to program the NXP LPC4350 ARM Cortex-M4 based microcontroller. The flowchart of the firmware is shown in Fig. 5.14.

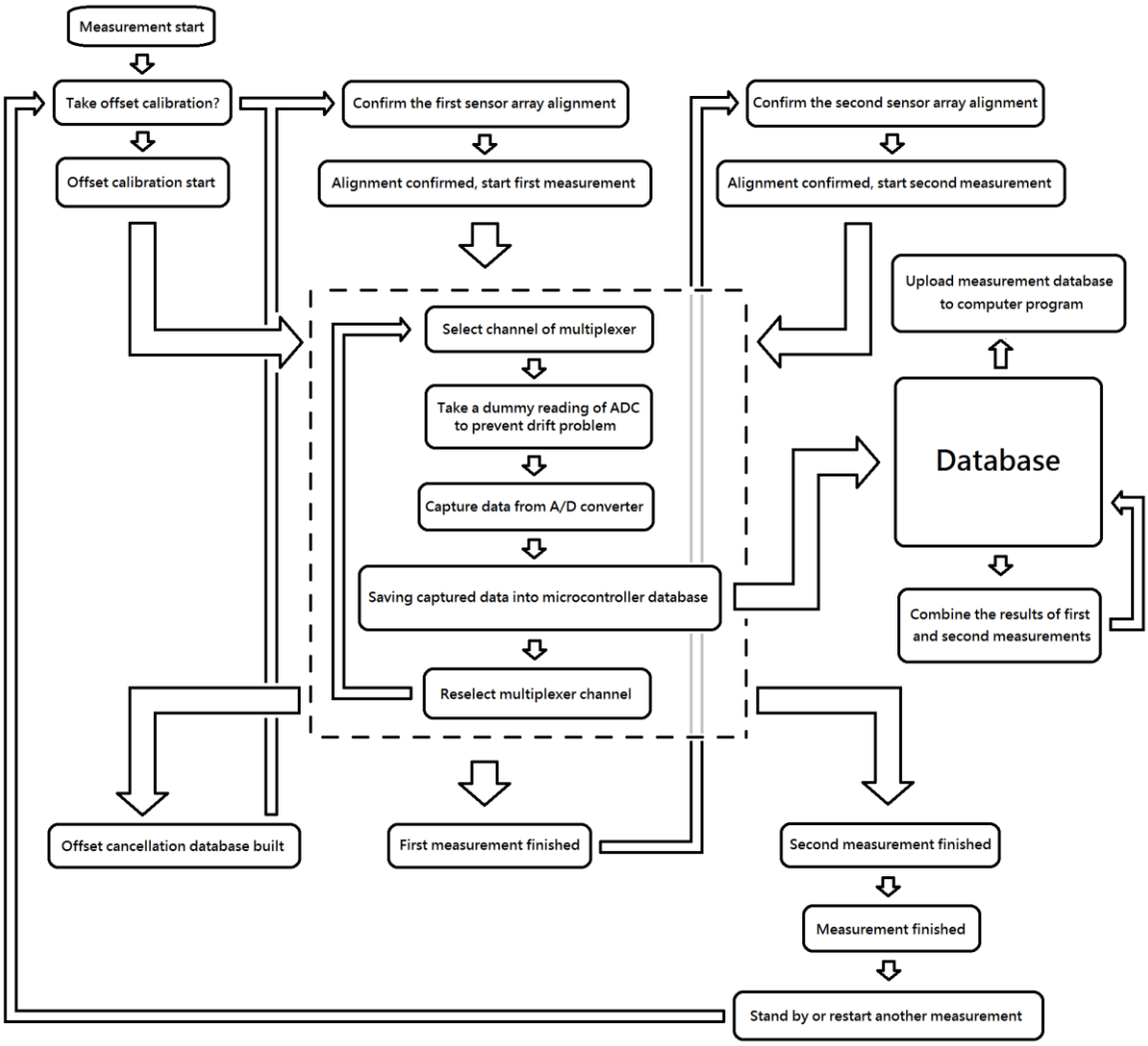

Fig. 5.14 Flowchart of micro-controlled QWHE 32×2 staggered linear array magnetic field scanner.

This magnetic field scanner was designed to be used with a laptop computer with the measurement data upload to the computer software for further digital signal processing. To achieve alternating magnetic field measurement in of the 32 × 2 QWHE sensor array, a high-speed analogue to digital converter, a powerful processor and a high-speed protocol port were required. The NXP LP4350 ARM Cortex-M4 based microcontroller contains a Fast Ethernet controller, a Cortex-M4 core and a Cortex-M0 core which makes it suitable for this magnetic field scanner prototype. When the magnetic field scanner powers on, the program stays in standby until a measurement is started manually. After the measurement start, the offset voltage of each individual sensor is recorded for automatic null offset. The microcontroller

automatically switches the multiplexer channel to select different QWHE sensors. After the offset of each individual sensor is recorded, the program will pause until the next operation. Manually aligning the first sensor array to the test object is required. When the alignment is completed, the program starts the array measurement sequence. The same operating procedure is required for the second sensor array measurement. After both measurements are completed, all measured data sets are combined into one final data set. With the combination of these two measurements, a resolution of 15.4 point per inch (PPI) in the direction of scanning could be achieved.

5.3.3 Staggered Quantum Well Hall effect 32 × 2 array magnetic-field scanner prototype

Fig. 5.15 shows the top and bottom pictures of the 32×2 staggered linear QWHE sensor array magnetic field scanner prototype. It consisted of a staggered 32×2 sensor array analogue circuit, a digital circuit section which includes the power section, one acrylic frame and four slide rails. The set of slide rails could slide the magnetic field scanner in one direction for scanning purposes.

This staggered 32 × 2 array was designed as an analogue swap module for the QWHE real-time 16 × 16 array magnetic-field camera which will be described in chapter 7. With an addition of a stepper motor, automatic magnetic field scanning could be done with this magnetic field scanner. The staggered arrangement of two 32 × 1 sensor array could increase the scanning resolution in the direction of scanning as discussed previously. The increase of magnetic field measurement spatial resolution could help on detecting tiny defect with MFL inspection as described later in Chapter 6.

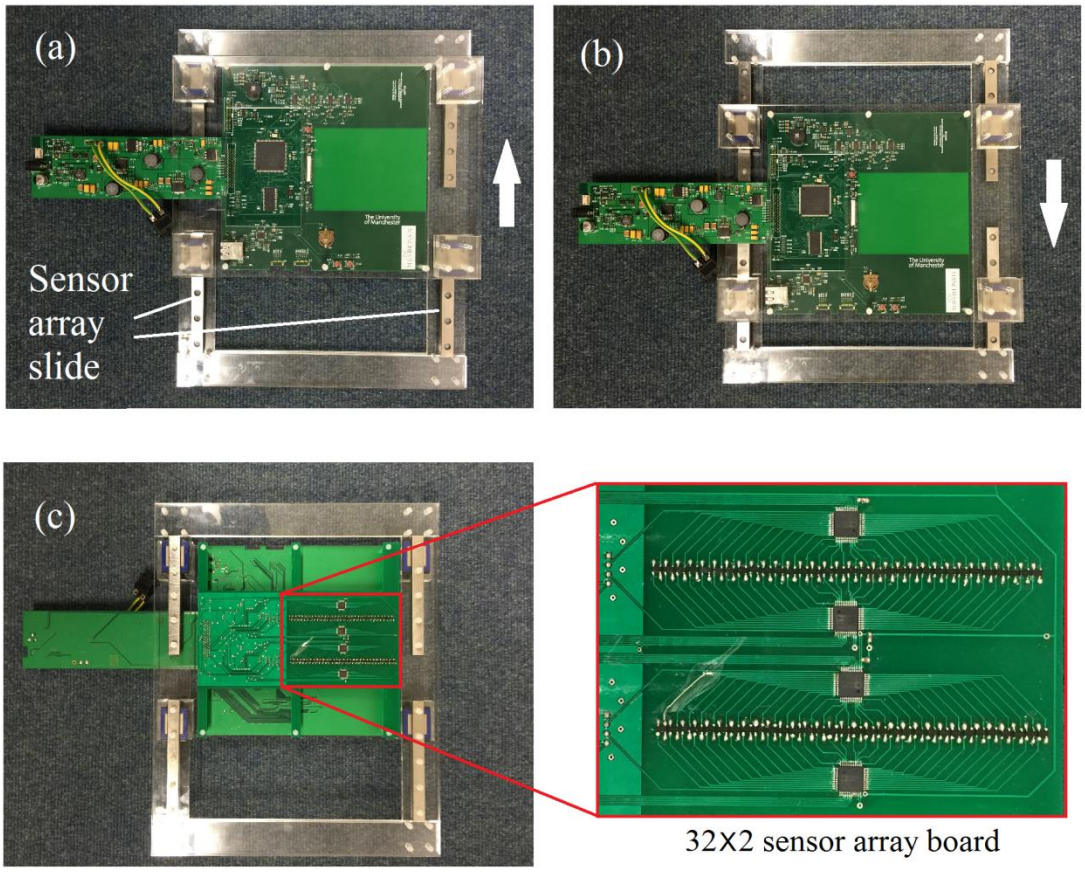

Fig. 5.15 (a) and (b) are the top pictures of the 32×2 staggered linear Hall array magnetic field scanner into up and down slide positions, respectively; (c) is the bottom picture of the magnetic field scanner. The inset shows the staggered 32×2 QWHE sensor array.

5.4 Conclusion

Non-destructive Electromagnetic testing techniques are widely used in industry. By remotely measuring electromagnetic field which are caused by defects and non-uniform magnetic permeability of tested objects, defect and stress can be identified. Search coils are the commonly used magnetic field detection methods but have many drawbacks. To improve these disadvantages, QWHE sensor can be used to replace the search coils in electromagnetic non-destructive methods. Compared to search coils, the QWHE sensors have the advantage of:

1. High sensitivity in both static and alternating magnetic field.
2. Static and alternating magnetic field detection capability.
3. High linearity in field-sensitivity and wide dynamic range.

4. High frequency-sensitivity linearity.
5. Easy to operate.
6. Low temperature coefficient of output Hall voltage.
7. Compact size.

To test the capability of these QWHE sensor in real case, non-destructive testing situations, a magnetometer, a 16 × 1 flexible sensor array magnetic field scanner and a high spatial resolution 32 × 2 staggered sensor array magnetometer based on the P2A sensor were designed and built. The single QWHE magnetometer has a field strength resolution up to 0.1 μT (100 nT), and a measurement dynamic range of 138 dB. Both static magnetic field and alternating magnetic field up to 4 kHz can be measured. The flexible Quantum Well Hall effect 16 × 1 sensor array magnetic field scanner can be used in uneven and curved surface conditions. This gives the magnetic field scanner better inspection capability in both welding hump samples and pipe samples. The staggered 32 × 2 magnetic field scanner has a high spatial resolution. By the staggered arrangement of two sensor arrays, a 15.4 point per inch (PPI) horizontal spatial resolution can be achieved. With the high magnetic field scanning spatial resolution, smaller defect can be found. Further non-destructive testing experiments using the magnetometer and magnetic field scanner will be described in the next chapter.

Chapter 6
Direct and Alternating magnetic flux leakage testing with Quantum Well Hall effect magnetometer and magnetic field scanner

Magnetic Flux Leakage (MFL) testing is one of the most commonly used electromagnetic non-destructive testing technique in industry. It requires an external source to bias a strong magnetic field across testing subjects. Unlike search coils which detect magnetic flux, the P2A QWHE sensor detects magnetic flux density in a very small area (70 μm × 70 μm) with a good sensitivity for used in the electromagnetic non-destructive testing methods. As a proof of concept and developing steps, A QWHE magnetometer and two QWHE magnetic field scanner prototypes had been designed and built.

The QWHE magnetometer is the fundamental building block of all magnetic field scanners and magnetovision systems which makes it important in this research. In this chapter, both QWHE magnetometer and flexible QWHE 16 × 1 sensor array magnetic field scanners had been used in the measurements of DC Magnetic Flux Leakage (MFL) testing. Furthermore, the QWHE magnetometer which can measure both DC and AC magnetic field were also used in the AC MFL testing.

6.1 Magnetic Flux Leakage (MFL) testing: measurements

MFL testing is a non-destructive testing method which uses a set of static magnetic field magnets or electromagnets to apply the bias magnetic flux across testing objects. In this research, Neodymium magnets were used to supply strong static magnetic fields. Different from the industrial standard MFL method, QWHE sensors were used to replace search coils. The QWHE sensors have advantages in measuring static magnetic field in MFL testing compare to coils. The sensitivity of the QWHE sensor is independent of magnetic field frequency which also makes it easy to use in a non-constant scanning speed robot scanning

situation.

6.1.1 Static (DC) magnetic field calibration

Calibration is important for all kind of magnetic field measurement methods. With calibration, the strength of magnetic field can be measured accurately. With the QWHE magnetometer / magnetic field scanner being calibrated, the correctness of each measurement could be certified and the results could be compared to others NDT methods. To calibrate both the QWHE magnetometer and the flexible QWHE 16 × 1 sensor array magnetic field scanner, a Helmholtz coil was designed and built as shown in Fig. 6.1 (a).

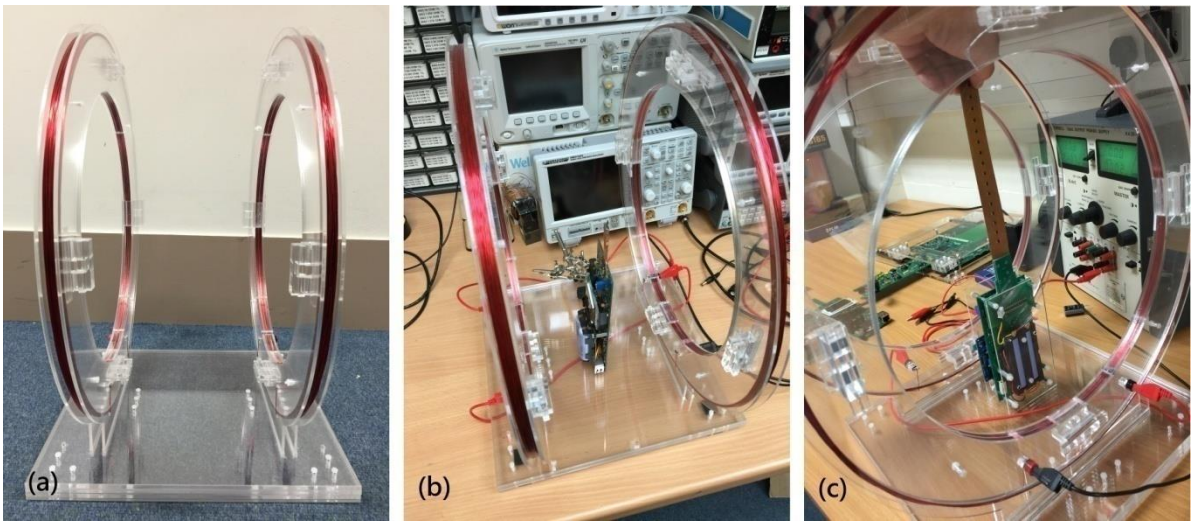

Fig. 6.1 The static and alternating magnetic field calibration setup: (a) 200 mm radius Helmholtz coil with 51 turns in each coil, (b) the calibration setup of the Quantum Well Hall effect magnetometer, (c) the calibration setup of the flexible Quantum Well Hall effect 16 × 1 sensor array magnetic field scanner.

The radius R and the number of each turns N are R = 200 mm and N = 51 turns respectively. The magnetic field strength B inside the Helmholtz coil can be calculated using the following equation:

$$B = \frac{8 \cdot \mu_0 \cdot N \cdot I}{5 \cdot \sqrt{5} \cdot R} = \frac{8 \cdot 1.2566 \times 10^{-6} \cdot 51 \cdot I}{5\sqrt{5} \cdot 0.2} \tag{6.1}$$

Where μ_0 is the vacuum permeability ($\mu_0 = 4\pi \times 10^{-7}$ N/A^2) and I is the coil bias current

in Ampere. The magnetic field strength B (in Tesla) of this Helmholtz coil can be described by the following equation:

$$B \cong 2.29 \times 10^{-4} \times I \tag{6.2}$$

In the calibration, an Agilent E3643A DC Power Supply and an Agilent 34461A Digital Multimeter were used to supply the power and to measure the bias current across the Helmholtz coil respectively. The theoretical magnetic field strength inside the coils can be calculated from the measured coil bias current with the equation showing above. The calibration setup for both QWHE magnetometer and QWHE flexible magnetic field scanner are shown in Fig. 6.1 (b) and (c).

Table 6.1 Calibration results of the QWHE magnetometer.

Coil bias current I (mA)	Theoretical B (μT)	Measured B (μT)	Absolute error (%)
135	30.92	31.06	0.47%
255	58.40	57.87	0.90%
510	116.79	117.01	0.19%
1007	230.60	229.77	0.36%
1400	320.60	319.55	0.33%

Table 6.2 Calibration results of flexible QWHE 16 × 1 sensor array magnetic field scanner.

Coil bias current I (mA)	Theory B (μT)	Measured B (μT)	Absolute error (%)
149	34.12	34.65	1.54%
282	64.58	65.91	2.06%
523	119.77	118.30	1.22%
1000	229.00	226.46	1.11%
1400	320.60	320.26	0.11%

The calibration results for the QWHE magnetometer are shown in table 6.1, and for the flexible QWHE 16 × 1 array are shown in table 6.2. The results show that both systems after calibration could achieve accuracy ≤ 2%.

6.1.2 Magnetic Flux Leakage testing

To prove the concept of using QWHE sensor to replace search coils in MFL testing, a Martensitic stainless steel MFL testing sample was prepared as shown in Fig. 6.2. A coordinate system for manual mapping measurement purpose was drawn on the sample as shown in Fig. 6.2 (c).

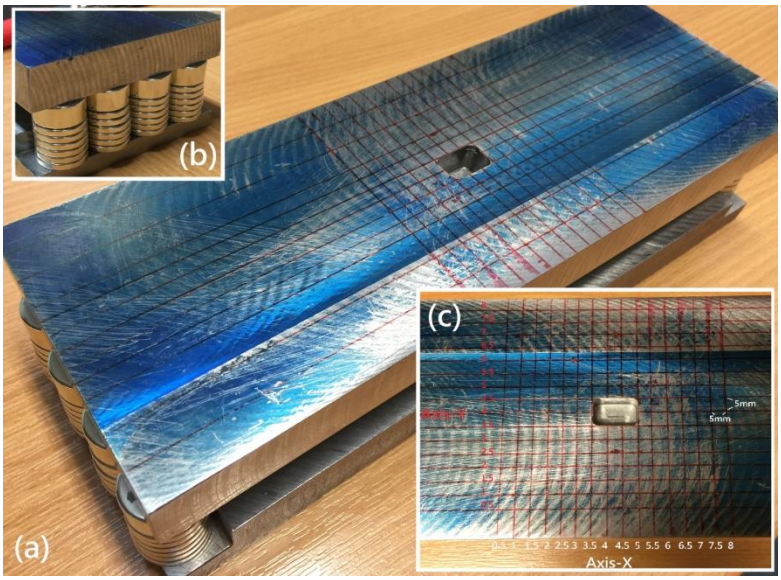

Fig. 6.2 430 Martensitic stainless steel sample for magnetic flux leakage testing: (a) sample overview, (b) magnet cylinder bars for applying bias magnetic fields, (c) the coordinate system for manual mapping measurements.

This test sample was manufactured from a 430 Martensitic stainless steel sheet which has an electromagnetism relative permeability of about 1000 μ/μ_0. The sample contained a rectangular groove, 8 sets of magnet cylinder bars and a magnetic flux return sink (430 stainless steel). Each magnet cylinder bar had a B-field strength of 460 mT. Both the test sample and the magnetic flux return sink were based on 18.4 mm × 250 mm × 90 mm stainless steel plates. A rectangular groove with a dimension of 9.2 mm × 15 mm × 10 mm was cut out on test sample. All dimensions and configurations of the MFL sample are shown in Fig. 6.3.

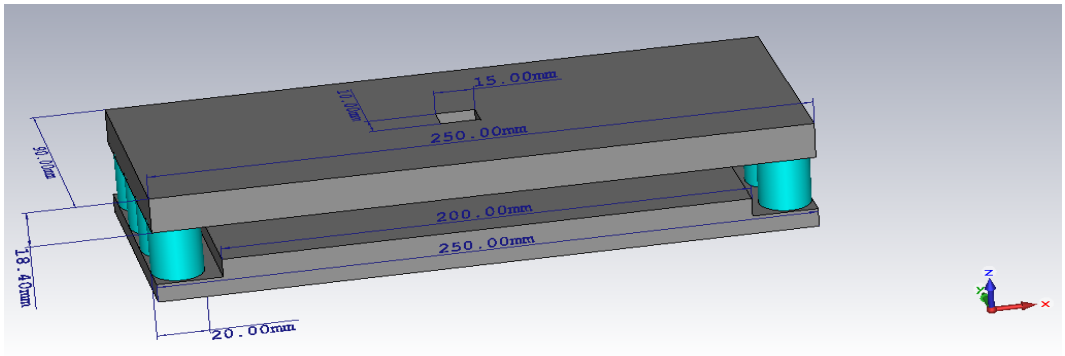

Fig. 6.3 The dimensions of Martensitic stainless steel magnetic flux leakage test sample.

Another NDT defect sample which consists of weld cracked block from the New Nuclear Manufacturing (NNUMAN) group at Manchester was shown in Fig. 6.4. This sample was also used to proof of concept for real defect identification.

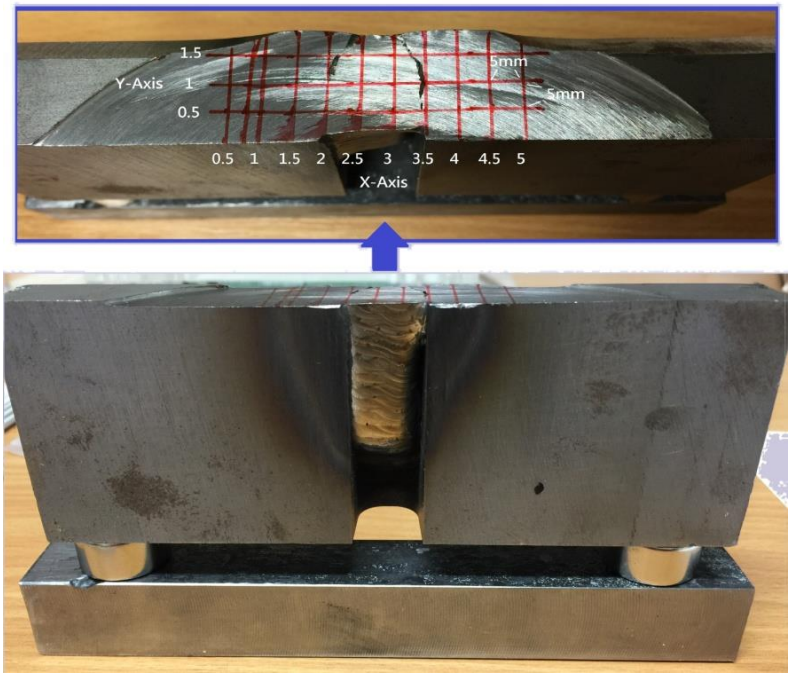

Fig. 6.4 A weld cracked block sample form the New Nuclear Manufacturing (NNUMAN) group, and the coordinate system for manual mapping measurements.

The weld block has a dimension of 20 mm × 143 mm × 50 mm. Two button magnets with B-field strength of 350 mT were used to magnetise the sample. A magnetic flux return sink with a dimension of 20 mm × 20 mm × 157 mm was also used for supplying the bias magnetic flux. A coordinate system for manual mapping purpose was drawn near the crack

location as shown in Fig. 6.4.

6.1.2.1 Magnetic Flux Leakage testing using the Quantum Well Hall effect magnetometer

In this section, the QWHE magnetometer was used to measure the flux leakage from the ferromagnetic materials. The measurement setup for 430-stainless steel sample was shown in Fig. 6.3. Four sets of magnet cylinder bars were placed on the left-hand side with the north poles facing up, and another four with opposite B-field orientation on the right-hand side. Manual mapping was performed on the 430-stainless steel sample to acquire 2D magnetic field distribution images and to simulate the magnetovision system measurement results described in Chapter 8. The measured data was then plotted as a 3D graph with both colours and heights representing the strength of the measured magnetic field as shown in Fig. 6.5. The distance between each measurement point was 5 mm in both the X and Y directions. Fig. 6.6 shows a linear measurement result which was taken across the centre of the square groove in the X-axis direction. Two red lines representing the edges of the groove.

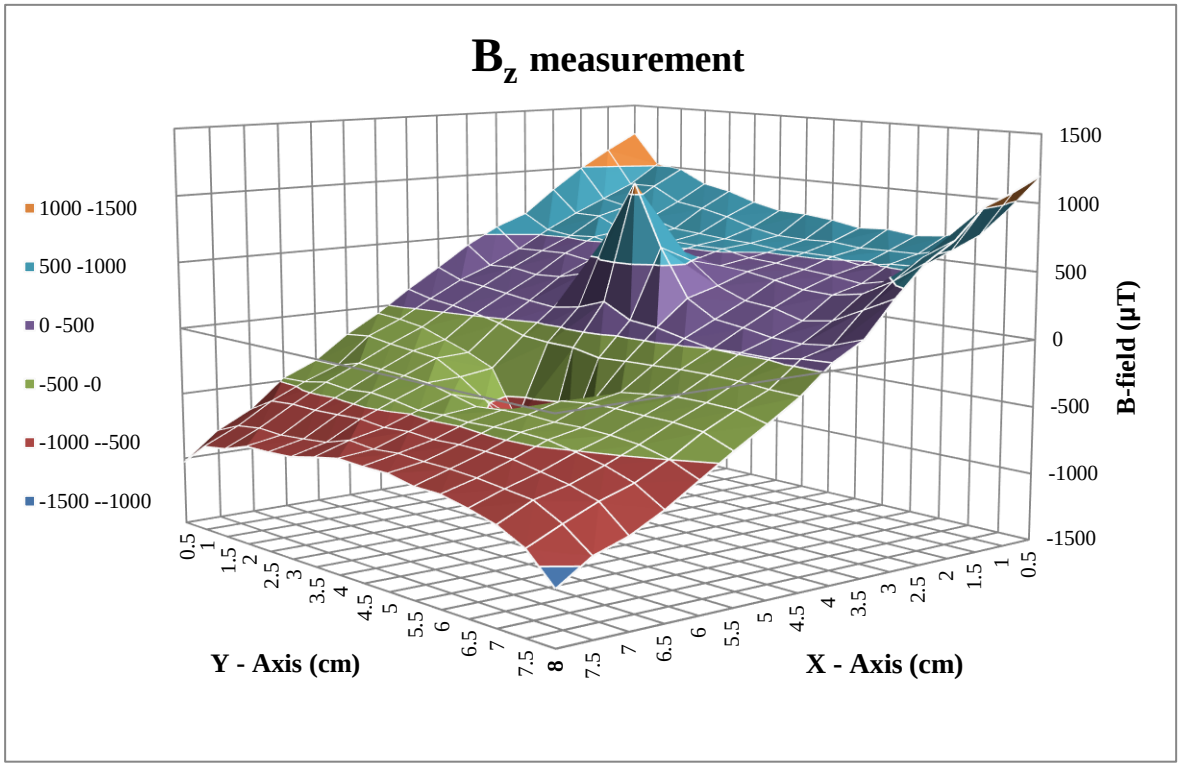

Fig. 6.5 Three dimensional graphical results of the manual mapping measurements on the 430 stainless steel sample.

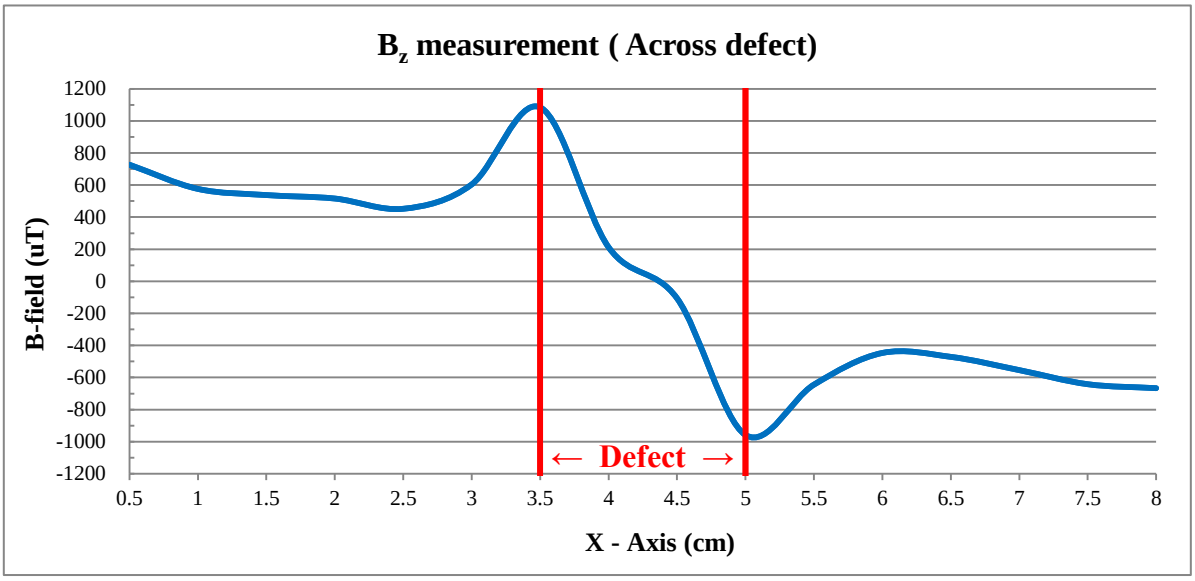

Fig. 6.6 Linear measurement taken across the centre of the square groove on the 430-stainless steel sample.

In MFL testing, magnetic flux will leak out from the non-continuous cross section due to the change of magnetic permeability. In both Fig. 6.5 and Fig. 6.6, two non-continuous peak can be seen and which represent the edges of the square groove on the 430-stainless steel sample. Compared to the linear measurement results, the 3-dimensional graphical results can show both the edge and the shape of the defect. The 3-dimensional graphical result covers both X and Y direction measurement results. The groove could clearly be seen and the maximum in the MFL signal was close to 1mT which was easily detectable by the QWHE magnetometer.

The MFL test set up for the NNUMAN sample is shown in Fig. 6.4. Both Fig. 6.7 and Fig. 6.8 show the magnetometer manual mapping measurement results of the cracked weld sample. Fig. 6.7 is a 3-dimensional graphical plot with both colours and heights representing the magnetic field strength, and Fig. 6.8 is the standard line chart result with different lines representing different linear measurement results. Two cylinder magnets and a metal bar were used to supply the bias magnetic field. Two magnets were placed in the bottom side of the NNUMAN sample with opposite magnetic field orientations. The coordinate system shown in Fig. 6.4 was used for the manual mapping measurements. The manual mapping pitch in

both direction was 5 mm.

There were two crack defects in the NNUMAN sample and these could be easily detected as seen in Fig. 6.4. Both welding crack defects were curved in shape. As shown in Fig. 6.8, the non-continuous peak points represent the location of both crack defects. However, the width of the crack defects could not be identified in either the 3-dimensional graphical results or the line chart results. This was due to the fact that the mapping spatial resolution was not high enough to define the edge of the crack defect precisely. Moreover, the high peak and low peak shown in Fig. 6.8 does not represent the two edges of a crack defect. Nevertheless, the magnetic flux leakage which happens in a non-continuous region is much wider than the defect itself. This means a smaller defect can still be measured in a low spatial resolution setting.

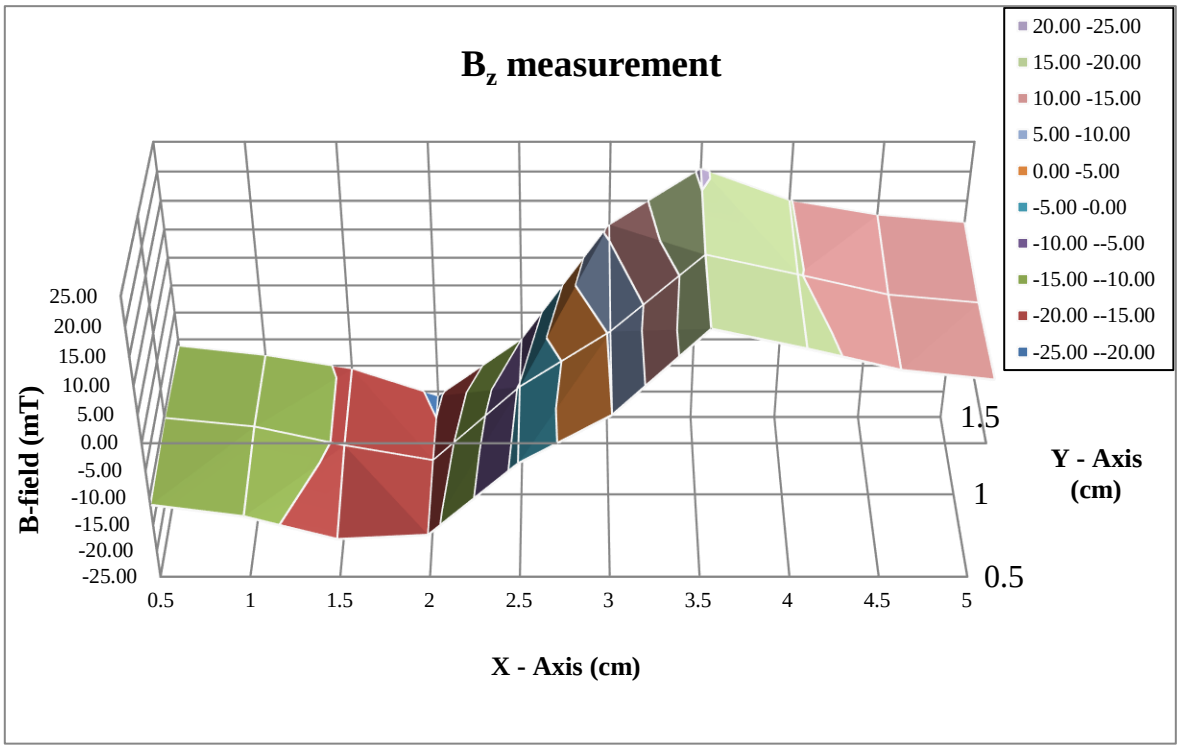

Fig. 6.7 Three dimensional graphical results of the manual mapping measurements on the NNUMAN weld cracked block sample.

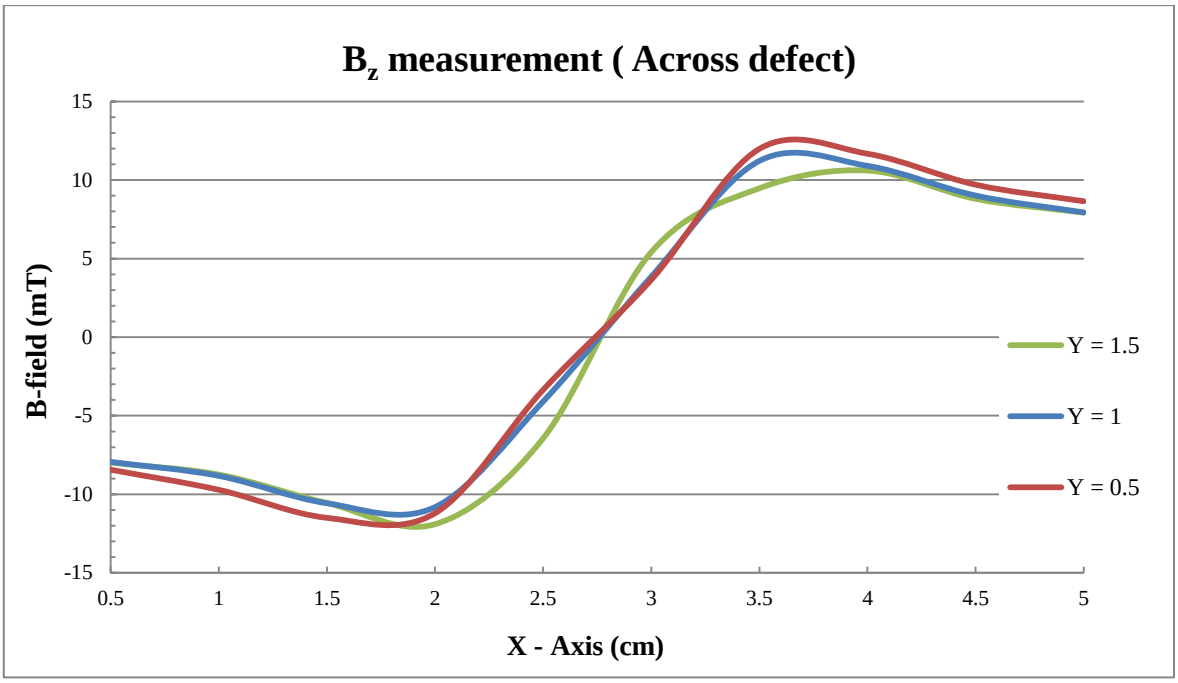

Fig. 6.8 Linear measurement results of the manual mapping measurements on the NNUMAN weld cracked block sample.

6.1.2.2 Magnetic Flux Leakage testing with the flexible Quantum Well Hall effect 16 × 1 sensor array magnetic field scanner

The flexible magnetic field scanner had a bendable sensor array which could be used on uneven and/or curved surfaces. The magnetic field strength decays exponentially with the increase in distance following an inverse cubic law. This means the stand-off distance of the QWHE sensor can greatly affect the strength of the magnetic flux leakage signals. With a flexible sensor array, each sensor stand-off distances could be decreased (or made the same) due to the flexible structure which could help in obtaining stronger magnetic flux leakage signals.

A magnetic flux leakage testing of the 430-stainless steel sample was performed with the flexible QWHE 16 × 1 sensor array magnetic field scanner. The test setup was the same in the previous section as shown in Fig. 6.3. Three different stand-off distance were used in these measurements. The magnetic flux leakage results of the three different sensor stand-off distances are shown in Fig. 6.9.

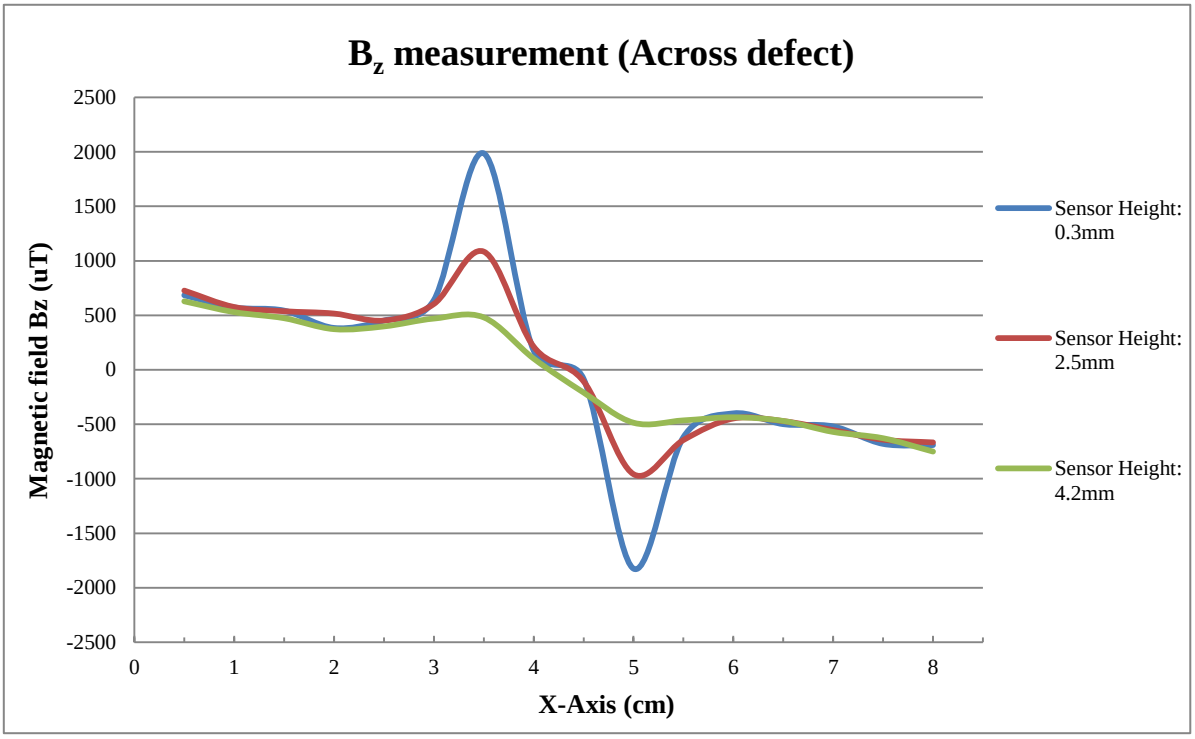

Fig. 6.9 Linear measurement results of the 430 stainless steel sample with different sensor stand-off height.

In this figure, the two peaks represent the magnetic flux leakage signals which were generated from the edges of the square groove. From the results shown in Fig. 6.9, the magnetic flux leakage signal strength decrease rapidly with the increase of stand-off distance as expected. The background magnetic field strength remains the same in all three measurements though. It is clear that if the stand-off distance is too high, the magnetic flux leakage signal can disappear altogether in the background magnetic field signal. In real world cases, a lot of samples under test have uneven surfaces, such as welding humps, curved pipe surfaces and so on. This point out to the importance to the benefit of a flexible sensor array magnetic field scanner.

6.2 Alternating magnetic-field measurements and applications

Alternating magnetic field non-destructive testing measurements with search coil are commonly used in industry. The alternating magnetic field testing methods include eddy Current Testing (ECT), Alternating Current Field Measurement (ACFM) and Alternating Current Magnetic Flux Leakage (AC-MFL). Both alternating magnetic field and alternating current have skin effects which describe the decrease of the penetration depth of electromagnetic fields with the increase of frequency. With the skin effect, alternating magnetic field can easily saturate the surface and sub-surface of objects under test. The detection sensitivity of QWHE sensors is linear with both magnetic field strength and magnetic field frequency making them an optimum choice for alternating magnetic field testing methods.

In this section, the QWHE magnetometer was used to measure the non-continuous change of magnetic field strength which represent the magnetic flux leakage signals. The magnetometer which used the P2A QWHE sensor had the capability to measure magnetic field strengths in the micro to nano Tesla resolution with the magnetic field from static to 4 kHz. Both linear measurement and manual mapping measurement were performed in this research to simulate the behaviour of magnetic field scanner and magnetovision system for proving the concept of building the magnetivision system in this research as described in

chapter 7.

6.2.1 Alternating magnetic field calibration

In the design of the QWHE magnetometer, true signal processing of root mean square conversion were used to capture the alternating magnetic field strength. A calibration of the measured magnetic field at different frequencies was undertaken using the same Helmholtz coil shown in Fig. 6.1 (a) previously. The alternating current signal was generated from an Agilent 33500B function generator. An audio amplifier circuit which contain two parallel working 100 W ST TDA7293 audio amplifier chips were used to supply the bias voltage to the Helmholtz coil. An Agilent 34461A digital multimeter with a 10 A current measurement capability was used to monitor the strength of the coil bias current. The calibration results are shown in table 6.3.

Table 6.3Alternating magnetic field calibration results of the QWHE magnetometer.

Frequency (Hz)	Coil Bias Current (mA_{RMS})	Theory Magnetic Field (μT_{RMS})	Measured magnetic field (μT_{RMS})	Absolutely error (%)
50Hz	1006	230.37	231.9	0.65%
100Hz	1006	230.37	226.4	1.73%
200Hz	1015	232.44	236.0	1.53%
500Hz	1004	229.80	226.8	1.31%
1000Hz	504	115.42	117.6	1.89%

By using equation (6.2), the theoretical magnetic field strength generated in the Helmholtz coil could be calculated from the coil bias current. The calibration results show that the QWHE magnetometer can achieve an accuracy ≤ 2% in alternating magnetic field measurement between 50 Hz to 1 kHz.

6.2.2 Alternating magnetic field Magnetic Flux Leakage testing

In static magnetic MFL, the object under test need to be magnetically saturated by applying a strong magnetic field to obtain stronger flux leakage signals. If the testing is focused on surface and subsurface defects, the object can easily be saturated by using

alternating magnetic fields. This is due to the skin effect which at high frequency alternating magnetic field will only be distributed on conductive material surface and subsurface area. Alternating magnetic field magnetic flux leakage testing can also be used on non-ferromagnetic materials due to the eddy current effects which are described in the following section.

In this section, the QWHE magnetometer was used for detecting the alternating magnetic field flux leakage signals. An electromagnet was used to supply the bias alternating magnetic field on the tested object. The electromagnet and its dimension is shown in Fig. 6.10 (a) and (b). Silicon steel was used as the electromagnet core material due to its wide frequency response range. An audio amplifier circuit, shown in Fig. 6.10 (c) which contain two parallel working 100 W ST TDA7293 audio amplifier chips was used the power the electromagnet bias voltage. An Agilent 33500B function generator was used to supply the sine wave alternating current signals for the audio amplifier. By using this setup, alternating magnetic field with frequencies between 20 Hz and 1 kHz could be generated.

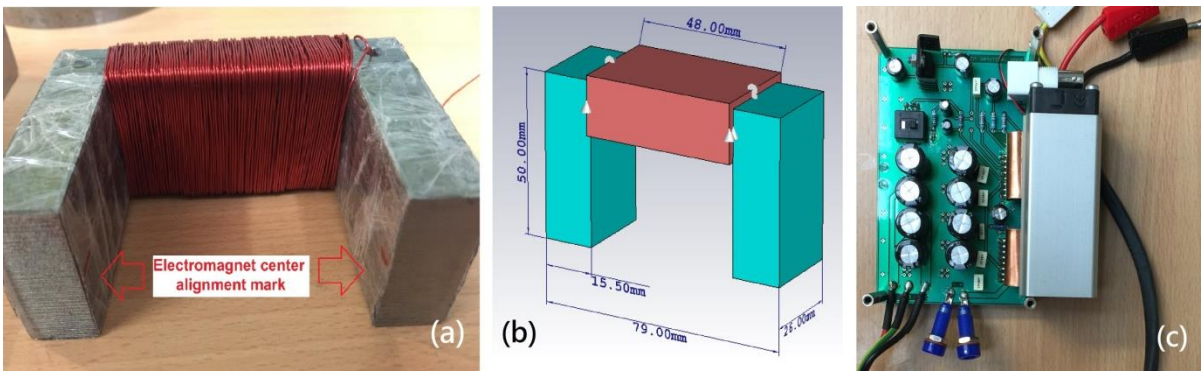

Fig. 6.10 Electromagnet and its driving circuit: (a) overview of the electromagnet, (b) the dimensions of the electromagnet, (c) overview of the electromagnet driving circuit (audio amplifier circuit).

6.2.2.1 Alternating Magnetic Flux Leakage testing with control sample

To understand the behaviour of AC-MFL and to test the performance of the QWHE magnetometer, a control experiment using with two different samples was undertaken. Both samples were based on stainless steel cylinders with 5-inch diameter and 0.75-inch height.

One sample was kept free from defects as shown in Fig. 6.11 (a), and the other one was machined with a 1 mm wide by 2 mm deep groove across the centre of sample as shown in Fig. 6.12 (a). Five different alternating frequency of the magnetic field namely 50 Hz, 100 Hz, 200 Hz, 500 Hz and 1 kHz were chosen for this experiment.

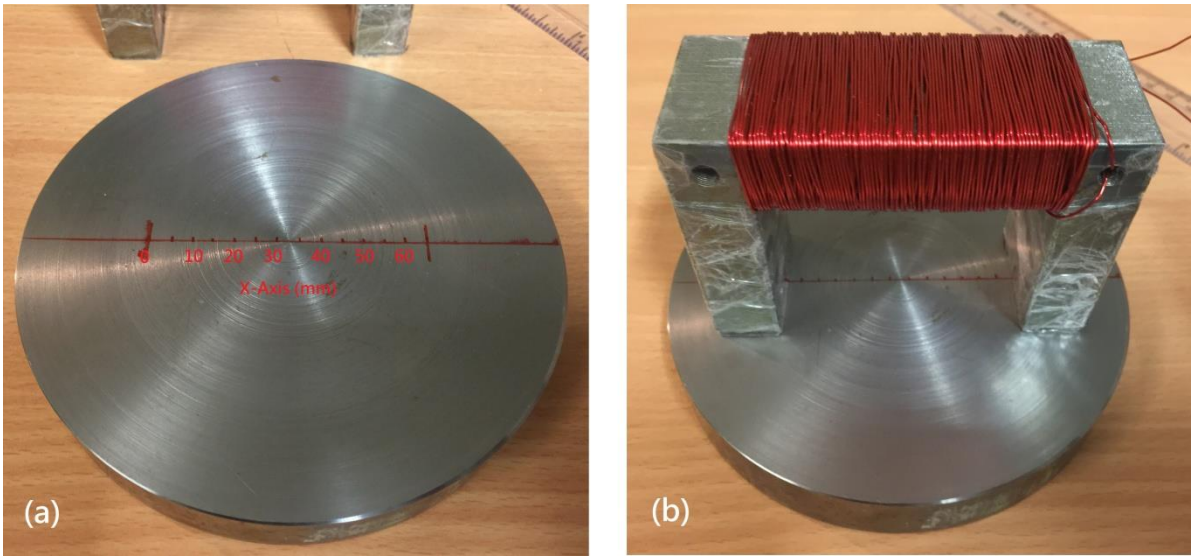

Fig. 6.11 Control stainless steel sample cylinder without defect: (a) cylinder overview and the coordinate system for linear measurement alignment, (b) alternating magnetic field magnetic flux leakage measurement setup.

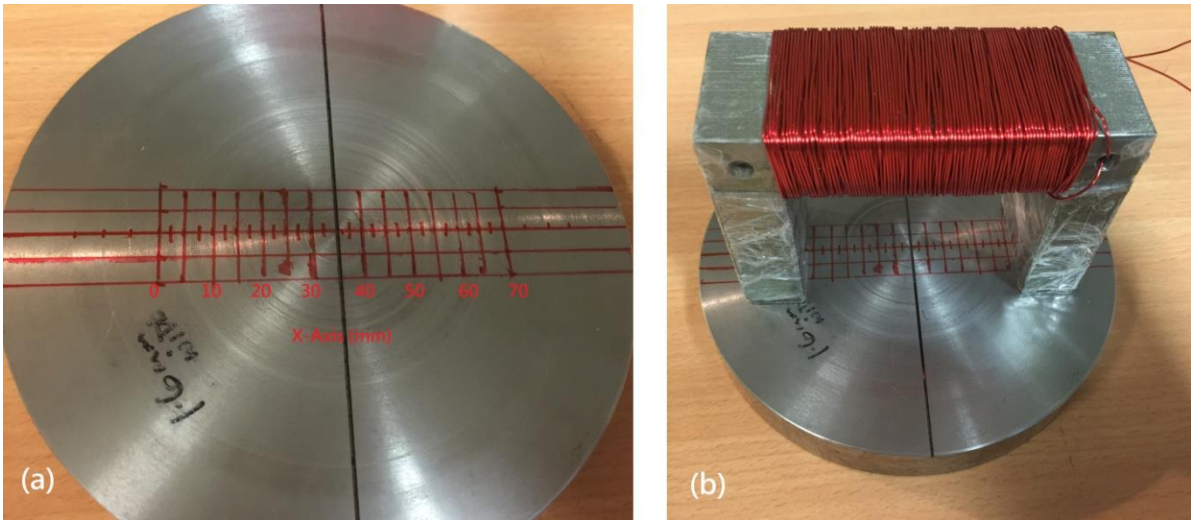

Fig. 6.12 Stainless steel sample cylinder with defect: (a) cylinder overview and the coordinate system used for linear measurement, (b) alternating magnetic field magnetic flux leakage measurement setup.

The magnetic flux leakage setup for both samples are shown in Fig. 6.11 (b) and Fig.

6.12 (b). Coordinate systems were used for manual linear measurement alignment in both samples as shown in Fig. 6.11 (a) and Fig. 6.12 (a). In all measurements, the electromagnet bias current was kept at 1 A_{RMS}. The measurement results at different bias AC magnetic field for undisturbed sample (no defect sample) and for the sample with groove (defect sample) are shown in Fig. 6.13 and Fig. 6.14 respectively.

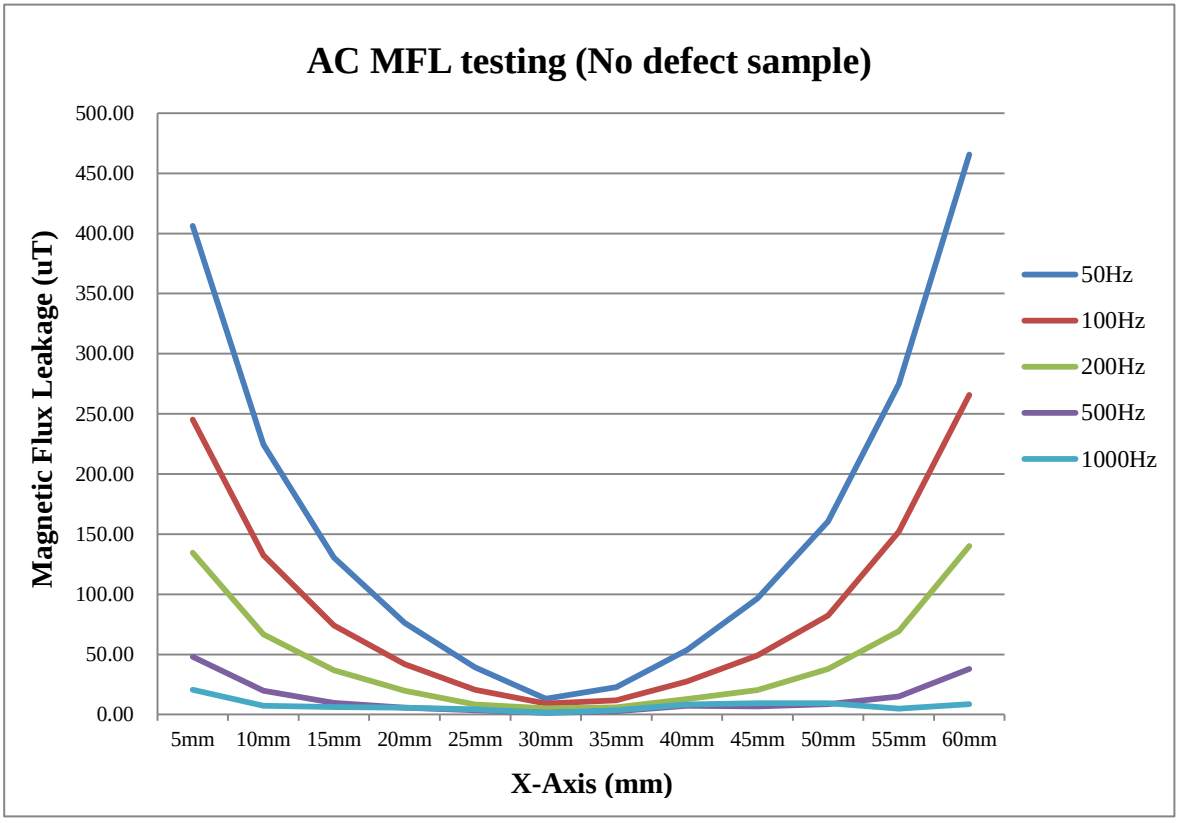

Fig. 6.13 Different AC magnetic field flux leakage measurement results of the control sample stainless steel cylinder without defect.

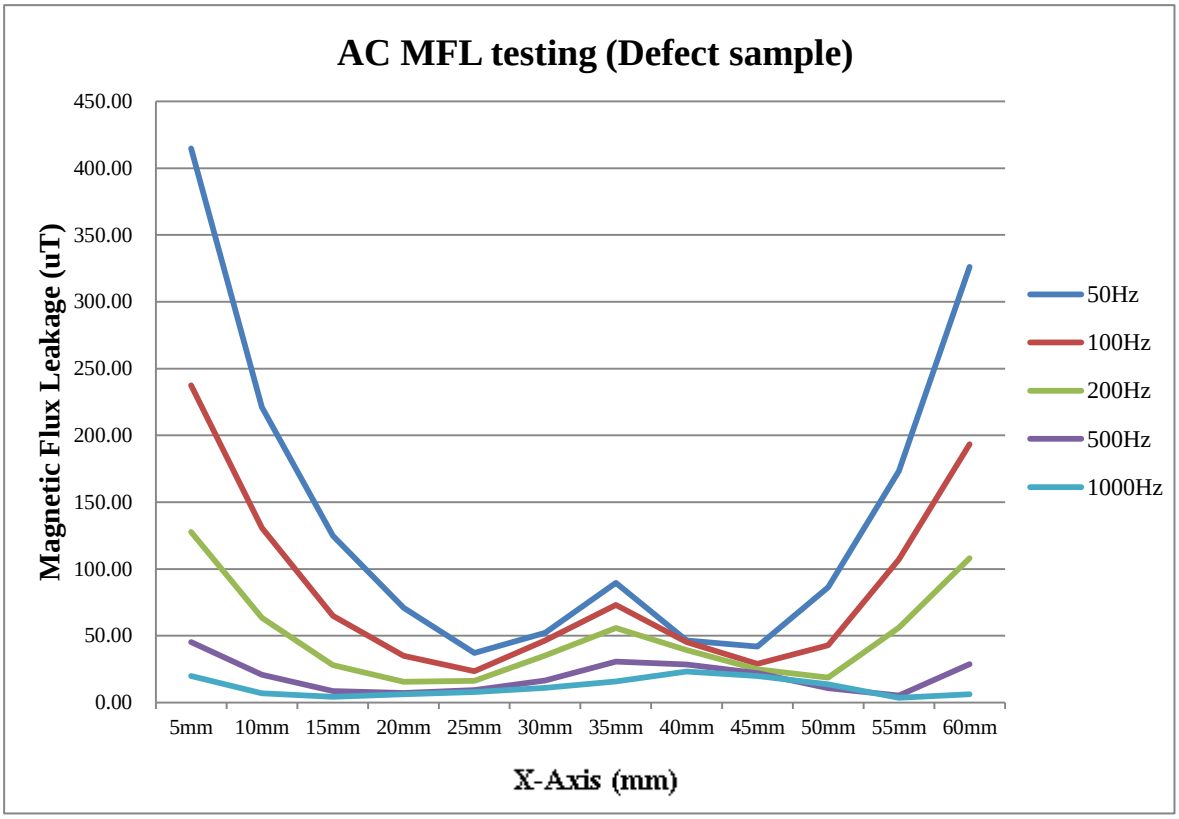

Fig. 6.14 Different AC magnetic field flux leakage measurement results of the defective stainless steel cylinder sample.

It can be seen from the results of the undisturbed control sample that the magnetic fields are stronger on both side which are close to the electromagnet, and are weaker around the centre of the sample. This is due to the background magnetic field leaking from the electromagnet due to the sharp edge between the sample under test and the electromagnet port. The result also shows that the magnetic field strength decreases with an increase of frequency when the electromagnet bias current was kept at 1 A. This was caused by the hysteresis effect of both core and sample materials affecting the direction of changing speed of the magnetic field. However, the magnetic flux leakage signal should be a non-continuous change of magnetic field strength which was not found in the test results of this defect-free sample as shown in Fig. 6.13.

By contrast, for the defective sample there was clear observation of magnetic flux leakage. The shift of the peak signal at 1 kHz could be caused by the tested object not being fast enough to response to the changing speed of the bias alternating magnetic field. Apart

from the 1 kHz data, all other results had the peak magnetic flux leakage signals appear in the location where the machined groove was present. Although the signal strength decreases with the increase of magnetic field frequency, the magnetic flux leakage signal strength was still strong enough to be detected by the high sensitivity QWHE sensor. Both results show that The QWHE sensor can be successfully used in AC-MFL.

6.2.2.2 AC Magnetic Flux Leakage testing with ferromagnetic materials

In this section, a real case non-destructive testing sample from BAE systems was used to test the capability of the QWHE sensor based AC-MFL. The sample under test was a weld crack block with a polished welding hump as shown in Fig. 6.15 (a). The sample block has dimensions of 160 mm × 134 mm × 24 mm. The location of the welding crack is labelled in Fig. 6.15 (a). This welding crack had a dimension of 50 mm length, ≤ 10 μm width and unknown depth. A coordinate system shown in Fig. 6.15 (a) was used for manual mapping measurements. The same electromagnet setup was used to supply the bias alternating magnetic field as shown in Fig. 6.15 (b). The centre of the electromagnet is aligned with the measurement line parallel to X-axis during the manual mapping measurements. In this AC-MFL, four different alternating frequency were used namely 50 Hz, 100 Hz, 200 Hz and 500 Hz. Based on the different bias magnetic field frequency, the measurement results are divided into four different groups.

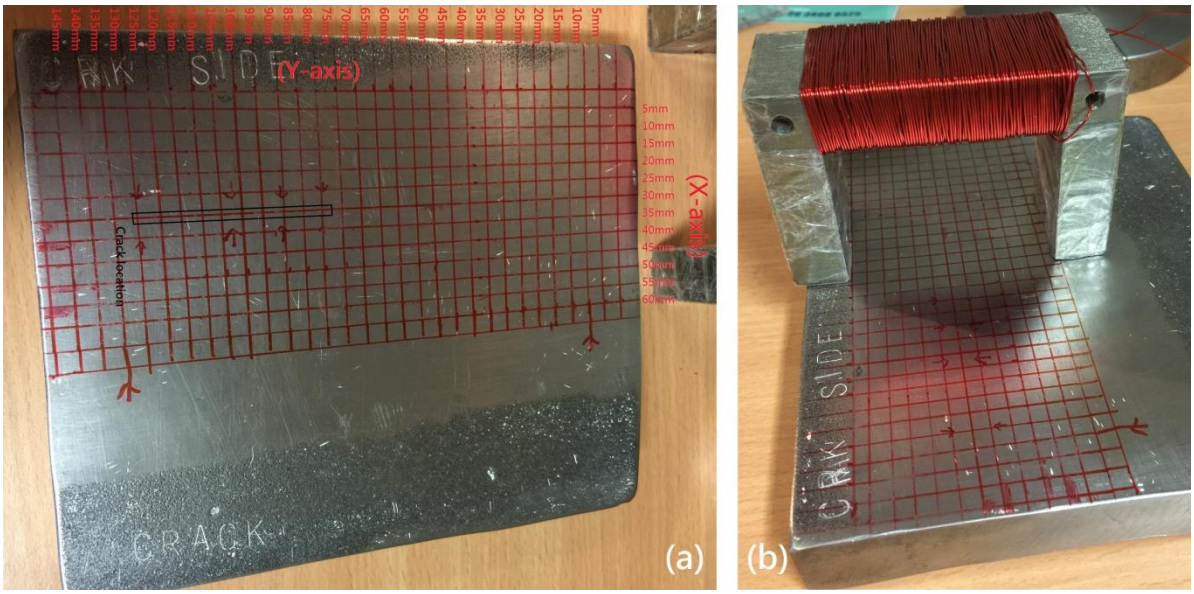

Fig. 6.15 BAE Systems welding crack sample: (a) sample overview and the coordinate system for manual mapping measurement, (b) the alternating magnetic field magnetic flux leakage measurement setup.

The measurement results using a 50 Hz field alternating frequency are shown in Fig. 6.16 and Fig. 6.17. Fig. 6.16 is a 3-dimensional graphical plot with the X-Y planes representing the location of the manual mapping measurements and both colour and height representing the strength of the measured magnetic field. Fig. 6.17 is a 2-dimensional waterfall graph of six different linear measurement results parallel to the X-axis.

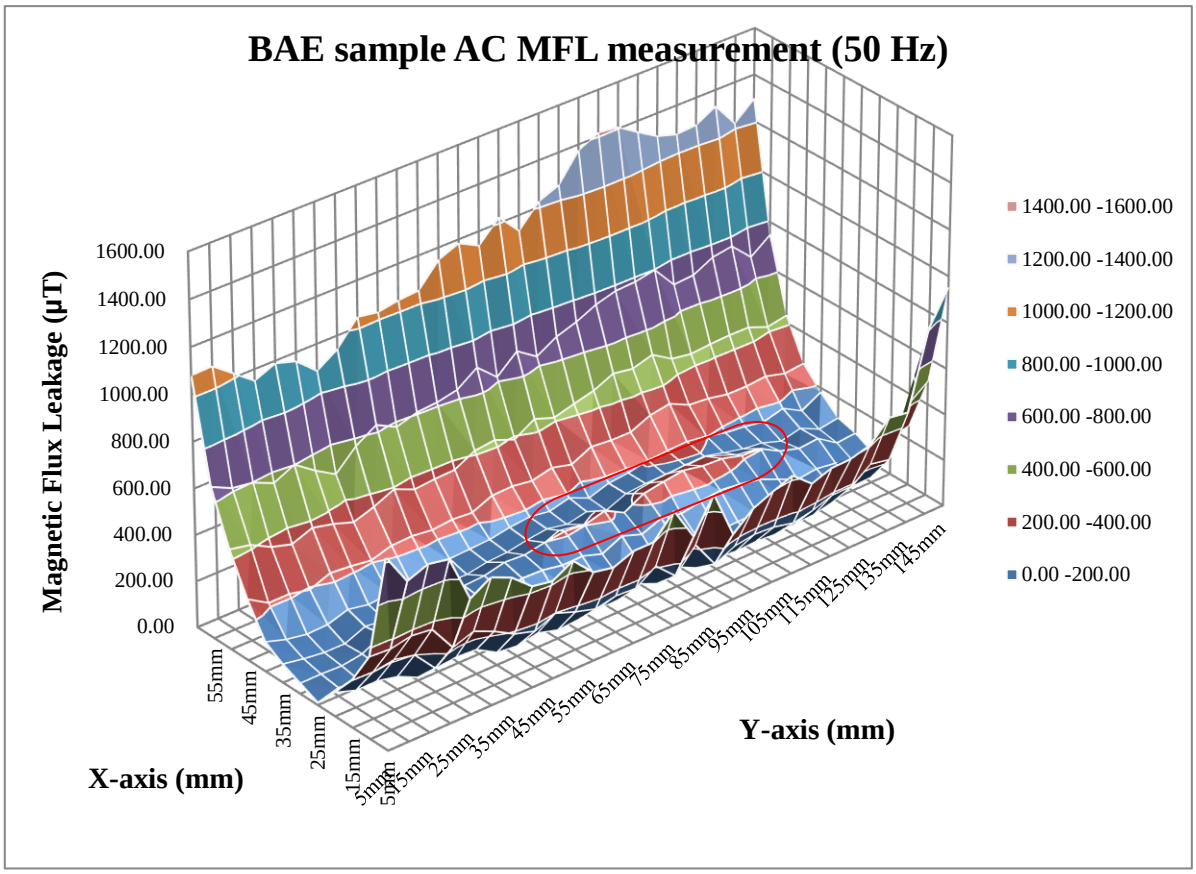

Fig. 6.16 Three dimensional graphical results of the BAE Systems welding crack sample manual mapping measurements at 50 Hz field alternating frequency.

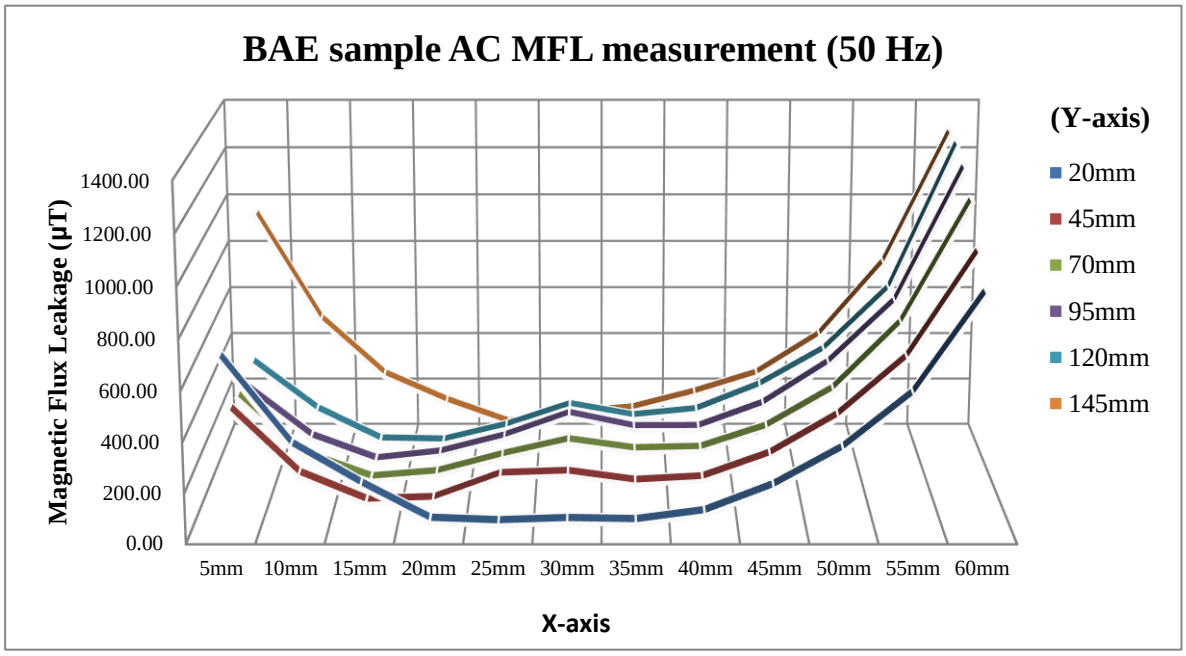

Fig. 6.17 Two-dimensional waterfall graph results of the BAE Systems welding crack sample manual mapping measurements at 50 Hz.

From the 3-dimensional graphical results, the magnetic flux leakage signal can be clearly identified as a hump in the valley. The same result can be found in the 2-dimensional waterfall graph results. The non-continuous strength changes of magnetic field represent the magnetic flux leakage signals in both figures. The result shows that the welding crack can be detect with a 50 Hz alternating magnetic field.

The same magnetic flux leakage measurements were also performed at 100 Hz, 200 Hz and 500 Hz. The 3-dimensional results and 2-dimensional waterfall graph results for the 100 Hz, 200 Hz and 500 Hz conditions are shown in Fig. 6.18 and Fig. 6.19, in Fig. 6.20 and Fig. 6.21, and Fig. 6.22 and Fig. 6.23 respectively. The results show that the magnetic flux leakage signal could be clearly identified at 100 Hz but the magnetic flux leakage signals become fainter at 200 Hz and disappear altogether at 500 Hz measurements. These could be caused by the bias magnetic field strength becoming too weak at higher field frequency as seen in Fig. 6.13 and thus not able to saturate the sample under test.

The results of these ac magnetic flux leakage testing measurements show that the QWHE sensor has indeed enough sensitivity to detect magnetic flux leakage signals from extremely narrow width defects (~ 10μm). The manual mapping measurement results and the linear measurement results also demonstrate the potential of the QWHE for implementation as a magnetovision system as demonstrated later in chapter 8.

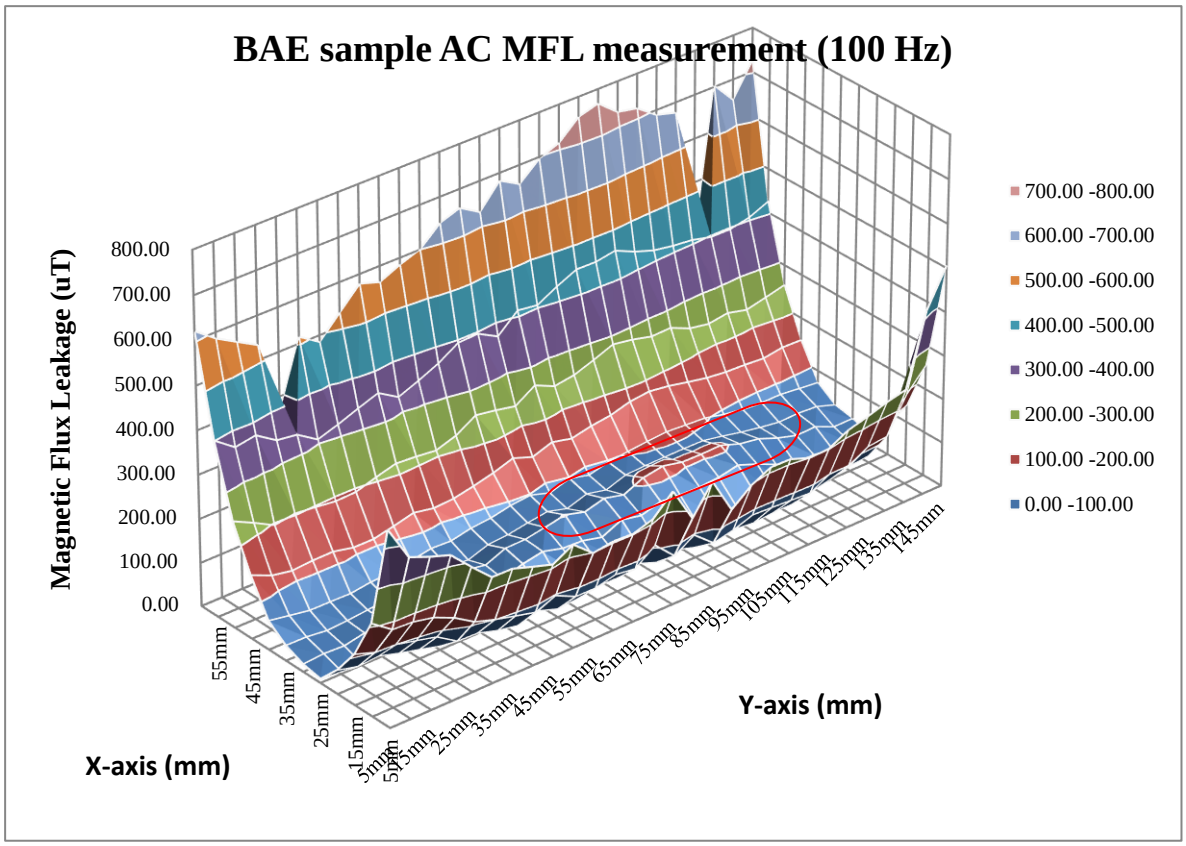

Fig. 6.18 Three dimensional graphical results of the BAE Systems welding crack sample manual mapping measurements at 100 Hz magnetic field.

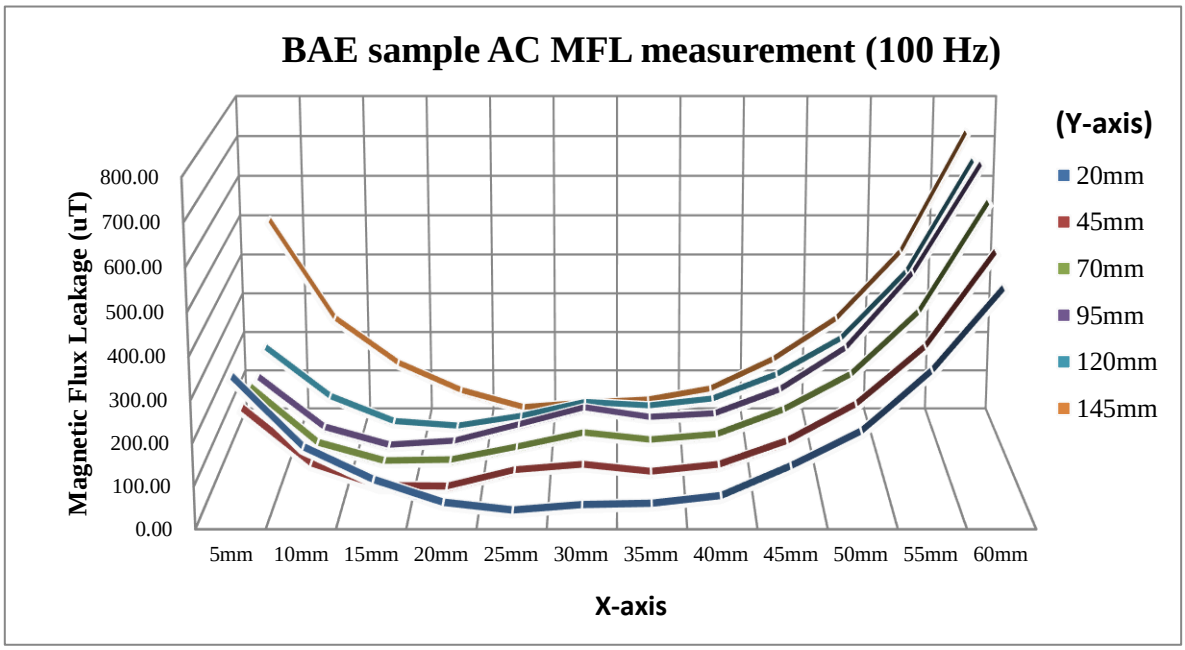

Fig. 6.19 Two-dimensional waterfall graph results of the BAE Systems welding crack sample manual mapping measurements at 100 Hz magnetic field.

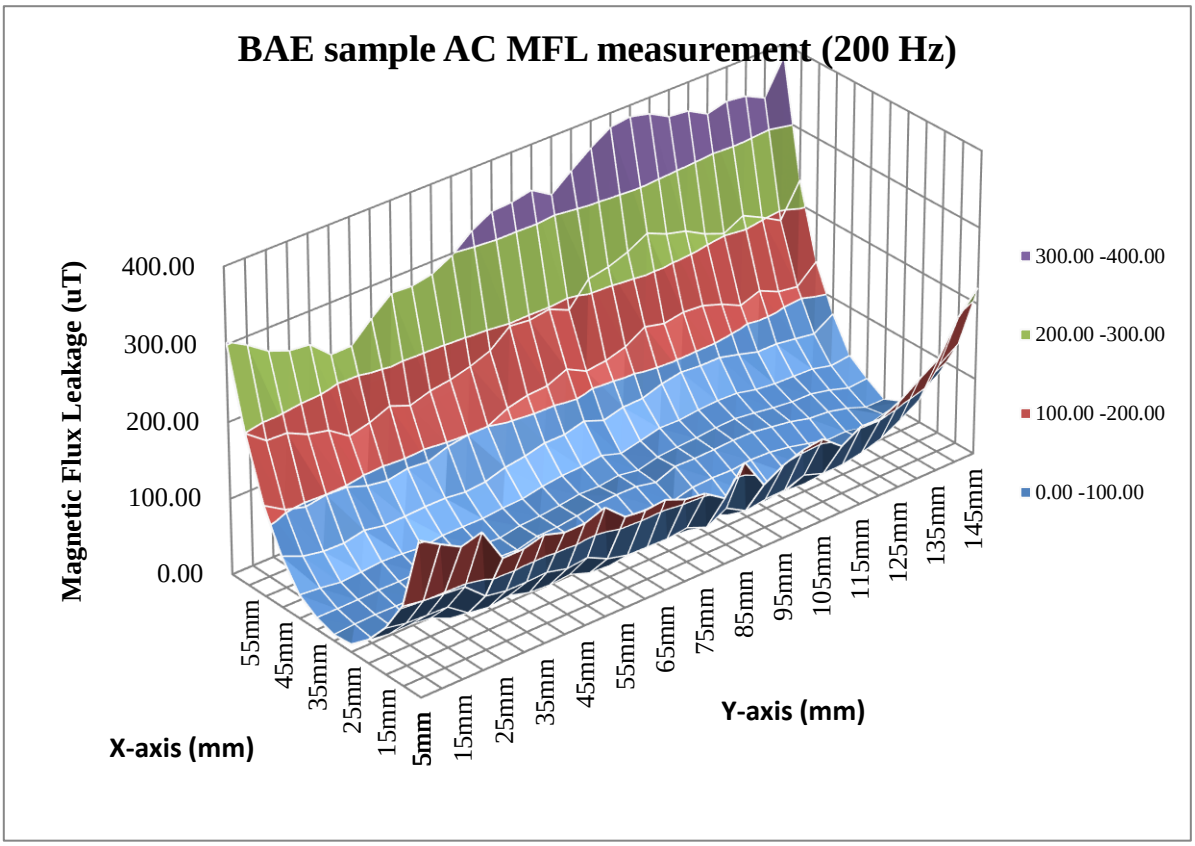

Fig. 6.20 Three dimensional graphical results of the BAE Systems welding crack sample manual mapping measurements at 200 Hz magnetic field.

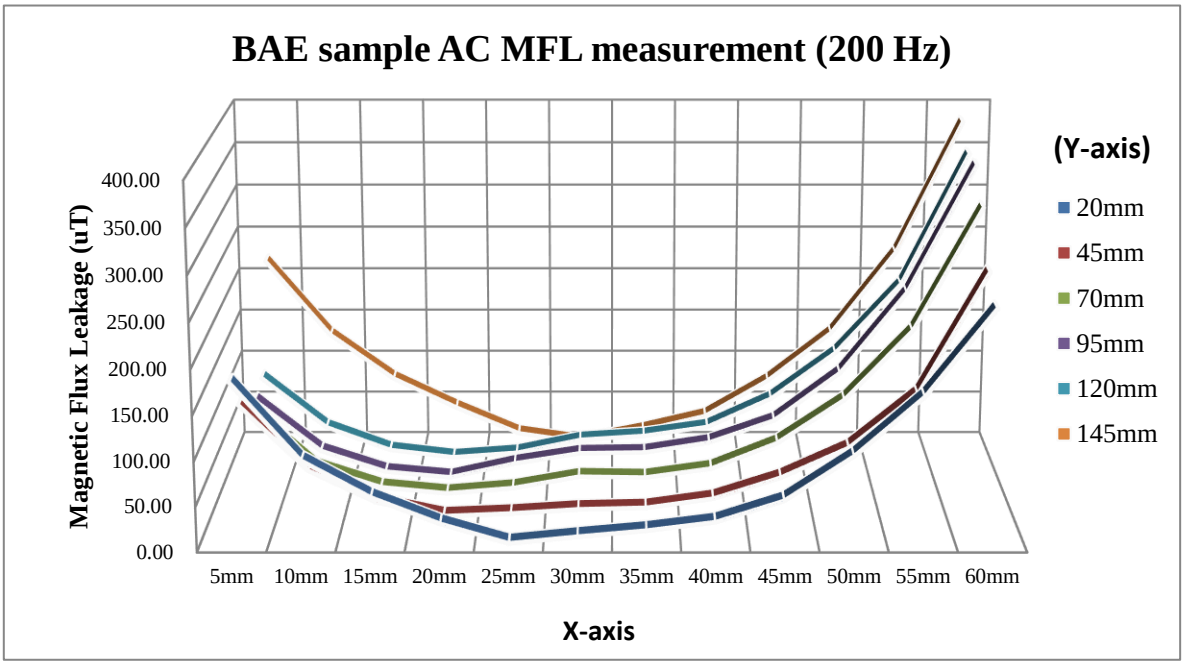

Fig. 6.21 Two-dimensional waterfall graph results of the BAE System welding crack sample manual mapping measurements at 200 Hz magnetic field.

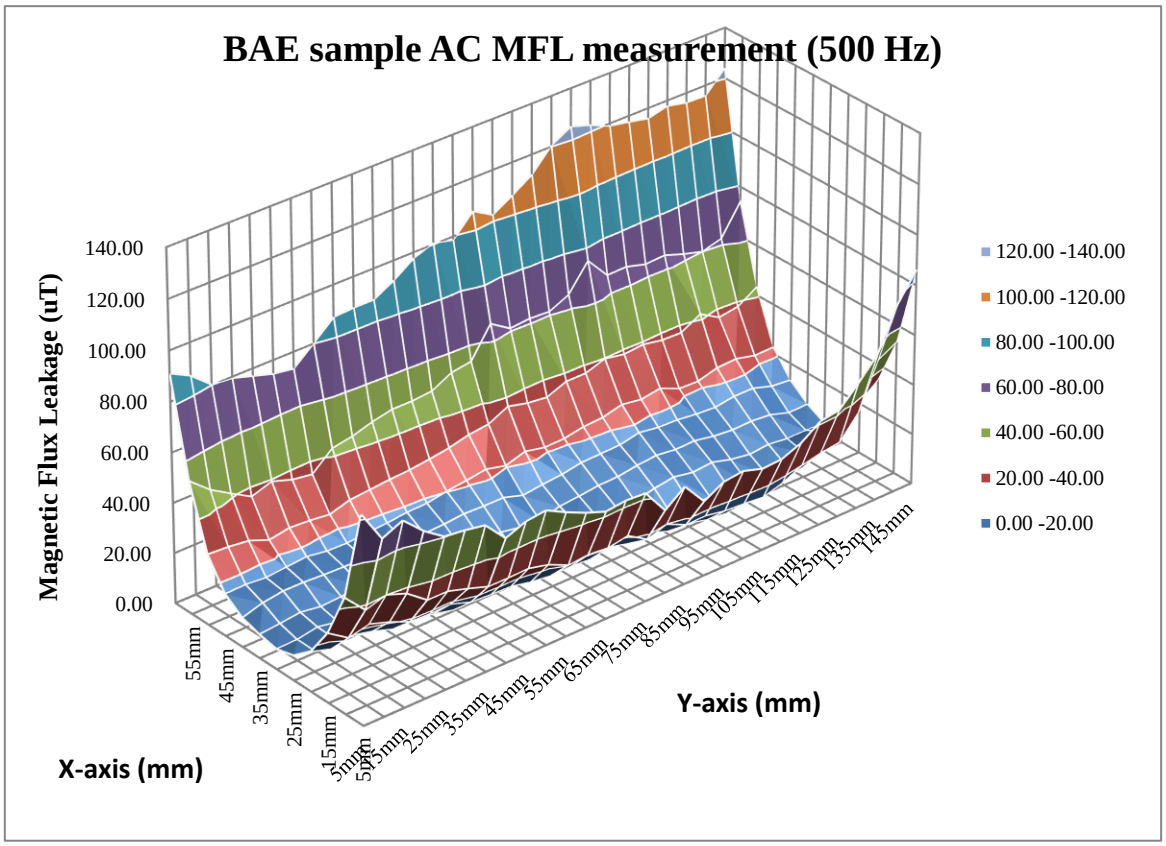

Fig. 6.22 Three dimensional graphical results of the BAE Systems welding crack sample manual mapping measurements at 500 Hz magnetic field.

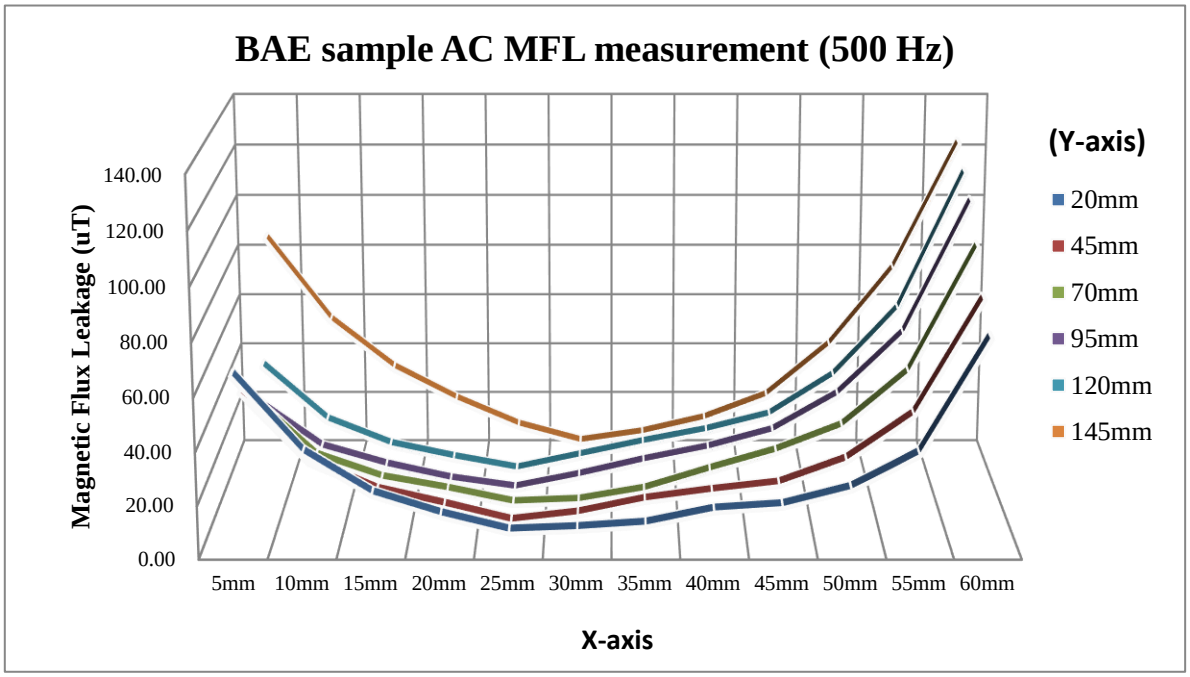

Fig. 6.23 Two-dimensional waterfall graph results of the BAE Systems welding crack sample manual mapping measurements at 500 Hz magnetic field.

6.2.2.3 Alternating Magnetic Flux Leakage testing with non-ferromagnetic materials

A good feature of the AC-MFL technique is that both ferromagnetic and non-ferromagnetic materials can be tested. This is due to the eddy current which are generated from the bias alternating magnetic field creating an opposing magnetic field against the bias magnetic field. When a defect is present, a non-continuous region will change the distribution of an eddy current. The non-continuous region of a conductive material can force the eddy current to go around the defect which can create an area with higher current density. Compared to other regions, the area with higher current density will generate a stronger magnetic field.

To demonstrate the eddy current effect in ACMFL testing, four different materials, namely a wood block (non-conductive material), a carbon steel block (ferromagnetic material), an aluminium plate (non-ferromagnetic material) and an aluminium plate with a round groove (non-ferromagnetic material with defect) were prepared. The same electromagnet setup shown in Fig. 6.11 and the QWHE were used. The bias current of the electromagnet was kept as 1 A_{RMS}. As before, four different field alternating frequency (50 Hz, 100 Hz 200 Hz and 500 Hz) were used in the measurements.

Fig. 6.24 (a), (b), (c) and (d) shows the setup and a simple coordinate system for the linear magnetic flux leakage testing measurements on a 24 mm thick carbon steel block (ferromagnetic material), a 25 mm thick wood block (non-conductive material), a 3 mm thick aluminium plate (non-ferromagnetic material) and a 3 mm thick aluminium plate with 20 mm diameter round groove (non-ferromagnetic material with defect) respectively. The measurement results are shown in Fig. 6.25, Fig. 6.26, Fig. 6.27 and Fig. 6.28 respectively.

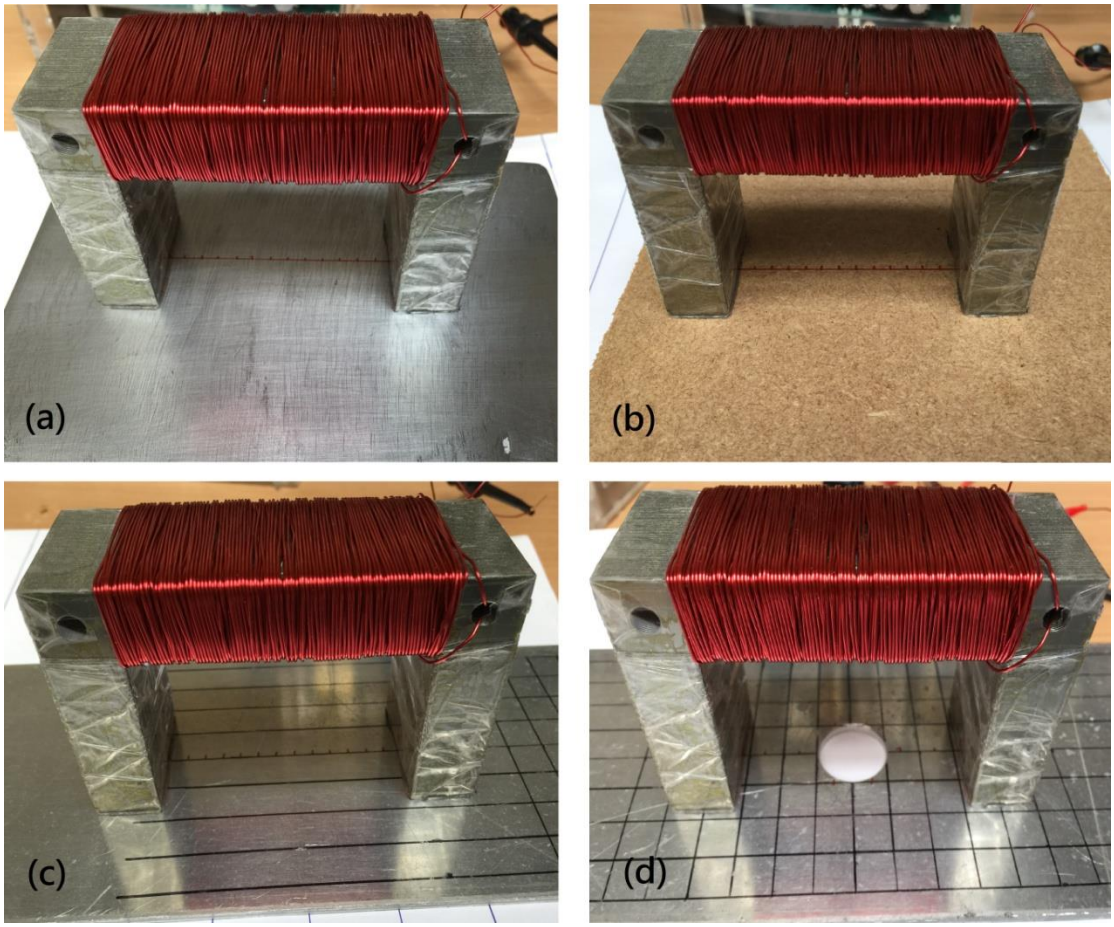

Fig. 6.24 The AC-MFL measurement setup of: (a) carbon steel block (ferromagnetic material), (b) wood block (non-conductive material), (c) aluminium plate (non-ferromagnetic material), (d) aluminium plate with 20 mm diameter groove (non-ferromagnetic material with defect).

Fig. 6.25 shows the AC-MFL test results at 50 Hz, 100 Hz, 200 Hz and 500 Hz. The measurement results are parabola shaped graphs. The magnetic flux is trapped inside the ferromagnetic materials which causes minimum flux leakage around the centre of the test object. The results also show that the bias alternating magnetic fields are stronger than other sample due to higher effective permeability with the same electromagnet bias current. The non-symmetrical results can be caused by the object under test not being fully demagnetised.

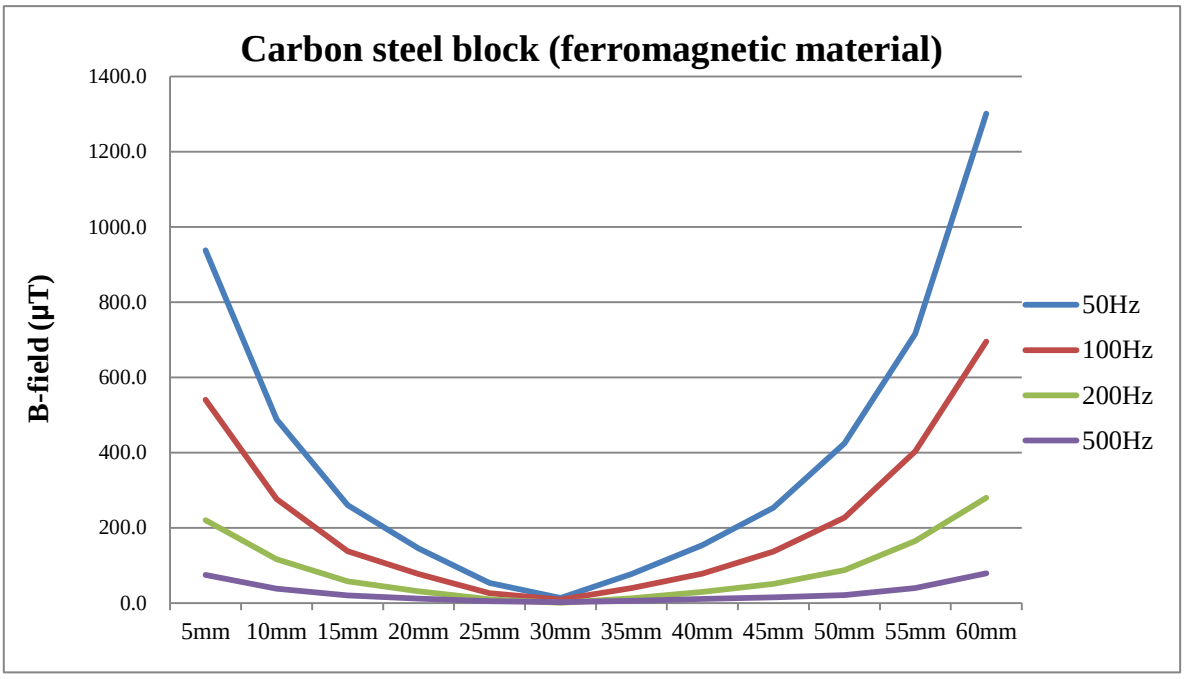

Fig. 6.25 Different alternating frequency magnetic flux leakage measurement results of the carbon steel block (ferromagnetic material).

The results for the wood block are shown in Fig. 6.26. Wood is an insulator which will not generate any kind of induced current inside the material and therefore the magnetic fields detected by the QWHE magnetometer are background magnetic fields leaking out from the electromagnet. The result shows a symmetrically linear decreasing magnetic field strength graph. Compared to the ferromagnetic material sample, the bias magnetic field is weaker in this wood block sample.

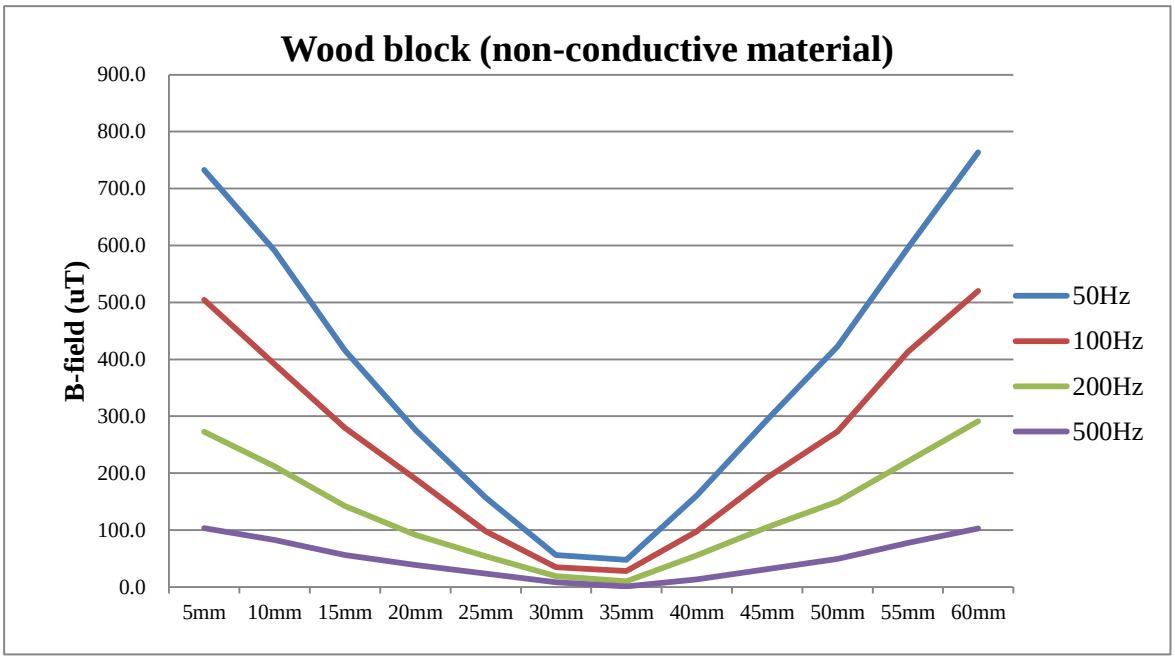

Fig. 6.26 Different alternating frequency magnetic flux leakage measurement results for the wood block (non-conductive material).

Fig. 6.27 shows the AC-MFL results for the aluminium plate (non-ferromagnetic material). These are similar to the wood block results. However, aluminium is a conductive material in which will be induced eddy currents from the external alternating magnetic field. The induced eddy current will generate an opposing magnetic field against the bias magnetic field. The results of this effect are that a weaker magnetic field will be measured in the AC-MFL testing. This eddy current effect will also be more important when subjected to higher magnetic field alternating frequency due to the stronger induced eddy currents. These can all be observed in the test results in Fig. 6.27.

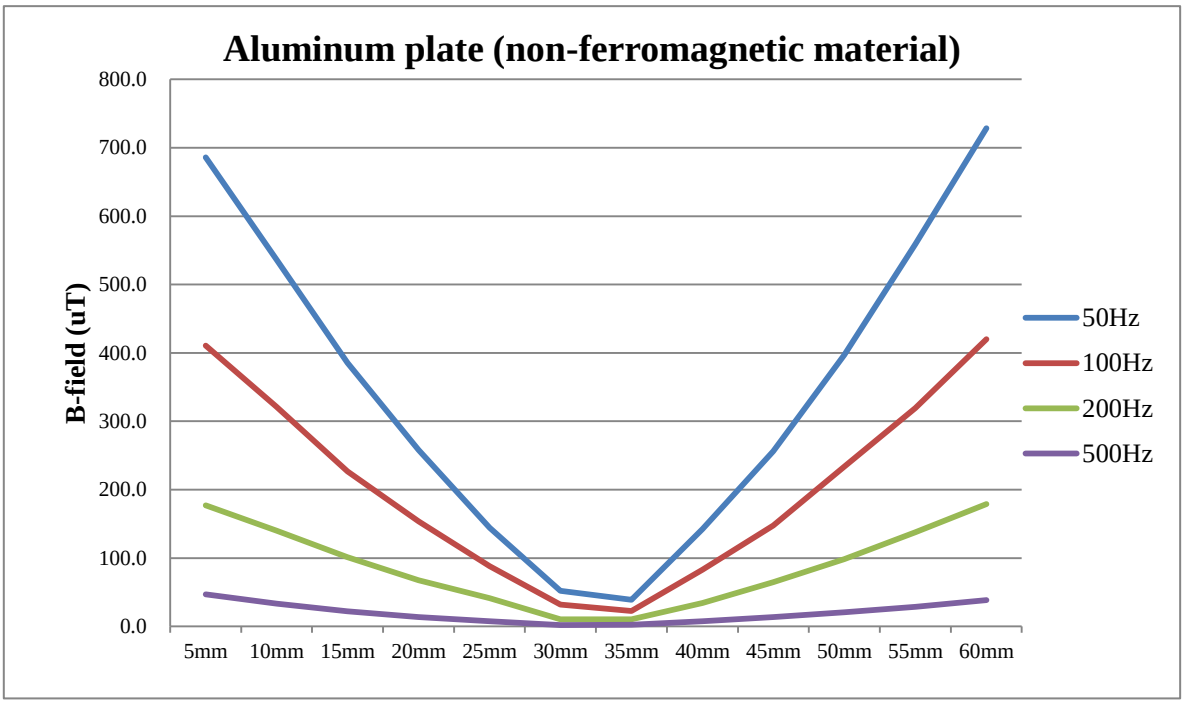

Fig. 6.27 Different alternating frequency magnetic flux leakage measurement results of the aluminium plate (non-ferromagnetic material).

The aluminium plate sample with a 20 mm diameter round groove test results are shown in Fig. 6.28. With a 20 mm diameter round groove located in the centre of the tested object, the induced eddy current are forced to go through a smaller area. This generate a higher current density area around the round groove which generates a stronger magnetic field. The stronger magnetic field become a region which could be easily identified in the measurement results. With the increase of the field alternating frequency, stronger eddy current are induced in the test subject. The increase of eddy current also increasing the magnetic field strength generated from the induced eddy current. The results are that a stronger magnetic field signals can be identified in the AC-MFL test measurements.

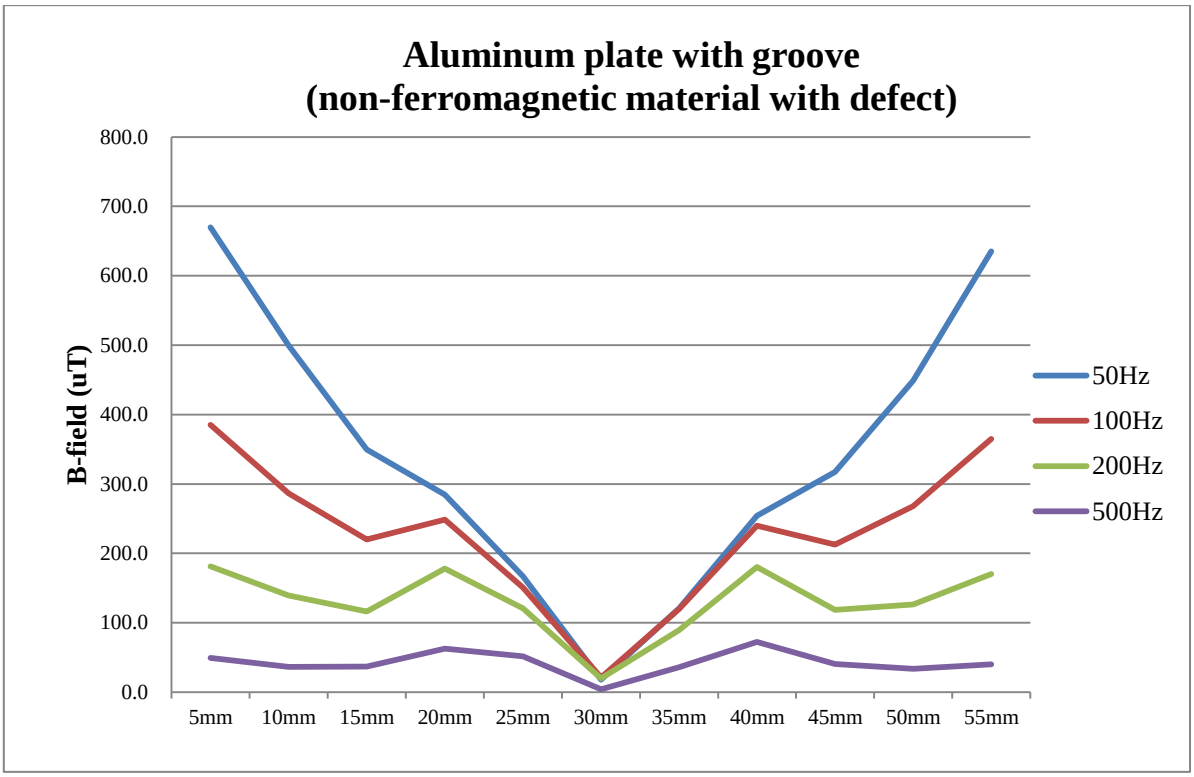

Fig. 6.28 Different alternating frequency magnetic flux leakage measurement results of the aluminium plate with a 20mm diameter groove (non-ferromagnetic material with defect).

The results show that AC-MFL can be used on both ferromagnetic and non-ferromagnetic materials. With the use of the high sensitivity QWHE sensor, small non-continuous magnetic field signals can also be identified easily. The results also point out the potential of a QWHE sensor array magnetic field scanner system.

6.2.3 Direct AC current injection magnetic field measurements with non-ferromagnetic materials

Direct alternating current injection magnetic field measurement is another commonly used electromagnetic non-destructive testing method. The advantage of this measurement is that both ferromagnetic and non-ferromagnetic materials can be tested. Unlike magnetic particle inspection (MPI), a high sensitivity QWHE sensor is used to replace the magnetic particle in this research. Compared to MPI, the QWHE sensor has the advantage of reusability, has a higher sensitivity, lends itself to digitised results and does not require harmful solvent which makes it an optimum choice to replace MPI in direct alternating current injection

magnetic field measurements.

In this experiment, two copper wire clamps were used to make direct contact for injecting bias current into samples under test. The direct contact current injection setup is shown in Fig. 6.29. The dimension of the aluminium plate sample was 480 mm × 93 mm × 3 mm. An alternating current was applied through the long side of aluminium plate. A 20mm diameter round groove was present in the centre of the aluminium plate.

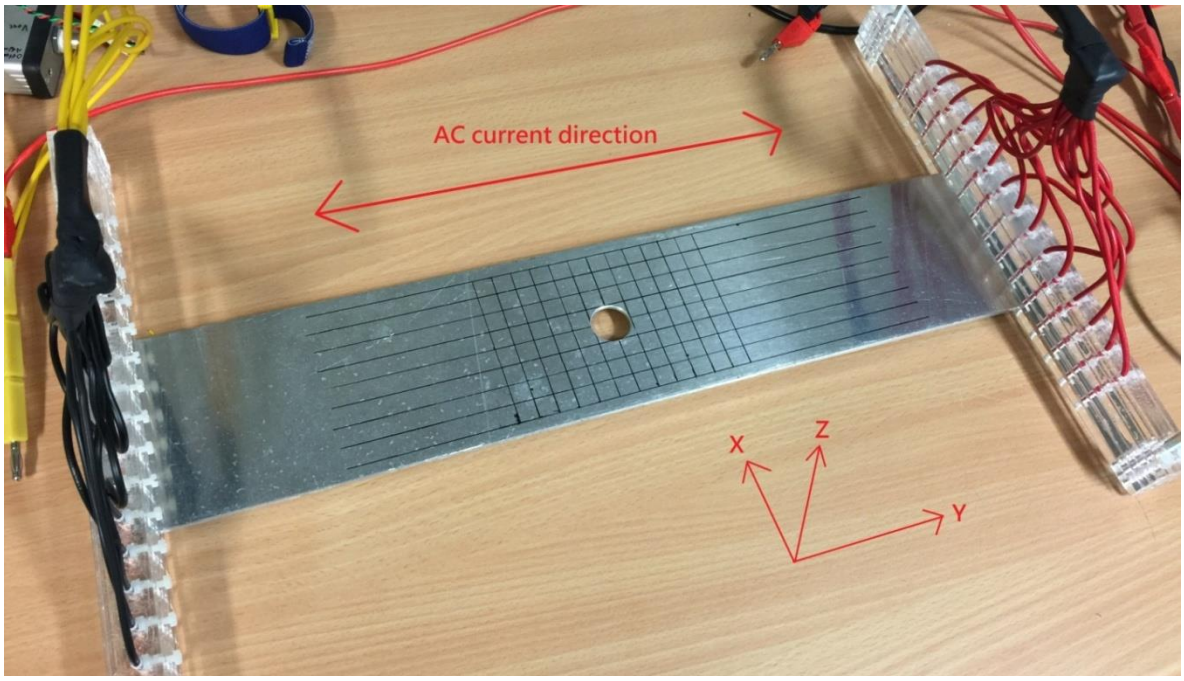

Fig. 6.29 Aluminium plate with 20 mm diameter groove using direct alternating current injection magnetic field measurement setup.

Both magnetic field B_x in the X -axis direction and B_z in the Z-axis direction were measured in this test. A coordinate system shown in Fig. 6.30 was used for the alignment of the manual mapping measurements. The scale pitch of the coordinate system in both X-axis and Y-axis are 10 mm. The direct contact injected alternating current was 3 A_{RMS} at 50 Hz. The measurement results of the horizontal magnetic field B_x are shown in Fig. 6.31 and Fig. 6.32, and the measurement results of the vertical magnetic field B_z are shown in Fig. 6.33 and Fig. 6.34.

When an alternating current flow through the aluminium plate in the Y direction, an X direction horizontal alternating magnetic field will be generated above the aluminium plate.

By measuring the uniformity of the horizontal magnetic field B_x, the current distribution of the aluminium plate could also be measured. When defects are present on the aluminium plate, the current distribution will be changed due to the non-conductive area caused by the defects. By measuring the horizontal direction of magnetic field B_x, the non-continuous magnetic field strength changes could be identified as the location of the defects.

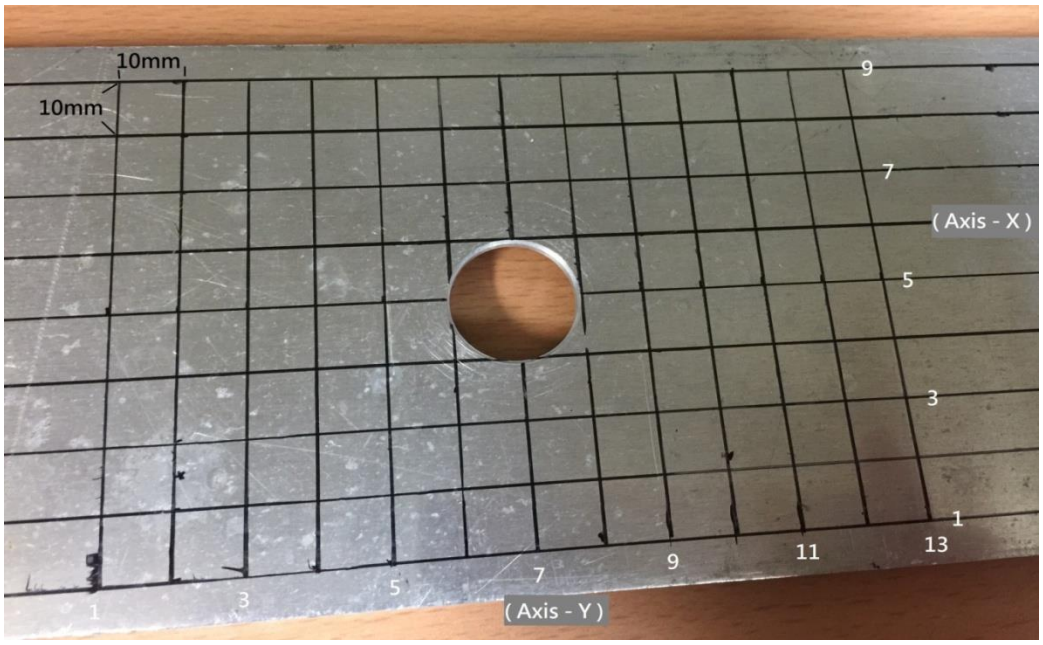

Fig. 6.30 Coordinate system for manual mapping measurement alignment on the aluminium plate with a 20mm diameter groove.

Fig. 6.31 is the 3-dimensional graphical results with the X-Y plane representing the location of the manual mapping measurements and height and colour representing the strength of the magnetic fields. Fig. 6.32 is the line chart graph results which are measured across the centre of the groove parallel to the X-axis. From the horizontal magnetic field B_x measurement results, the non-continuous region of magnetic field strength signal could be identified which represent the edge of the round groove. This was due to the groove creating a non-conductive area which forces the current to go around the groove. When more current was forced to go around the edge of the groove, the area around the groove will have a higher current density. A stronger horizontal direction magnetic field B_x will be generated in these high current density areas which create a non-continuous non-uniform magnetic field

distribution. The centre of the groove had a very weak magnetic field which is due to the fact that no current passes through this area.

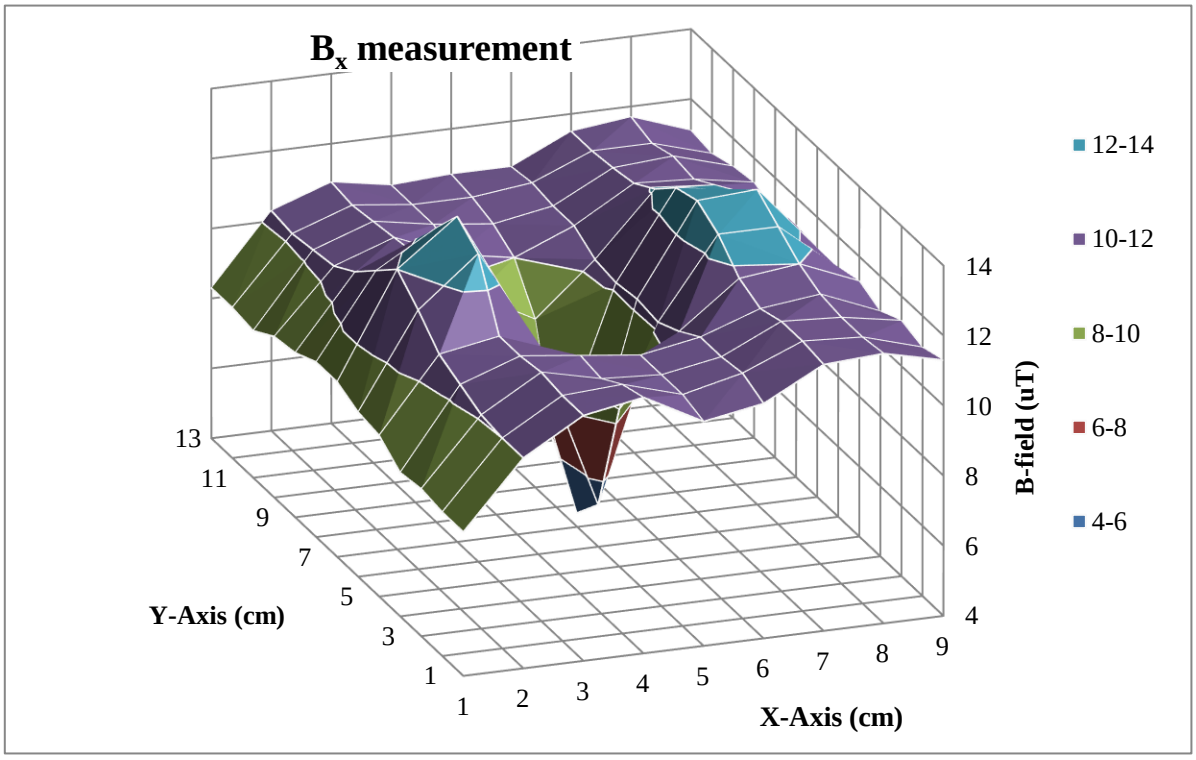

Fig. 6.31 Three-dimensional horizontal magnetic field B_x graphical results of the aluminium plate at 50 Hz bias current.

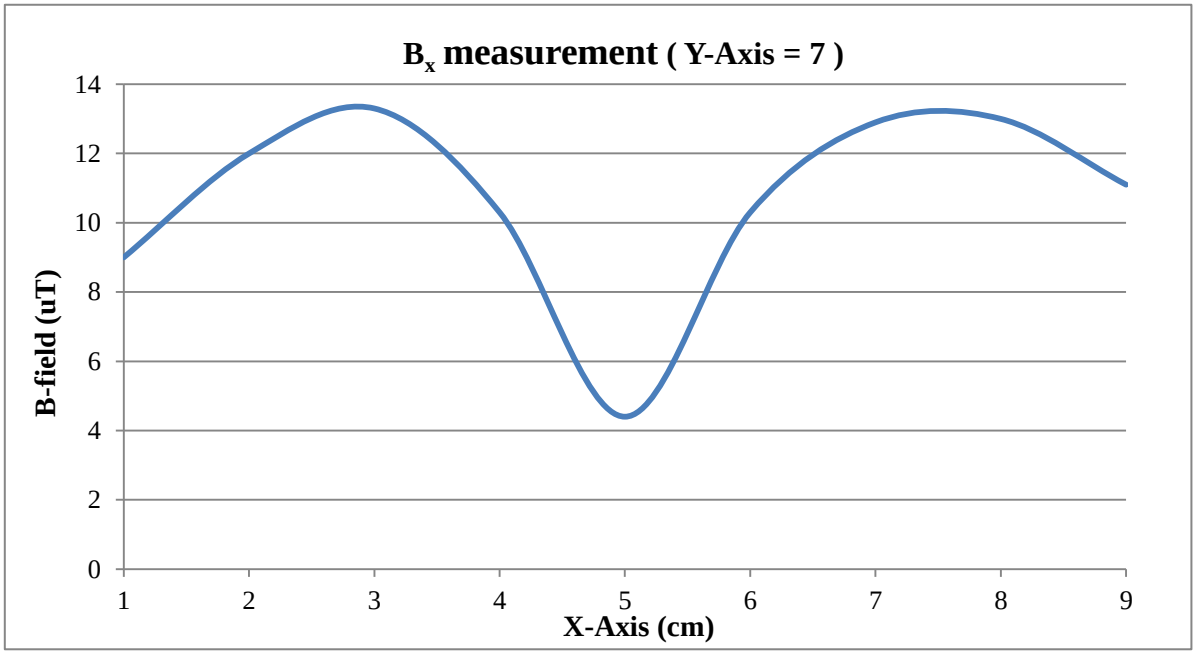

Fig. 6.32 Horizontal magnetic field B_x linear measurement results of the aluminium plate at 50 Hz bias current.

When the alternating current passes through the aluminium plate in the Y direction, a vertical magnetic field will not be generated above the aluminium plate. This is due to that the vertical magnetic field will be cancelled by the opposing vertical magnetic field generated from the parallel nearby current flow. When the measurement is taking place on the edge of the aluminium plate or on the edge of the groove, no parallel nearby current is present, and the vertical magnetic field will not be cancelled. By measuring the vertical magnetic field B_z, the edges of defects can be identified.

The results shown in Fig. 6.33 and Fig. 6.34 are the vertical magnetic field B_z measurement results. Fig. 6.33 is the 3-dimensional graphical results with the X-Y plane representing the location of the manual mapping measurements and height and colour representing the strength of the measured horizontal magnetic field B_z. Fig. 6.34 is the line chart graph which represents the linear measurement result across the round groove parallel to the X-axis. In the measurement results, the non-continuous changes of the vertical magnetic field which represent the edge of the defect could be identified.

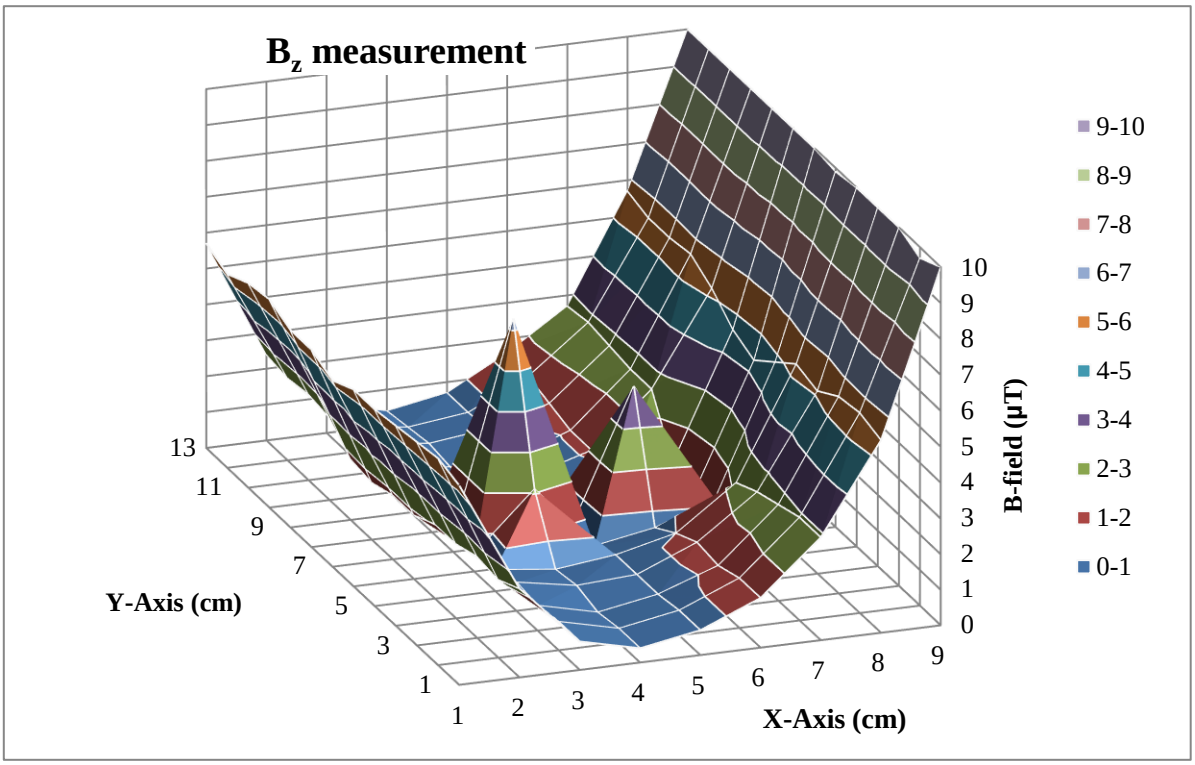

Fig. 6.33 Three-dimensional vertical magnetic field B_z graphical results of the aluminium plate at 50 Hz bias current.

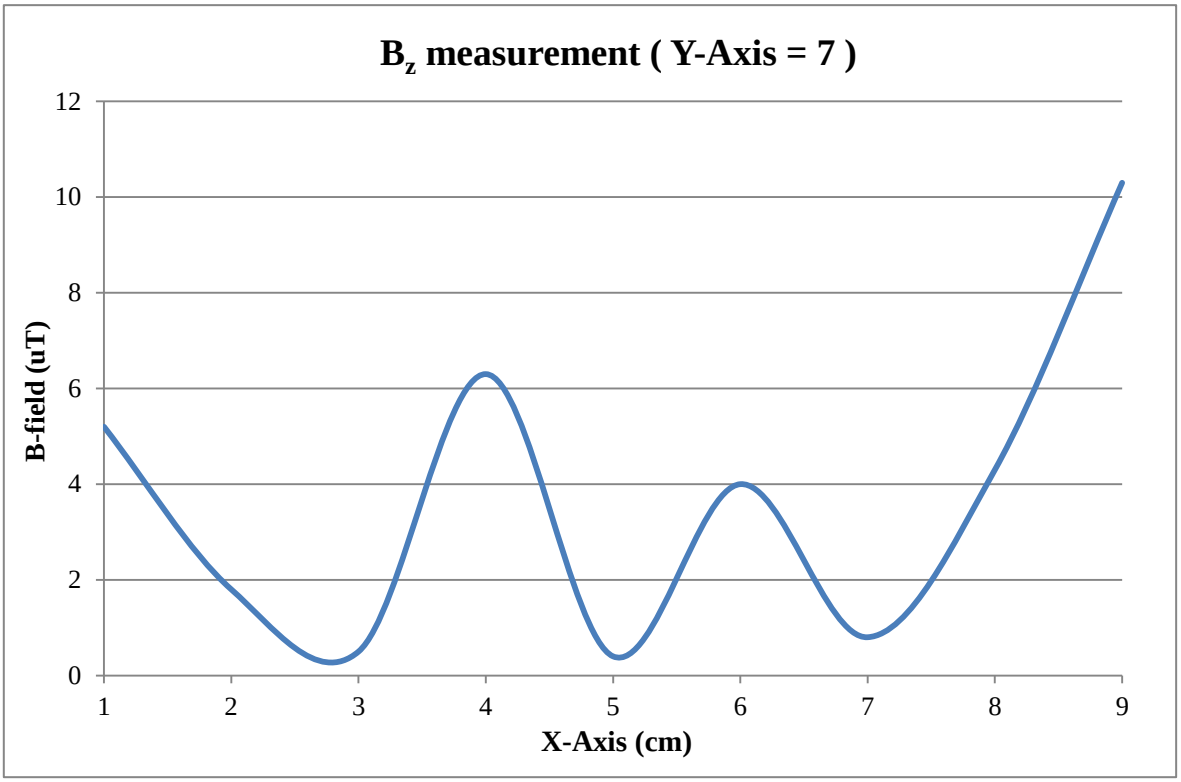

Fig. 6.34 Vertical magnetic field B_z linear measurement results of the aluminium plate at 50 Hz bias current.

From these results, the possibility of using QWHE sensors to replace the magnetic particle inspection technique in direct contact alternating current injection measurement can be demonstrated. Due to the skin effect, when the alternating current frequency increases, the current flow will be distributed on a thinner surface area. With the change of alternating current frequency, deep profile of the defect can be measured. The 2-dimensional manual mapping results also shows the potential of using a QWHE magnetovision system in non-destructive testing measurements as will be demonstrated in chapter 8.

6.3 Conclusion

In this chapter, a 200 mm diameter Helmholtz coil was used for both static magnetic field and alternating magnetic field calibration. Both Quantum Well Hall effect magnetometer and flexible Quantum Well Hall effect 16 × 1 sensor array magnetic field scanner could achieve an accuracy of ≤ 2 % after calibration.

In the static magnetic field, Magnetic Flux Leakage (MFL) testing, manual mapping

measurements with a QWHE magnetometer shows the potential of building a magnetovision system to obtain 2-dimensional magnetic field distribution graphical results. By capturing 2-dimensional graphical results of the magnetic field distribution in magnetic flux leakage testing, both the shape and the location of the defect can be easily identified.

The sensor stand-off measurements performed with the flexible QWHE 16 × 1 sensor array magnetic field scanner also shows the importance of reducing the distance between sensor and the surface of tested objects. By using a flexible sensor array structure, the stand-off distance can be kept at a minimum to obtain stronger signals.

In the alternating magnetic field Magnetic Flux Leakage (AC-MFL) testing, the results of a BAE Systems weld crack block shows that the QWHE sensor has not only high sensitivity and linearity in a wide frequency response but is also capable of detecting micron wide defects which makes it an optimum choice to be used for the alternating MFL testing. By changing the testing sample bias magnetic field frequency, data of different skin depth can be obtained which makes depth profiling a possibility. The test results of the aluminium plate show that the AC-MFL testing can be used not just on ferromagnetic materials but also on non-ferromagnetic materials. This is due to the induced eddy current generating opposing magnetic fields against the applied alternating magnetic field, and this eddy current can be disturbed by surface defects.

In the direct contact alternating current injection testing, the test results using the QWHE magnetometer show that this later has many advantages as an alternative to the magnetic particle inspection method. The advantages are reusability, higher sensitivity, easy digitisation of the results and the lack of harmful solvent.

The results shown in this chapter demonstrate the advantages and possibility of using Quantum Well Hall effect sensor in electromagnetic methods non-destructive testing. This is largely due to Quantum Well Hall effect sensor having the advantage of:

1. High sensitivity which can measure down to μT range in DC and nT range in AC.
2. Linear sensitivity with wide dynamic range.

3. Linear frequency-sensitivity with wide frequency response.
4. Compact size.
5. Easy to operate.

The results presented strongly show the potential of using the QWHE sensors in a magnetovision system in non-destructive testing measurements as will be demonstrated in chapter 8.

Chapter 7
Quantum Well Hall effect real-time magnetic-field cameras

In real non-destructive testing situations, large surface areas are usually need to be fully inspected. Both operational times and accuracy are required for detecting small, mm or sub-mm size defects which might be hidden in the inspected large surface area. Failure to inspect and detect surface defects can cause dramatic failure in safety critical structures. A non-destructive testing magnetovision system can improve inspection efficiency substantially and increase tolerance for operations. This is due to the 2-dimensional graphical results captured by magnetovision systems providing both visualised and continuous inspection information.

A magnetovision system can be based on three different system architectures, which are:

(1) A single sensor magnetometer with 2-dimensional multi-positioning setup mechanisms.

(2) A linear array magnetic field scanner with a linear slide mechanism.

(3) A 2-dimensional sensor array magnetic field camera.

Both options (1) and (2) require mechanical movement mechanisms which can have limited scanning speed and possibly introduce further mechanical noise which limits the ultimate detect ability of the system. To avoid these drawback, 2-dimensional sensor array magnetic field camera is the optimum architecture choice for building up a magnetovision system. This chapter discusses in details, the design and build of two 2-dimensional sensor array magnetic field cameras.

7.1 Quantum Well Hall effect 8 × 8 array magnetic-field camera

A magnetovision system contains an external source for applying electromagnetic fields, a position scanning mechanism and a magnetic field detection method. A magnetic field camera can achieve both requirements of multi position scanning and magnetic field strength

data acquisition. A magnetic field camera consists of a 2-dimensional magnetic field sensor array, sensor bias sources, signal amplification units and signal capture sections. As described previously, a P2A QWHE sensor which has both a small size and ultra-high sensitivity was used in the magnetic field camera design. In this section, an8×8QWHE sensor array magnetic field camera is designed and built.

7.1.1 Circuit design and PCB layout

Fig. 7.1 shows the block diagram of the 8×8 QWHE sensor array magnetic field camera. This camera design consists of a 2-dimensional sensor array, analogue signal 1:8 multiplexers, instrumentation amplifiers, 16-bit analogue to digital converters, two voltage references, an AVR multiplexer, a set of control buttons and a colour liquid crystal display (LCD).

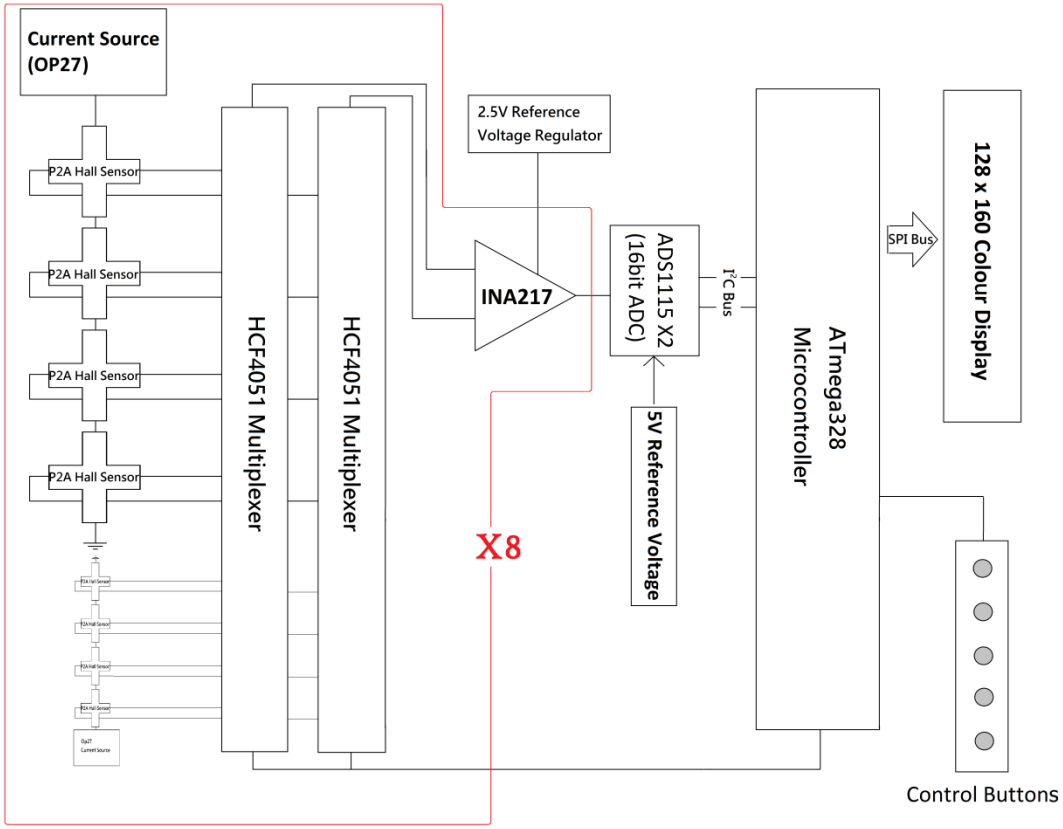

Fig. 7.1 8 × 8 Quantum Well Hall effect sensor array magnetic field camera block diagram.

The 2-dimensional sensor array is a combination of eight 8 × 1 linear sensor array modules as depicted in Fig. 7.1. In each module, four sensors are connected serially for

supplying constant current bias. Two sets of Howland current sources are used to supply the constant bias currents. A set of two signal multiplexers are used for selecting the differential Hall voltage signals. An instrumentation amplifier is used to amplify the Hall voltage signals and convert the differential signals to single-ended signals. Two 4-channel 16-bit analogue to digital converter are used to digitise the Hall voltage signals. The digitised signals are then converted into 2-dimensional graphical results with red and blue colour representing the polarities and colour depth representing the strength of the measured magnetic fields. The 2-dimensional graphical results are shown on the liquid-crystal display.

The circuit schematic of the 8×8 sensor array magnetic field camera is shown in Fig. 7.2. The 1 × 8 linear sensor array magnetic field sensing module is represented in the green frame shown in Fig. 7.2. In each module, eight P2A sensors (which are shown as Wheatstone bridges in the figure) are disposed in a linear arrangement with 10 mm pitch between each sensor. Two sets of Howland current sources which are based on Analog Devices OP27 operation amplifiers are used to provide bias constant current for the QWHE sensors. Two STMicroelectronics 8-channel analogue multiplexers with low "On" resistance are used to select the differential Hall voltage signals between sensors. A Texas Instruments INA 217 instrumentation amplifier with a 1.3 nV/√Hz input noise is used to amplify the differential Hall voltage signals. The amplified signals from eight different modules are digitised by two Texas Instruments ADS1115 delta-sigma 16-bit analogue to digital converters. A 2.5 V reference voltage regulator and a 5 V reference voltage regulator are used to supply constant voltages to the instrumentation amplifiers and the analogue to digital converters respectively. The digitised signal are then converted into 2-dimensional graphical results by an AVR ATmega328 8-bit microcontroller, and the results displayed on a 128 × 160 colour display.

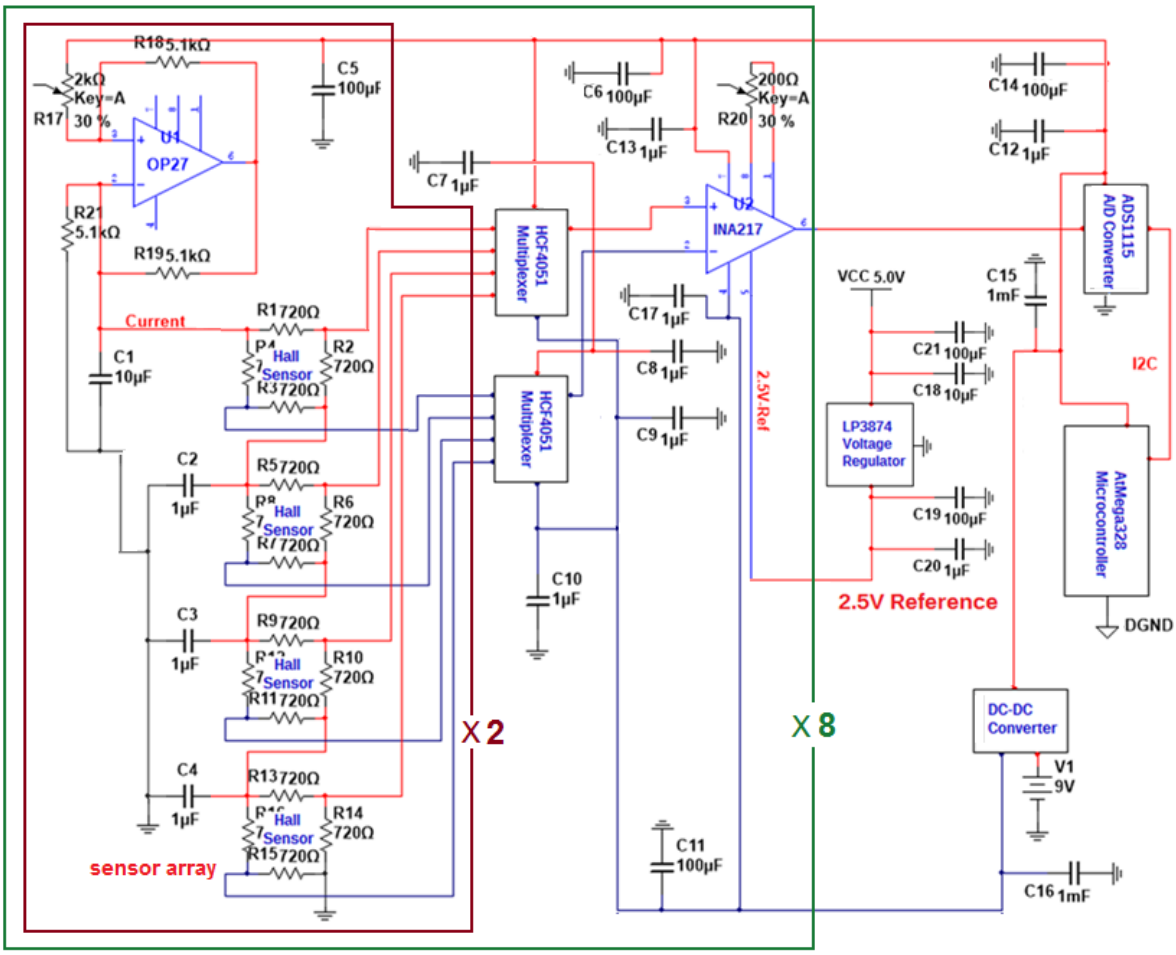

Fig. 7.2 Circuit schematic the 8×8 Quantum Well Hall effect sensor array magnetic field camera.

Fig. 7.3 shows the PCB layout of the 8×8 sensor array magnetic field camera. The dimensions of the PCB are 133 mm × 215 mm. Four layers PCB are used in this design. In the PCB design, the top two layers are mainly used for analogue signal traces, and the bottom layer is mainly used for digital signal traces. The analogue signal layers and digital signal layer are separated by a ground layer for reducing electromagnetic interference. The PCB top layer consists of components such as sensors, multiplexers, amplifiers, microcontroller and DC-DC converters.

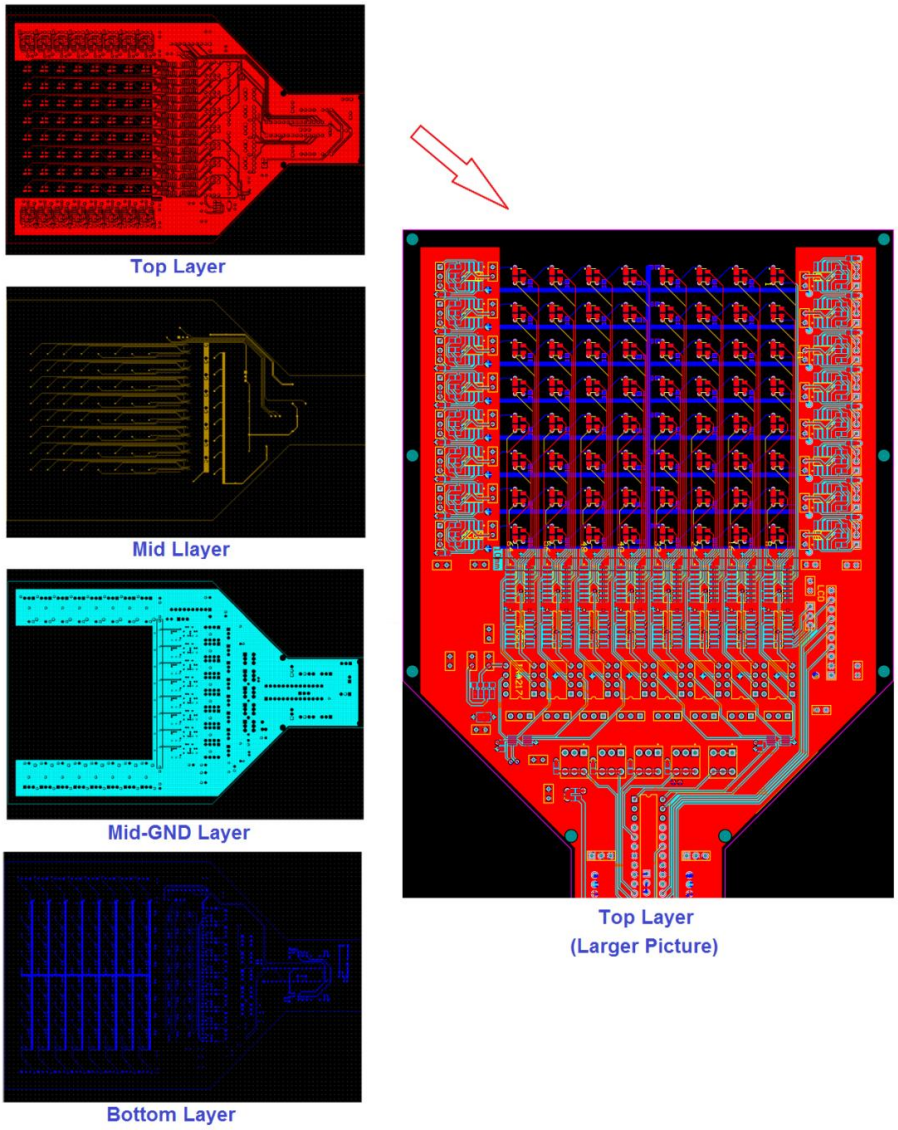

Fig. 7.3 Four layers PCB layout of the 8×8 Quantum Well Hall effect sensor array magnetic field camera, with dimensions 133 mm × 215 mm.

In the 2-dimensional sensor array, the shortest connection distances are routed to reduce the amount of induced noise. The sensor array is not covered by ground copper plate to avoid the inducing of eddy currents. The pitch between QWHE sensors in both horizontal and vertical directions are 10 mm. Further PCB designs rules of the 8×8 array are described below:

- Top layer: The top layer is covered by a power signal V_{cc} plate. A few decoupling capacitors are placed on the power traces between the analogue and digital circuits sections to reduce high frequency noise from the digital chips. Other surface mount decoupling capacitors are also used to reduce the possibility of noise effects between different circuit parts (current

source circuit, multiplexer circuit, and amplifier circuit) in the analogue circuit section.

- Mid layer: Most of the analogue signals pass through the copper traces located on the top layer and mid layer.
- Mid ground Layer: the mid ground layer is used to separate the analogue signal traces (top two layers) and digital signal traces (bottom layer). This layer is covered by ground for the analogue circuits. A digital ground for both liquid crystal display and microcontroller are routed separately.
- Bottom layer: Most of the digital signals pass through the copper traces in this layer. Digital ground traces are also routed in this layer. The digital ground and analogue ground are joined through a single point connection to reduce noise effects.

7.1.2 Program flowchart

As mentioned earlier, the 8×8 sensor array contains an 8-bit AVR microcontroller. This microcontroller can be used to automatic control the multiplexers for selecting between different sensors and recording the measurement reading from each sensor. An Arduino UNO development kit is used to program the microcontroller. The firmware of the microcontroller is written in C language which is then transferred to a Low-level programming language through Arduino IDE software.

The flowchart of the main firmware program is shown in Fig. 7.4. When the 8×8 sensor array magnetic field camera is turned on, the program starts with shifting the midpoint value to prevent overflow and underflow problems. Following this, the program runs a loop to capture all sensors offset voltage readings. The acquired offset voltage data from each sensor is then used in the software offset cancellation routine. The Offset reducing function can also be executed manually. After offset cancelation, the program continues the loop of selecting between different rows of linear sensor array and acquires measured signals. The captured signals are then converted into 2-dimensional graphical results. The conversion will follow the magnetic field camera setting which define the resolution of the magnetic field camera

graphical results. The graphical plots are 2-dimensional results with different colour depth to represent the strength of the measured magnetic field, with blue and red colour representing the magnetic field polarities. The default resolution setting is ×1 which means the 15-bit signed data is converted into an 8-bit colour depth data with a ratio of 128:1. When the resolution setting is increased to ×2, the conversion ratio is increased to 64:1, and so on. The converted graphical data which represent the strength and polarities of the measured magnetic fields is then displayed on the colour liquid crystal display in real time.

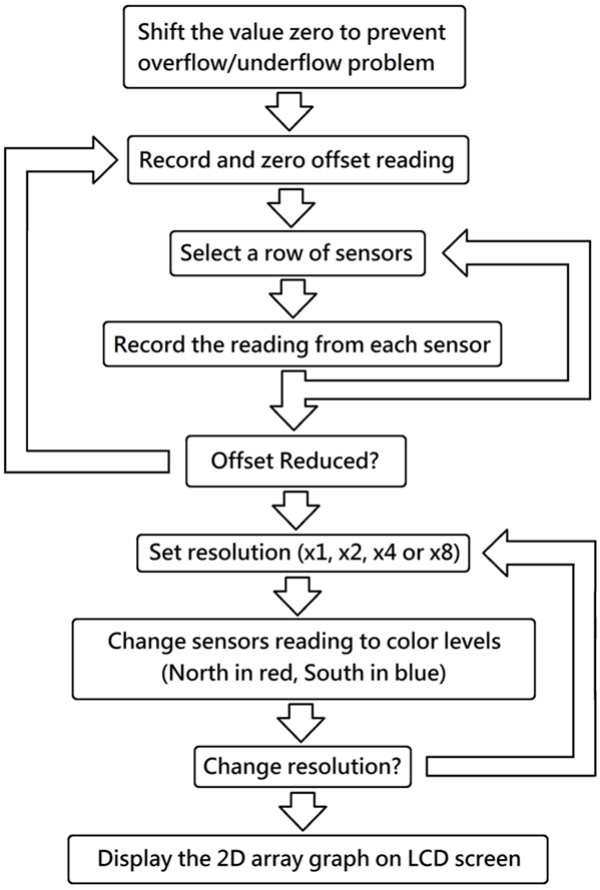

Fig. 7.4 Flowchart of micro-controlled 2D 8×8 QWHE array magnetometer.

Fig. 7.5 show the schematic illustration of the measurement procedures of the 8×8 array 2D magnetometer. Note that the program control the scanning from a left to right cycle. Each cycle includes eight times selection between different sensor rows. Each sensor row contains eight QWHE sensors. There are eight amplifier circuits, and a total of eight capture channels from a set of two analogue to digital converters in the magnetic field camera. This means the

measurement data from 8 different sensors in each row can be captured in parallel. By using this optimised measurement procedure, the measurement efficiency of the 8×8 sensor array magnetic field camera is increased substantially.

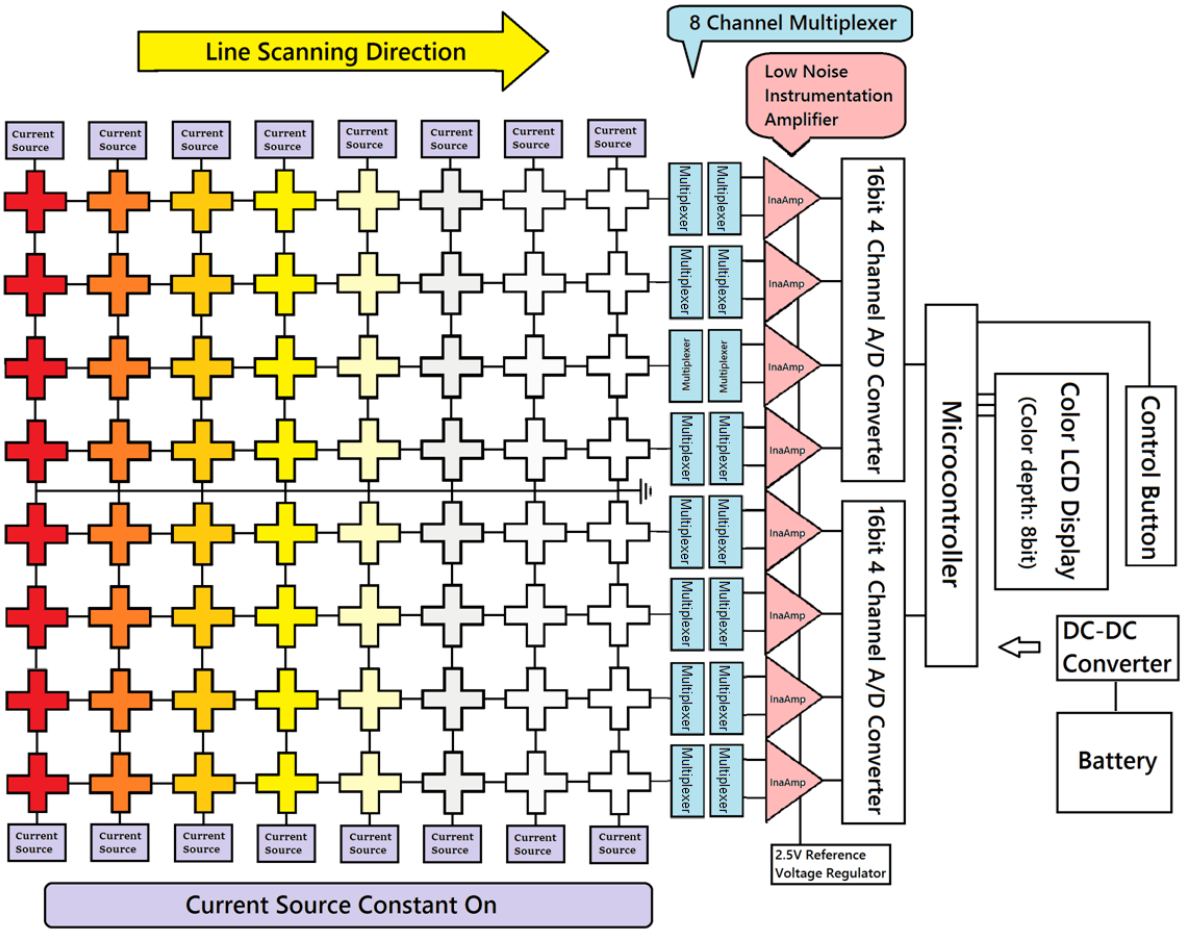

Fig. 7.5 Schematic illustration of the measurement procedures of the 8×8 Quantum Well Hall effect sensor array magnetic field camera. Note that the program control of the scanning process is a left to right cycle.

7.1.3 Quantum Well Hall effect 8 × 8 array magnetic-field camera prototype

A picture of the prototype 8×8 Quantum Well Hall effect sensor array magnetic field camera is shown in figure7.6 (a). This magnetic field camera has dimensions of 140 mm × 270 mm × 25mm. The camera has a resolution of 3.05 μT, and a dynamic range of 66 dB (the minimum and maximum fields measurable are 3.05 μT and 6.25 mT). The real time magnetic field measurement rate is about 13 frame per second (FPS). The measurement spatial resolution is 2.54 point per inch (PPI) in both horizontal and vertical directions.

The characterisation of the 8×8 sensor array is carried out by using a demo board with rectangle and button magnets as shown in Fig. 7.6 (b). From the detection measurement of a rectangular magnet, the shape of the magnet can be identified as a clear rectangular magnetic field image as shown in Fig. 7.6 (c). Fig. 7.6 (d) shows the measurement results of a pair of magnets with opposite polarities. The results indicate that the magnetic field camera can detect both the strength of the magnetic field and the polarity orientation of the measured magnetic field.

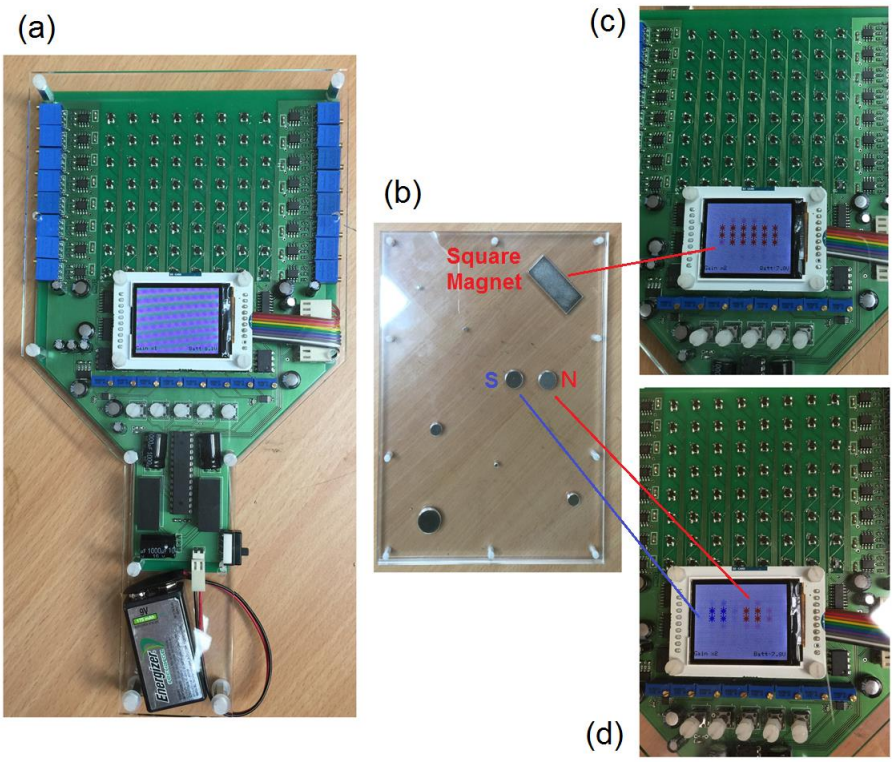

Fig. 7.6 (a) The final product picture, (b) demo board with square and button magnets, (c) magnetic image of square magnet test, and (d) magnetic image of N- and S-poles magnetic tests.

Fig. 7.7 demonstrate the magnetic field camera under different resolution settings. With different resolution settings, the conversion rate between analogue to digital converter reading and the colour depth will change. With different resolution settings, the 8×8 camera can be used to measure both weak and strong magnetic fields to obtain the best measurement graphical results.

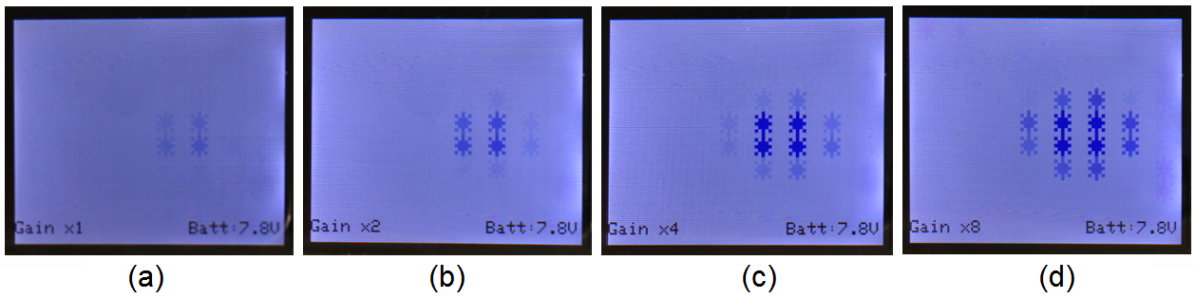

Fig. 7.7 Different resolution settings of the 8×8 Quantum Well Hall effect sensor array magnetic field camera, (a) resolution setting = ×1, (b) resolution setting = ×2, (c) resolution setting = ×4, and (d) resolution setting = ×8.

The 8×8 sensor array magnetic field camera has a reasonable spatial resolution and a good update frame rate which makes it a good choice for detecting strong static magnetic field distributions. It also demonstrates the advantages of real time, high update frame rate 2-dimensional sensor array magnetic field imaging systems for visualisation and continuous graphical measurement results. To increase the spatial resolution and improve the update frame rate, a second version of the magnetic field camera was designed and built which as described in the next section.

7.2 Quantum Well Hall effect real-time 16 × 16 array magnetic-field camera

A second version of the magnetic field camera incorporating 16 × 16 array sensors was subsequently designed and built. This camera has a much higher magnetic field capture frame rate for alternating magnetic field detection purpose (up to 600 capture frames per second maximum). A higher measurement spatial resolution is also achieved by decreasing the pitch between sensors. New digital signal processing functions and different sensor bias techniques were also used in this second version prototype.

7.2.1 Circuit design

Fig. 7.8 shows the block diagram of the real-time 16 × 16 QWHE array magnetic-field camera.

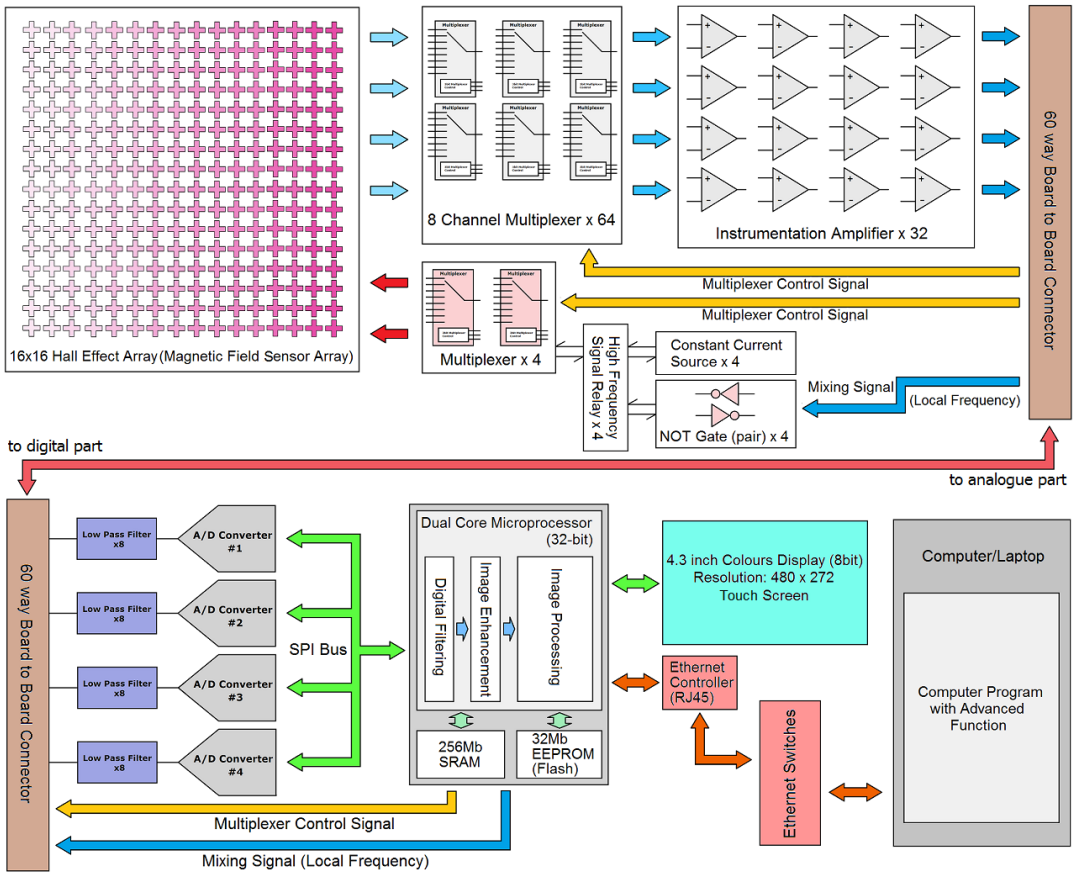

Fig. 7.8 Circuit block diagram of the real-time 16 × 16 Quantum Well Hall effect array magnetic-field camera.

In this design, the analogue and digital circuits sections were separated into two different parts. The separated analogue circuit part was designed as a swappable module. With different analogue circuit modules, different applications can be pursued. One of the analogue module, which was used for the staggered 32 × 2 sensor array magnetic field scanner, has already been described in chapter 5.3. A 60-way board to board connector was used to connect between the analogue modules (daughter boards) and the digital circuit board (motherboard).

An analogue circuit module of the 16 × 16 sensor array with both sensor bias source circuits and amplification circuits was used for the magnetic field camera design. A total of 256 P2A sensors were used to compose the 16 × 16 2-dimensional sensors array. The sensor pitch in both direction is 5 mm, which is half that used for the 8x8 camera. With the sensor array arrangement, a raw measurement spatial resolution of 5 point per inch can be achieved. 32 pairs of the 8-channel analogue signal multiplexers were used to switch between different

sensors to obtain the differential Hall voltage signals. 32 instrumentation amplifiers were used to amplify the differential Hall voltage signals. The differential signals were then converted into single ended signals and the amplified signals are sent to the digital circuit section. To reduce the number of sensor bias sources, eight sensors in each row were connected in series. Four extra pairs of the analogue signal multiplexers were used to select between different sensors rows. Two types of sensor bias sources could be chosen, which were: a pair of NOT gates for the voltage bias method, and a voltage reference constant current source for the current bias method. The orientation of the sensor bias voltage from the NOT gates could be swapped which could be used to supply alternating bias voltages. This alternating bias voltage sources can be used on the superheterodyne technique which will be described in section 7.22.

In the digital circuit section, four 16-bit 8-channel high speed (500 k samples^{-1}) analogue to digital converters (ADC) were used to digitise the signals. The communication between analogue to digital converters and the main microprocessor was maintained at high speed (21 MHz) using an SPI bus. Low pass filters were used between the ADCs and amplification sections to eliminate high frequency noise. Sampled and converted data were collected by a dual core ARM cortex microcontroller with built-in DSP capabilities. A 32 Megabyte Electrically-Erasable Programmable Read-Only Memory (EEPROM) and a 256 Megabyte Static Random-Access Memory (SRAM) were used with the microcontroller for both buffering and data storage. Digital filtering was used to improve signal to noise ratio with user programmable parameters for different requirements. Incoming data was converted to the frequency domain by means of a Fast Fourier Transformation for spectral analysis. The processed data were converted into a two-dimensional Fig. and displayed on a 24 bit RGB LCD display. User interaction was established by means of a capacitive touch pad on the LCD display. For further signal processing purposes, the data was uploaded to a personal computer via a 100 Base-T Ethernet connection.

7.2.1.1 Analogue circuit section

The analogue circuit of the real-time 16 × 16 array is constituted of four identical 8 × 8

QWHE sensor array magnetic field sensing circuit modules. Each 8 × 8 module consists of 64 QWHE sensors, 18 8-channel multiplexers, 8 instrumentation amplifiers and two different sensor bias sources. The schematic of the 8 × 8 module is shown in Fig. 7.9.

The 8 × 8 sensor array had a pitch between each sensor of 5 mm in both horizontal and vertical directions. The signal multiplexers were arranged in pairs to transfer the differential Hall voltage signals from sensors. With 8 pairs of 8-channel Texas Instruments CD4051 CMOS analogue multiplexers being used to select between sensors, the number of the amplifier circuit requirement could be reduced. Eight Texas Instruments INA217 low noise instrumentation amplifiers were used to amplify the differential Hall voltage signals which were converted to single-ended signals. The external voltage reference signals which were applied from the digital circuit section were used to define a midpoint voltage for the amplifier circuits. The amplified signals were transferred to the analogue to digital converters on the digital circuit section through a 60-way board to board connector.

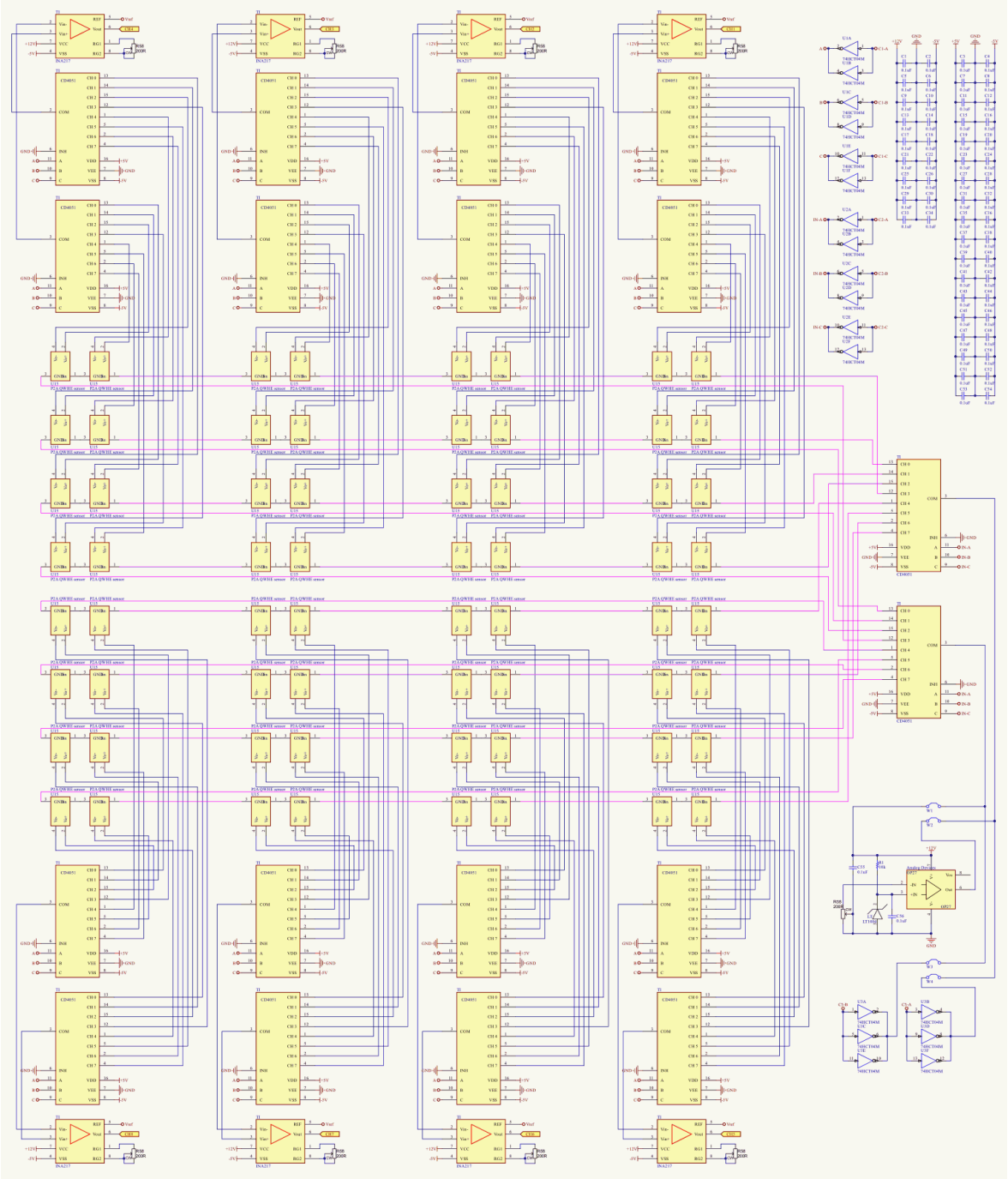

Fig. 7.9 Circuit schematic of a single 8 × 8 Quantum Well Hall effect sensor array magnetic field sensing circuit module. (High resolution version can be found in appendix **03**)

Eight QWHE sensors in each row were connected in series. Two extra CD4051 multiplexers were used to select between different sensor rows for applying sensor bias currents. Two different sensor bias source were connected through jumpers to these two multiplexers. One of the sensor bias source was a voltage source which was based on parallel

connected NOT-gates. The orientation of the voltage bias source could be switched by the microcontroller. By switching the orientation of the voltage bias source, alternating bias voltage could be applied to the QWHE sensors for the superheterodyne technique method. The detail of the superheterodyne technique measurement method will be described in section 7.2.2. The other sensor bias source was a voltage reference constant current source which was based on an Analog Devices OP27 low noise operation amplifier and Linear Technology LT1004 micropower voltage reference. The advantage of using a constant current to bias the QWHE sensors was the ultra-low temperature coefficient behaviour of the sensors.

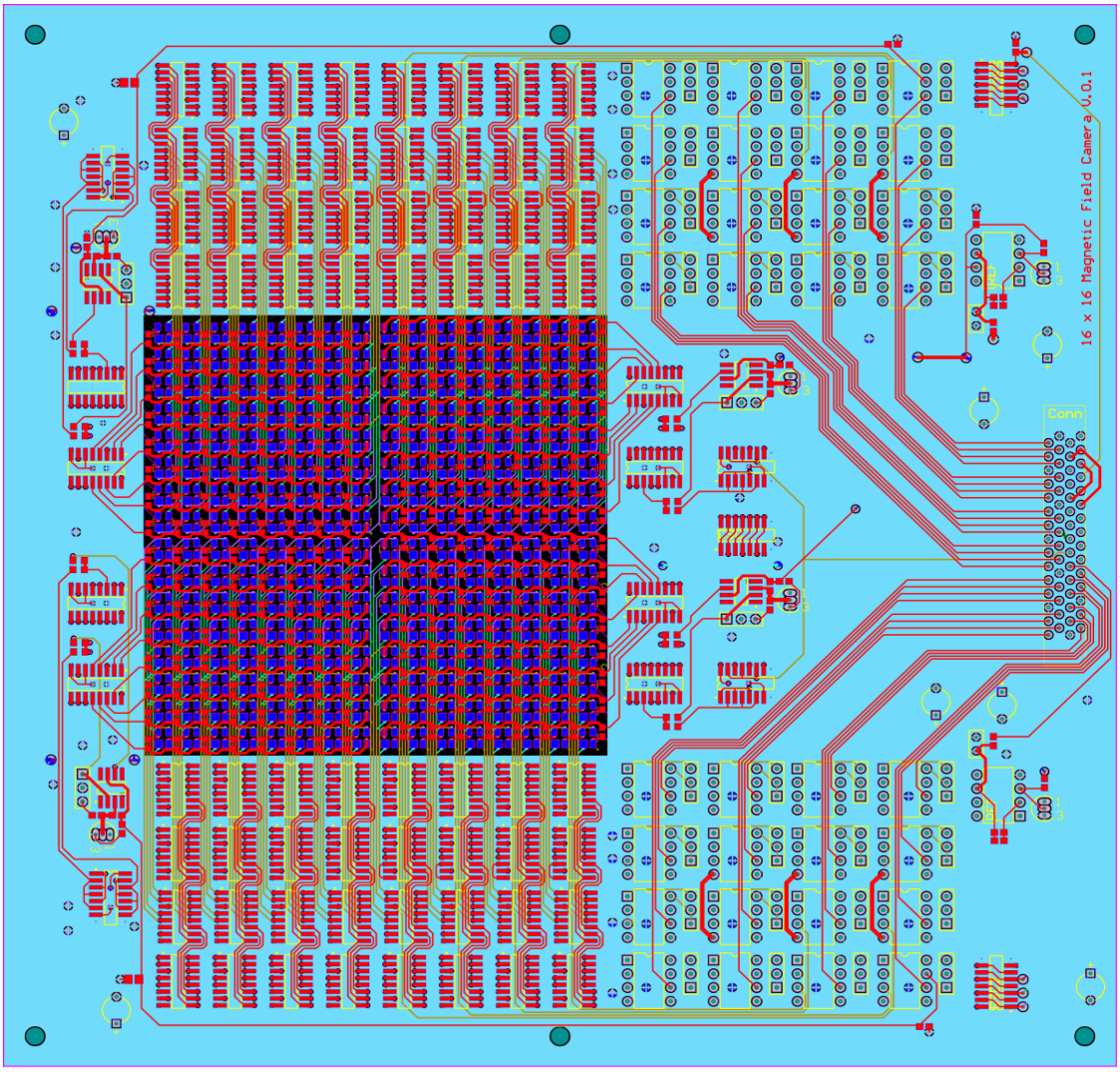

Fig. 7.10 Analogue circuit PCB layout of the real-time 16 × 16 Quantum Well Hall effect array magnetic-field camera.

With the combination of four 8 × 8 module, a 2-dimensional 16 × 16 sensor array

analogue circuit section could be designed. An eight-layer PCB was used to route the traces of the analogue circuits section. The PCB layout of the 16 × 16 array was shown in Fig. 7.10. The PCB has dimensions of 200 mm × 200 mm. The sensitive analogue signal traces are laid on the top five layers, and the digital control signal traces and power traces are located in the mid and bottom layers. A grounded layer is located between the analogue trace layers and digital signal trace layers to reduce electromagnetic interferences. The final analogue circuit PCB is shown in Fig. 7.11. The inset shows the 16×16 QWHE sensor array located in an 80 mm × 80 mm area. The 16 × 16 sensor array is located on the bottom side of the analogue circuit PCB to reduce the stand-off distance.

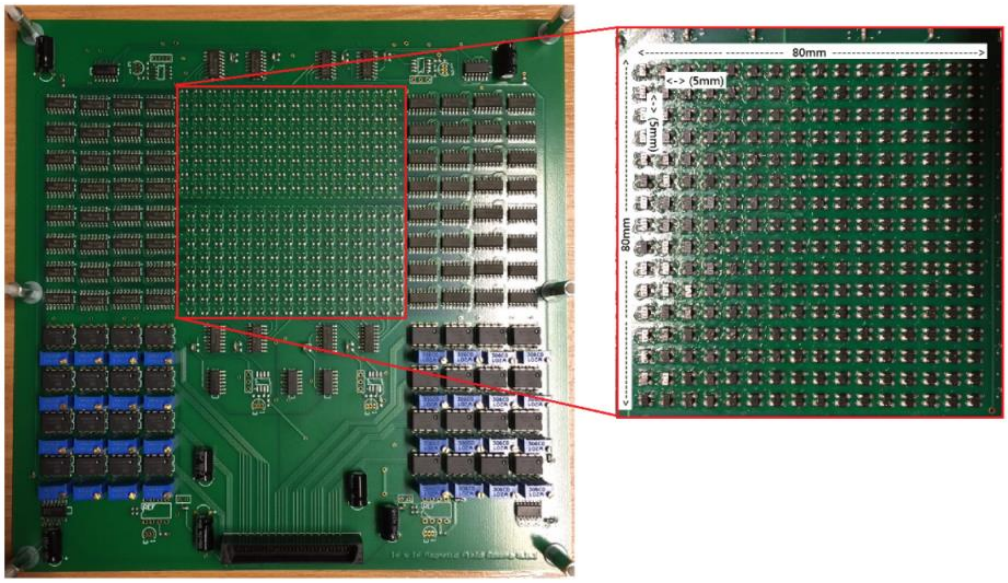

Fig. 7.11 Analogue circuit PCB of the real-time 16 × 16 Quantum Well Hall effect array magnetic-field camera. The inset shows the 2-dimensional 16×16 Quantum Well Hall effect sensor array in an area of 80 mm × 80 mm.

7.2.1.2 Digital circuit section

The digital circuit section of the 16 × 16 array can be separated into four different sections, which are the analogue to digital converter section, microcontroller section, Ethernet transceiver circuit section and additional functions section. The analogue to digital converter section contains the analogue to digital converters, signal buffers and reference voltage circuits. The microcontroller section contains an ARM cortex microcontroller, a synchronous

dynamic random-access memory (SDRAM) and a flash memory. The additional functions of the digital circuit are temperature sensor, notification speaker and liquid crystal display (LCD) with touch screen functions.

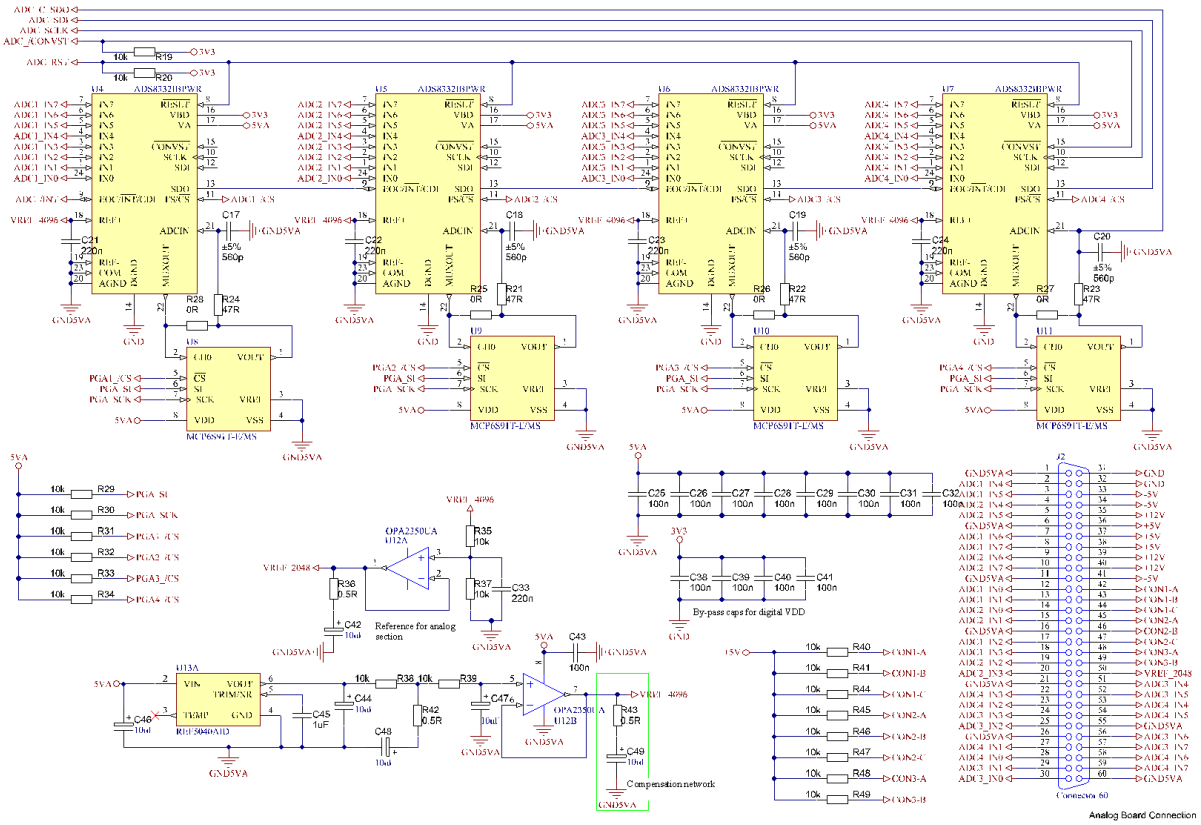

Fig. 7.12 Schematic of the analogue to digital converter section of the real-time 16 × 16 Quantum Well Hall effect array magnetic-field camera. (High resolution version can be found in appendix **04**)

The circuit schematic of the analogue to digital converter section is shown in Fig. 7.12. In this section, four Texas Instruments ADS8332 16-bit 8-channel analogue to digital converters with a sample rate of 500 kilo samples per second (kSPS) are used to convert the amplified Hall voltage signals from the analogue circuits. Four Microchip MCP6S91 rail-to-rail programmable gain amplifiers are used as buffers to supply the analogue to digital converters requirements of input signal current for sampling capacitors. An RC low pass filter circuit is used to restrict the high frequency noise for each analogue to digital converter input. A Texas Instruments REF5040 low noise low drift precision voltage reference is used to apply

the reference voltage to the analogue to digital converters. This precision voltage reference is also used to supply the reference voltage to the instrumentation amplifiers in the analogue circuit section. With the use of high sample rate analogue to digital converters, alternating Hall voltage signals generated from the measured alternating magnetic fields can be captured and digitised. The board to board connector pin layout are also shown in Fig. 7.12.

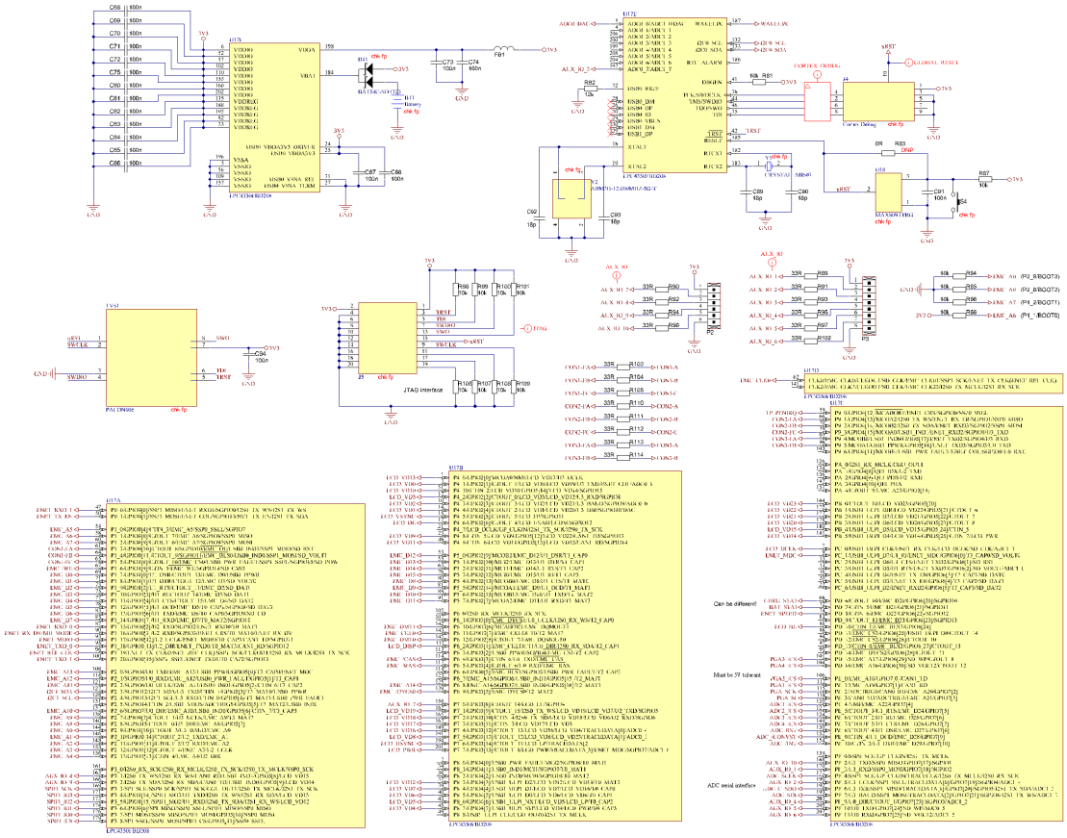

Fig. 7.13 Schematic of the microcontroller section of the real-time 16 × 16 Quantum Well Hall effect array magnetic-field camera. (High resolution version can be found in appendix **05**)

The circuit schematic of the microcontroller section is shown in Fig. 7.13. An NXP LPC 4350FBD208 32-bit Cortex-M4/M0 dual core microcontroller is used to collect and transfer the digitised Hall voltage signals. This microcontroller has a built-in Ethernet controller with Ethernet media access control (MAC) address, and a liquid crystal display (LCD) controller. The Ethernet controller is used to transfer the collected Hall voltage data to a computer program through the 100BASE Ethernet connection. A Joint Test Action Group connector

(JTAG connector) is arranged with the microcontroller for future extension requirements.

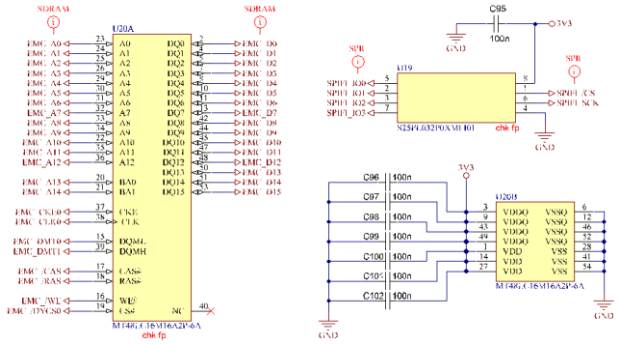

Fig. 7.14 Schematic of the memory unit section of the real-time 16 × 16 array Quantum Well Hall effect magnetic-field camera. (High resolution version can be found in appendix 06)

The microcontroller also has an external memory controller. Asynchronous dynamic random-access memory (SDRAM) and a flash memory are used with the microcontroller. The memory units' connections are shown in Fig. 7.14. The Micron MT48LC16M16A2 single data rate synchronous dynamic random-access memory (SDR SDRAM) which has a memory size of 256 megabit (Mb) is used to temporary store the digitised data collected from the analogue to digital converters. Another Cypress S25FL032P flash memory with 32- megabit (Mb) size is used to store the firmware program.

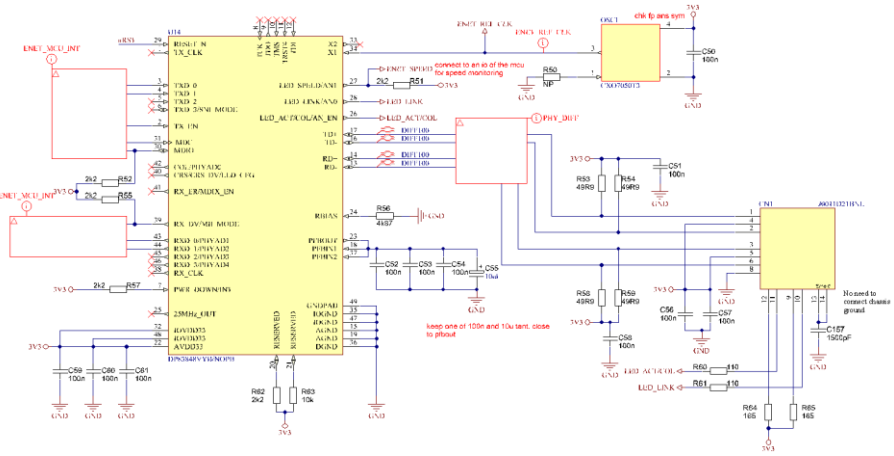

Fig. 7.15 Schematic of the Ethernet transceiver section of the real-time 16 × 16 array Quantum Well Hall effect magnetic-field camera. (High resolution version can be found in appendix **07**)

In the Ethernet transceiver section, a Texas Instruments DP83848 single 10/100 Base Ethernet transceiver is used to communicate between the 16 × 16 array and computers. This is used for transferring and receiving data and control setting commands between computer programs. An oscilloscope is used to supply a reference clock to the Ethernet transceiver. A RJ45 connector is used to connect the Ethernet.

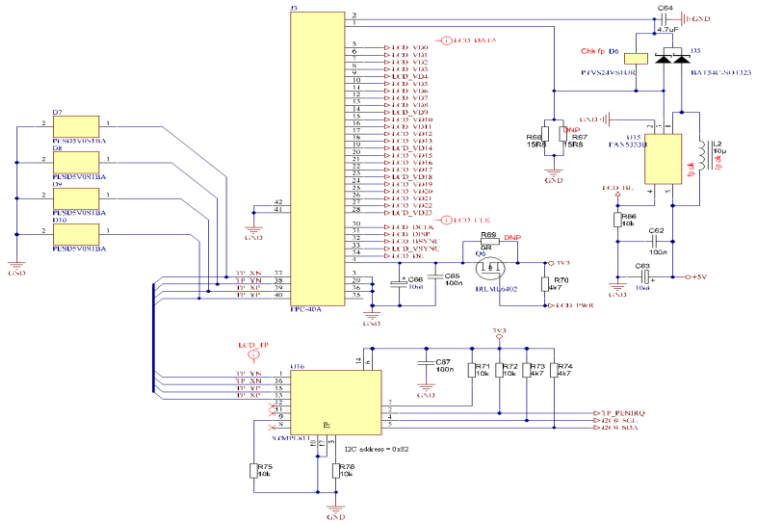

Fig. 7.16 Schematic of the liquid crystal display section of the real-time 16 × 16 array Quantum Well Hall effect magnetic-field camera. (High resolution version can be found in appendix **08**)

A liquid crystal display, a temperature sensor and an audio speaker circuit are included in the additional functionality section. A Kentec K430WQA-V4-F 4.3-inch liquid crystal display (LCD) module with 480 × 272 × RGB dots resolution is used to display the control setting and the status of the 16 × 16 array magnetic-field camera. The schematic of the liquid crystal display section circuit schematic is shown in Fig. 7.16. This LCD module also contains a light-emitting diode (LED) backlit and a resistive touch screen. A Fairchild FAN5333A high efficiency LED driver is used to drive the LED backlit. Another STMicroelectronics STMPE811 advance resistive touch screen controller is used to identify the touch screen operation. The touch screen is used to change the settings of the real-time 16 × 16 array magnetic-field camera.

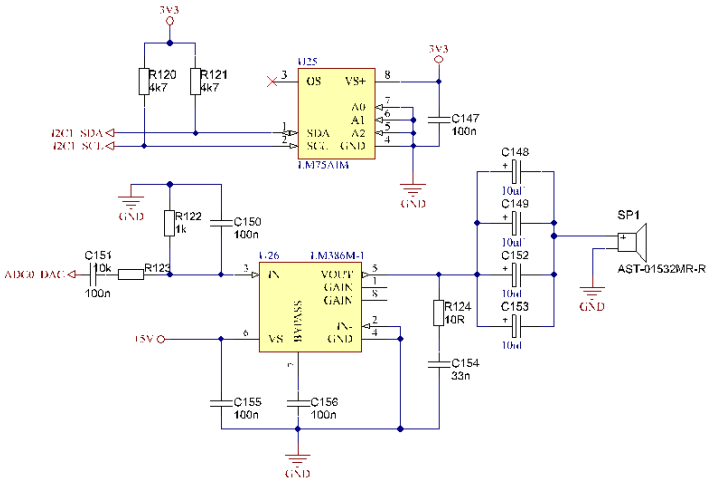

Fig. 7.17 Schematic of the temperature sensor and audio speaker section of the real-time 16 × 16 array Quantum Well Hall effect magnetic-field camera. (High resolution version can be found in appendix **09**)

The schematic of the temperature sensor and the audio speaker circuit is shown in Fig. 7.17. A Texas Instruments LM75A digital temperature sensor is used to monitor the camera temperature for both sensitivity autocorrecting and overheat protection purposes. An audio speaker circuit is used to provide touch screen feedback by playing beep tone when the touch screen is being operated. The beep tone is generated by using a pulse width modulation (PWM) function from the microcontroller. A Texas Instruments LM386 audio power amplifier is used to amplify the PWM signals for speaker driving purpose. The PUI Audio AST-01532MR-R 15 mm speaker is used to generate the beep tone sound.

The PCB layout of the digital circuit and power supply circuit are shown in Fig. 7.18. Four-layer PCB is used to design the PCB layout. In this PCB design, the digital signal traces are routed on the top PCB layer, and the analogue Hall voltage signal traces between board to board connectors and analogue to digital converters are placed on the bottom layer. A ground layer with grounded copper polygon plane and a power layer with power supply copper polygon planes is placed between top and bottom layers to eliminate electromagnetic interferences.

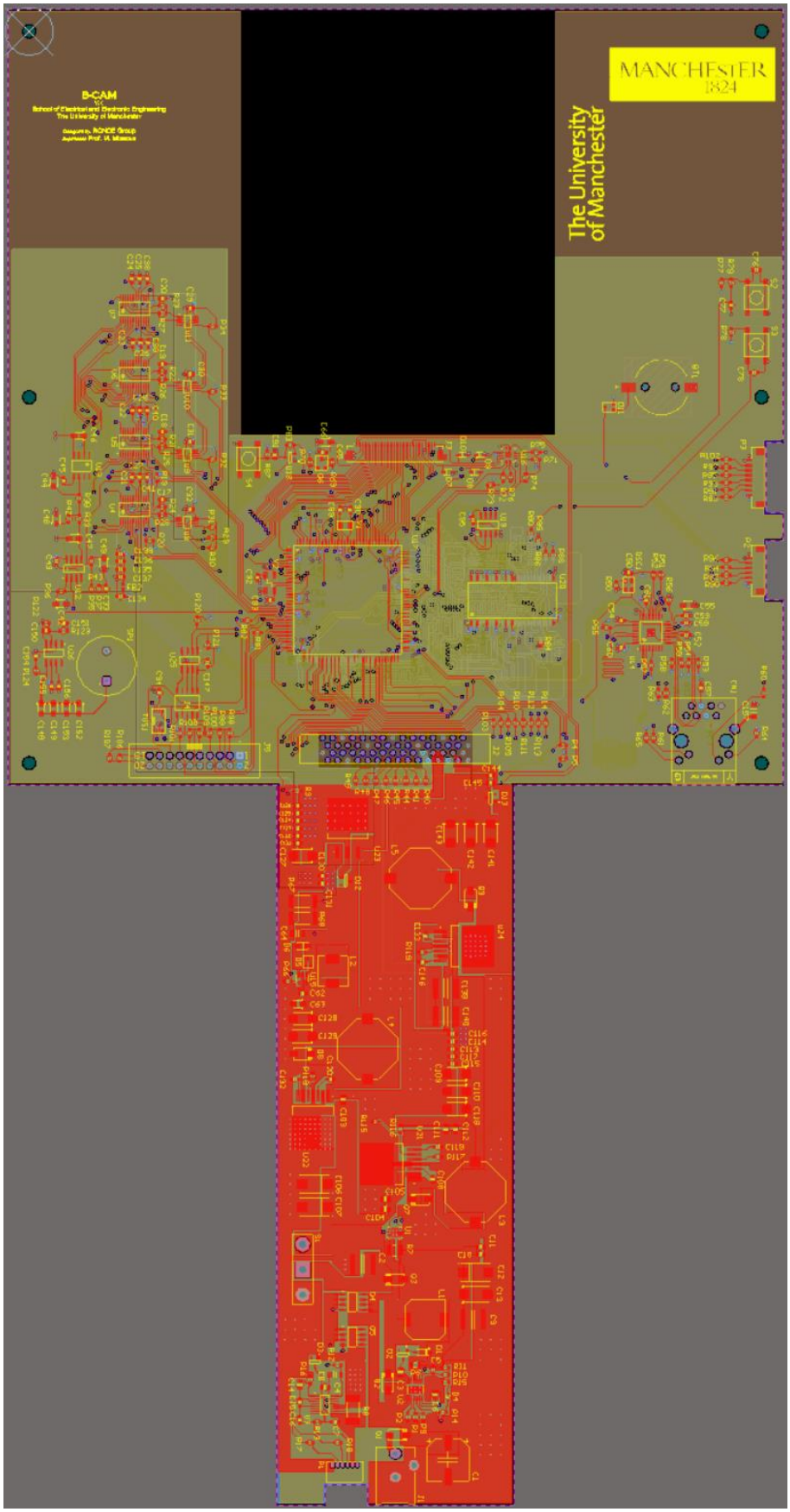

Fig. 7.18 Digital circuit and power supply circuit PCB layout of the real-time 16 × 16 array Quantum Well Hall effect magnetic-field camera.

In Fig. 7.18, a rectangular area (black colour in the figure) is left as a blank with no copper trace and no components. This is due to the fact that the circuit section on the analogue circuit module is the 16 × 16 sensor area which is exactly under this blank rectangular area. With minimum conductive material and components placed in this area, the induced eddy current can be avoided when measuring alternating magnetic fields. The red colour area in Fig. 7.18 is the power supply and battery charging circuits which will be described next.

7.2.1.3 Power supply and battery charging circuits section

The power supply circuit consist of three DC-to-DC converters and a voltage regulator and is shown in Fig. 7.19. Four different voltages, namely +5V, +12V, -12V and +3.3V are supplied to both analogue and digital circuits. Three Texas Instruments LM2673 step down voltage regulators with 3 amps driving capacities are used to supply +5V, +12V and -12V. A Texas Instruments LM1117 linear regulator is used to step down the +5V to +3.3V for the digital circuits.

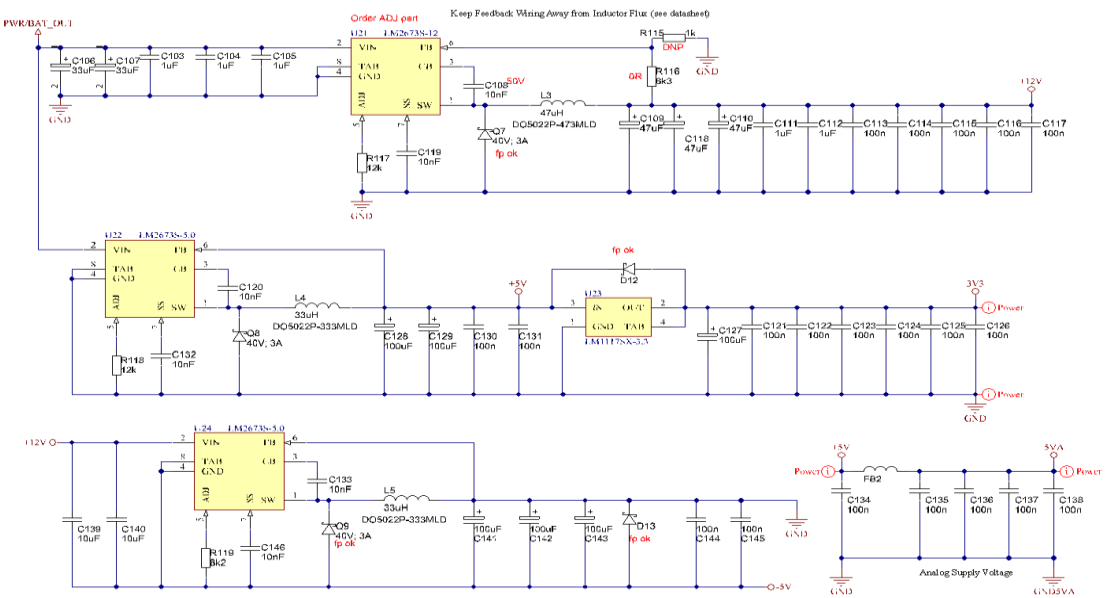

Fig. 7.19 Schematic of the power supply circuit section of the real-time 16 × 16 array Quantum Well Hall effect magnetic-field camera. (High resolution version can be found in appendix **10**)

A set of four 18650 rechargeable lithium-ion battery cells are used to supply the power

for the camera. The lithium-ion batteries are connected in series to supply 14.8V to the power supply circuit. A total of 38.5 watt-hours (Wh) capacities is contained in the battery unit which can provide the magnetic field camera with an autonomous operative time of up to 1.5 hours.

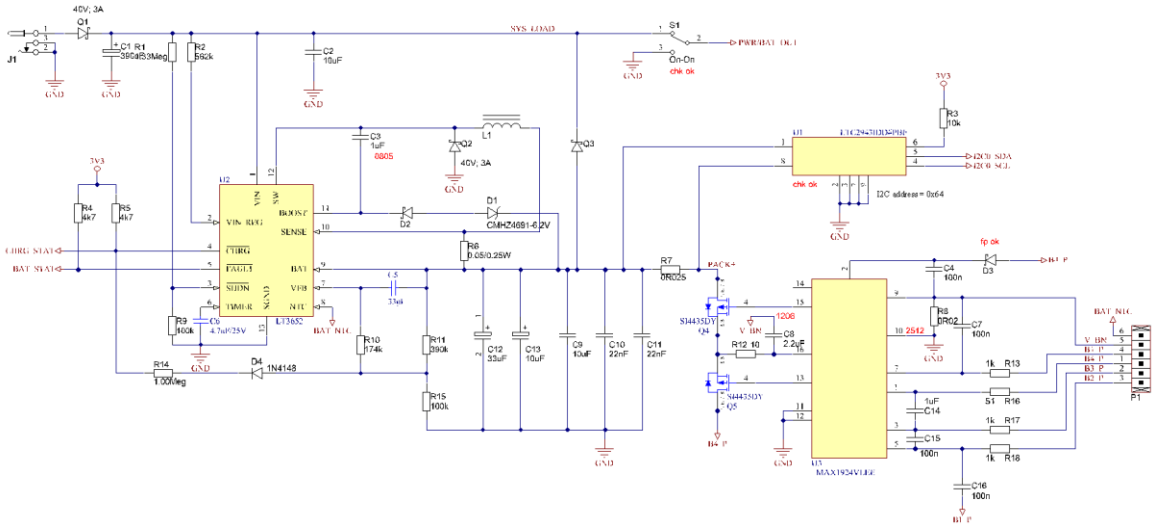

Fig. 7.20 Schematic of the battery charging circuit section of the real-time 16 × 16 array Quantum Well Hall effect magnetic-field camera. (High resolution version can be found in appendix **11**)

To charge the battery cells, a battery charging circuit is designed in the power supply section. The schematic of the battery charging section is shown in Fig. 7.20. A Linear Technology LT3652 battery charger with 2 amps charging capacity is used to charge the 4 cells battery unit. This charger IC has a 5% charge current accuracy, and a 0.5% float voltage reference accuracy which makes it an optimum choice to charge the 4-cells lithium-ion battery units. As the rechargeable lithium battery is very sensitive to both charging and discharging voltages, a Maxim MAX1894 Li+ battery protector is used to protect the 4-cells lithium-ion battery unit. This battery protector has overvoltage and under-voltage protection functions which are both programmable. A Linear Technology LTC2943 multi-cell battery gas gauge is used to measure the charging and discharging capacities. This battery gauge can also monitor the battery temperature to protect against overheat problems.

7.2.2 Sensor excitation using a superheterodyne technique

Different from using a constant voltage or a constant current as the bias source, a new

way is devised to activate the Quantum Well Hall effect sensors biasing as shown in Fig. 7.21. Two gate inverters controlled by two different clock signals are used to bias the QWHE sensors.

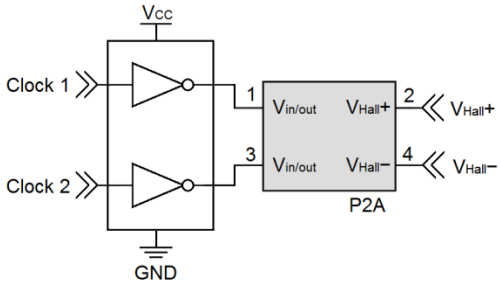

Fig. 7.21 Schematic of two gate inverters as sensor bias voltage source.

In figure7.21, clock 1 and clock 2 are used to control the inverters. When one of the inverters output is high (1) and the other is low (0), the bias voltage is applied to the sensors. By adjusting clock 1 and clock 2, the direction of bias voltage can be controlled. When the direction of bias voltage is changed from 0 to 180 degree, the Hall voltage output will also change from 0 to 180 degree. This gives the circuit the opportunity to shift the detected magnetic field signal from DC or low frequency to a higher frequency. Therefore, the signal to noise ratio can be improved tremendously. The circuit described above can be used as a magnetic field superheterodyne spectrum analyser by using the Quantum Well Hall effect sensors as frequency mixers, where clock 1 and clock 2 function as local oscillators (LO). The AC magnetic field can then be captured at different frequencies.

To reduce $1/f$ noise without using magnetic-field modulation, one can use the superheterodyne technique [68–70]. This technique uses frequency mixing to convert a received signal to a fixed frequency which can be more conveniently processed than the original carrier frequency. In this study, the external magnetic field is detected by the QWHE sensors. This magnetic field is then converted to a Hall voltage by the QWHE sensor. Because the bias voltage changes with the frequency generated by the local oscillator, the Hall voltage will change sign with this local frequency. In this situation, the AC magnetic-field frequency (F_M) will be mixed with the local frequency (F_L). This will generate two middle frequencies

output from the Hall effect sensor (F_H). One is equal to $F_L + F_M$ and the other is equal to $F_L - F_M$. With a suitable band pass filter, digital signal processing can focus on a specific frequency range. When the frequency spectrum is required, the local oscillator can be controlled to generate different local frequency for mixing to do the frequency scanning (F_H). The schematic illustration of the frequency mixing for the superheterodyne technique in this work is shown in Fig. 7.22. In this approach, the QWHE sensors are used as signal mixers. A local oscillator is used as a standard signal generator. The output frequency of the local oscillator can be varied from 100 Hz to several kHz for signal averaging with DC magnetic-field signals.

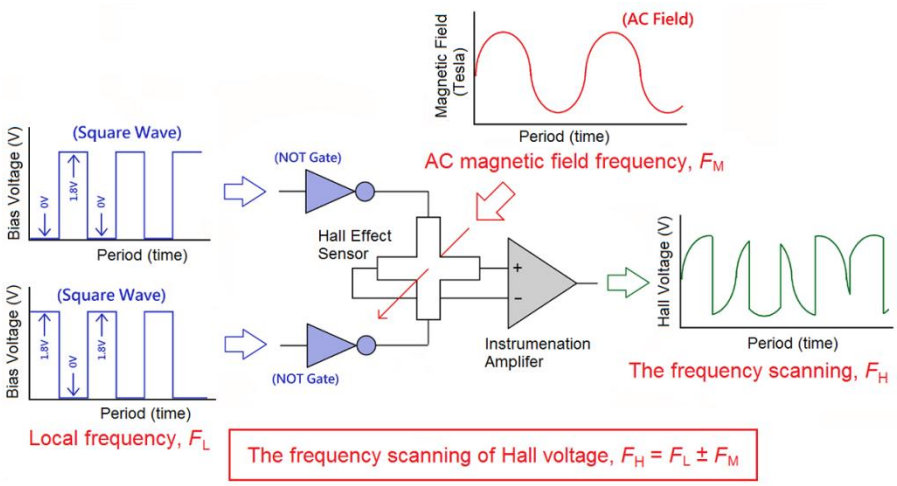

Fig. 7.22 Schematic illustration of the frequency mixing as applied to the Quantum Well Hall effect sensors.

While the heterodyne technique is well known in microwave communication system, and used extensively with Schottky diodes, this is the first time it is applied to QWHE sensors

7.2.3 Firmware design and flowchart

The 16 × 16 array camera uses a microcontroller to automatically record, process and upload the measured magnetic field data. The microcontroller is a 32-bitdual core ARM Cortex-M4/M0 microcontroller which contains serial general-purpose I/O (SGPIO) interfaces, high-speed USB controllers, Ethernet controller with media access control (MAC) address, LCD controller and an external memory controller. An NXP LPCXpresso IDE software is used to program the dual core ARM Cortex-M4/M0 microcontroller. The firmware of the 16 × 16 array camera is written in C language which is then transferred to Low-level programming language through LPCXpresso IDE software. In this design, the main task of the firmware is to collect, combine and upload the Hall voltage data from the 16 × 16 sensor array. The firmware main program flowchart is shown in Fig. 7.23.

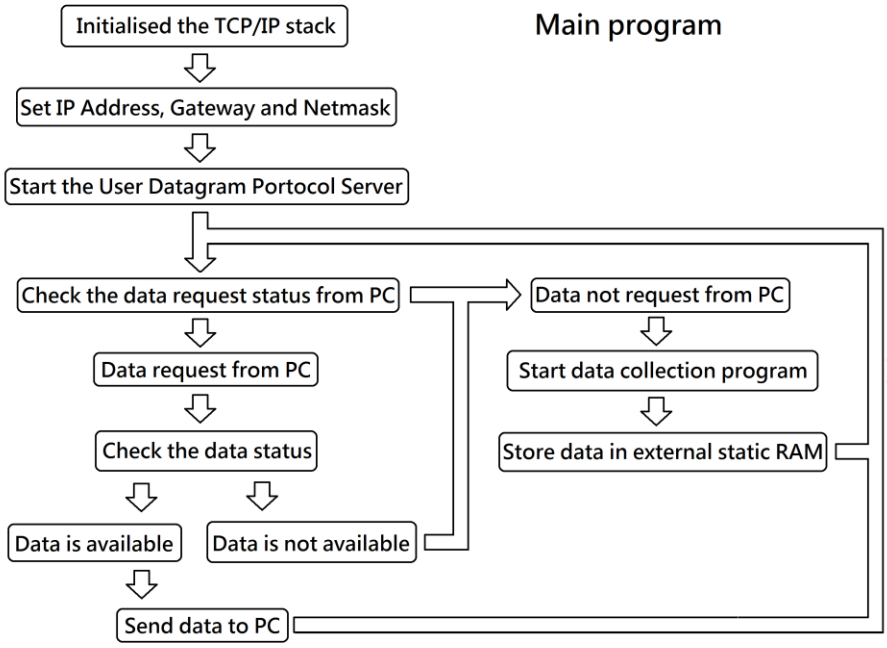

Fig. 7.23 Firmware main program flowchart of the real-time 16 × 16 array Quantum Well Hall effect magnetic-field camera.

The main task of the firmware main program is to communicate between the computer program and the magnetic field camera, and upload the measurement data through an Ethernet connection. By initialising the TCP/IP stack, define IPv4 address and start the user datagram protocol (UDP) server, the Ethernet connection between computer and magnetic field camera

can be connected.

After the Ethernet connection, the program checks the computer requirement. If the computer is not requiring any data, the main program will move to data collecting state. The collected data will then be stored in the external synchronous dynamic random-access memory (SDRAM). If data is required from the computer, the prepared data will be uploaded to the computer through a user datagram protocol (UDP). The uploaded data must be filled up with certain amount of measurement results to 512 megabytes, otherwise the data will not be sent.

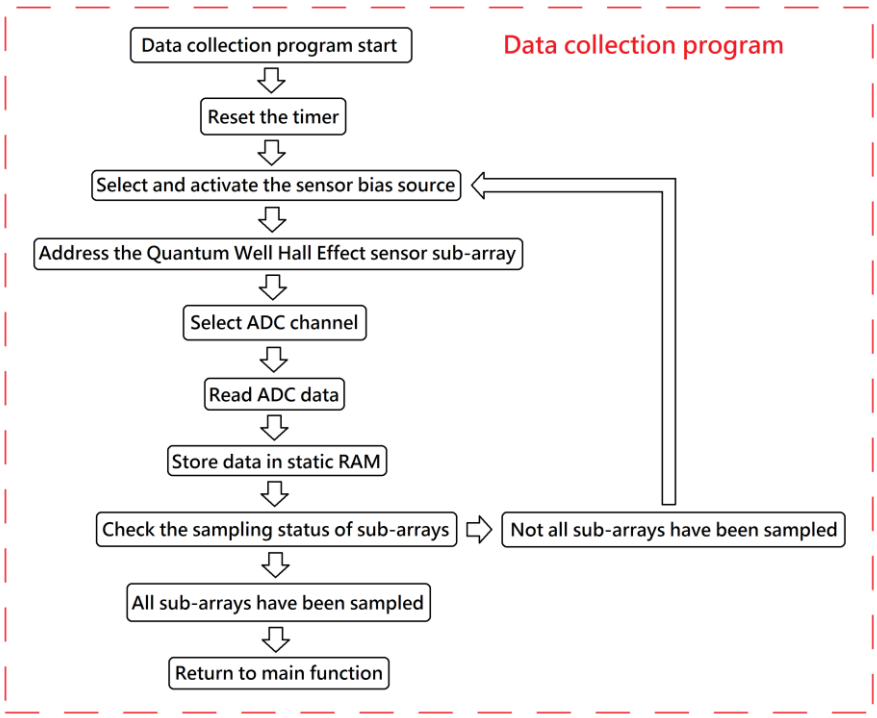

Fig. 7.24 Firmware data collection program flowchart of the real-time 16 × 16 array Quantum Well Hall effect magnetic-field camera.

The data collection program is separated from the main program for data reading and collecting purpose. The data collection program of the firmware is shown in Fig. 7.24. This program will automatically control the multiplexers in the analogue circuit to select between different sensors for digitising and recording the Hall voltage signals. Due to the total number of 32 analogue to digital converter channels being placed on the 16 × 16 array magnetic-field camera, the 16 × 16 sensor array has been divided into eight sub-array for eight cycles of

digitising operations. The digitised data is stored in the microcontroller internal memory temporarily.

User datagram protocol (UDP) is used on the Ethernet connection between the magnetic field camera and computer. The UDP packet structure firmware is shown in Fig. 7.25. The UDP has a higher transmission efficiency compared to transmission control protocol (TCP). However, the reliability of UDP is not as good as that of TCP. In the 16 × 16 array, the transmission efficiency is very crucial for alternating magnetic field measurements, and there is some tolerance for the transmission accuracy. From these reasons, the UDP is more suitable for the real-time 16 × 16 array magnetic-field camera.

Ipv4 Header									
20 Byte									
Version (4 Bit) + IHL (4 Bit)	DSCP (6 Bit) + ECN (2 Bit)	Total Length	Identification	Flags (3 Bit) + Fragment Offset (13 Bit)	Time To Live	Portocol	Header Checksum	Source IPv4 Address	Destination IPv4 Address
1 Byte	1 Byte	2 Byte	2 Byte	2 Byte	1 Byte	1 Byte	2 Byte	4 Byte	4 Byte

Ipv4 Pseudo Header					UDP Header				Data
12 Byte					8 Byte				512 Byte
Source IPv4 Address	Destination IPv4 Address	Zeroes	Portocol	UDP Length	Source Port	Destination Port	Length	Checksum	Data
4 Byte	4 Byte	1 Byte	1 Byte	2 Byte	2 Byte	2 Byte	2 Byte	2 Byte	512 Byte

Fig. 7.25 Packet structure of the user datagram protocol (UDP) data under IPv4 for the real-time 16 × 16 array Quantum Well Hall effect magnetic-field camera.

7.2.4 MATLAB based computer software for Quantum Well Hall effect real-time 16 × 16 array magnetic-field camera.

To process the measurement data and convert the measurement results into 2-dimensional graphical results with colour depth representing magnetic field strength and polarity, a computer program based on MATLAB was developed for the real-time 16 × 16 array camera. The graphical user interface (GUI) of this program is shown in Fig. 7.26. The Ethernet connection between the program and the magnetic field camera can be setup by defining the camera IP address and communication port. Before any signal processing, the captured 14-bit unsigned ADC reading is converted into a 13-bit signed data with different sign representing the magnetic field polarity. This program consists of three main functions

which are static magnetic field measurement function, alternating magnetic field measurement function and single QWHE sensor cell Fast Fourier transform (FFT) spectrum analysis function. An extra programmable signal filter function can be used to eliminate unwanted frequency signals. This programmable signal filter can be set as a high pass, low pass or band pass filter.

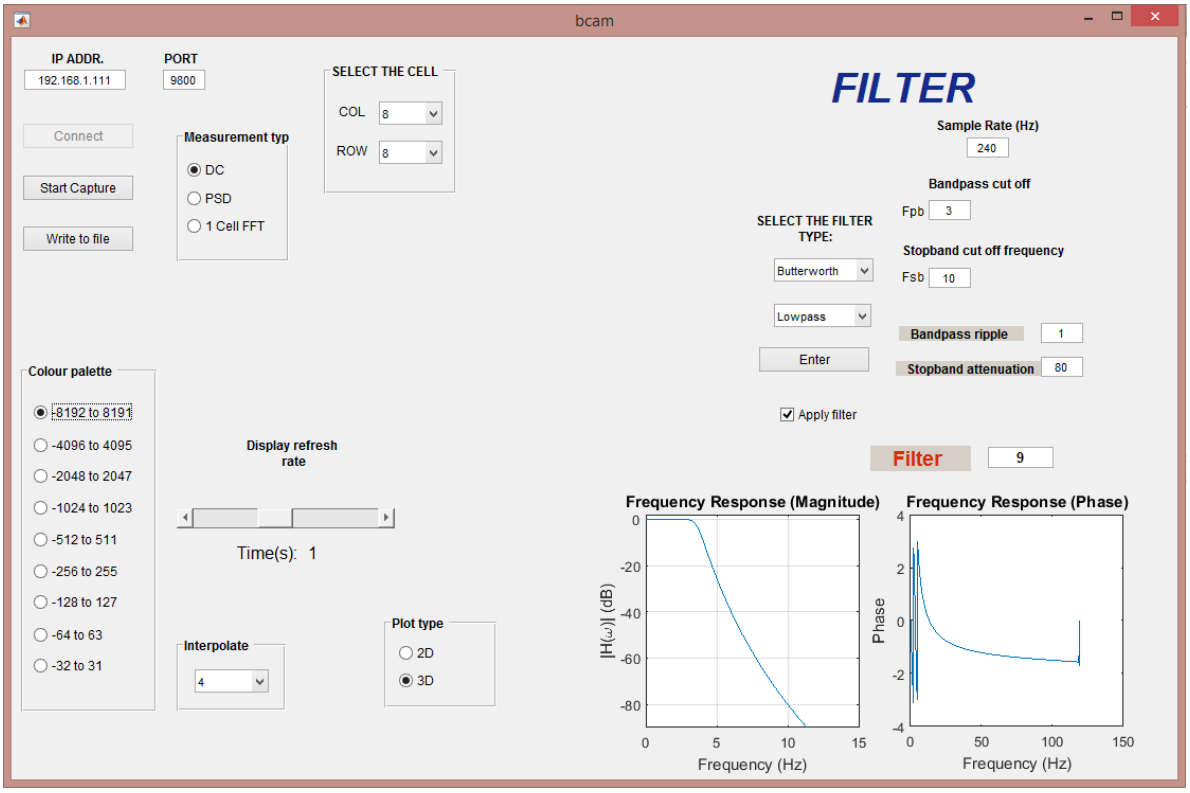

Fig. 7.26 Graphical user interface of the computer program for the real-time 16 × 16 array Quantum Well Hall effect magnetic-field camera.

In the static magnetic field measurement function, an average is taken from the captured Hall voltage signal data based on the display refresh rate setting. The average data is then converted into a 2-dimensional graphical result with colour depth representing the measured magnetic field strength with blue and red colours representing the measured magnetic field polarities. The colour palette absolutely-red and absolutely-blue corresponding to ADC reading can be set to change the conversion ratio between measured data and the colour depth on the 2-dimensional graphical results.

In the alternating magnetic field measurement function, the spectral power is computed

for the last 256 samples. For calculations, the following equation is used:

$$P = \lim_{T \to \infty} \frac{1}{2T} \int_{-T}^{+T} \left| x(t) \right|^2 dt \tag{7.1}$$

where $x(t)$ is the signal, T is the period of sampling and P is the power of the signal, respectively. The measurement data is stored inside a 3 dimensional FIFO (first in/first out) buffer. For each QWHE sensor ADC reading, the last 256 samples stored in the FIFO buffer are used in the calculations; their Fourier components are calculated and then squared, and hence the power of each component is calculated. The power of the signal is then used to convert to 2-dimensional graphical results with colour depths representing the measured magnetic field strengths.

From the single sensor cell Fast Fourier transform (FFT) spectrum analysis function, the measured magnetic field frequency spectrum can be obtained by using the Fast Fourier transformation with the captured data from the selected sensor cell. This frequency spectrum can be used to analyse the measures magnetic field alternating frequency composition.

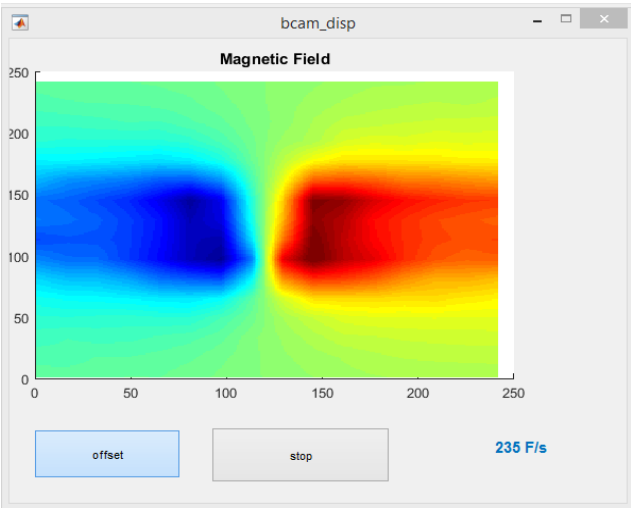

Fig. 7.27 Real-time 16 × 16 array Quantum Well Hall effect magnetic-field camera computer program sub-window for displaying measured graphical results.

The 2-dimensional graphical results are displayed in a sub-window of the program which is shown in Fig. 7.27. A software auto zero is used to cancel the offset voltage from each of the 256 sensors in the array. A bilinear interpolation [67] is used to produce a reasonably

realistic magnetic image, with a spatial resolution of 40.6 point per inch (PPI) with 128 × 128 = 16384 pixels in a detection area of 80 mm × 80 mm.

7.2.5 Quantum Well Hall effect real-time 16 × 16 array magnetic-field camera prototype

The real-time 16 × 16 array magnetic-field camera prototype physical structure schematic is shown in Fig. 7.28. This prototype physical structure consists of two acrylic covers, a liquid crystal display with touch screen functions, four 18650 Lithium-ion battery, a battery container PCB, an analogue circuit PCB module and a digital circuit board with power supply unit. A 4.3 inch 16.7 M colour resistive touch screen LCD display is placed on the top of an acrylic cover layer. The second layer consists of the main digital circuit and power regulating circuits. A third layer contains the architecture of the 16×16 QWHE sensor array analogue circuit. Rechargeable lithium batteries are placed on the handle part with the final layer being the bottom acrylic cover.

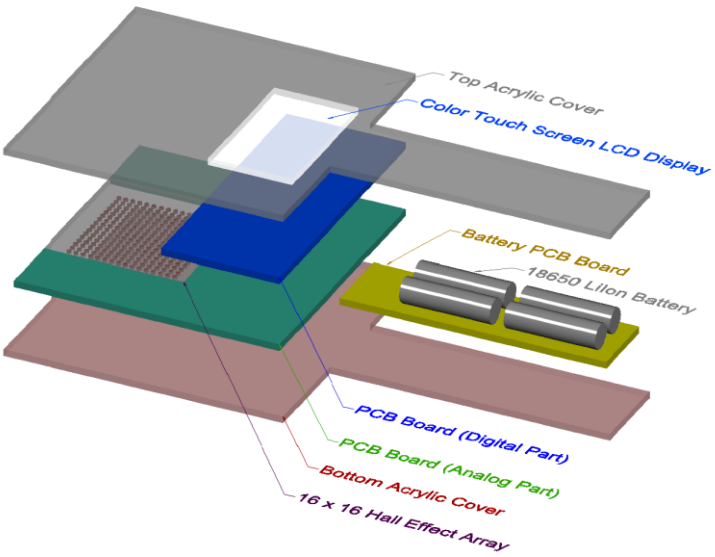

Fig. 7.28 The schematic of the physical structure of the real-time 16 × 16 array Quantum Well Hall effect magnetic-field camera.

The 16 × 16 array camera prototype is shown in figure. 7.29. The prototype has dimensions of 400 mm × 225 mm × 52 mm. The 16 × 16 sensor array was designed to reduce

the stand-off distance between sensors and testing objects as shown in Fig. 7.29 (b). A 1.5 mm thick acrylic cover was used to protect the sensor array. The touch screen liquid crystal display is used to display the status and to change the setting of the magnetic field camera. Two 40 mm × 40 mm fan are used to produce airflow for device cooling purpose. An RJ45 socket is placed on the side for Ethernet connection. The real-time 16 × 16 array camera prototype can be operated with both built in battery unit and external DC jack power input. The prototype was designed as a handheld device with a handle shape battery section.

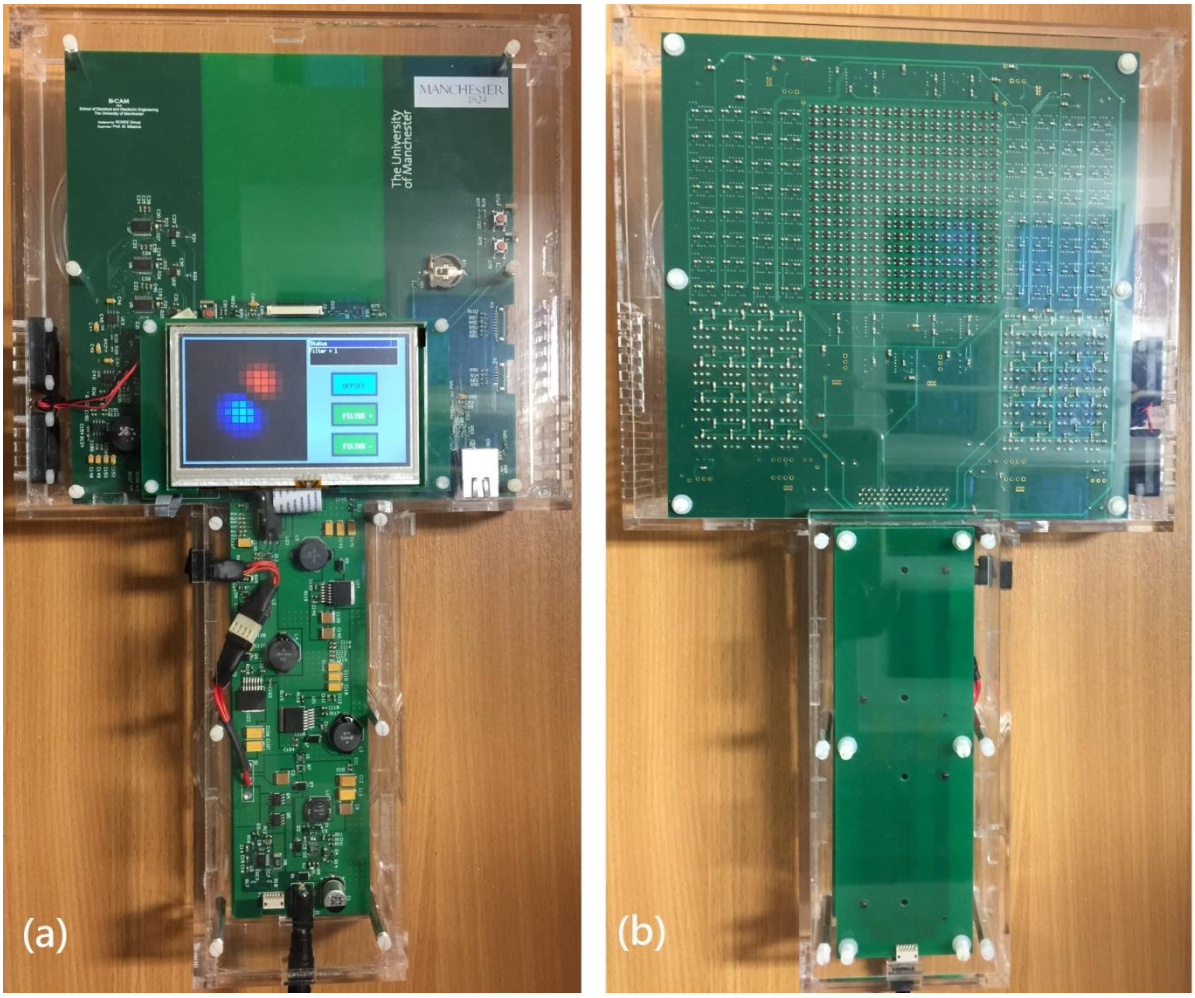

Fig. 7.29 Picture of the real-time 16 × 16 array Quantum Well Hall effect magnetic-field camera with a touch screen LCD display: (a) top view and (b) bottom view.

For the particular QWHE sensor (P2A) used, the voltage sensitivity after amplification is 138.6 mV/mT at 0.815 mA sensor bias current (the amplifier gain is set to 1000). In the digitised section, 14-bit data are obtained from each analogue to digital converter. The

minimum detectable magnetic field (B_{min}, which is same as the maximum sensitivity) for each ADC reading at a bias current of 0.815 mA can be calculated as follows:

$$B_{min} = \frac{\text{ADC reference voltage}}{\text{14-bit ADC reading} \times \text{circuit sensitivity}} = \frac{4.096\ \text{V}}{16384\ \text{pixel} \times 138.6(\frac{\text{mV}}{\text{mT}})} = 1.8\mu\text{T pixel}^{-1} \quad (7.2)$$

The maximum detectable field is 29.5 mT giving the device a dynamic range of 84 dB.

7.2.5.1 Calibration and characterisation

A Helmholtz coil was fabricated for calibration purposes as described previously. The Helmholtz coils has 51 turns in each loop (N = 51) with a radius of the coils (R) and diameter distance between two coils (L) being 200 mm. The calibration results of DC magnetic fields generated by the Helmholtz coil are listed in Table 7.1. The absolute relative error between measured and calculated values is reasonably low but also decreases with increasing input operation voltage, these can be caused by noise effects from the circuits. Thus, the calibration results of the 16×16 QWHE sensors array magnetometer shows that the device can be used to detect in the micro-Tesla range magnetic field with an absolute error lower than 3 %.

Table 7.1 Summary of the DC calibration results.

Coil voltage (V)	Coil current(mA)	Calculated B (μT)	Measured B (μT)	Absolute relative error (%)
0.5	61.7	14.1	13.7	2.8
2	246.6	56.5	55.7	1.4
4	493.2	113.0	114.7	1.5
8	986.4	225.9	223.24	1.2

7.3 Conclusion

In this chapter, two magnetic field camera prototype were designed and built.

The first prototype was an 8 × 8 sensor array. This prototype has capabilities for measuring static magnetic field strength in 2-dimensional plane with minimum and maximum detection limits of 3.05 μT and 6.25 mT giving it a 66dB dynamic range. Both magnetic field

strength and polarity can be measured. Measurement of different shapes of magnet with different magnets magnetic field strength, polarity and shape could all be successfully identified.

A second higher spatial resolution prototype consisting of a real-time 16 × 16 array was also designed and built. With the used of interpolation techniques, a spatial resolution of 40.6 point per inch (PPI) could be achieved with this magnetic field camera. With the invertible orientation sensor-bias source, this magnetic field camera can be operated with a superheterodyne technique to avoid flicker noise for better signal to noise ratio. The minimum and maximum detectable magnetic field for this magnetic field camera are 1.8 μT and 29.5 mT giving a dynamic range of 84 dB. A MATLAB based computer program was developed for processing and displaying the measurement results of both static magnetic field and alternating magnetic field.

The 2-dimensional sensor array based magnetic field cameras can provide real-time measurement results without the need for multi-position setup mechanisms. The 2-dimensional graphical results can provide continuous magnetic field distribution results with any discontinuity readily identified. The experimental measurements of the real-time 16 × 16 array magnetic-field camera and its applications in both DC and AC magnetic field, non-destructive testing are described in the following chapter.

Chapter 8
Magnetovision systems based on Quantum Well Hall effect real-time 16 × 16 array magnetic-field camera

Magnetovision is a measurement method to visualise the magnetic flux or the change of the magnetic flux density. This type of system usually contains a magnetometer, a multi-position setup mechanism and a magnetic field generation source. Most of the existing magnetovision systems use multi-position setup mechanisms to measure the magnetic flux density distribution in both 2- and 3-dimensional space. However, this type of camera is not a real-time analysis system, and can only be used in static magnetic field situations. A great deal of time is also required for the mechanical scanning for full data acquisition.

To overcome these drawback, a real time magnetic field camera based on a 16 × 16 Quantum Well Hall effect sensor array is designed and built. This magnetic field camera uses a 2-dimensional 16 × 16 sensor array to capture the magnetic flux distribution information in 2-dimensional space. With a combination of different magnetic field biasing methods, magnetovision systems for specific applications can be developed.

In this research, the real-time 16 × 16 array magnetic-field camera prototype was mainly developed to be used in the electromagnetic method of non-destructive testing (NDT). The main magnetic field biasing methods in electromagnetic NDT are:

1. Neodymium magnets and electromagnets for static magnetic field biasing in magnetic flux leakage testing (MFL) and magnetic particle inspection (MPI) methods.
2. Search coils and electromagnets for alternating magnetic field biasing in eddy current testing (ECT) and alternating current field measurement (ACFM).
3. Direct current and alternating current for electromagnetic field biasing in magnetic particle inspection (MPI).

8.1 Review of current magnetic vision system technique

The method of magnetic imaging is a useful technique to determine the distribution of magnetic fields where they reflect the conditions of a material. Turnanski and Stabrowski [71] used a giant magnetoresistive (GMR) probe with eight Permalloy sensors to analysis the magnetic field distributions at the surface of electrical steel sheets. The results were presented in the form of a contour map on a visual display unit. Lo et al. [71] developed a magnetic imaging system for non-destructive evaluation of structural and mechanical conditions of materials. This system used magnetic hysteresis and Barkhausen effect to measure magnetic properties while scanning the surface of a material, and converting the data into an image to show variations in the material conditions from one location to another. Tumanski and Baranowski [72] designed an anisotropic magnetoresistance (AMR) sensor array for investigation of the magnetic field distribution during testing of electrical steel strip magnetised by a magnetising winding.

A magnetovision system can directly display magnetic field distributions in the form of colour maps without converting the data into an image [73]. Baudouin et al. [74] used a magnetovision method to test non-oriented steels after tensile deformation. Other applications of this system are in non-destructive testing (NDT) of materials or in the experimental determination of magnetic field distribution. Tumanskiy and Stabrowski [75] used a magnetovision system to provide a versatile tool for non-destructive quality control and for the determination of the structural uniformity of electrical steel. Tumanski and Liszka [76] demonstrated a magnetovision system using a linear eight-sensor array module, robotic scanning mechanisms and a software numerical method for image reconstruction. Nowicki and Szewczyk [20] designed and built an XY scanning system with a tri-axial magnetoresistive sensor (Honeywell HMR2300) for detection of contraband ferromagnetic objects. Their system's ability for passive detection of hidden or buried contraband objects and the determination of their location was demonstrated.

Magnetic sensor arrays are very convenient for rapid magnetic imaging. However, in

comparison with light sensors, magnetic sensor arrays are still rarely used [42]. The most commonly used magnetic field sensors in NDT are induction coils, magnetodiodes, fluxgates, GMR, AMR and Hall effect sensors. As each different NDT method relies on different types of magnetic field sensors, the detection limits are thus set by the limitations of each particular sensor. Among all magnetic field sensors, Quantum Well Hall effect (QWHE) sensors fulfil the requirements of high magnetic sensitivity and reliability, low power consumption and small dimensions, large signal-to-noise ratios and low temperature dependence, together with reduced process and cost [42, 61]. Hall effect sensors have found increasing usage in the fields of automation, medical treatment and detection [77, 78].

In this work, a prototype handheld real-time magnetic field camera was developed by using 16×16 2-dimensional QWHE sensor array. A software with a bilinear interpolation [67] method was used to produce a reasonably realistic magnetic image, resulting in a high spatial resolution of 40.6 ppi. By using a superheterodyne technique, magnetic fields in the ranges of nano to micro Tesla can be detected for alternating and static magnetic field operations respectively. The system can be used in multiple sampling measurements enhancing the signal to noise ratios and for use in real time measurements for fast scan speed requirements. In the following section, the real-time 16 × 16 array magnetic-field camera is used with different magnetic field biasing methods to demonstrate improved electromagnetic non-destructive testing.

8.2 Static magnetic-field measurements

Static magnetic field non-destructive testing methods is widely used in the industry to detect material or structure defects. This testing methods usually contain a static magnetic field biasing source which can be a strong neodymium magnets, an electromagnets or a direct current biasing source. One of the most commonly used method is the magnetic flux leakage (MFL) testing. This electromagnetic method relies on strong magnets or electromagnets for applying the bias magnetic flux through the objects under tests. The magnetic flux leaks out from a non-continuous defective region such as crack and imprint defects. This magnetic flux

leaking signal can be detected by a search coil or a magnetic field sensor. The other commonly method is direct contact current injection magnetic particle inspection (MPI). By applying a low voltage, a high direct current can be generated through the objects under test, an electric field combined with a magnetic field are generated in the samples. When the magnetic field passes through a non-continuous, defective region, the magnetic flux will leak out from the sample, attracting magnetic particle in suspensions to decorate the defects.

In both situation, search coil and magnetic particle are the main methods to detect the changes of the magnetic field. Compare to these two methods, QWHE sensor have the advantages of higher sensitivity for static magnetic field, ease of operation and ease of digitisation of the measured data and reusability.

8.2.1 Static magnetic field magnetic flux leakage (MFL) testing

In static magnetic flux leakage testing, permanent magnets are usually used to supply the bias magnetic flux. Both search coils and magnetic field sensor can be used to detect the change of magnetic field strength caused by the magnetic flux leaking out from non-continuous defective region. However, as search coils cannot detect static magnetic field, a continuously rotating and moving mechanism is required for the search coil magnetic flux leakage testing methods. The sensitivity of a search coil depends on both covering area and number of turns which is not suitable for high spatial resolution inspection, limiting it to defects that are greater than 1 mm in most instances. The Quantum Well Hall effect sensor has ultra-high sensitivity in both static and alternating magnetic field and very small size (in the micron size) making it an optimum choice to replace the search coils in magnetic flux leakage testing. The 16 × 16 array magnetic-field camera developed here for static magnetic field magnetic flux leakage testing can improve the measurement spatial resolution. Complicated rotating and moving mechanism can also be avoided. The 2-dimensional graphical results of the magnetic field camera can provide accurate and clear information compared to traditional measurement methods.

In this study, two magnetic flux leakage sample were inspected with the Quantum Well Hall effect real-time 16 × 16 array magnetic-field camera and are described in the following section.

8.2.1.1 430 stainless steel sample

To test the performance of the 16 × 16 array camera, two 430 stainless steel plates with dimensions of 250 mm × 90 mm × 19.2 mm were prepared for magnetic flux leakage measurements as shown in Fig. 8.1. Additionally, a single sensor Quantum Well Hall effect magnetometer was used to manually scan over the sample surface for comparison purposes. The upper stainless steel plate is designed to simulate a defect by cutting out a hole of size 15 mm × 10 mm × 9.2 mm located in the middle of the top surface. The lower stainless steel plate is used as the field sink plate. A coordinate system and reticular scale on the sample are shown in figure8.1 (c). Figs. 8.1 (a) and (b) depicts the 3D and cross section schematic images of this test sample with defect for magnetic flux leakage testing. 8 neodymium magnet cylinder bars with magnetic strength of 460 mT were used to provide the bias magnetic flux through the test sample.

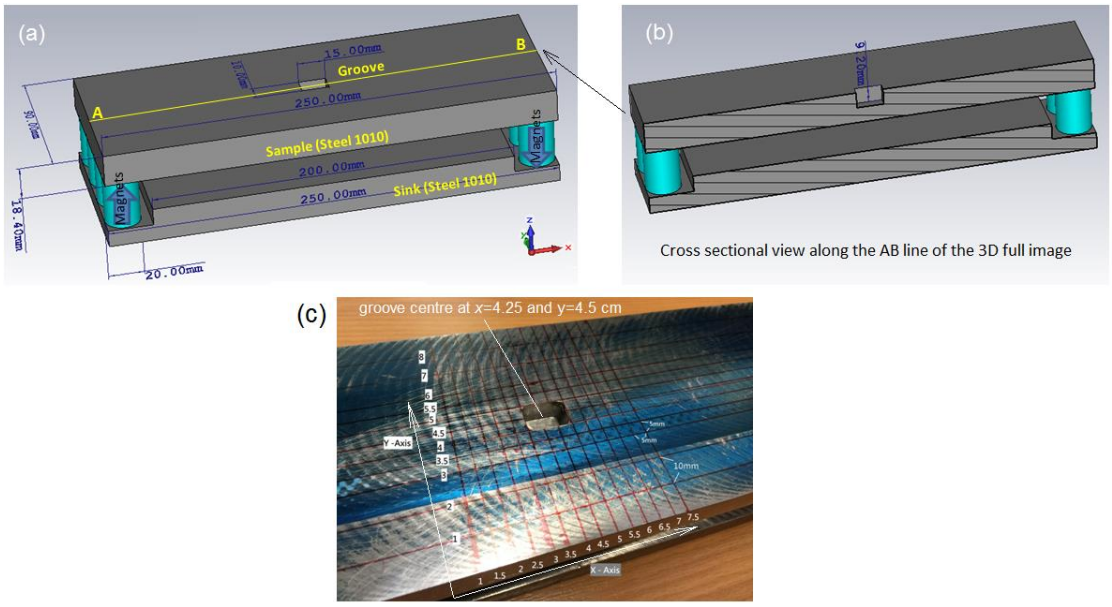

Fig. 8.1 Schematic illustration of (a) full 3D and (b) cross section schematic images of the test work piece with defect for MFL testing, (c) the coordinate system and reticular scale on the test sample with a groove. The centre of the groove is situated at 4.25 cm along the *x*-axis.

The experimental mapping results of the single QWHE sensor magnetometer and the measured graphical result of the 16 × 16 array camera are shown in Fig. 8.2 (a) and (b) respectively. Figure8.2 (c) and (d) are the corresponding 3-dimensional magnetic field strength images. It is clear from both measurement results that the magnetometer manual mapping experimental results and the magnetic field camera measurement results are very similar. This validate the measurement reliability of the magnetic field camera. The measured magnetic field strengths for the single sensor mapping are larger than those for the magnetic field camera. This is mainly because of the small difference in stand-off distances and misalignment of the two measurements. The stand-off distances are 2.2 mm for the single sensor magnetometer and 4.3 mm for the 16 × 16 array camera. Note that Fig. 8.2 (b) is the real image acquired during testing (real time image) while Fig. 8.2 (a) is a plotted graph using an excel program with the scanned experimental data. The acquisition time was more than 2 hours for the manually scanned image compared with less than a second for the magnetic field camera!

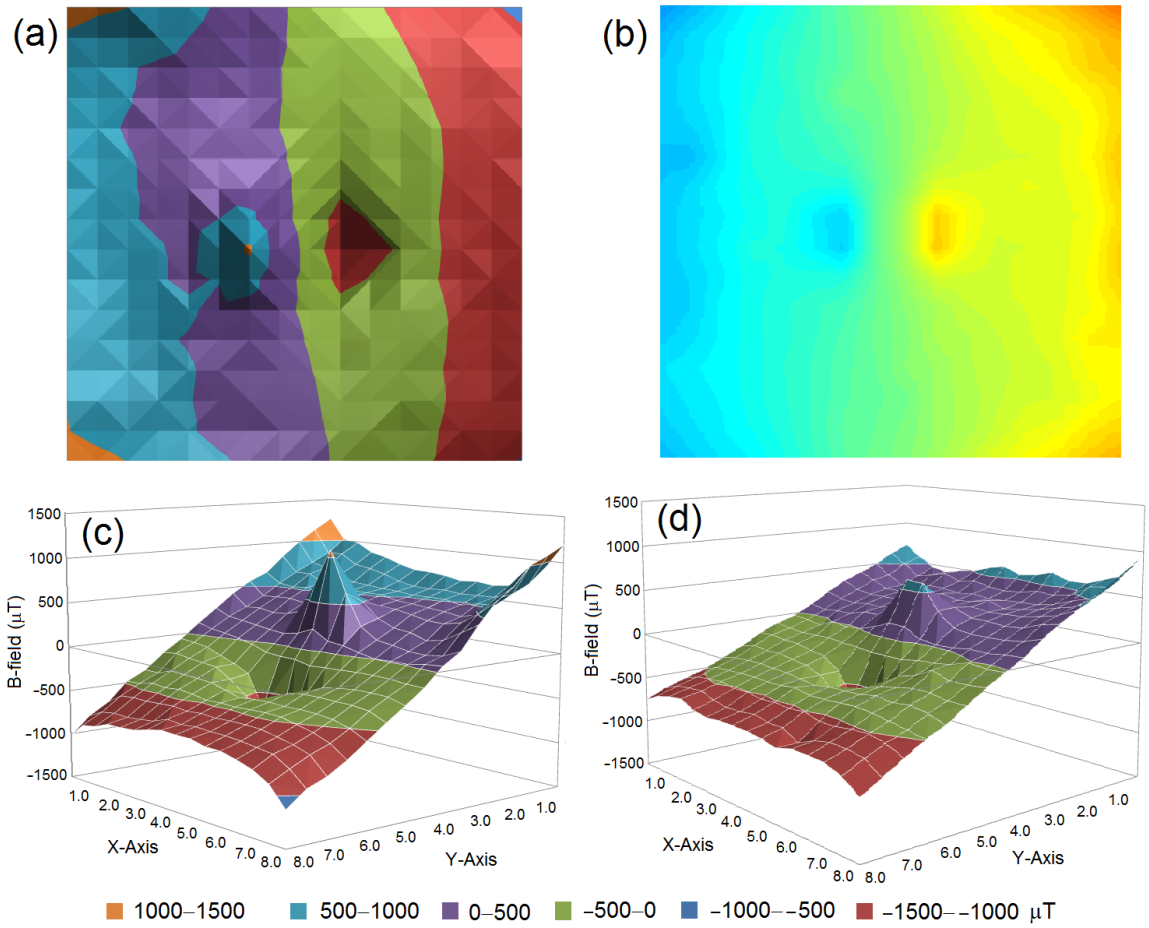

Fig. 8.2 (a) and (b) are the experimental manually scanned maps using a single Quantum Well Hall effect sensor and the real-time image using the 16×16 Quantum Well Hall effect sensor array; (c) and (d) are the corresponding 3D magnetic field images from the single sensor and 2D 16×16 Quantum Well Hall effect array magnetometer, respectively.

8.2.1.2 Weld cracked block sample from New Nuclear Manufacturing (NNUMAN) group

In order to test the 16 × 16 array camera for real case non-destructive testing, a sample with a welding crack from the New Nuclear Manufacturing (NNUMAN) group at Manchester was studied. The welding defect (crack) can be seen on the top cross section shown in Fig. 8.3.

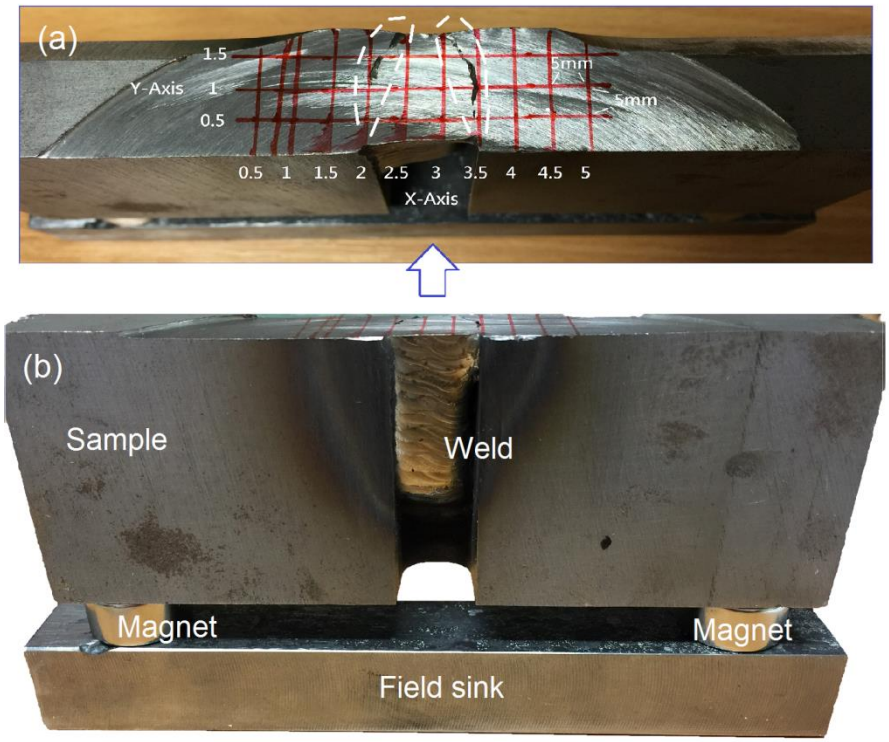

Fig.8.3 (a) Top view showing the crack geometry and position and (b) side view of the setup of the welding defect sample.

This sample is attached with two 20 mm diameter cylinder shaped magnets with magnetic field strength of 350 mT to provide the bias magnetic flux. The bottom rectangular metal bar is the field sink. The magnetic flux leakage signal is measured with both the single sensor magnetometer and the magnetic field camera. The measurement results are shown in Fig. 8.4. In the 2-dimensional image results, the presence of the crack is registered once again as a higher contrast along the crack line on Fig. 8.4 (a) and (b). Both the 2-dimensional images are similar in nature. This confirms that the 16 × 16 array magnetic-field camera is capable of fast detection of flaws in real sample scenarios. Fig. 8.4 (b) is the real-time image acquired from the software which is much faster than the manually plotted experimental data (Fig. 8.4 (a)). The experimental results of the two cases demonstrate that fast static magnetic Flux leakage can be successfully used to detect flaws using the proposed 16 × 16 array magnetic-field camera.

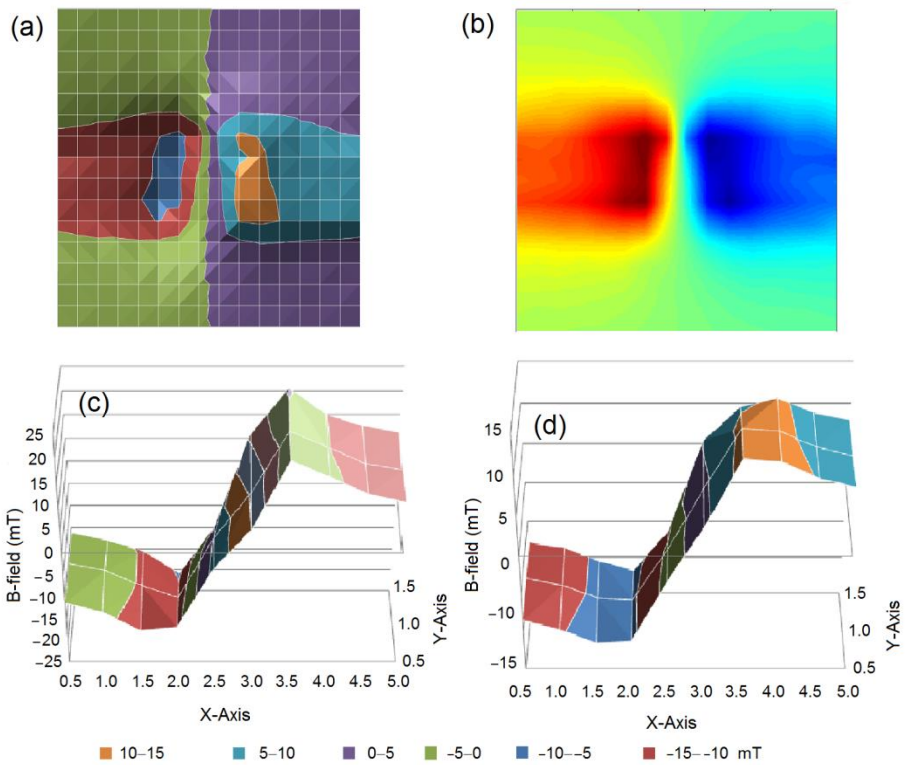

Fig. 8.4 (a) and (b) are the experimental 2D-mapping using single Quantum Well Hall effect sensor and 16×16 Quantum Well Hall effect sensor array, respectively. The white dashed line outlines the position of the crack; (c) and (d) are 3D field images of magnetic flux leakage obtained by the single sensor magnetometer and 2D 16×16 AC/DC Quantum Well Hall effect array magnetometer, respectively.

8.3 Alternating magnetic field measurements

Alternating magnetic field measurement methods in non-destructive testing uses mainly eddy current testing (ECT), alternating current field measurement (ACFM) and direct contact alternating current injection magnetic particle inspection (MPI).

Both ECT and ACFM use search coil as their magnetic field sensor. A search coils measures both magnetic and electric fields at the same time and this limits its capacity to be used with external coil magnetic field bias source. A search coil is also very susceptible to interfere with background high frequency noise. The result is that a search coil is not suitable for measuring alternating magnetic field distribution in 3-dimensional space.

A QWHE measure flux density and compared to a search coil, has better immunity against electric field interference. This makes the 16 × 16 array magnetic-field camera an optimum choice to measure alternating magnetic field distribution in 3-dimensional space.

By measuring the changes of the background alternating magnetic field distribution, both ferromagnetic and non-ferromagnetic materials can be detected and visualised.

8.3.1 Background magnetic-field distribution measurements

In this study, the external magnetic field is formed using either an electromagnet or a Helmholtz coil in AC mode to measure the magnetic material geometry and orientation. Fig. 8.5 shows the picture of tests on a coupling nut using both an electromagnet and a Helmholtz coil to form the external magnetic fields. The alternating magnetic field distribution in 3-dimensional space is measured by the 16 × 16 array camera. Prior to the test runs, the background magnetic field was removed. The scale colour bar shown in Fig. 8.5, has a range of -230 to 230 μT. The "U" shaped ferrite core of the electromagnet located above the outside of the 16 × 16 sensor array forms a closed loop for the magnetic flux, with an air gap between the two magnetic poles in it (Fig. 8.5 (a)). The coupling nut on the16 × 16 sensor array is magnetised due to the magnetic induced polarisation. The field lines of the coupling nut come out of the near magnetic flux side (dark red) and go in to other side (navy blue). The result shows that the16 × 16 array magnetic-field camera can visualise magnetic induction vector distribution even if it is not in a uniform magnetic field.

When the coupling nut is placed in the uniform magnetic field of a Helmholtz coil, the axial direction of the coupling nut is perpendicular to the magnetic field, (Fig. 8.5 (b)), the magnetic image of the coupling nut can be clearly identified.

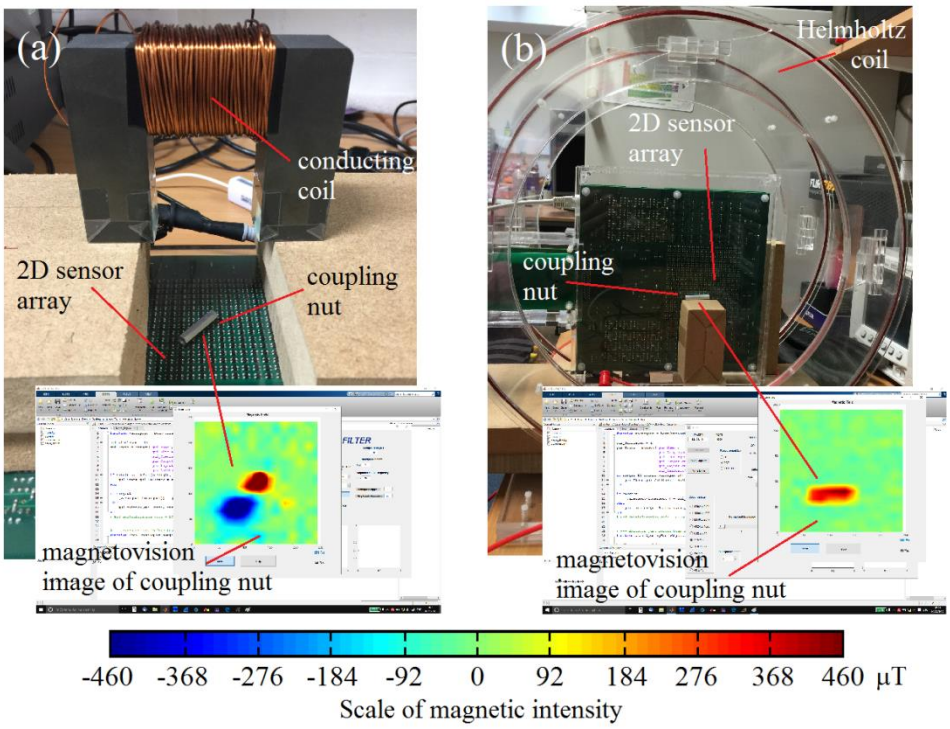

Fig. 8.5 2D images of the coupling nut tests via (a) conducting coil and (b) Helmholtz coil to form an external magnetic field. The insets in (a) and (b) show the software interfaces and output magnetic images in the two types of measurements.

8.3.2 Non-contact ferromagnetic material sensing and imaging

In this case, the background magnetic field is removed via the developed computer software before identification. Fig. 8.6 show the 2D images of materials (metals) identification using a Helmholtz coil in AC mode to form an external magnetic field. The insets in (a) and (b) show the output magnetic field images of a key (without cladding layer) and crocodile clip (with a cladding layer of plastic). The results show that the magnetic image accurately reproduces the configuration of the key (Fig. 8.6 (a)). The dark red curve depicts the magnetic spatial response of the key. In the inset of Fig. 8.6 (b), a configuration consisting of a plastic-clothed crocodile clip can also be identified accurately. The dark red region depicts correctly the magnetic spatial response of the spring coil in the clip. This real time 2-dimensional graphical image has considerable potential in several applications such as security screening, markers for analysis, bio-imaging detection, and medical treatments, etc...

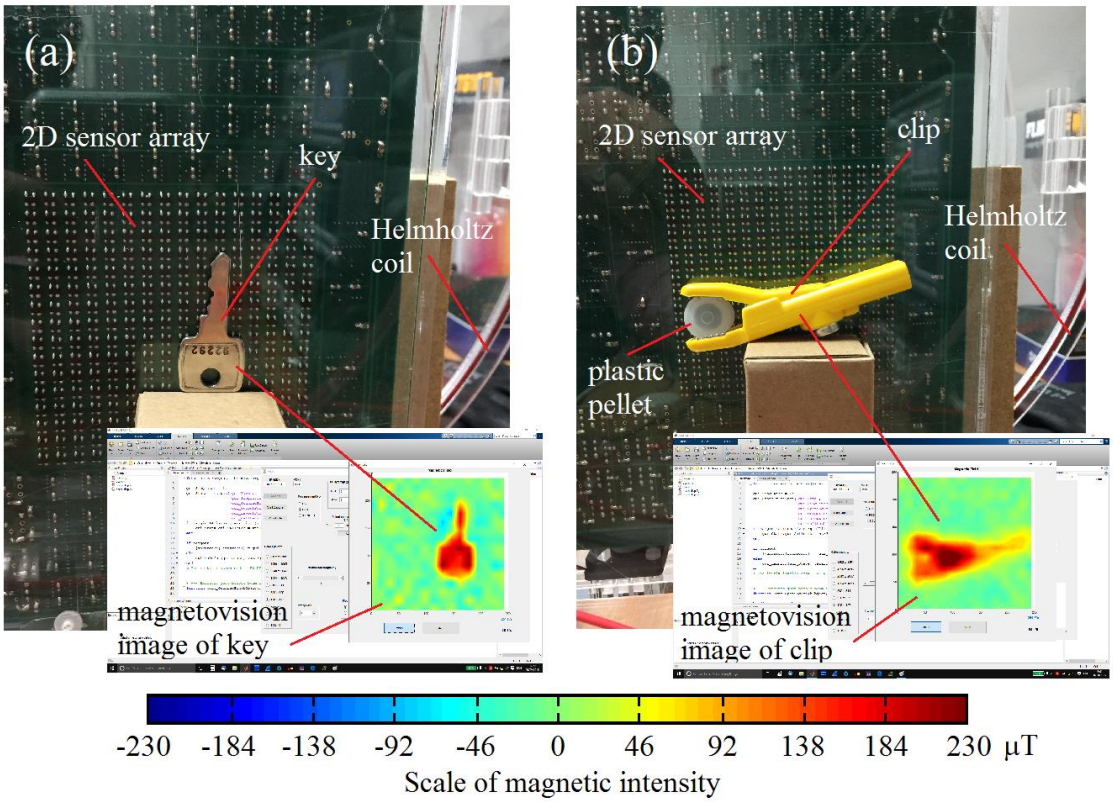

Fig. 8.6 2D images of mass distribution tests via Helmholtz coil to form an external magnetic field. The insets in (a) and (b) show the software interfaces and output magnetic images of a key and clip.

8.3.3 Direct contact alternating current injection for non-ferromagnetic material inspection

In alternating magnetic field measurement, the non-destructive testing of non-ferromagnetic metals or alloy can be inspected by using direct alternating current injection through materials. An aluminium bar with a whole cut was measured in alternating magnetic field measurement mode. A directly applied alternating current of 3 amps was injected into the aluminium bar creating an alternating magnetic field around it. The detected magnetic image shows the defect position in the material and is used to understand the relationship between material geometry and defect shape. The 2-dimensional graphical image is shown in Fig. 8.7. The inset in Fig. 8.7 shows the image of the magnetic field distribution of the aluminium with the hole in the form of a colour map which clearly shows the defect position. The result shows that the 16 × 16 array magnetic-field camera is capable of accurately

measuring non-ferromagnetic materials.

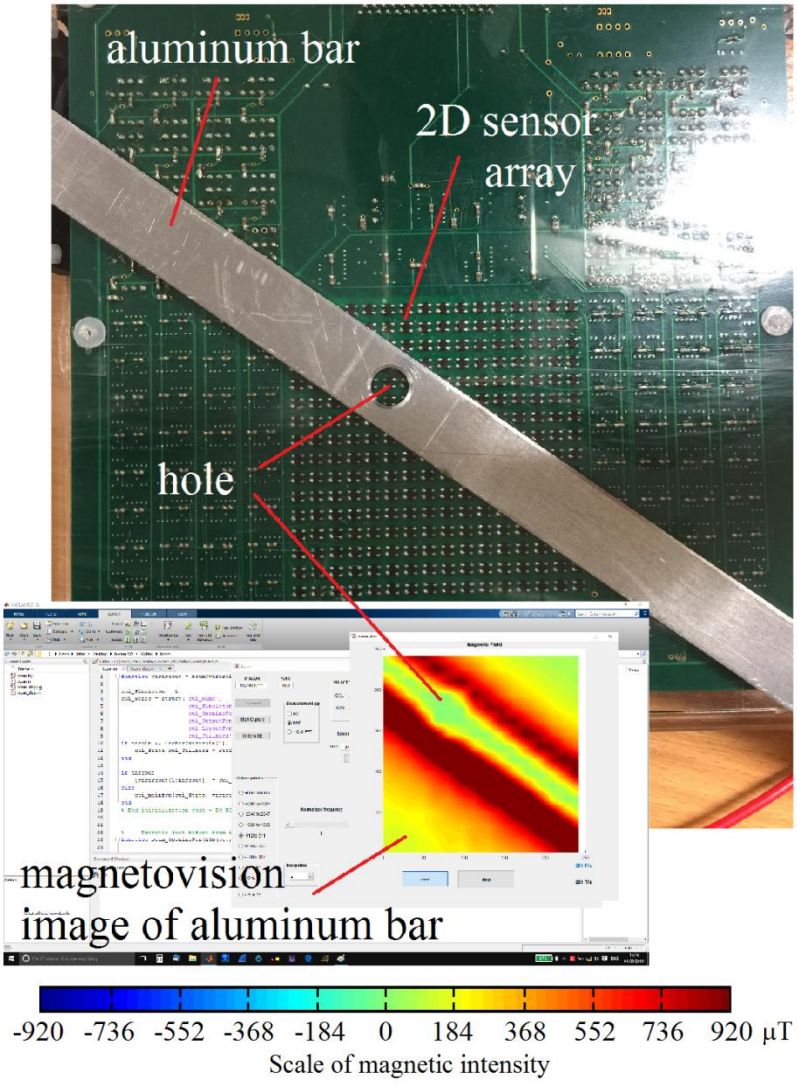

Fig. 8.7 2-dimensionalgraphical result of aluminium bar with a hole using direct contact alternating current injection method. The inset shows the software interfaces and measured magnetic field distribution image.

8.4 Conclusion

Magnetic flux leakage and eddy current testing are the most commonly used electromagnetic NDT methods in various industries [18]. However, most of the existing ECT techniques use wired coils as magnetic field sensors which have many drawbacks, such as, non-portability due to large size, slow scanning speed, low spatial resolution, and complicated mechanical structure required for auto testing systems. These are circumvented to some extent using conventional Hall effect sensing for magnetic flux leakage testing using either silicon

or GaAs elements. These works well (including static magnetic field) but are limited in their sensitivities due to the relatively low electron mobility inherent in these materials. By contrast, the 2D Quantum Well Hall effect sensors reported here [42, 61] use high mobility semiconductors which supersede and overcomes many of the disadvantages including orders of magnitude higher resolution (~ nano Tesla). These new sensors have been built into a Magnetic-field camera, which has been developed to improve DC and AC electromagnetic NDT testing that permits going beyond traditional surface and subsurface defects identification.

Major advantages of the16 × 16 array magnetic-field camera include:

(1) Its ease of use as a magnetic flux leakage (MFL) testing equipment in DC and AC electromagnetic NDT measurements.

(2) Its ability to provide 2D graphical images similar to magnetic particle inspection (MPI) but without its inherent drawbacks.

(3) Its capability to test non-ferromagnetic materials such as aluminium, copper, and stainless steels for deep defects below the surface using low frequency alternating magnetic fields.

(4) Materials (metals) identification by alternating external magnetic field illuminations and which has considerable potential in several applications such as security checking and labelling, magnetic markers for analysis, bio-imaging detection, and medical treatments amongst others.

Chapter 9
Conclusions and future works

9.1 Conclusions

As mentioned previously, the present research has concentrated on a detailed and systematic development of magnetovision scanning systems using ultra-high sensitivity QWHE in single, linear and 2D sensor array configurations to solve many of problems of present electromagnetic NDT techniques. The major conclusions of the works are described below.

9.1.1 Quantum Well Hall effect sensors characteristics

All QWHE sensors investigated here, namely P2A, P3A and P15A, were grown by Solid Source Molecular Beam Epitaxy in a VG V90H system and fabricated into 70x70 μm^2 size sensors. A noise measurement setup for these QWHE sensors was designed and noise characteristics of these sensors were measured. The results indicate that the measured data agrees well with the calculations for thermal and shot noise when the input bias current is < 3 mA though there are still benefits in operating the P2A sensor under input bias current ≥ 3 mA conditions when the measured magnetic field is greater than 10 kHz or an AC superhetrodyne technique for bias current is used. The drift voltage of the QWHE sensors are highly dependent on the input bias voltage of the sensors. The measured drift voltage of all QWHE sensors are less than 800 µV when the sensor bias voltage is less than or equal to 2 V. Among all three sensors, the P2A QWHE sensor (which has the highest electron concentration) has the lowest drift behaviour at less than 90 uV when the sensor bias voltage is 2 V.

The mathematics of automatic offset cancellation using a 4-type spinning-current technique was described. A DC offset cancellation circuit was designed, built, and tested. The results demonstrated excellent cancelling of the residual magnetic offset closer to the magnitude of the Earth's magnetic field when the applied switching frequency is higher than

1 kHz. The drift voltage variations of the Hall voltage with applied current are small when the applied frequency higher than 1 kHz which is thus a critical factor in determining the suitability of the proposed spinning current offset cancellation technique.

9.1.2 Quantum Well Hall effect magnetometer and Quantum Well Hall effect linear array magnetic-field scanner

A QWHE magnetometer with a single P2A sensor had a field strength resolution of 0.1 μT, and a measurement dynamic range of 138 dB. Both static magnetic field and alternating magnetic field up to 4 kHz can be measured.

A flexible 16 × 1 array scanner, and a 32×2 staggered array magnetic-field scanner based on the P2A QWHE sensors were designed, built, and tested. The flexible 16 × 1 array magnetic field scanner can be used for uneven and/or curved surface measurements. This gives the magnetic field scanner better inspection capability in both welding hump and circular pipe samples. By the staggered arrangement of two sensor arrays, a 15.4 point per inch horizontal spatial resolution can be achieved in the staggered 32×2 magnetic field scanner. With the high magnetic field scanning spatial resolution, smaller defect can be detected.

Both QWHE magnetometer and flexible 16 × 1 sensor array magnetic field scanner can achieve an accuracy of ≤ 2% after calibration. DC and AC magnetic flux leakage tests by the flexible 16 × 1 array were undertaken to obtain 2-dimensional magnetic field distribution graphical results. The results of magnetic field distribution in MFL testing show that both the shape and the location of the defect can be easily identified. By using a flexible sensor array structure, the stand-off distance can be kept at a minimum to obtain stronger signals.

In AC-MFL testing, the results showed that the QWHE sensor has not only high sensitivity and linearity in a wide frequency range but is also capable of detecting micron wide defects which makes it an optimum choice to be used for AC-MFL testing. By changing the sample bias magnetic field frequency, data on different skin depth can be obtained which makes depth profiling a possibility. The test results of the aluminium plate show that the AC-

MFL testing can be used not just on ferromagnetic materials but also on non-ferromagnetic materials.

Compared to search coils, the QWHE sensors have the advantage of:(1) high sensitivity in both static and alternating magnetic field, (2) static and alternating magnetic field detection capability, (3) high linearity in field-sensitivity and wide dynamic range, (4) high frequency-sensitivity linearity, (5) easy to operate, (6) low temperature coefficient of output Hall voltage, and (7) compact size.

9.1.3 Quantum Well Hall effect real-time magnetic-field cameras

Real-time 8 × 8 and 16×16 QWHE array magnetic-field cameras were designed, built, and tested. These prototypes can measure static magnetic field strengths in a 2-dimensional plane. Different shapes of magnets and magnetic field polarities can all be identified by the 8 × 8 magnetic field camera. The camera has a resolution of 3.05 μT, and a dynamic range of 66 dB (the minimum and maximum fields measurable are 3.05 μT and 6.25 mT) and a real time magnetic field measurement rate of 13 frames per second (FPS). By contrast the 16×16 array magnetic field camera has an improved sampling rate of 600 frame per second and with the use of an interpolation technique, a spatial resolution of 40.6 point per inch can be achieved. The minimum and maximum detectable magnetic field for this magnetic field camera are 1.8 μT and 29.5 mT respectively leading to a record dynamic range of 84dB for high quality imaging. The 2-dimensional graphical results measured by this magnetic field camera can provide continuous magnetic field distributions. Therefore, the non-continuous magnetic field signal generated by defect regions can be easily identified.

9.1.4 Magnetovision systems based on 16 × 16 array magnetic-field camera

A novel magnetovision system based on a real-time 16 × 16 QWHE array was developed to improve DC and AC electromagnetic NDT testing that permits going beyond traditional surface or subsurface defects identification using search coils. The experimental results of five case studies demonstrate that the MFL and configuration identification in DC and AC

magnetic field resulting from defects and shape can be successfully measured. The major advantages of this real-time magnetic-field camera are: (1) it easy to use as a MFL testing equipment in DC and AC electromagnetic NDT testing, (2) its ability to provide 2D graphical images similar to MPI but without its inherent drawbacks, (3) its capability to test non-ferromagnetic materials for deep defects below the surface using low frequency alternating magnetic fields, and (4) its ability to identify materials (metals) by alternating external magnetic field illuminations, which has considerable potential in several applications such as security checking and labelling, magnetic markers for analysis, bio-imaging detection, and medical treatments, amongst many others.

9.2 Future work

The potential of the QWHE sensor magnetometer in NDT have been demonstrated in chapter 6 and different type of AC magnetic field visualised inspection/scanning were illustrated in chapter 8 where the many advantages and features of the 16 × 16 QWHE magnetic field camera for use in electromagnetic NDT were also described. Further improvements for practical applications, require more research to be carried out. The following section proposed the short-term and long-term research plans:

9.2.1 Short-term research plans

In the short-term, undertaking the following tasks can benefit the developed single magnetometer and magnetovison system:

1. Inclusion of automatic 4-direction spinning current offset cancellation circuits.
2. Study of QWHE sensor noise and drift behaviour after offset cancellation operation.
3. Study of minimum detectable static and alternating magnetic field of QWHE sensor using the superhetrodyne technique.
4. More research and testing on real NDT samples using AC magnetic field magnetic flux leakage for defect sizing.
5. Improve the sampling rate and accuracy of QWHE magnetic field camera for higher

frequency (≥ 100 kHz) alternating magnetic field measurements.

9.2.2 Long-term research plans

In the long-term, the QWHE magnetovision system needs to be optimised for even better performance. The following subjects are particularly worthy of further research:

1. Design of robotic scanning mechanisms for smooth and accurate measurement.
2. Development of the depth profile technique with variable AC magnetic field to give 3D imaging.
3. Development of image reconstruction techniques for reconstructing images different sensor array stand-off distances.
4. Development of an integrated, micron-sized, high density QWHE sensor array chips for ultra-high spatial resolution inspection including domain walls detection for microstructural inspections.
5. Development of a QWHE sensor IC with integrated s bias current source, amplifier, and offset cancellation features.
6. Development of metal composition analysing techniques for QWHE magnetic field cameras.

References

[1] S. Yanhua, K. Yihua, Magnetic compression effect in present MFL testing sensor, Sensors and Actuators A 160 (2010) 54–59.

[2] J.W.K. Smith, B.R. Hay, Magnetic flux leakage inspection tool for pipelines, US Patent 6,023,986, February 2000.

[3] J.P. Rogers, Magnetic flux leakage system and method, US Patent 11591712, November 2006.

[4] R. Brandstrom, Apparatus and method for detection of defects using flux leakage techniques, US Patent 11411235, April 2006.

[5] M. Katoh, N. Masumoto, K. Nishio, T. Yamaguchi, Modeling of the yoke magnetisation in MFL-testing by finite elements, NDT and E International 36 (2003) 479–486.

[6] D. Jinfeng, K. Yihua, W. Xinjun, Tubing thread inspection by magnetic flux leakage, NDT and E International 39 (2006) 53–56.

[7] L. Clapham, V. Babbar, J. Byrne, Detection of mechanical damage using the magnetic flux leakage technique, Queen's University, Kingston, Ontario, Canada. Available from: http://www.ndt.net/article/wcndt2004/pdf/petrochemical_industry/26_clapham.pdf

[8] Bhag Guru and Hüseyin Hiziroğlu, Electromagnetic Field Theory Fundamentals, 2nd edition, Cambridge University Press (2004).

[9] N. Yusa, E. Machida, L. Janousek, M. Rebican, Z. Chen, K. Miya, Application of eddy current inversion technique to the sizing of defects in Inconel welds with rough surfaces. Nuclear Engineering and Design 235 (2005) 1469–1480.

[10] U. Radtke, R. Zielke, H.-G. Rademacher, H.-A. Crostack, R. Hergt, Application of magneto-optical method for realtime visualization of eddy currents with high spatial resolution for nondestructive testing. Optics and Lasers in Engineering 36 (2001) 251–268.

[11] W. Li, G. Chen, W.Y Li, Z. Li, F. Liu, Analysis of the inducing frequency of a U-shaped ACFM system. NDT & E International 44 (2011) 324–328.

[12] M. Ravan, S.H.H. Sadeghi, R. Moini, Using a wavelet network for reconstruction of fatigue crack depth profile from AC field measurement signals. NDT & E International 40 (2007) 537–544.

[13] R.K. Amineh, M. Ravan, S. H. H. Sadeghi, R. Moini. Removal of probe liftoff effects on crack detection and sizing in metals by the AC field measurement technique. IEEE Transactions on Magnetics 44 (2008) 2066–2073.

[14] G.L. Nicholson, C.L. Davis, Modelling of the response of an ACFM sensorto rail and rail wheel RCF cracks, NDT & E International 46 (2012) 107–114.

[15] R.P.R. Hasanzadeh, S.H.H. Sadeghi, M. Ravan, A.R. Moghaddamjoo, R. Moini, A fuzzy alignment approach to sizing surface cracks by the AC field measurement technique, NDT & E International 44 (2011) 75–83.

[16] G.M. Chen, W. Li, Z.X. Wang, Structural optimization of 2-D array probe for alternating current field measurement. NDT & E International 40 (2007) 455–461.

[17] M.J. Knight, F.P. Brennan, W.D. Dover, Effect of residual stress on ACFM crack measurements in drill collar threaded connections, NDT & E International 37 (2004) 337–343.

[18] J. Xu, X. Wu, C. Cheng, A. Ben, A Magnetic Flux Leakage and Magnetostrictive Guided Wave Hybrid Transducer for Detecting Bridge Cables, Sensors 12 (2012) 518–533.

[19] M. Division, Mobile testing and measuring equipment, for maintenance, laboratory and production monitoring, Available from: http://www.foerstergroup.com/Leakage-flux-method.358+ M5ebe6ef33aa.0.html

[20] M. Nowicki, R. Szewczyk, Ferromagnetic Objects Magnetovision Detection System, Materials6 (2013) 5593–5601.

[21] M. Nowicki, R. Szewczyk, Magnetovision Scanning System for Detection of Dangerous Objects. Acta Physica Polonica A 126 (2014) 382–383

[22] J. Kaleta, P. Wiewiórski, Magnetic field distribution detecting and computing methods for experimental mechanics. Engineering Transactions 58(3–4)(2010) 97–118.

[23] J. Lenz, A.S. Edelstein, Magnetic Sensors and Their Applications, IEEE Sensors Journal 6(3) (2006) 631–649.

[24] V. Cambel, P. Eeliáš, R. Kúdela, B. Olejniková, J. Novák, M. Durica, M. Majoroš, J. Kvitkovic, Ž. Mozolová, P. Hudek, Preparation, characterisation and application of microscopic linear Hall probe arrays, Solid-State Electronics 42(2) (1998) 247–251.

[25] V. Cambel, G. Karapetrov, V. Novosad, E. Bartolomé, D. Gregušová, J. Fedora, R. Kúdela, J. Šoltýs, Novel Hall sensors developed for magnetic field imaging systems, Journal of Magnetism and Magnetic Materials 316 (2007) 232–235.

[26] Y. Haddab, V. Mosser, F. Kobbi, R. Pond, Reliability and stability of GaAs-based pseudomorphic quantum wells for high-precision power metering, Microelectronics Reliability 40 (2000) 1443–1447.

[27] O. Yilmazoglu, M. BralKit, J. Sigmund. E. Gene, H.L. Harinagel, Integrated InAs/GaSb 3D magnetic field sensors for “the intelligent tyre”, Sensors and Actuators A 94 (2001) 59–63.

[28] A. Sandhu, Y.iKumagai, A. Lapicki, S. Sakamoto, M. Abe, H.I. Handa, High efficiency Hall effect micro-biosensor platform for detection of magnetically labeled biomolecules, Biosensors and Bioelectronics 22 (2007) 2115–2120.

[29] Z. Primadani, A. Sandhu, Variable temperature scanning Hall probe microscopy of ferromagnetic garnet thin films, Journal of Magnetism and Magnetic Materials 310 (2007) 2693–2695.

[30] K.S. Novoselov, S.V. Morozov, S.V. Dubonos, M. Missous, A.O. Volkov, D.A. Chirstian, A.K. Geim, Submicron probes for Hall magnetometry over the extended temperature range from helium to room temperature, Journal of Applied Physics, Vol. 93 (2003) 12.

[31] M. Sadeghi, Highly Sensitive Nano Tesla Quantum Well Hall effect Integrated Circuits using GaAs-InGaAs-AlGaAs 2DEG, PhD thesis, the University of Manchester, Faculty of Engineering and Physical Sciences, 2015

[32] E.H. Hall, On a new action of the magnet on electric currents, American Journal of Mathematics 2(3) (1879) 287–292.

[33] G. Căruntu, C. Panait, The stability and the detection limit for hall microsensors, international workshop "Computational Problems of Electrical Engineering", http://cpee.iem.pw.edu.pl/2004/CD/035.pdf

[34] K.S. Popovic, J.A. Flanagan, P.A. Besse, The future of magnetic sensors, Sensors and Actuators A 56 (1996) 39–55.

[35] R.L. Ross, S.P. Svensson, P. Lugli, Pseudomorphic HEMT technology and applications, Kiuwer Academic Publishers, Dordrecht, The Netherlands, 1996.

[36] R. Ramanathan, Compound Semiconductors: Process Flow, Process Integration, Devices and Testing. Skyworks Solutions, Inc. http://www.gaasmantech.org/ Conference%20 Information/workshops/2010/04_ramanathan%20presentation.pdf)

[37] H. Sghaier, L. Sfaxi, L. Bouzaïene, H. Maaref, Sensitivity enhancement of AlGaAs-GaAs heterojunction-based Hall sensor designed for low magnetic field measurements, Sensors and Actuators A 113 (2004) 147–150.

[38] V.P. Kllnets, W. Hoerstel, H. Kostial, H. Kissel, U. Millier, G.G. Tarasov, Y.I. Mazur, Z.Ya. Zhuchenko, W.T. Masselink, High electric field performance of $Al_{0.3}Ga_{0.7}As/GaAs$ and $Al_{0.3}Ga_{0.7}As/GaAs/In_{0.3}Ga_{0.7}As$ quantum well micro-Hall devices, Sensors and Actuators A 101 (2002) 62–68.

[39] L. Sileo, M.T. Todaro, V. Tasco, M. De Vittorio, A. Passaseo, Fully integrated three-axis Hall magnetic sensor based on micromachined structures, Microelectronic Engineering 87 (2010) 1217–1219.

[40] J.S. Lee, K.H. Ahn, Y.H. Jeong, D.M. Kim, Highly-sensitive $Al_{0.25}Ga_{0.75}As/$ $In_{0.25}Ga_{0.75}As/$ GaAs quantum-well Hall devices with Si-delta-doped GaAs layer grown by LP-MOCVD, Sensors and Actuators A 101 (1996) 183–185.

[41] S. Del Medico, T. Benyattou, G. Guillot, M. Gendry, M. Oustric, T. Venet, J. Tardy, G. Hollinger, A. Chovet, N. Mathieu, High-sensitivity Hall sensors using GaInAs/AlInAs

pseudomorphic heterostructures, Sensors and Actuators A 46–47 (1995) 298–301.

[42] N. Haned, M. Missous, Nano-tesla magnetic field magnetometry using an InGaAs-A1GaAs-GaAs 2DEG Hall sensor, Sensors and Actuators A 102 (2003) 216–222.

[43] V. Cambel, G. Karapetrov, P. Eliáš, S. Hasenöhrl, W.-K. Kwok, J. Krause, J Mañka, Approaching the pT range with a 2DEG InGaAs/InP Hall sensor at 77 K Microelectronic Engineering 51–52 (2000) 333–342.

[44] M. Morvic, J. Betko, Planar Hall effect in Hall sensors made from InP/InGaAs heterostructure, Sensors and Actuators A 120 (2005) 130–133.

[45] J. Bekaert, V.V. Moshchalkov, Y. Bruynseraede, M. Behet, J. De Boeck, G. Borghs, InAs/$Al_{0.2}Ga_{0.8}Sb$ quantum well Hall sensors with improved temperature stability, Review of Scientific Instruments 70(6) (1999) 2715–2718.

[46] M. Behet, J. Bekaert, J. De Boeck, G. Borghs, InAs/$Al_{0.2}Ga_{0.8}Sb$ quantum well Hall effect sensors, Sensors and Actuators A 81 (2000) 13–17.

[47] O.A. Mironov, M. Myronov, S. Durov, O. Drachenko, J. Leotin, Microminiature Hall probes basedon n-InSb(Sn)/i-GaAs heterostructure for pulsedmagneticfieldapplications up to 52 T, Physica B 346–347 (2004) 548–552.

[48] O.A. Mironov, M. Myronov, S. Durov, V.T. Igumenov, V.M. Konstantinov, V.V. Paramonov, T. Zhang, L.F. Cohen, The sub-micrometer thickness n-InSb/i-GaAs epilayers for magnetoresistor applications at room temperatures of operation, Physica E 20 (2004) 52–526.

[49] M. Sadeghi, Ultra high sensitive InGaAs-GaAs-AlGaAs 2DEG Hall effect integrated circuits, PhD program 1st year report, Microelectronic and Nanostructures Group, The University of Manchester, 2012.

[50] E.F. Schubert, A. Fischer, K. Ploog, The delta-doped field-effect transistor (δFET), IEEE Transactions on Electron Devices ED-33(5) (1986) 625–632.

[51] E. F. Schubert, K. Ploog. The δ-doped field-effect transistor, Japanese Journal of Applied Physics 24 (1985) L608–L610.

[52] A. Doolittle, Advanced field effect transistor (FET) devices, Georgia Institute of Technology, U.S.A. http://users.ece.gatech.edu/~alan/ECE3080/Lectures/ECE3080-L-12b-Advanced FETDevices.pdf

[53] C. Gaquiere, J. Grünenpütt, D. Jambon, E. Delos, D. Ducatteau, M.Werquin, D. Théron, A high-power W-band pseudomorphic InGaAs channel PHEMT, IEEE Electron Device Letters, 26(8) (2005) 533–534.

[54] C. Gaquiere, S. Bollaert, M. Zaknoune, Y. Cordier, D. Theron, Y. Crosnier, Influence on power performances at 60 GHz of Indium composition in methamorphic HEMTs, Electron Letters 35(17) (1999) 1489–1490.

[55] Y. Dai, A precision noise measurement and analysis method used to estimate reliability of semiconductor devices. Microelectron Reliab 37(6) (1997) 893–899.

[56] H.F. Teng, S.L. Jang, M.H. Juang, A unified model for high-frequency current noise of MOSFETs. Solid-State Electronics 47 (2003) 2043–2048.

[57] K.D. Wesson, R.M. Ochshorn, B.R. Land, Low-cost, high-fidelity, adaptive cancellation of periodic 60 Hz noise, Journal of Neuroscience Methods 185 (2009) 50–55.

[58] Y. Dai, The time-frequency analysis approach of electric noise based on the wavelet transform, Solid-State Electronics 44 (2000) 2147–2153.

[59] S. Khunkhao, T. Masui, K. Sato, Matrix representation of shot noise due to carrier generation in planar double Schottky-barrier structures. Solid-State Electronics 47 (2003) 913–917.

[60] Ch.S. Roumenin, D. Nikolov, A. Ivanov, A novel parallel-field hall sensor with low offset and temperature drift based 2D integrated magnetometer, Sensors and Actuators A 115 (2004) 303–307.

[61] I.I. Barbolina, K.S. Novoselov, S.V. Morozov, S.V. Dubonos, M. Missous, A.O. Volkov, D.A. Christian, I.V. Grigorieva, A.K. Geim, Submicron sensors of local electric field with single-electron resolution at room temperature. Applied Physics Letters88 (2006) art 013901.

[62] X. Chen, T. Ding, Flexible eddy current sensor array for proximity sensing, Sensors and

Actuators A 135 (2007) 126–130.

[63] S. Turnanski, A. Liszka, The methods and devices for scanning of magnetic fields. Journal of Magnetism and Magnetic Materials 242–245 (2002) 1253–1256.

[64] G. Reyne, Electromagnetic actuation for MOEMS, examples, advantages and drawbacks of MAGMAS. Journal of Magnetism and Magnetic Materials 242–245 (2002) 1119–1125.

[65] D. Tomasi, H. Panepucci, E.L. Vidoto, E. Ribeiro Azevedo, Use of a Phase Reference for Field Mapping with Amplitude Images at Low Field. Journal of Magnetic Resonance 131(1998)310–314.

[66] S. Turnanski, M. Stabrowski, Magnetovision system: new method of investigating steel sheets. Journal of Magnetism and Magnetic Materials 160(1996) 165–166.

[67] K.T. Chang, Computation for bilinear interpolation. Introduction to Geographic Information Systems 5thed. New York, NY: McGraw-Hill, 2009.

[68] G.A. Rinard, R.W. Quine, B.T. Ghim, S.S. Eaton, G.R. Eaton, Dispersion and superheterodyne EPR using a bimodal resonator. Journal of Magnetic Resonance Series A122 (1996)58–63.

[69] I. Kostanic, W. Mikhael, Independent component analysis based QAM receiver. Digital Signal Processing 14 (2004) 241–252.

[70] Y. Tian, S. Li, H. Lv, J. Wang, X. Jing, Smart radar sensor for speech detection and enhancement. Sensors and Actuators A 191 (2013) 99–104.

[71] C.C.H. Lo, J.A. Paulsen, D.C. Jiles, Development of a magnetic NDE imaging system using magnetoresistive devices. AIP Conference Proceedings 657 (2003) 931–938.

[72] S. Tumanski, S. Baranowski, Magnetic sensor array for investigations of magnetic field distribution. Journal of Electrical Engineering 57 (8/S) (2006) 185–188.

[73] C.K. Hou, S. Lee, Effect of rolling strain on the loss separation and permeability of lamination steels. IEEE Transactions on Magnetics 30 (2)(1994) 212–216.

[74] P. Baudouin, Y. Houbaerta, S. Tumanski, Magnetic local investigations of non-oriented

electrical steels after tensile deformation. Journal of Magnetism and Magnetic Materials 254–255 (2003) 32–35.

[75] S. Tumanskiy, M. Stabrowski, The magnetovision method as a tool to investigate the quality of electrical steel. Measurement Science and Technology 9 (1998) 488–495.

[76] S. Tumanski, A. Liszka, The methods and devices for scanning of magnetic fields. Journal of Magnetism and Magnetic Materials 242–245 (2002) 1253–1256.

[77] R. Edward. Hall-effect Sensors: Theory and Application. 2nd ed., Newnes, 2006.

[78] J. Cholewicki, M.M. Panjabi, K. Nibut, M.E. Macias. Spinal ligament transducer based on a Hall effect sensor. Journal of Biomechanics 30(3) (1997) 291–293.

Appendix 01. Circuit schematic of the Quantum Well Hall effect magnetometer.

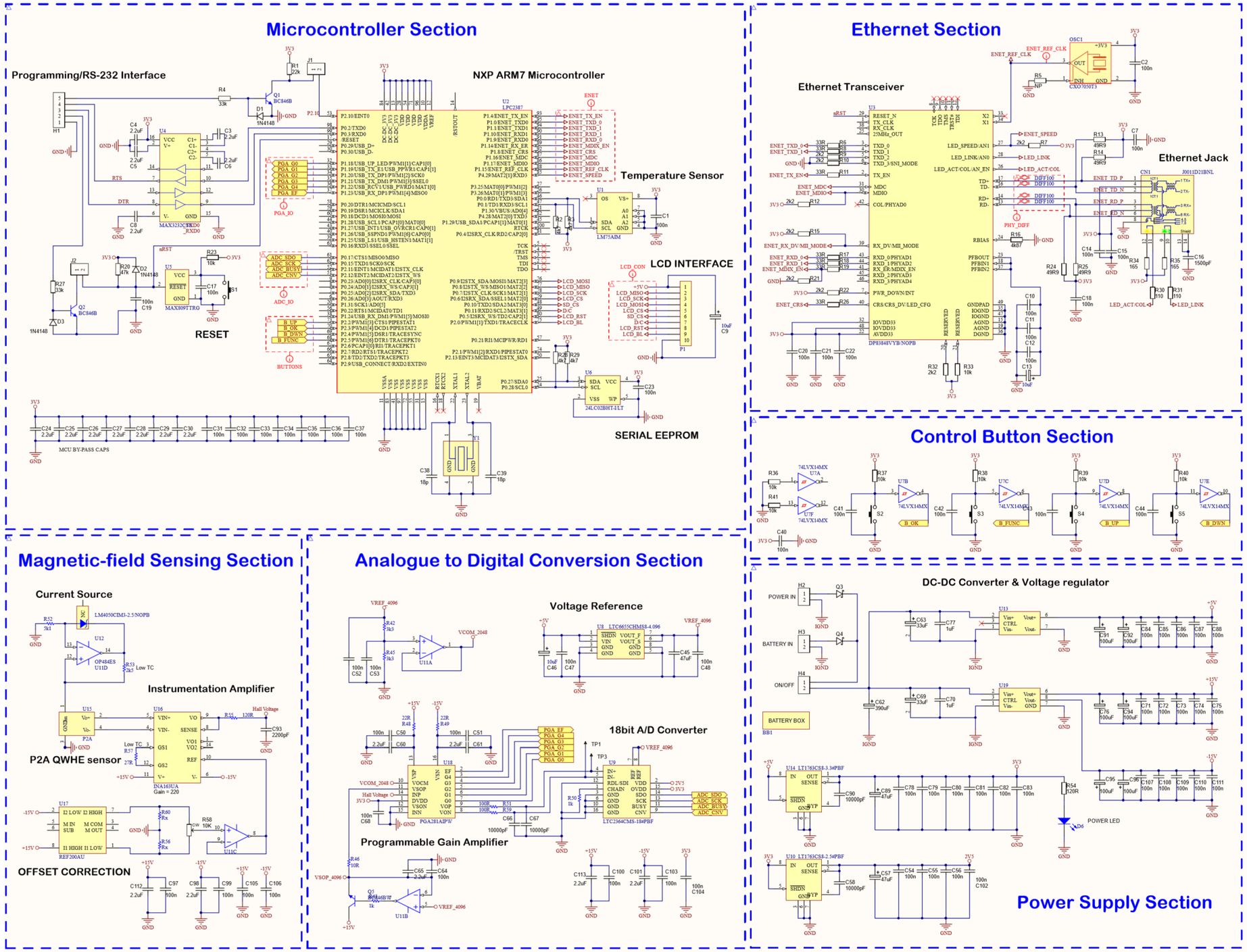

Appendix 02

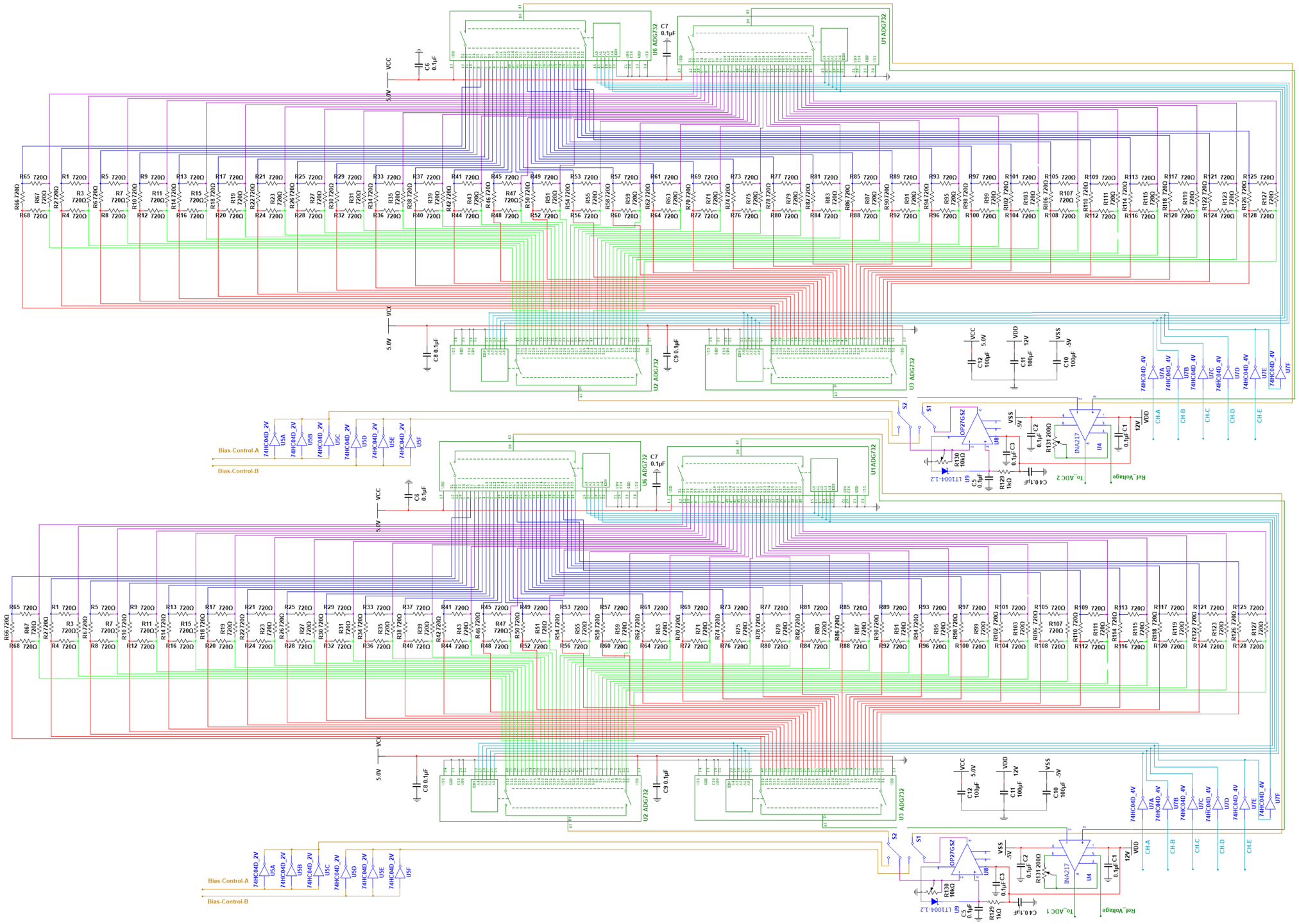
U1 ADG732
U2 ADG732
U3 ADG732
U5 ADG732
U6 ADG732
VCC
5.0V
VDD
12V
VSS
-5V
Bias_Control-A
Bias_Control-B
74HC04D_2V
74HC04D_4V
CH-A
CH-B
CH-C
CH-D
CH-E
To_ADC 1
To_ADC 2
Ref_Voltage
OP27GSZ
INA217
LT1004-1.2

Appendix 03

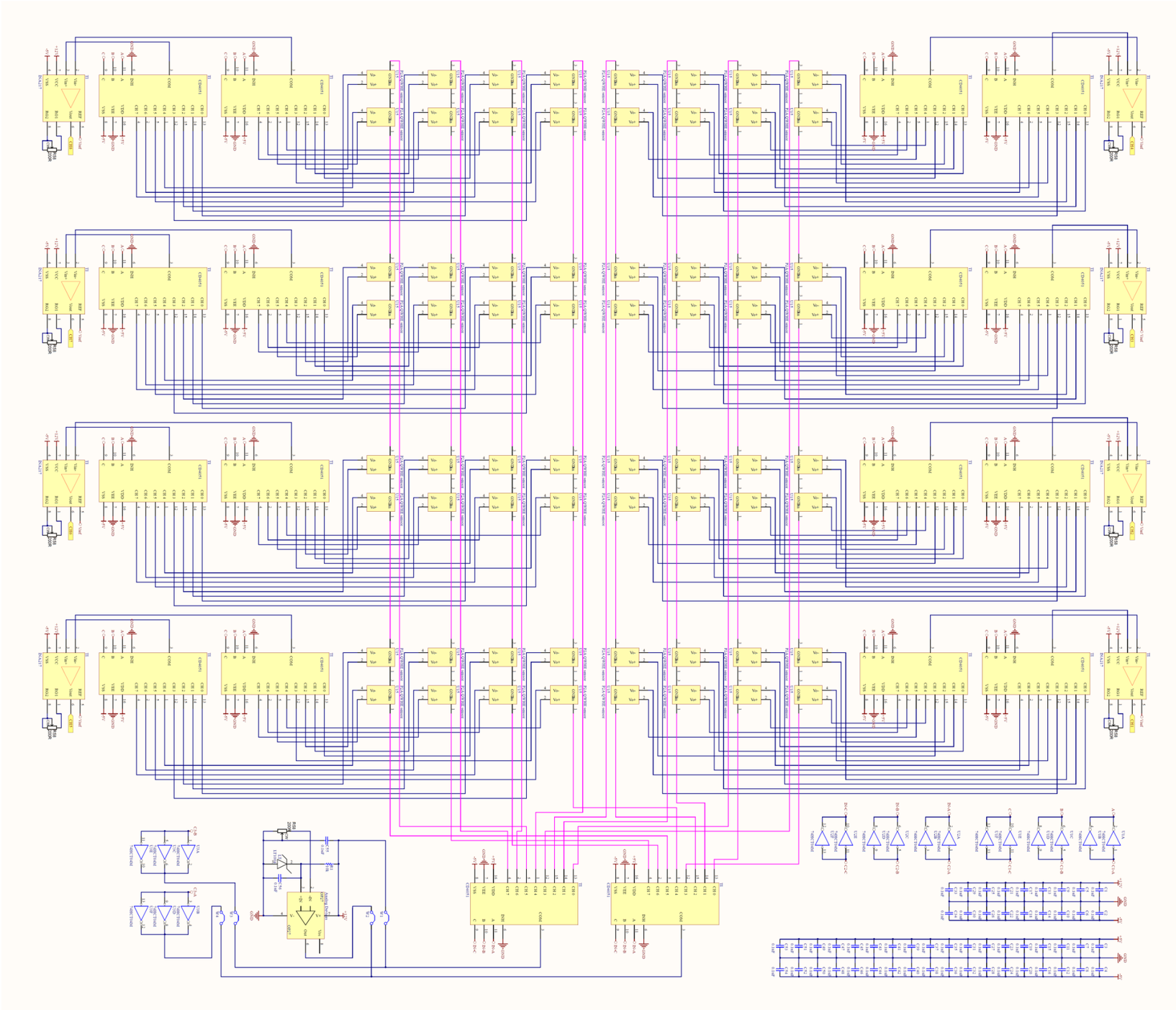

Appendix 04

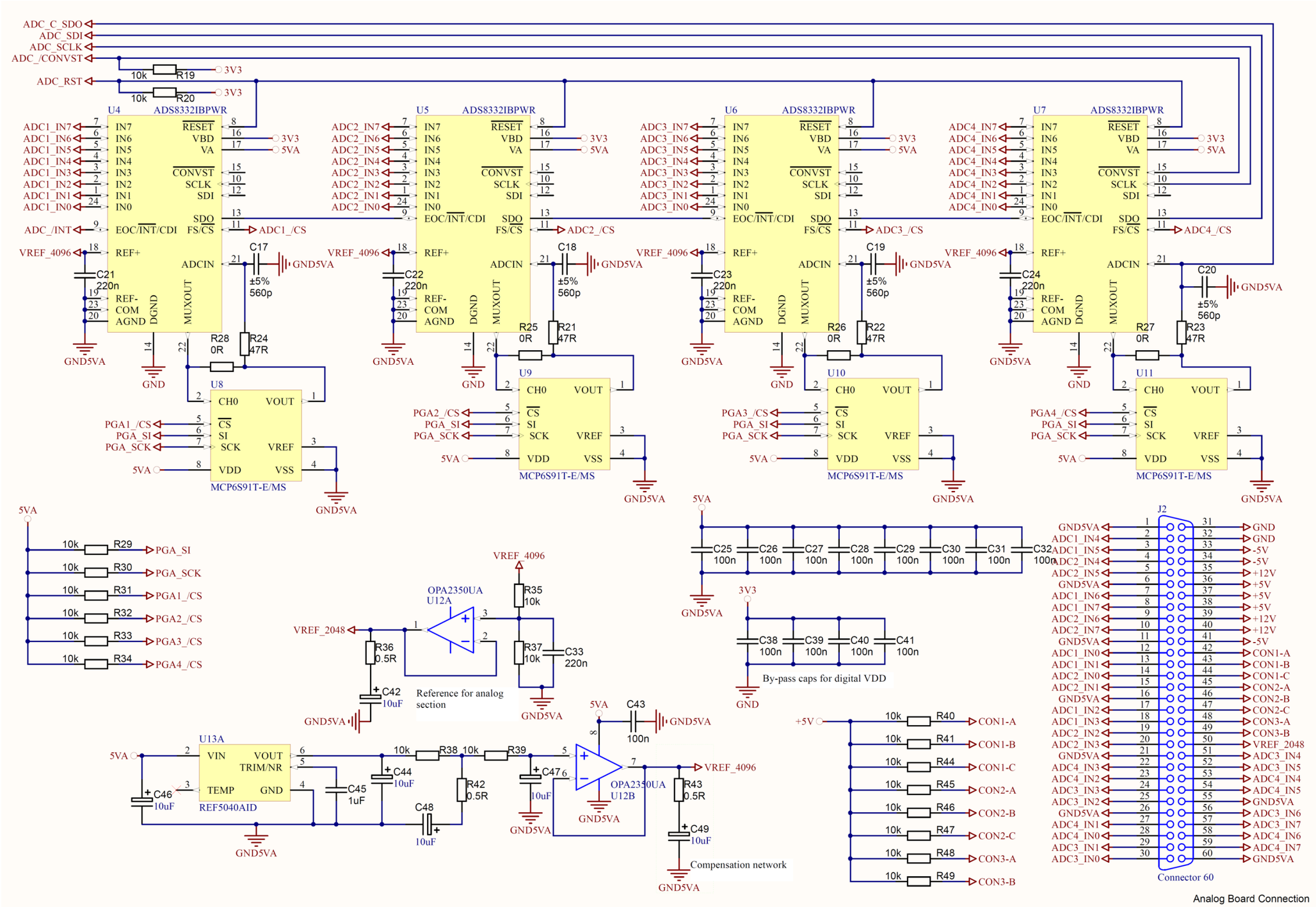
ADC_C_SDO
ADC_SDI
ADC_SCLK
ADC_/CONVST
ADC_RST
10k R19 3V3
10k R20 3V3
U4 ADS8332IBPWR
U5 ADS8332IBPWR
U6 ADS8332IBPWR
U7 ADS8332IBPWR
ADC1_IN7
ADC1_IN6
ADC1_IN5
ADC1_IN4
ADC1_IN3
ADC1_IN2
ADC1_IN1
ADC1_IN0
ADC2_IN7
ADC2_IN6
ADC2_IN5
ADC2_IN4
ADC2_IN3
ADC2_IN2
ADC2_IN1
ADC2_IN0
ADC3_IN7
ADC3_IN6
ADC3_IN5
ADC3_IN4
ADC3_IN3
ADC3_IN2
ADC3_IN1
ADC3_IN0
ADC4_IN7
ADC4_IN6
ADC4_IN5
ADC4_IN4
ADC4_IN3
ADC4_IN2
ADC4_IN1
ADC4_IN0
IN7
IN6
IN5
IN4
IN3
IN2
IN1
IN0
RESET
VBD
VA
CONVST
SCLK
SDI
SDO
EOC/INT/CDI
FS/CS
ADC_/INT
ADC1_/CS
ADC2_/CS
ADC3_/CS
ADC4_/CS
VREF_4096
REF+
ADCIN
REF-
COM
AGND
DGND
MUXOUT
3V3
5VA
C21 220n
C22 220n
C23 220n
C24 220n
C17 ±5% 560p
C18 ±5% 560p
C19 ±5% 560p
C20 ±5% 560p
GND5VA
GND
R28 0R
R24 47R
R25 0R
R21 47R
R26 0R
R22 47R
R27 0R
R23 47R
U8
U9
U10
U11
CH0
VOUT
CS
SI
SCK
VREF
VDD
VSS
PGA1_/CS
PGA_SI
PGA_SCK
PGA2_/CS
PGA3_/CS
PGA4_/CS
MCP6S91T-E/MS
5VA
10k R29 PGA_SI
10k R30 PGA_SCK
10k R31 PGA1_/CS
10k R32 PGA2_/CS
10k R33 PGA3_/CS
10k R34 PGA4_/CS
VREF_4096
OPA2350UA U12A
VREF_2048
R36 0.5R
R35 10k
R37 10k
C33 220n
C42 10uF
Reference for analog section
U13A
VIN
VOUT
TRIM/NR
TEMP
GND
REF5040AID
C46 10uF
C45 1uF
C44 10uF
C48 10uF
R38 10k
R39 10k
R42 0.5R
C47 10uF
C43 100n
OPA2350UA U12B
R43 0.5R
C49 10uF
Compensation network
C25 100n
C26 100n
C27 100n
C28 100n
C29 100n
C30 100n
C31 100n
C32 100n
C38 100n
C39 100n
C40 100n
C41 100n
By-pass caps for digital VDD
+5V
10k R40 CON1-A
10k R41 CON1-B
10k R44 CON1-C
10k R45 CON2-A
10k R46 CON2-B
10k R47 CON2-C
10k R48 CON3-A
10k R49 CON3-B
J2
GND5VA
ADC1_IN4
ADC1_IN5
ADC2_IN4
ADC2_IN5
ADC1_IN6
ADC1_IN7
ADC2_IN6
ADC2_IN7
ADC1_IN0
ADC1_IN1
ADC2_IN0
ADC2_IN1
ADC1_IN2
ADC1_IN3
ADC2_IN2
ADC2_IN3
ADC4_IN3
ADC4_IN2
ADC3_IN3
ADC3_IN2
ADC4_IN1
ADC4_IN0
ADC3_IN1
ADC3_IN0
GND
-5V
+12V
+5V
CON1-A
CON1-B
CON1-C
CON2-A
CON2-B
CON2-C
CON3-A
CON3-B
VREF_2048
ADC3_IN4
ADC3_IN5
ADC4_IN4
ADC4_IN5
ADC3_IN6
ADC3_IN7
ADC4_IN6
ADC4_IN7
Connector 60
Analog Board Connection

Appendix 05

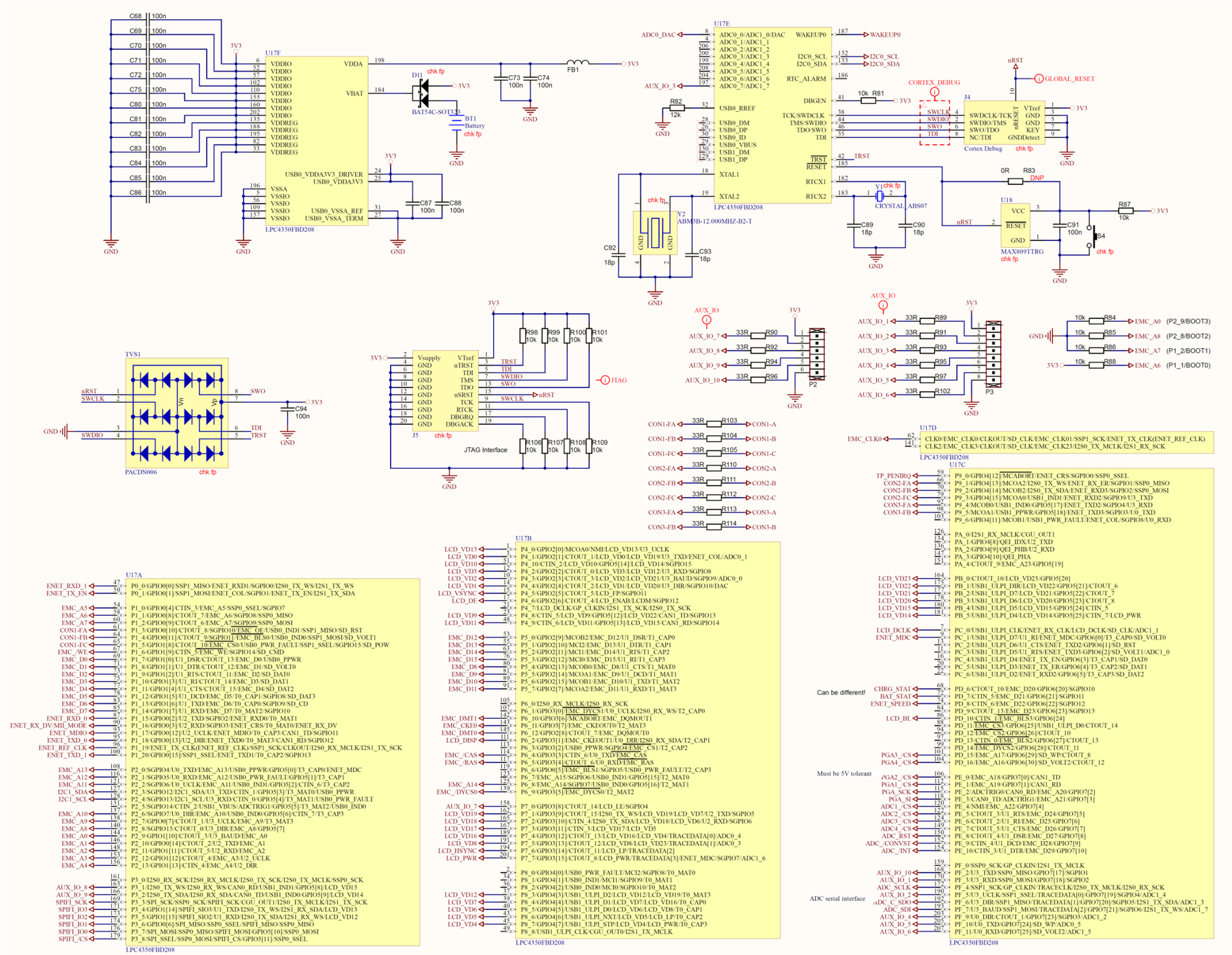
U17E
LPC4350FBD208
U17A
U17B
U17C
U17D
TVS1
PACDN006
J5
JTAG Interface
J4
Cortex Debug
U18
MAX809TTRG
CRYSTAL_ABS07
ABM3B-12.000MHZ-B2-T
BAT54C-SOT323
P2
P3
GND
3V3

Appendix 06

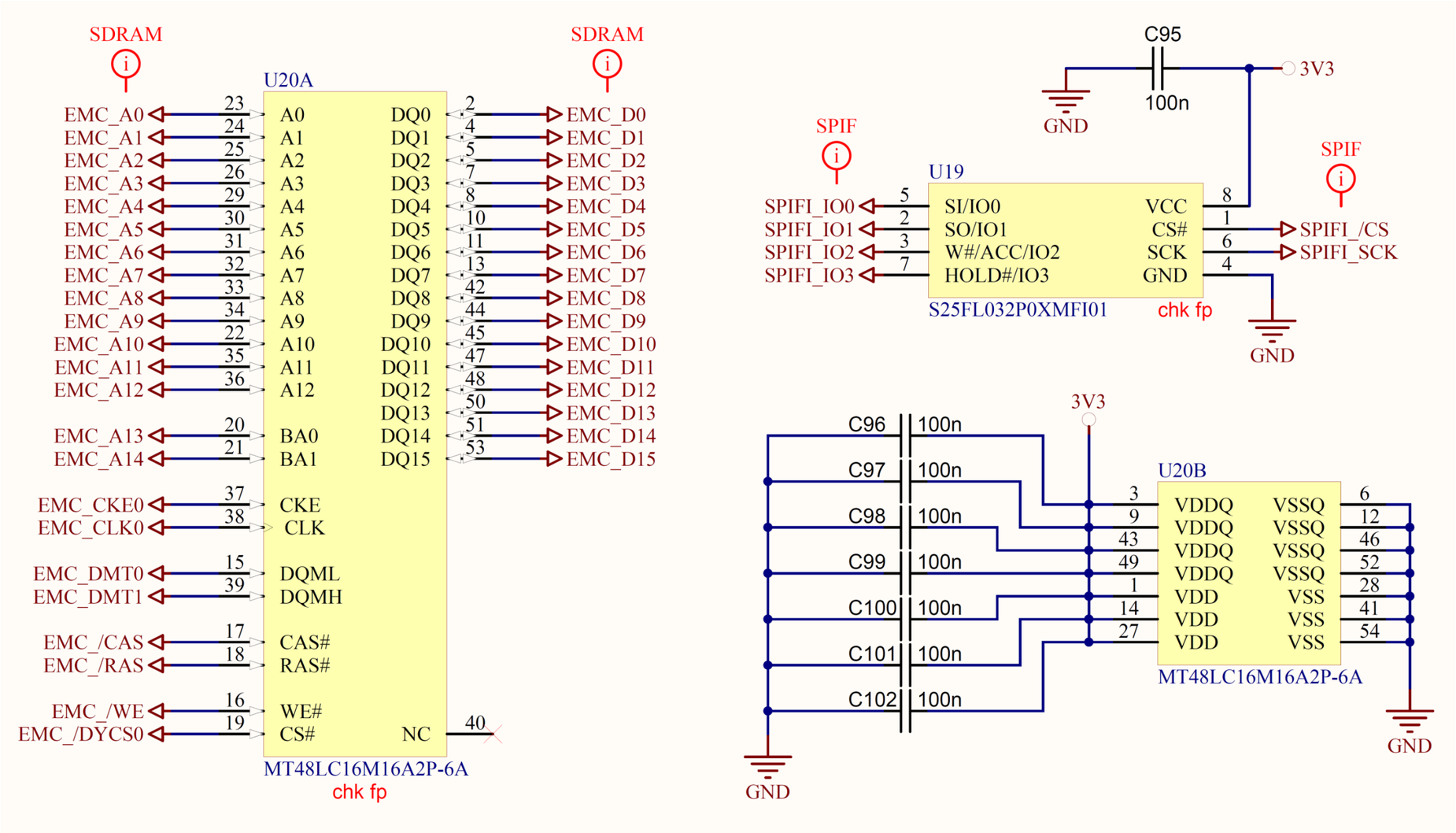
SDRAM
U20A
EMC_A0
EMC_A1
EMC_A2
EMC_A3
EMC_A4
EMC_A5
EMC_A6
EMC_A7
EMC_A8
EMC_A9
EMC_A10
EMC_A11
EMC_A12
EMC_A13
EMC_A14
EMC_CKE0
EMC_CLK0
EMC_DMT0
EMC_DMT1
EMC_/CAS
EMC_/RAS
EMC_/WE
EMC_/DYCS0
A0
A1
A2
A3
A4
A5
A6
A7
A8
A9
A10
A11
A12
BA0
BA1
CKE
CLK
DQML
DQMH
CAS#
RAS#
WE#
CS#
NC
DQ0
DQ1
DQ2
DQ3
DQ4
DQ5
DQ6
DQ7
DQ8
DQ9
DQ10
DQ11
DQ12
DQ13
DQ14
DQ15
EMC_D0
EMC_D1
EMC_D2
EMC_D3
EMC_D4
EMC_D5
EMC_D6
EMC_D7
EMC_D8
EMC_D9
EMC_D10
EMC_D11
EMC_D12
EMC_D13
EMC_D14
EMC_D15
MT48LC16M16A2P-6A
chk fp
C95
100n
3V3
GND
SPIF
U19
SPIFI_IO0
SPIFI_IO1
SPIFI_IO2
SPIFI_IO3
SI/IO0
SO/IO1
W#/ACC/IO2
HOLD#/IO3
VCC
CS#
SCK
GND
SPIFI_/CS
SPIFI_SCK
S25FL032P0XMFI01
chk fp
C96
C97
C98
C99
C100
C101
C102
U20B
VDDQ
VDD
VSSQ
VSS
MT48LC16M16A2P-6A

Appendix 07

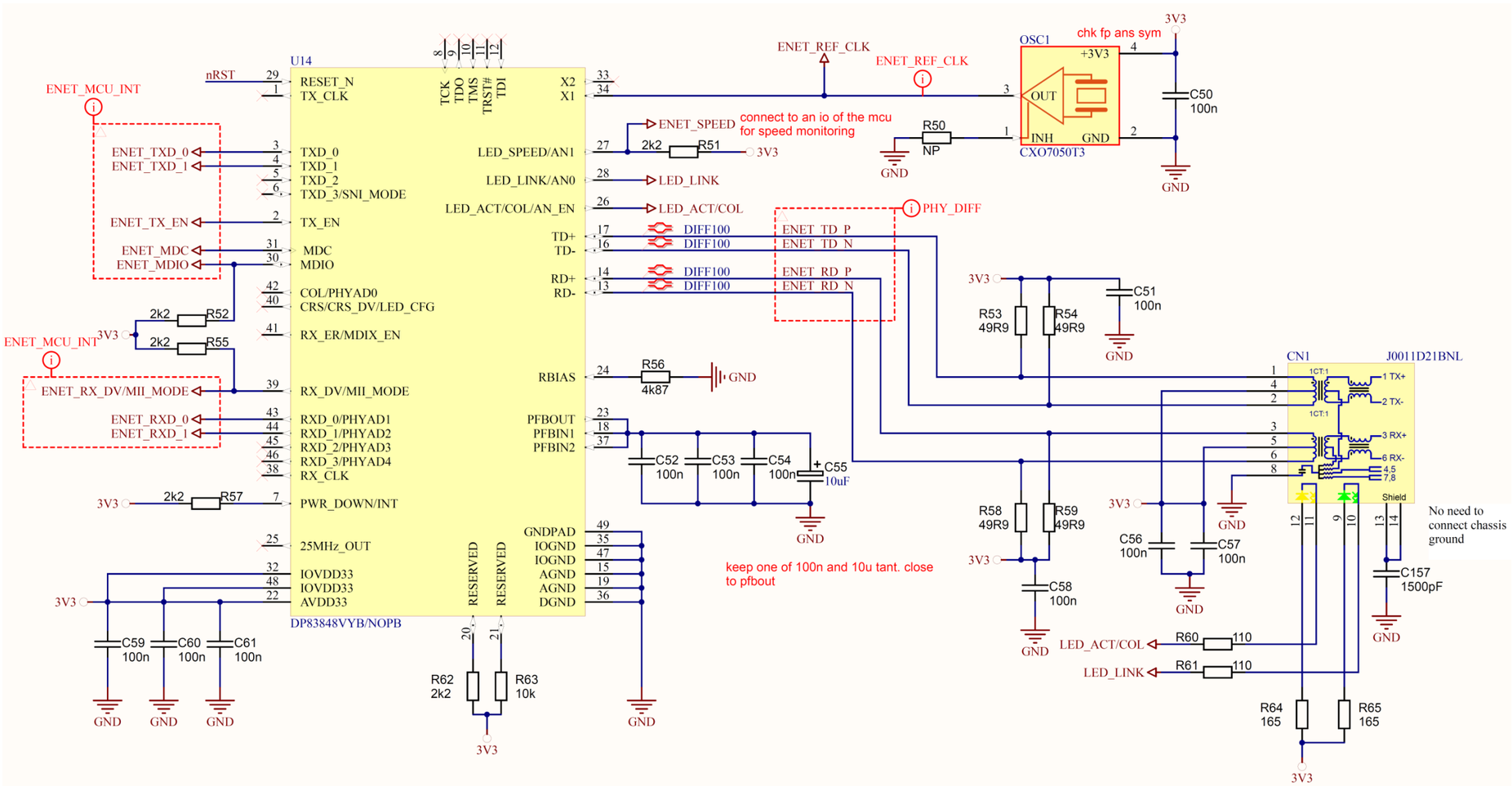
U14
DP83848VYB/NOPB
RESET_N
TX_CLK
TXD_0
TXD_1
TXD_2
TXD_3/SNI_MODE
TX_EN
MDC
MDIO
COL/PHYAD0
CRS/CRS_DV/LED_CFG
RX_ER/MDIX_EN
RX_DV/MII_MODE
RXD_0/PHYAD1
RXD_1/PHYAD2
RXD_2/PHYAD3
RXD_3/PHYAD4
RX_CLK
PWR_DOWN/INT
25MHz_OUT
IOVDD33
IOVDD33
AVDD33
RESERVED
RESERVED
TCK
TDO
TMS
TRST#
TDI
X2
X1
LED_SPEED/AN1
LED_LINK/AN0
LED_ACT/COL/AN_EN
TD+
TD-
RD+
RD-
RBIAS
PFBOUT
PFBIN1
PFBIN2
GNDPAD
IOGND
IOGND
AGND
AGND
DGND
nRST
ENET_MCU_INT
ENET_TXD_0
ENET_TXD_1
ENET_TX_EN
ENET_MDC
ENET_MDIO
ENET_RX_DV/MII_MODE
ENET_RXD_0
ENET_RXD_1
ENET_REF_CLK
ENET_SPEED
connect to an io of the mcu for speed monitoring
LED_LINK
LED_ACT/COL
PHY_DIFF
DIFF100
ENET_TD_P
ENET_TD_N
ENET_RD_P
ENET_RD_N
OSC1
chk fp ans sym
+3V3
OUT
INH
GND
CXO7050T3
3V3
GND
CN1
J0011D21BNL
1CT:1
1 TX+
2 TX-
3 RX+
6 RX-
4,5
7,8
Shield
No need to connect chassis ground
keep one of 100n and 10u tant. close to pfbout
LED_ACT/COL
LED_LINK
R50 NP
R51 2k2
R52 2k2
R53 49R9
R54 49R9
R55 2k2
R56 4k87
R57 2k2
R58 49R9
R59 49R9
R60 110
R61 110
R62 2k2
R63 10k
R64 165
R65 165
C50 100n
C51 100n
C52 100n
C53 100n
C54 100n
C55 10uF
C56 100n
C57 100n
C58 100n
C59 100n
C60 100n
C61 100n
C157 1500pF

Appendix 08

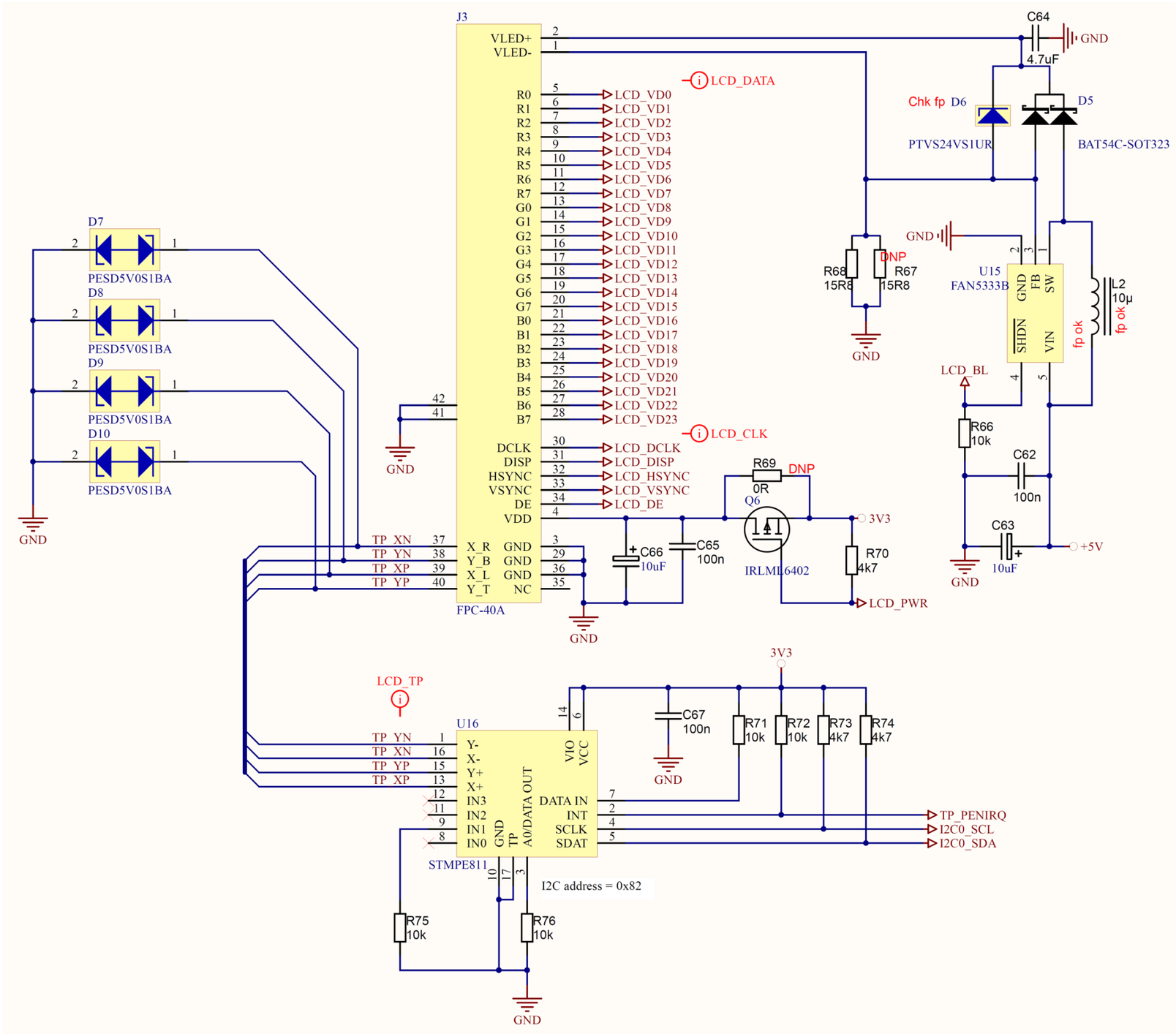
J3
VLED+
VLED-
R0
R1
R2
R3
R4
R5
R6
R7
G0
G1
G2
G3
G4
G5
G6
G7
B0
B1
B2
B3
B4
B5
B6
B7
DCLK
DISP
HSYNC
VSYNC
DE
VDD
X_R
Y_B
X_L
Y_T
GND
NC
LCD_VD0
LCD_VD1
LCD_VD2
LCD_VD3
LCD_VD4
LCD_VD5
LCD_VD6
LCD_VD7
LCD_VD8
LCD_VD9
LCD_VD10
LCD_VD11
LCD_VD12
LCD_VD13
LCD_VD14
LCD_VD15
LCD_VD16
LCD_VD17
LCD_VD18
LCD_VD19
LCD_VD20
LCD_VD21
LCD_VD22
LCD_VD23
LCD_DATA
LCD_CLK
LCD_DCLK
LCD_DISP
LCD_HSYNC
LCD_VSYNC
LCD_DE
TP_XN
TP_YN
TP_XP
TP_YP
FPC-40A
D7
D8
D9
D10
PESD5V0S1BA
GND
C64
4.7uF
Chk fp D6
PTVS24VS1UR
D5
BAT54C-SOT323
R68
15R8
DNP
R67
15R8
U15
FAN5333B
GND
FB
SW
SHDN
VIN
L2
10µ
fp ok
LCD_BL
R66
10k
C62
100n
C63
10uF
+5V
R69
0R
Q6
IRLML6402
3V3
C66
10uF
C65
100n
R70
4k7
LCD_PWR
LCD_TP
U16
Y-
X-
Y+
X+
IN3
IN2
IN1
IN0
VIO
VCC
DATA IN
INT
SCLK
SDAT
A0/DATA OUT
STMPE811
C67
100n
R71
10k
R72
10k
R73
4k7
R74
4k7
TP_PENIRQ
I2C0_SCL
I2C0_SDA
I2C address = 0x82
R75
10k
R76
10k

Appendix 09

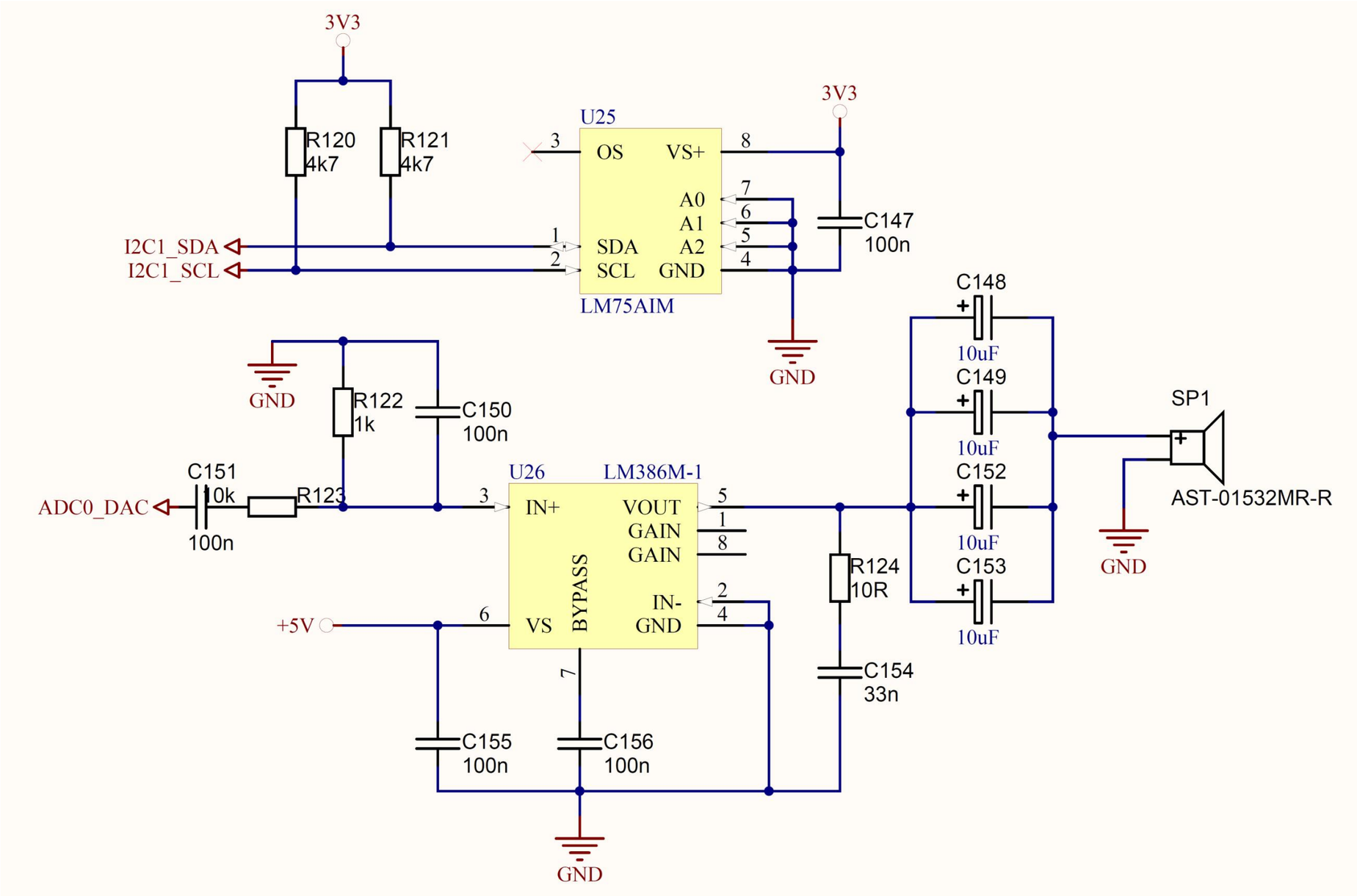
3V3
R120
4k7
R121
4k7
U25
OS
VS+
A0
A1
A2
SDA
SCL
GND
LM75AIM
3V3
C147
100n
I2C1_SDA
I2C1_SCL
GND
C148
10uF
C149
10uF
C152
10uF
C153
10uF
SP1
AST-01532MR-R
GND
GND
R122
1k
C150
100n
C151
10k
100n
ADC0_DAC
R123
U26
LM386M-1
IN+
VOUT
GAIN
GAIN
BYPASS
IN-
GND
VS
+5V
R124
10R
C154
33n
C155
100n
C156
100n
GND

Appendix 10

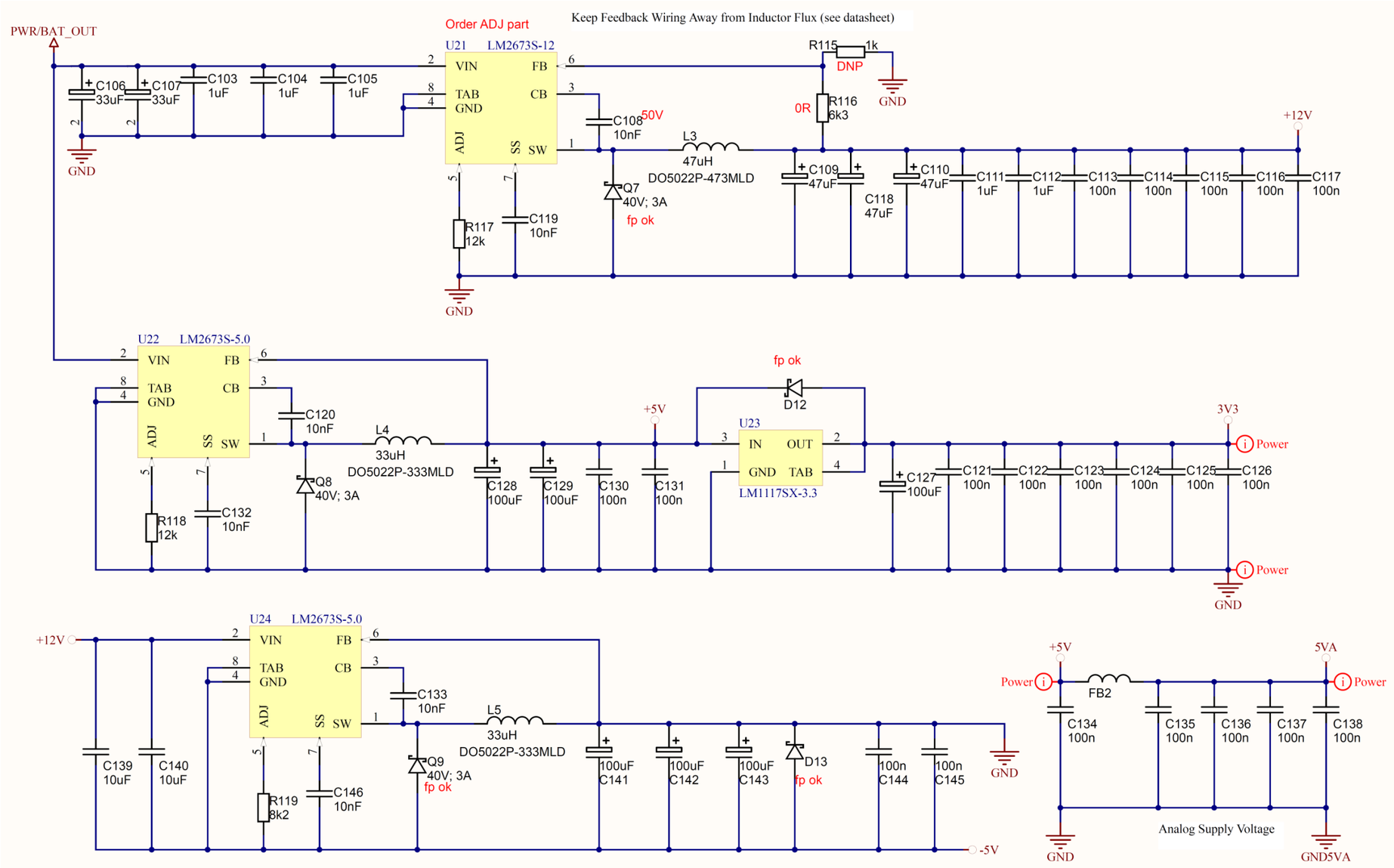
PWR/BAT_OUT
Order ADJ part
Keep Feedback Wiring Away from Inductor Flux (see datasheet)
U21 LM2673S-12
VIN
TAB
GND
ADJ
SS
FB
CB
SW
C106 33uF
C107 33uF
C103 1uF
C104 1uF
C105 1uF
C108 10nF
50V
L3 47uH
DO5022P-473MLD
Q7 40V; 3A
fp ok
R117 12k
C119 10nF
R115 1k
DNP
0R
R116 6k3
C109 47uF
C118 47uF
C110 47uF
C111 1uF
C112 1uF
C113 100n
C114 100n
C115 100n
C116 100n
C117 100n
+12V
GND
U22 LM2673S-5.0
C120 10nF
L4 33uH
DO5022P-333MLD
Q8 40V; 3A
R118 12k
C132 10nF
C128 100uF
C129 100uF
C130 100n
C131 100n
+5V
fp ok
D12
U23
IN
OUT
GND
TAB
LM1117SX-3.3
C127 100uF
C121 100n
C122 100n
C123 100n
C124 100n
C125 100n
C126 100n
3V3
Power
U24 LM2673S-5.0
C133 10nF
L5 33uH
DO5022P-333MLD
Q9 40V; 3A
fp ok
R119 8k2
C146 10nF
C139 10uF
C140 10uF
100uF C141
100uF C142
100uF C143
D13
fp ok
100n C144
100n C145
-5V
FB2
5VA
C134 100n
C135 100n
C136 100n
C137 100n
C138 100n
Analog Supply Voltage
GND5VA

Appendix 11

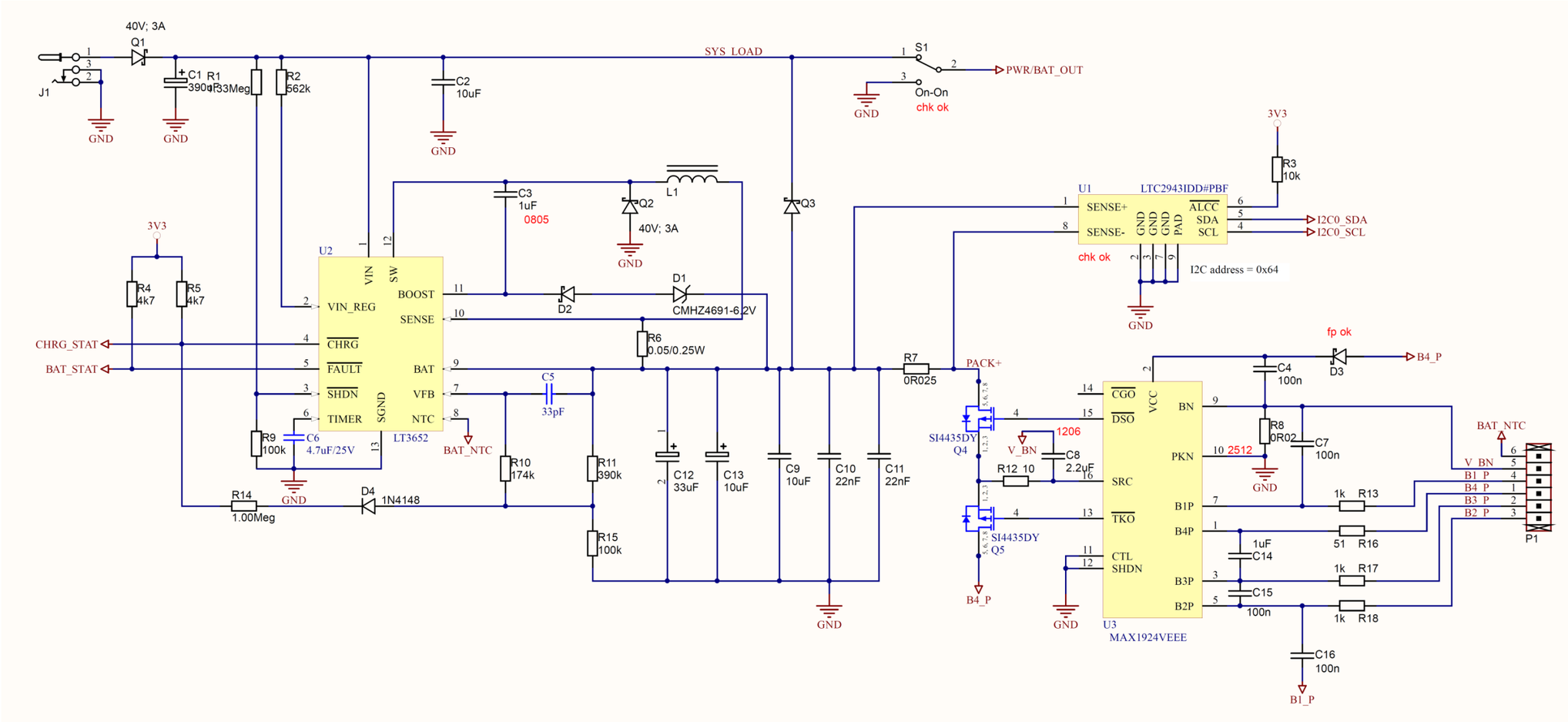
40V; 3A
Q1
J1
C1
390uF
R1
3.33Meg
R2
562k
C2
10uF
SYS_LOAD
S1
On-On
chk ok
PWR/BAT_OUT
GND
3V3
R3
10k
U1
LTC2943IDD#PBF
SENSE+
SENSE-
ALCC
SDA
SCL
I2C0_SDA
I2C0_SCL
chk ok
I2C address = 0x64
C3
1uF
0805
L1
Q2
40V; 3A
Q3
U2
VIN
SW
VIN_REG
BOOST
SENSE
CHRG
FAULT
SHDN
TIMER
BAT
VFB
NTC
SGND
LT3652
D1
CMHZ4691-6.2V
D2
R6
0.05/0.25W
R4
4k7
R5
4k7
CHRG_STAT
BAT_STAT
R9
100k
C6
4.7uF/25V
C5
33pF
BAT_NTC
R10
174k
R11
390k
R15
100k
R14
1.00Meg
D4
1N4148
C12
33uF
C13
10uF
C9
10uF
C10
22nF
C11
22nF
R7
0R025
PACK+
SI4435DY
Q4
SI4435DY
Q5
B4_P
V_BN
1206
C8
2.2uF
R12 10
CGO
DSO
SRC
TKO
CTL
SHDN
VCC
BN
PKN
B1P
B4P
B3P
B2P
U3
MAX1924VEEE
fp ok
D3
C4
100n
R8
0R02
2512
C7
100n
1k R13
51 R16
1k R17
1k R18
1uF
C14
C15
100n
C16
100n
B1_P
BAT_NTC
V_BN
B1_P
B4_P
B3_P
B2_P
P1